THÈSE

En vue de l'obtention du

DOCTORAT DE L'UNIVERSITÉ DE TOULOUSE

Délivré par :

Institut National Polytechnique de Toulouse (Toulouse INP)

Discipline ou spécialité :

Génie Electrique

Présentée et soutenue par :

M. ELIE HLEIHEL

le mardi 28 novembre 2023

Titre :

Optimisation multi objectif d'un micro-réseau DC

Ecole doctorale :

Génie Electrique, Electronique, Télécommunications (GEETS)

Unité de recherche :

Laboratoire Plasma et Conversion d'Energie (LAPLACE)

Directeurs de Thèse :

M. MAURICE FADEL

M. HADI KANAAN

Rapporteurs :

M. MOHAMED BENBOUZID, UNIVERSITE DE BRETAGNE OCCIDENTALE

M. NAZIH MOUBAYED, UNIVERSITE LIBANAISE

Membres du jury :

M. JOSEPH EL ASSAD, UNIVERSITE SAINT-ESPRIT DE KASLIK, Président

M. HADI KANAAN, UNIVERSITE ST JOSEPH DE BEYROUTH, Membre

M. MAURICE FADEL, TOULOUSE INP, Membre

MME FLAVIA KHATOUNIAN, UNIVERSITE ST JOSEPH DE BEYROUTH, Membre

M. RABIH JABR, UNIVERSITE AMERICAINE DE BEYROUTH, Membre

Acknowledgment

Closing this thesis after more than three years of research, I would like to thank all those who contributed to the accomplishment of this work, and who marked, by their presence, an essential step in my life.

Best regards to the members of the jury of this thesis for whom I am honored by their presence and participation in the evaluation of my work.

I am sincerely grateful to my thesis directors Professor Maurice Fadel and Professor Hadi Kanaan for their technical and moral support during the thesis, and for the trust and opportunities they offered to me. I was honored to participate with them in several International Conferences and have my name, as a co-author, next to theirs in several publications.

Much appreciation to the Plasma and Energy Conversion Laboratory (LAPLACE) at the Ecole Nationale Supérieure d'Electrotechnique, Electronique, Informatique, Hydraulique et des Télécommunications (ENSEEIHT) of the Institut National Polytechnique de Toulouse (INPT) who welcomed me during my visit to France. I would also like to thank the Centre des industries électriques et des télécommunications (CINET) at the École Supérieure d'Ingénieurs de Beirut (ESIB) of Saint Joseph University (USJ), which has offered me technical support from the engineering years, through the master's degree, to the Ph.D.

Many thanks to Professors Ragi Ghosn, Marc Ibrahim, and Jean Sawma, for their help and technical advice throughout the thesis.

Infinite gratitude to my friends Georges Saade, Anthony Hatem, Anthony Chalhoub, Bernard Makhraz, Charbel Habib, Hanaa Habib, Ralph Chamoun, Elie Nassar, Joe Feghali, Tony Nicolas, and Fadi El Nahri for offering me the moral support and being a second family, a big family, especially during hard moments.

To God, the cause of my existence and what I am today.
To my parents and two brothers Eddy and Etienne for their continued dedication and encouragement.

To my beloved Patron Saint Mother Teresa of Calcutta.

Table of content

List of Figures 1
List of Tables i
List of Acronyms 7
List of Symbols 9
Introduction 12
Chapter 1 : Review of Energy Management and Optimization Techniques Applied to DC Microgrids 18
1.1 The advent of centralized energy generation and related drawbacks 18
1.2 Distributed energy sources as alternatives to centralized energy generation 24
1.3 Microgrid concept and advantages of DC over AC microgrids 27
1.4 Control and energy management techniques in DC microgrids 30
1.4.1 Three-level hierarchical control 30
1.4.2 Tertiary control level to achieve smart energy management in DC microgrids 32
1.5 - Optimal sizing and optimal power scheduling of a DC Microgrid 33
1.5.1 - Optimal sizing of a DC Microgrid 33
1.5.2 -Optimal scheduling of a DC Microgrid 34
1.6 - Offline optimization based on heuristic, metaheuristic, and deterministic methods 35
1.6.1 - Heuristic and metaheuristic methods 35
1.6.2 - Deterministic methods 36
1.7 - Online optimization techniques 37
1.8 - Applied optimization strategy and main outcomes of this thesis 39
1.9 -Conclusion 41
Chapter 2 : Modeling of the 24-hour DC Microgrid 43
2.1 Introduction 43
2.2 Configuration, energy management problem formulation, and sizing of the DC microgrid 44
2.2.1 DC microgrid configuration 44
2.2.2 Energy management problem formulation 45
2.2.3 Sizing of the DC microgrid 47
2.3 Instantaneous and 24-hour DC microgrid modeling 49
2.4 PV energy conversion chain 50

2.4.1 PV array 50
2.4.2 DC/DC boost converter 51
2.4.3 DC/DC boost control strategy 60
2.5 Wind turbine energy conversion chain 63
2.5.1 Wind turbine model 63
2.5.2 Permanent magnet synchronous machine 66
2.5.3 3ϕ Rectifier 67
2.6 Diesel generator and utility-grid energy conversion chains 81
2.7 ESS conversion chain 82
2.7.1 Lithium-ion battery model 83
2.7.2 Bidirectional DC/DC converter 86
2.8 Simulation test of the 24-hour assembled DC microgrid 90
2.8.1 Applied EMS strategy 90
2.8.2 EMS control parameters and 24-hour variable input profiles 92
2.8.3 Simulation tests 94
2.9 Conclusion 101
Chapter 3 : DC Microgrid Offline Optimization 102
3.1 Introduction 102
3.2 Inclusion of input data and converters' losses in the DC microgrid configuration 103
3.2.1 Losses inclusion 104
3.2.2 Winter and summer days scenario 106
3.3 Total cost function in the absence of the ESS and the DG 108
3.4 Optimization objectives, cost function, and constraints 110
3.4.1 Operating cost function 111
3.4.2 Pollutant gas emissions cost function 113
3.4.3 Converters losses cost function 113
3.4.4 Problem constraints 114
3.5 Implementation of optimization approaches 116
3.5.1 Dynamic programming 117
3.5.2 Preference between optimization objectives 129
3.5.3 Genetic algorithm 135
3.6 Conclusion 144

Chapter 4 : DC Microgrid Online Optimization 146
4.1 Introduction 146
4.2 Online optimization stage 147
4.2.1 Online optimization stage target 148
4.3 Online optimization algorithm 149
4.3.1 GS algorithm 153
4.4 Simulation tests 167
4.5 Conclusion 180
Chapter 5 : Conclusion and Perspectives 182
Appendix A 189
A.1 PV module data 189
A.2 Incremental conductance MPPT technique 190
Appendix B 192
B.1 DC/DC boost components' selection and parameters calculation for conduction losses. 192
B.1.1 Diode selection 192
B.1.2 IGBT selection 192
B.2 DC/DC boost parameters calculation for switching losses 193
B.2.1 IGBT parameters 193
B.2.2 Calculation of t_{f_D} and I_{RM_D} 194
Appendix C 196
C.1 PMSM parameters 196
C.2 3ϕ rectifier IGBTs and diodes selection, and parameters calculation for conduction and switching losses 196
C.3 Optimal torque MPPT technique 197
Appendix D 201
D.1 Battery thermal expressions and parameters 201
D.2 Bidirectional DC/DC converter parameters 202
Appendix E 204
E.1 Battery-discretized dynamic model 204
E.2 Dynamic programming principle 205
Appendix F 207
F.1 Parameters of the " ga " function 207
References 209

List of Figures

Fig.1.1 Transmission and distribution losses in the World, EU, U.S., and China. 19
Fig.1.2 Access to electricity, rural is the percentage of the rural population with access to electricity in 2020. 20
Fig.1.3 Annual major U.S utility spending on electric distribution (2000-2019) 21
Fig.1.4 U.S. electric distribution spending, customers, and retail electricity sales (2000-2019). 21
Fig.1.5 Average duration of total annual electric power interruptions, U.S (2013-2020). 22
Fig.1.6 Average total annual electric power interruption duration and frequency per customer, by U.S. state (2020). 23
Fig.1.7 Share of electricity production from fossil fuels, 2021. 24
Fig.1.8 Carbon intensity of electricity for 2021. 25
Fig.1.9 Annual U.S. short-term energy outlook for electric sector generation by energy source (2012-2023) 26
Fig.1.10 Primary energy production of EU28 (1970-2020). 27
Fig.1.11 Hierarchical control of a DC microgrid. 30
Fig.1.12 A basic simplified diagram example of an MPC-based optimization technique. 38
Fig.2.1 DC microgrid applied configuration. 45
Fig.2.2 Flow chart of the general EMS strategy. 47
Fig.2.3 PV array conversion chain. 51
Fig.2.4 PV array electrical circuit. 51
Fig.2.5 Electrical circuit of the DC/DC boost converter (detailed model). 52
Fig.2.6 Electrical circuit of the DC/DC boost converter (average model). 53
Fig.2.7 DC bus voltage of the DC/DC boost in the detailed and average model representations (on the left side: the whole curves over the full-time simulation, on the right side: a zoom over the transient state) 54
Fig.2.8 Inductor current of the DC/DC boost in the detailed and average model representations (on the left side: the whole curves over the full-time simulation, on the right side: a zoom over the transient state). 54
Fig.2.9 Electrical circuit of the DC/DC boost converter including the conduction and switching losses. 56
Fig.2.10 Approximation of (a) IGBT voltage and current, (b) diode reverse recovery current and voltage during the switching time interval. 58
Fig.2.11 PV array characteristics ($S = 1000\ W/m^2$, $T = 25°C$) (a) $I_{PV} = f(V_{PV})$, (b) $P_{PV} = f(V_{PV})$, and (c) $V_{PV} = f(D_{PV})$ 59
Fig.2.12 The total losses, the conduction losses, and the switching losses as functions of V_{PV} ... 60
Fig.2.13 Boost converter efficiency in (%) as a function of D_{PV}. 60
Fig.2.14 $PPV = f(V_{PV}, S)$ characteristic for a constant temperature ($T = 25°C$). 61

Fig.2.15 $P_{PV} = f(V_{PV}, T)$ characteristic for a constant irradiance ($S = 1000\ W/m^2$). 61
Fig.2.16 Block diagram of the lookup table MPPT control. 62
Fig.2.17 Comparison between the proposed lookup table and incremental conductance MPPT techniques. 63
Fig.2.18 Wind turbine energy conversion chain. 64
Fig.2.19 Turbine power characteristics as a function of the turbine speed for different wind speeds. 65
Fig.2.20 Simulink Block diagram of the pitch angle controller. 66
Fig.2.21 Electrical circuit of the 3ϕs rectifier (detailed model). 67
Fig.2.22 Electrical circuit of the 3ϕs rectifier (average model). 70
Fig.2.23 Three-phase voltages representation in the time domain (on the right) and phasor domain (on the left). 71
Fig.2.24 Block diagram of the complex (dq) and positive sequence power control. 73
Fig.2.25 (a) Active, and (b) reactive power curves of the three models. 75
Fig.2.26 (a) current waveforms of $ia(t)$ in the detailed and average models, the magnitude, and phase shift of i_a in the phasor model (b) A zoom of i_a curves of the three models ($1.96s \leq t \leq 2.04s$). 75
Fig.2.27 (a) A zoom on the phase to neutral voltage V_{AN} waveforms of the detailed and average models, the magnitude, and phase-shift of V_{AN} in the phasor model ($1.78s \leq t \leq 1.83s$), (b) common DC bus voltage (V_{BUS}) of the detailed, average, and phasor models. 76
Fig.2.28 (a) 3ϕ rectifier losses as a function of the input electrical power, (b) efficiency of the 3ϕ rectifier losses as a function of the input electrical power. 78
Fig.2.29 Block diagram of the (WT) (dq) frame control in the phasor domain. 79
Fig.2.30 MPPT characteristic for different wind speed values. 79
Fig.2.31 The mechanical and electrical wind power, and the 3ϕ rectifier power output as functions of the wind speed. 80
Fig.2.32 The PMSM power efficiency in (%) as a function of the mechanical wind power. 81
Fig.2.33 ESS conversion chain. 82
Fig.2.34 The battery voltage discharge curve as a function of the SOC at $0.43C$ ($217.4\ A$). 84
Fig.2.35 (a) Battery voltage discharge characteristic for different constant discharge currents at 25°C, (b) voltage discharge characteristic at a constant current of $1C$ ($500A$) for variable temperatures. 85
Fig.2.36 Electrical circuit of the bidirectional DC/DC converter (detailed model). 87
Fig.2.37 (a) Bidirectional DC/DC converter total losses, conduction, and switching losses in boost operating mode (b) in buck operating mode. 89
Fig.2.38 Bidirectional DC/DC converter power efficiencies curves in boost and buck operating modes. 89
Fig.2.39 Flow chart of proposed EMS strategy. 91

Fig.2.40 Battery-cascaded loop control. 92
Fig.2.41 Variable Input profiles: (a) Irradiance (W/m^2), (b) Temperature (°C), (c) Wind speed (m/s), and (d) residential load demand (W). 93
Fig.2.42 Power flow of all operating units of the 24-hour DC microgrid model in (W). 94
Fig.2.43 (a) Losses in all operating converters in (W) and (b) Common DC bus voltage in (V). 95
Fig.2.44 (a) Battery's voltage (V) and (b) SOC (%)..... 95
Fig.2.45 Obtained PV (a) power and (b) boost-losses of the detailed and 24-hour models. 96
Fig.2.46 WT (a) mechanical power, (b) electrical power, (c) (dq) current components, (d) phase A current, (e) phase A to neutral voltage, and (f) losses in PMSM and 3Φ rectifier of the detailed and 24-hour models..... 97
Fig.2.47 DG (a) power, (b) (dq) axes current components, (c) losses in 3Φ rectifier, and (d) phase A to neutral voltage of the detailed and 24-hour models..... 98
Fig.2.48 Utility grid (a) power, (b) (dq) current components, (c) losses in 3Φ converter, (d) Phase A current, and (e) Zoom on phase A current of the detailed and 24-hour models. 99
Fig.2.49 Battery (a) power, (b) voltage, (c) losses in the bidirectional DC/DC converter, (d) SOC, (e) common DC bus voltage, and (f) cell temperature of the detailed and 24-hour models..... 100
Fig.3.1 DC microgrid configuration……...105
Fig.3.2 (a) Wind speed, irradiance, and temperature profiles of the winter day (18/02/2021), (b) of the summer day (16/07/2021). 106
Fig.3.3 (a) The PV and wind-generated power on the winter day (18/02/2021), (b) on the summer day (16/07/2021). 107
Fig.3.4 (a) The residential load, the RESs power profiles, and the electricity pool price on the winter day (18/02/2021), (b) on the summer day (16/07/2021)..... 108
Fig.3.5 Piecewise approximation of the (DG) fuel consumption function. 113
Fig.3.6 Discretization of the decision variables to states characterized by a time step Δt: (a) SOC discretized with a sampling step ΔSOC and (b) P_{DG_ref} discretized with a sampling step ΔP_{DG}. 118
Fig.3.7 (a) Example of two admissible control strategies π and π' in the SOC state space (b) Example of two admissible control strategies π and π' in the PDG_ref state space. 120
Fig.3.8 Illustrative diagram of the applied DP algorithm. 125
Fig.3.9 Optimal (DG), batteries, and grid power references on (a) the winter day and (b) the summer day. 126
Fig.3.10 Battery's SOC optimal trajectories on (a) the winter day and (b) the summer day. 126
Fig.3.11 Toxic gas emissions on (a) the winter day and (b) the summer day. 127
Fig.3.12 Losses in (DG), battery, and grid converters on (a) the winter day and (b) the summer day. 127

Fig.3.13 (a) E_{DG}, (b) E_{loss_conv}, and (c) J_{oc} as functions of ζoc, ζconv-losses for ζemissions= 1. 130
Fig.3.14 (a) E_{DG}, (b) E_{loss_conv}, and (c) J_{oc} as functions of ζemissions, ζconv-losses for ζoc= 1. 132
Fig.3.15 (a) E_{DG}, (b) E_{loss_conv}, and (c) J_{oc} as functions of ζoc, ζemissions for ζconv-losses= 1. 133
Fig.3.16 General structure of the (GA). 136
Fig.3.17 (GA) operation flow chart. 137
Fig.3.18 Parameters to be optimized forming a chromosome or an individual. 139
Fig.3.19 (GA) results of optimal (DG), battery, and grid power references on (a) the winter day and (b) the summer day. 141
Fig.3.20 (GA) results of optimal trajectories of the battery's SOC on (a) the winter day and (b) the summer day. 141
Fig.4.1 Block diagram of the applied offline and online optimization stage……...148
Fig.4.2 Flow chart of the proposed online optimization controller. 150
Fig.4.3 Illustrative example of $P_{DG_ref_online}(k^*)$ for the first and second sampling steps. 152
Fig.4.4 Illustrative example of $P_{batt_ref_online}(k^*)$or the first and second sampling steps. 153
Fig.4.5 Flow chart of the main steps performed by the GS when running. 164
Fig.4.6 An illustrative example of a two-dimensional variable curve plotted in the space as a function of the objective function, showing the basins of attraction and GS-generated trial points. 165
Fig.4.7 Predicted and actual data inputs P_{diff} and δ_{purch}^{grid} on the winter day (18/02/2021). 169
Fig.4.8 Predicted and actual data inputs P_{diff} and δ_{purch}^{grid} on the summer day (16/07/2021). ... 169
Fig.4.9 Winter Day (18/02/2021) results of (a) the grid power, (b) (DG) power, (c) battery power, and (d) the battery's SOC with and without online optimization stage. 170
Fig.4.10 Summer Day (16/07/2021) results of (a) the grid power, (b) (DG) power, (c) battery power, and (d) the battery's SOC with and without online optimization stage. 171
Fig.4.11 Predicted electricity pool price and applied actual scenarios of simulation test 2. 174
Fig.4.12 Predicted total energy difference and applied actual scenarios of simulation test 2. ... 175
Fig.4.13 Absolute value of ΔJ_{oc} as a function of E_{diff} for different δ_{purch}^{grid} mean values. 177
Fig.4.14 $\Delta Mgas$ (%) *as* a function of $Ediff$ for different $\delta gridpurch$ mean values. 177
Fig.4.15 (a) ΔE_{pur} (%), (b) ΔE_{sold} (KWh), (c) ΔE_{dis_batt} (%), and (d) ΔE_{ch_batt} (%) as a function of E_{diff} for different δ_{purch}^{grid} mean values. 178
Fig.a.1 SunPower SPR -415E-WHT-D module data. 189
Fig.b.1 (a) $I_f = f(V_f)$, and (b) $I_c = f(V_{CE})$ characteristics from the Infineon datasheets. 193

Fig.b.2 (a) diode switching losses $E_{rec} = F(I_f)$, (b) approximation of the reverse recovery current and reverse voltage. 195
Fig.c.1 (a) $I_f = f(V_f)$, and (b) $I_c = f(V_{CE})$ characteristics from the Infineon datasheets. 198
Fig.c.2 The block diagram of optimal torque control MPPT method. 199
Fig.c.3 MPPT characteristic curve as a function of the wind speed ($p.u.$ of rated wind speed). 200

List of Tables

Table 2.1 Sizing of DC microgrid principal units. 49
Table 2.2 Parameters of the three models. 75
Table 2.3 Comparison of simulation duration and calculation step size in the detailed, average, and phasor models. 76
Table 2.4 EMS and regulators control parameters. 93
Table 3.1 Cost functions for the two operating days in the absence of ESS and (DG). 110
Table 3.2 Optimization parameters. 116
Table 3.3 Summary of share of the energy mix and corresponding operating costs on the winter day (18/02/2021). 128
Table 3.4 Summary of share of the energy mix and corresponding operating costs on the summer day (16/07/2021). 129
Table 3.5 Optimal weights and corresponding results for $\zeta emissions = 1$ and different goals preferences. 131
Table 3.6 The minimum and maximum E_{DG}, E_{loss_conv}, and J_{oc} obtained results with the corresponding weights' combination. 134
Table 3.7 (GA) Standard operators. 138
Table 3.8 Parameters for setting the (GA) functions. 138
Table 3.9 (GA) summary results of the share of the energy mix and corresponding operating costs on the winter and summer days. 142
Table 3.10 Comparison between (DP) and (GA) 143
Table 4.1 Corresponding inequality and equality constraints of all operating conditions……..161
Table 4.2 Parameters for setting the *fmincon* solver. 162
Table 4.3 Applied parameters of the GS algorithm. 167
Table 4.4 Summary of the obtained results with and without the online optimization stage on the winter day (18/02/2021). 173
Table 4.5 Summary of the obtained results with and without the online optimization stage on the summer day (16/07/2021). 173
Table 4.6 All possible scenarios of simulation test 2 175
Table 4.7 Results of the ten applied scenarios of simulation test 2. 176
Table.D.1 Lithium-ion battery parameters extracted from MATLAB/Simulink. 202

List of Acronyms

RES	: Renewable Energy Sources
DER	: Distributed Energy Resources
ESS	: Energy Storage System
EMS	: Energy Management System
LVDC	: Low Voltage DC
DG	: Diesel Generator
WT	: Wind Turbine
MPPT	: Maximum Power Point Tracking
DP	: Dynamic Programming
GA	: Genetic Algorithm
GS	: Global Search
IEA	: International Energy Agency
O&M	: Operations and Maintenance
IRENA	: International Renewable Energy Agency
UNSD	: United Nations Statistics Division
WHO	: World Health Organization
FERC	: Federal Energy Regulatory Commission
T&D	: Transmission and Distribution
MPC	: Model Predictive Control
CC	: Central Control
PMSM	: Permanent Magnet Synchronous Machine
FLC	: Fuzzy Logic Control
MILP	: Mixed-Integer Linear Programming
NLP	: Non-Linear Programming
PSO	: Particle Swarm Optimization

SA : Simulated Annealing

GWO : Grey Wolf Optimization

SQP : Sequential Quadratic Programming

MINLP : Mixed-Integer Nonlinear Programming

RHC : Receding Horizon Control

lb : lower bound

ub : upper bound

WGN : White Gaussian Noise

NOAA : National Oceanic and Atmospheric Administration

CAIT : Climate Analysis Indicators Tool

STC : Standard Test Conditions

List of Symbols

P_{load} : Load power in (W)

P_{RESs} : RESs power in (W)

P_{wind_m} : Wind mechanical output power in (W)

S_{ref} : Reference irradiance at STC in (W/m^2)

V_{BUS} : Common DC voltage in (V)

v_{wind_pred} : Predicted wind speed in (m/s)

S_{pred} : Predicted solar irradiance in (W/m^2)

T_{a_pred} : Predicted ambient temperature in ($°C$)

$\delta_{grid_pred}^{pur}$: Electricity purchased price in ($¢/KWh$)

$P_{grid_ref_online}$: Optimal online grid power reference in (W)

$P_{batt_ref_online}$: Optimal online battery power reference in (W)

$P_{DG_ref_online}$: Optimal online (DG) power reference in (W)

N : Number of total sampling steps for the whole-time horizon

N^* : Number of total intrasample steps for the whole-time horizon

J_{oc} : Operation cost function in ($)

J_{batt} : Battery cost function in ($)

J_{DG} : (DG) cost function in ($)

J_{RESs} : RESs cost function in ($)

J_{grid} : Utility grid cost function in ($)

$\delta_{PV}^{O\&M}$: (O&M) cost per KWh of the PV in ($/KWh$)

$\delta_{WT}^{O\&M}$: (O&M) cost per KWh of the WT in ($/KWh$)

δ_{deg} : Degradation cost of the battery in ($/W^2h$)

f_{sw_PV} : Switching frequency of the PV' DC/DC boost in (Hz)

f_{sw_WT} : Switching frequency of the WT' 3ϕs rectifier in (Hz)

$Cycles$: Number of life cycles of the battery

SOC : State of charge of the battery in (%)

λ_{fuel} : Price of diesel per liter in ($\$/L$)

J_{DG}^{fuel} : Fuel consumption cost function in ($)

T_{is} : Intrasample period of the online optimization stage in (hours)

T_s : Sampling period of the offline optimization in (hours)

P_{DG_min} : Minimum admissible operating power of (DG) in (W)

ΔP_{batt_min} : Minimum allowable variation in the battery reference power in (W)

ΔP_{batt_max} : Maximum allowable variation in the battery reference power in (W)

SOC_{min} : Minimum admissible SOC value in (%)

SOC_{max} : Maximum admissible SOC value in (%)

P_{diff} : Power difference between the load and RESs in (W)

E_{diff_pred} : Predicted energy difference between the load and RESs in (KWh)

E_{diff_actual} : Actual energy difference between the load and RESs in (KWh)

ΔE_{pur} : Difference in purchased energy from the utility grid in (%)

ΔM_{gas} : Difference in total emitted toxic gas in (%)

ΔE_{sold} : Difference in sold energy to the utility grid in (KWh)

GA_{CT} : Convergence time of (GA) in (minutes)

DP_{CT} : Convergence time of (DP) in (minutes)

$c_p(\lambda, \beta)$: Performance coefficient of the turbine

η_{PMSM} : Efficiency of WT' PMSM in (%)

η_{boost} : Efficiency of DC/DC boost in (%)

P_{boost_looses} : Total losses in DC/DC boost in (W)

λ_i : Nominal tip speed ratio of the rotor blade tip speed to wind speed

β : Blade pitch angle of the WT in (degree).

Q_{batt} : Maximum battery capacity in (Ah)

β_{emiss} : Penalty coefficient of pollutant gas emissions in ($\$/KWh$)

$J_{emissions}$: Pollutant gas emissions cost function in ($)

J_{conv_losses} : Converters losses cost function in ($)

δ_{batt}^{loss} : Penalty coefficient for the losses in battery's converter in ($\$/KWh$)

δ_{DG}^{loss} : Penalty coefficient for the losses in DG's converter in ($\$/KWh$)

δ_{grid}^{loss} : Penalty coefficient for the losses in grid's converter in ($\$/KWh$)

ξ_{SU} : Start-up cost of the (DG) in ($)

σ_{DG}^{ON} : Binary variable equal to one if the (DG) is ON and zero otherwise

χ_M : Maintenance cost per hour of the (DG) in ($\$/h$)

CC : Battery capital cost per KWh in ($/KWh$)

DoD : Depth of discharge of the battery in (%)

Introduction

Thanks to the advent of alternating current and transformers, the shift from reciprocating engines to steam turbines, the low prices of fuel, the regulations and strategic policies, and the ease of overseeing and control, etc. electricity production in centralized power plants was favored since the 20th century. Then, in the late 20th, several drawbacks related to centralized power generation emerged such as the limitation in thermal efficiency of steam turbines, the high transmission and distribution losses, the high investments in transmission and distribution networks, the single point of failure, cascading outages, and the cyber and physical attacks. Due to all these downsides, the distributed generation approach was advanced as an alternative or supplement to centralized power generation.

Another setback of centralized power generation is that predominant electricity central power plants are of fossil fuel origins (coal, oil, and natural gas). Fossil fuels are being depleted and are the main producers of carbon dioxide emissions and other greenhouse gases, the principal cause of global climate change and the earth's temperature rise. A substantial increase in global carbon dioxide emissions from fossil fuels was noted with 6 billion tons of CO2 emissions in 1950, and 34.81 billion tons in 2020. This sharp rise in CO2 emissions and greenhouse gases during the last 70 years, is strongly related to and initiated the increasing rate of the average temperature per decade. The earth's global average surface temperature has roughly increased one degree Celsius since the preindustrial era (1880-1900). As a result of the increase in the global earth's average temperature, many other aspects of the global climate are changing. Several kinds of research documented changes in surface, atmospheric, and oceanic temperatures; melting glaciers; diminishing snow cover; shrinking sea ice; rising sea levels; ocean acidification; increasing atmospheric water vapor; and increasing heat waves and cold spells.
To alleviate this critical risk and impact, nearly 200 nations committed to holding the average earth temperature to well below 2 degrees Celsius in the 2015 Paris Climate Agreement. This is being realized by setting net-zero emissions targets for countries that have pledged to achieve this target in future years. Lately, in November 2021, countries participating in major UN climate talks (COP26) in Glasgow, Scotland, are announcing more ambitious plans for slashing their emissions for the next decade. the European Union (EU), setting a binding target to achieve climate neutrality by 2050, has further raised its 2030 climate ambition beyond the target agreed upon in 2018, committing to cutting greenhouse gas emissions by at least 55% by 2030 under the so-called “Fit for 55” package. All these plans and pledges of decarbonization essentially require a massive integration of renewable energy sources to shift the electricity generation mix and engender a large reduction in fossil fuel energy generation. Hence, the worldwide rapid expansion of renewable energy sources which are being integrated with different sizes and power scales ranging from a few KWs to GWs, contributed to the diversion from the centralized generation approach to the distributed one.

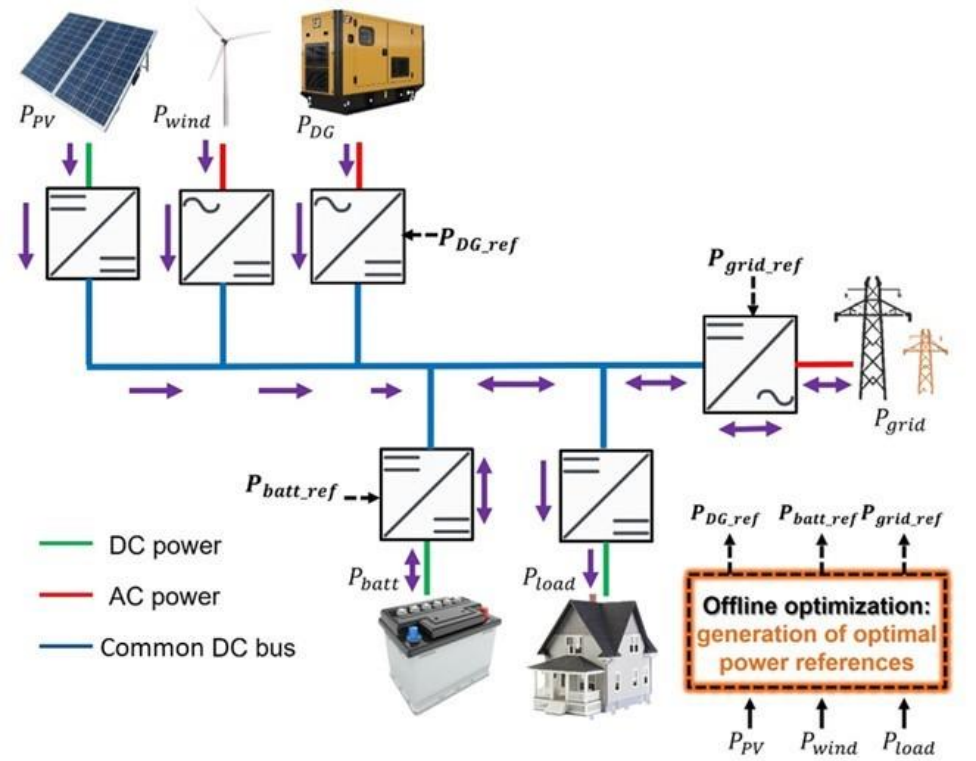
On the other hand, at the beginning of the 21st century and with the proliferation of distributed generation and renewable energy sources, the microgrid concept was proposed as a group of interconnected sources and loads that act as a single controllable entity to the grid. A microgrid can include several distributed energy resources (DERs) such as traditional pollutant ones, renewable energy sources, energy storage systems (ESSs), and a variety of loads. All these DERs are interconnected by local converters to a common bus that can be of AC or DC type. The common bus type defines whether the microgrid is of AC or DC type. Thanks to their maturity and standardization, AC microgrids prevailed and first captivated the attention of researchers more than DC microgrids. Since the last decade, high penetration of DC-type sources, ESS, and loads has been remarked. The expansion of RESs of which several are of a DC nature such as solar panels raised concern about power stability and availability due to the intermittent and unpredictable nature of RESs. The existence of a backup (ESS) is mandatory in such applications to secure an uninterruptible power supply for the microgrid. From here, increasing integration and reliance on (ESS)s such as batteries, and fuel cells which are of a DC nature is noted in microgrid applications. Moreover, owing to the advancement of power electronic devices, the number of DC-type loads such as laptops, phone devices, telecom equipment, etc. is surging. Due to all these grounds, and others such as the ease of control of DC systems, etc. DC microgrids have gained increased interest from researchers during the last decade. In this context, this thesis targets the power control and the energy management of a DC microgrid configuration consisting of RESs, traditional pollutant sources, loads, and an ESS.

Following the control objectives and the dynamic of targeted variables, the control of a DC microgrid is subdivided into three hierarchical levels. Known as the three-level hierarchical control, it is commonly investigated in the literature, especially the primary control level of which droop control is one of the most used techniques that ensures proper load sharing and common DC bus voltage stabilization. On the secondary level, decentralized coordination functions exist, e.g., local adaptive calculation of virtual resistances in which the robustness and stability of the primary control level are enhanced. The primary and secondary control levels target fast electrical variables to secure the stable operation of the DC microgrid and ensure robust power control. As redundant research can be found on these two control levels, lately, the tertiary control level is captivating the attention of researchers to achieve advanced energy management functionalities under the so-called “smart” control.

At the tertiary control level, optimization problems are formulated to attain one or several objectives. Following the objectives, the DC microgrid planning problem can be divided into three main categories: the optimal power generation mix selection and sizing, the optimal siting problem, and the optimal operation scheduling. In this thesis, the optimal operation scheduling, also known as the optimal energy management system (EMS) of a DC microgrid over a 24-hour time horizon is addressed to reach three distinct optimization goals. The optimization objectives were selected based on current international energy policies and targets for reducing carbon

dioxide emissions and saving energy by minimizing the losses in operating devices. Hence, the three main objectives of the optimal EMS are the minimization of the total operating cost of the DC microgrid, the reduction of pollutant gas emissions, and the improvement of converters' efficiency by minimizing converters' losses.

Accordingly, the work targeted by this thesis concerns a multisource DC microgrid combining RESs (photovoltaic, wind) and carbon energy via a Diesel Generator (DG), all connected to a distribution network and benefiting from an energy storage system. The prime objective is to meet consumer demand while favoring renewable energies and minimizing the cost of energy used while considering the operation and maintenance (O&M) costs of all operating units. For this, the efficiency of all devices is considered as well as the cost of purchased and sold energy from/to the grid. The DC microgrid configuration is depicted in the figure below.



The thesis manuscript consists of five chapters:

- Chapter 1: Review of energy management and optimization techniques applied to DC microgrids.
- Chapter 2: Modeling of the 24-hour DC Microgrid.
- Chapter 3: DC Microgrid Offline Optimization.
- Chapter 4: DC Microgrid Online Optimization.
- Chapter 5: Conclusion and Perspectives.

In Chapter 1, the shift from centralized energy generation to the distributed approach is first reviewed in detail. Then, the proliferation of the microgrid concept, especially DC ones along with the application of three-level hierarchical control are presented. Relevant research works on the tertiary control level are revealed as the thesis targets the optimal energy management of the DC microgrid. To ensure advanced EMS functionalities and attain predefined objectives, optimization problems are formulated and solved using metaheuristic or deterministic techniques. The commonly used metaheuristic and deterministic offline optimization techniques are stated. In addition to the offline optimization achieved the day ahead for the next 24 hours, an online optimization stage is suggested in the scope of this thesis to update the optimal references due to the existent mismatches between predicted and actual data. Thereby, the predominant online optimization techniques such as the receding horizon control are presented, and finally the main outcomes of the thesis are stated at the end of this chapter.

The modeling of the 24-hour DC microgrid is addressed in Chapter 2. First, the adopted configuration, the sizing, and the general EMS strategy of the DC microgrid are presented. The microgrid studied in this thesis is a low-voltage DC microgrid (LVDC) for residential loads with a common DC bus voltage reference of 800V. It consists of a PV array and a wind turbine as RESs, a backup diesel generator (DG) as a traditional pollutant source, a lithium-ion battery as ESS, and residential-type loads. Besides, the DC microgrid can operate in grid-connected as well as islanded modes following the EMS strategy of operation. Having set optimization goals over 24 hours, the hurdle of modeling the overall DC microgrid over the whole time horizon on a computer with limited CPU and memory is confronted. In most existing research works, simplified models of sources in steady state are adopted, and primary and secondary control levels of converters such as the MPPT are omitted to make the modeling of the 24-hour DC microgrid a viable solution. Though this simplified modeling strategy yields decent results, it induces computing errors of generated power, existing losses, etc. which are rarely addressed in the literature. In this chapter, the 24-hour modeling problem is confronted from a new perspective. First, the proposed approach presents a detailed model of each unit, converter, and corresponding strategy of control apart. Then, new averaging techniques are advanced to create the best trade-off between model precision, complexity, and simulation speed. The accuracy of each new averaging technique in reducing the model complexity and maintaining accurate modeling is verified through the comparison with the detailed models. The same approach is adopted to model operating units, converters, secondary control level techniques such as the MPPT, and the losses in operating converters. Finally, the assembled 24-hour DC microgrid model is validated through a comparison with the overall detailed model in two identical 15-minute simulations. Therefore, the 24-hour DC microgrid model is adopted in the next chapter to formulate the optimization problem.

The offline optimization accomplished the day ahead is detailed in Chapter 3. To mimic a real scenario, real profile data of solar irradiance, wind speed, ambient temperature, residential load

profile, and electricity pool prices are applied to winter and summer day case studies. Based on the predicted data for the next day, the offline optimization problem outputs the optimal power references of dispatchable sources for the next 24 hours. An optimization problem is formulated by setting a unique objective function to minimize. To include the three predefined optimization goals in one objective function, they are established as distinct cost functions expressed in $. Thus, the total objective function is formulated as a weighted sum of the three cost functions and expressed in $. Besides its mathematical necessity to yield a homogeneous objective function equation, the representation of the three cost functions in $ leads to a unified total energy bill. The obtained energy bill consists of the operating cost of the DC microgrid and penalty costs due to the emitted toxic gas and losses in operating converters. The first cost function to minimize consists of the operation cost of the overall DC microgrid in $, It includes the (O&M) cost of RESs, (DG), and ESS, and the cost of purchased/sold energy from/to the grid. However, to add pollutant gas emissions and converters' losses cost functions to the total objective function, respectively, the pollutant energy produced by the (DG) and the energy loss in converters over the whole time horizon are computed in (KWh). Next, penalty coefficients expressed in ($\$/KWh$) are assigned to each of the cost functions. By this, the obtained total objective function to minimize is expressed in $ and corresponds to the total energy bill over the control time horizon (i.e. 24 hours).
In addition, several constraints that delimit the minimum and maximum admissible power references of the utility grid, battery, and (DG) are added. Moreover, to secure a safe operation of the ESS, constraints on the minimum and maximum, initial, and last state of charge are added. As the formulated optimization problem includes several nonlinear and nonsmooth functions and is time-variant, the search for a global minimum requires the application of specific algorithms. Among several algorithms, dynamic programming (DP) and genetic algorithm (GA) are applied as deterministic and metaheuristic algorithms, respectively. The two algorithms are compared in terms of optimal solution finding, convergence speed, and sampling period selection. On the other hand, the preference criterion between the fixed optimization goals is tackled through a detailed analysis of the weights' selection.

Chapter 4 addresses the addition of an online optimization stage that updates the offline optimal power references of dispatchable sources due to existent uncertainties between predicted and actual data inputs. The data inputs consist of the electricity pool prices, the RESs generated power, and load demand over the 24-hour time horizon. These uncertainties create mismatches between the predicted and actual generated/consumed power which deteriorates the power balance equation in the DC microgrid and incurs deviations in the common DC bus voltage. In the absence of any online optimization correction part, the utility grid converter mostly operates as the slack bus for the corrective actions needed to compensate for the uncertainties in renewable resources and the load demand. The main goal of the online optimization stage is to find an improved solution for the new power mix in the DC microgrid compared to the above. This permits the re-establishment of the power balance conveniently to the optimization goals. Like offline optimization, a unified total objective function is established and expressed in $. The total objective function consists of

the sum of the operation, toxic gas emissions, and converters' losses cost functions. Hence, the online optimization stage always tends to reduce the total energy bill in $. Unlike the offline optimization problem which finds the set of optimal power references over the whole time horizon, the online optimization stage performs local optimizations at each intra-sample period and is time-invariant.

To prove the effectiveness and viability of the proposed online optimization stage, several simulation tests are conducted in which predicted input signals are modified differently to generate actual input signals with variable margins of error. The robustness of the online optimization stage is assessed according to the margin of error between predicted and actual data inputs. For all tested scenarios, a comparison between the obtained total energy bill with and without the online optimization stage is conducted and the resulting profits, in $, are revealed.

Finally, Chapter 5 concludes the manuscript and states the main outcomes of this thesis and future perspectives. Lastly, we take note that all obtained results are from simulation tests performed on MATLAB/Simulink software and have not been validated experimentally. Experimental validation can constitute a key work to accomplish in the future.

Chapter 1 : Review of Energy Management and Optimization Techniques Applied to DC Microgrids

1.1 The advent of centralized energy generation and related drawbacks

Since the 20th century, electricity has been produced in centralized power plants and delivered to customers through power transmission lines. This centralized approach was established due to several factors: the advent of alternating current and transformers made energy production in a remote central unit and transmission to consumers over long distances a viable and reliable solution. By adopting an AC-type transmission, the arising problem of voltage drop related to DC-type transmission and Edison's earlier innovation was overcome, and then electricity was enabled to flow for hundreds of miles without a significant loss in voltage magnitude. The shift from reciprocating engines, in earlier utilities, to steam turbines unleashed the centralization of power production. Steam turbines were more energy efficient, smaller, quieter, unchallenging to scale up, and less proportional in materials investment if a higher power was produced compared to the reciprocating engines. Hence, the adoption of steam turbines has applied to the concept of economies of scale in which larger units can produce more electricity at lower unit costs. Low prices of fuel that can be burned remotely far from city centers were another motif to endorse the centralized energy production approach. The reliability of one plant was improved by connecting multiple power plants by transmission lines which empowered the network growth and provided better service reliability than any single generator. In parallel, regulations favored the centralized power production technique, this was reflected in the historical strategic policies drivers to produce power in a centralized large-scale plant and supply it to consumers through electricity transmission and distribution three-phase systems. By this, the overseeing and control of the utility grid and market were facilitated [1].

However, in the late 20th century, steam turbines began to realize thermal efficiency limits (40% of thermal efficiency could theoretically be achieved but problems appeared with the high-temperature operation causing an increase in maintenance costs and thus, a decrease in reliability. Practically, a maximum of 35% energy efficiency is reached in such an application [2]). Other drawbacks related to centralized generation are the transmission and distribution costs which consist of line losses, unaccounted-for electricity, and conversion losses. The highest cost is achieved by small customers talking electricity from the end distribution network at low voltage. As shown in Fig.1.1, world transmission and distribution losses' percentages remain practically unchanged between (1990-2014) with values above 8%. Lower losses were recorded in the EU and China during the same period meanwhile, overall curves don't present a steep drop in losses [3]. Though a reduction of 2% in transmission and distribution losses was accomplished in the U.S. between 1990 and 2020 as shown in Fig.1.1, the total losses are still high at 207 billion kWh out of a net generation of 3930 billion kWh in 2020 [4].

Rural electrification with centralized generation is an additional drawback and a real challenge due to the extended capital to be spent to connect remote areas of small consumption with overhead.

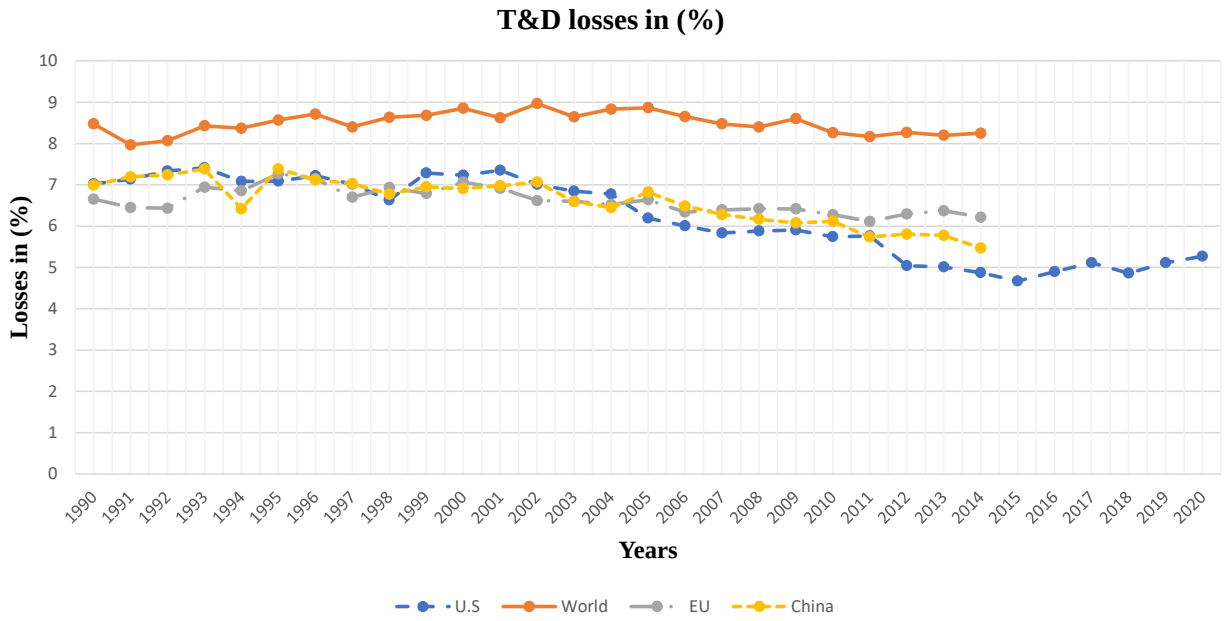


Fig.1.1 Transmission and distribution losses in the World, EU, U.S., and China.

Sources: - https://www.eia.gov/electricity/state/unitedstates/

- Electric power transmission and distribution losses (% of output) | Data (worldbank.org)

lines over long distances which might be uneconomical. In turn, the transmission and distribution losses are magnified because of the long-distance coverage. This results in a deferral of rural electrification projects. Based on the World Bank Global Electrification Database [5], 17.3 % of the world's rural population still have no access to electricity in 2020. It can be seen in Fig.1.2 that most rural populations in African countries have world lower rates of access to electricity (below 28%, with the lowest rate of 1% in the Democratic Republic of Congo). In this regard, the World Bank approved, in May 2017, a grant of $118 million and a credit of $27 million for the electricity access and services expansion project in the Democratic Republic of Congo. The undergoing project provides new and improved electricity service to about two million people. As mentioned in the report, the number of hours of available electricity per day that customers receive in the project intervention areas has increased from 4 hours/day in 2017 to 6 hours in 2022 and will reach 16 hours in October 2023 [6]. in [7], a study was conducted on how the centralized grid system impacts the rural economy of Nigeria which has a large geographical size. The study proves the inadequacy of the centralized grid in rural electrification and recommends a decentralized electricity structure with an emphasis on mini-grids and a priority on localized generation.

Besides, in a centralized generation, high investments in transmission and distribution networks are required to cover consumers' increasing need for electricity with highly reliable service. The

International Energy Agency (IEA) estimates the annual spending on the electricity distribution system by major U.S. utilities at $57.4 billion in 2019, 6% more than in 2018 and 64% more than

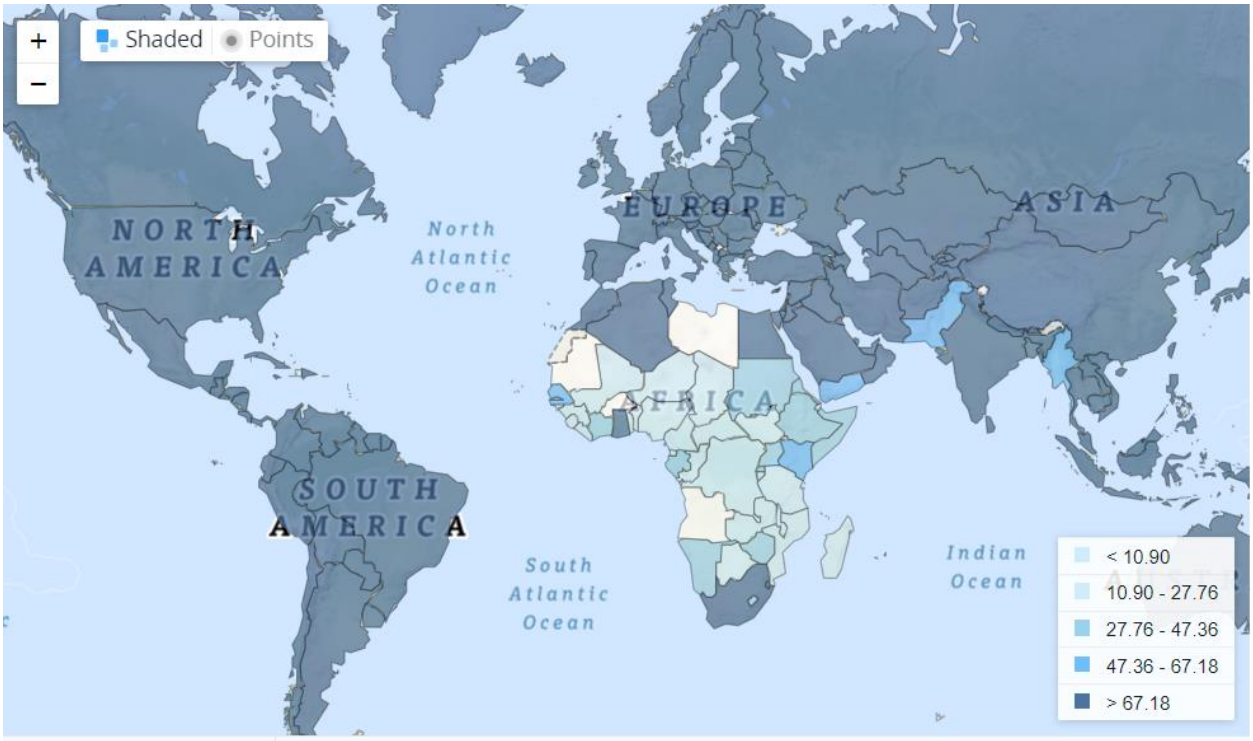


Fig.1.2 Access to electricity, rural is the percentage of the rural population with access to electricity in 2020.

Source: World Bank Global Electrification Database from "Tracking SDG 7: The Energy Progress Report" led jointly by the custodian agencies: the International Energy Agency (IEA), the International Renewable Energy Agency (IRENA), the United Nations Statistics Division (UNSD), the World Bank and the World Health Organization (WHO).

in 2000 as seen in Fig.1.3. The total amount is divided into $31.4 billion for capital investment as utilities worked to replace, modernize, and expand existing infrastructure, $14.6 billion for operations and maintenance (O&M), and $11.5 billion for customer expenses. Most of the $31.4 billion of capital investment, is spent on overhead and underground power lines. Distribution lines are added, and expanded, aging equipment is replaced, and operation and maintenance are modernized. Since most of the increased distribution spending does not directly target the end users, distribution spending outpaces the growth in both the number of electric customers and in retail electricity sales as seen in Fig.1.4 [8]. The deployment of distributed generation can help to bypass the increased investment in transmission and distribution networks since they are at most in proximity to load centers, unlike large central generation units.

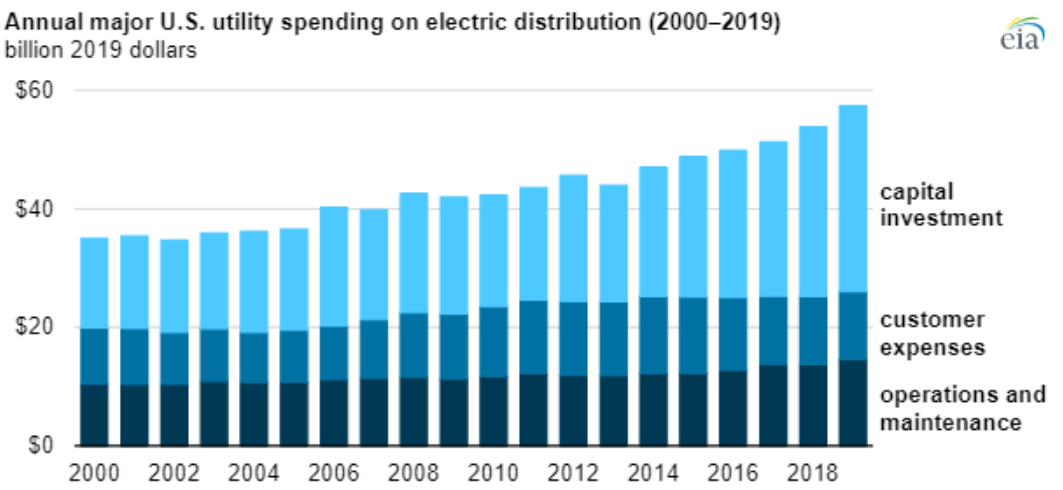


Fig.1.3 Annual major U.S utility spending on electric distribution (2000-2019)

Source: Graph created by EIA, based on data from Federal Energy Regulatory Commission (FERC) Financial Reports, as accessed by Ventyx Velocity Suite

Furthermore, centralized generation has manifested energy security problems such as grid outages during severe weather events. Projections indicate that the world is very likely to experience greater weather-related disruptions due to climate change. A recent example of a power outage was due to a cold spell that occurred in February 2021 in Texas, where large parts of the state were left without electricity for many days [9]. According to the U.S. Energy Information Administration, U.S. electricity customers have experienced just over eight hours of electric power interruptions in 2020, the most since 2013. As shown in Fig.1.5, six out of eight hours of power interruptions, in 2020, were caused by major events related to severe weather and natural conditions including snowstorms, wildfires, and hurricanes.

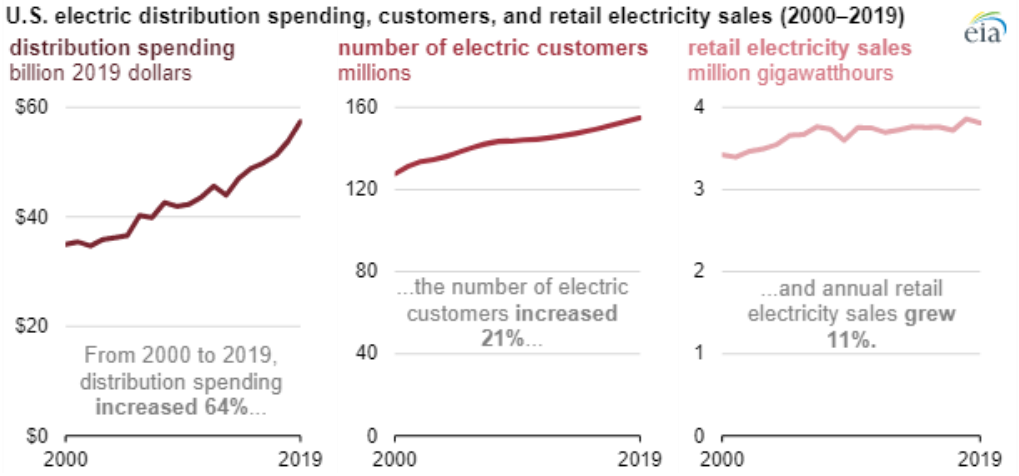


Fig.1.4 U.S. electric distribution spending, customers, and retail electricity sales (2000-2019).

Source: Graph created by EIA, based on data from *Annual Electric Power Industry Report*; Federal Energy Regulatory Commission (FERC) Financial Reports, as accessed by Ventyx Velocity Suite

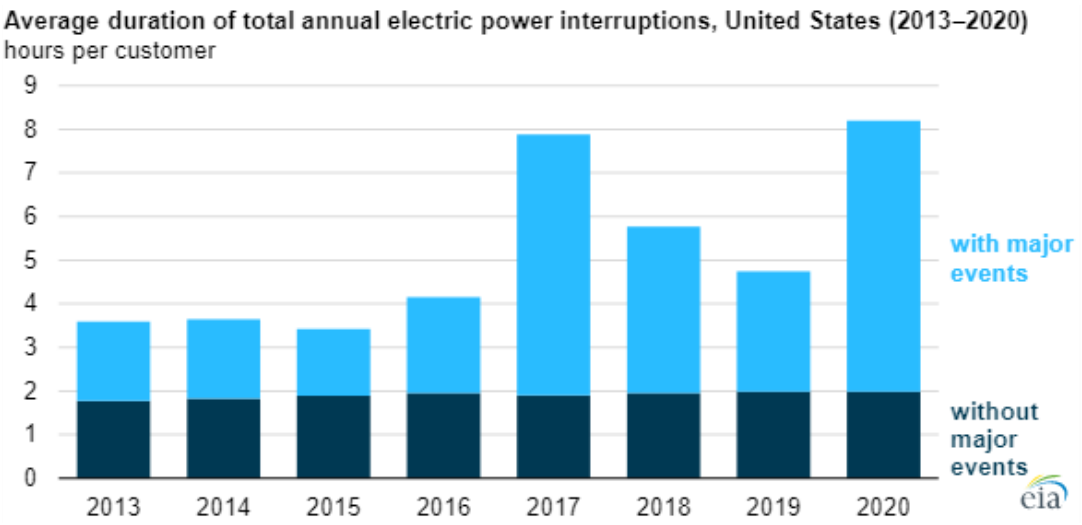


Fig.1.5 Average duration of total annual electric power interruptions, U.S. (2013-2020).

Source: U.S. Energy Information Administration, *Annual Electric Power Industry Report*

The impact of severe weather events on electric power interruptions can be deduced from the number of interrupts in 2020 as a function of the total duration of annual interruptions by the U.S. state (Fig.1.6): Louisiana, Oklahoma, Connecticut, and Alabama the states with the most time of interrupted power in 2020, knowing that 14 hurricanes and 11 major storms were experienced in the U.S in 2020. Noticeably, Louisiana experienced an active storm season, including Hurricane Laura. Same for Alabama which was hit by several hurricanes. Tropical storm Isaias affected Connecticut and left about 750,000 customers without electric power for over a week. Thus, these long interruptions were directly caused by major weather events[8]. In their report, the President's Council of Economic Advisers and the U.S. Department of Energy's Office of Electricity Delivery and Energy Reliability estimated the annual cost of power outages caused by severe weather between 2003 and 2012 in the U.S. from $18 billion to $33 billion[10]. Urgently, the grid resilience concern is addressed, and distributed generators are advanced as complements to the traditional centralized grid with a high potential to increase grid reliability and resiliency[11].

While most of the energy sources used to generate electricity in central power plants are of fossil fuel origins (coal, oil, and natural gas) or nuclear power, there is a critical hitch due to the depletion of these energy sources. Fig.1.7 represents the share of electricity production from fossil fuels in 2021, the map shows that world most countries rely on fossil fuels to produce electricity with an average percentage of 61.42%. South Africa, Australia, China, and the U.S. have the highest percentages of fossil fuel use: 86.42%, 70.94%, 65.9%, and 61.1% respectively, meanwhile other European countries such as France, Sweden, Iceland, and Norway have lower rates below 20%. However in 2021, France and Sweden relied more on nuclear power as an energy source to produce electricity with a share of electricity production of 69.33%, and 31.24% respectively[12].

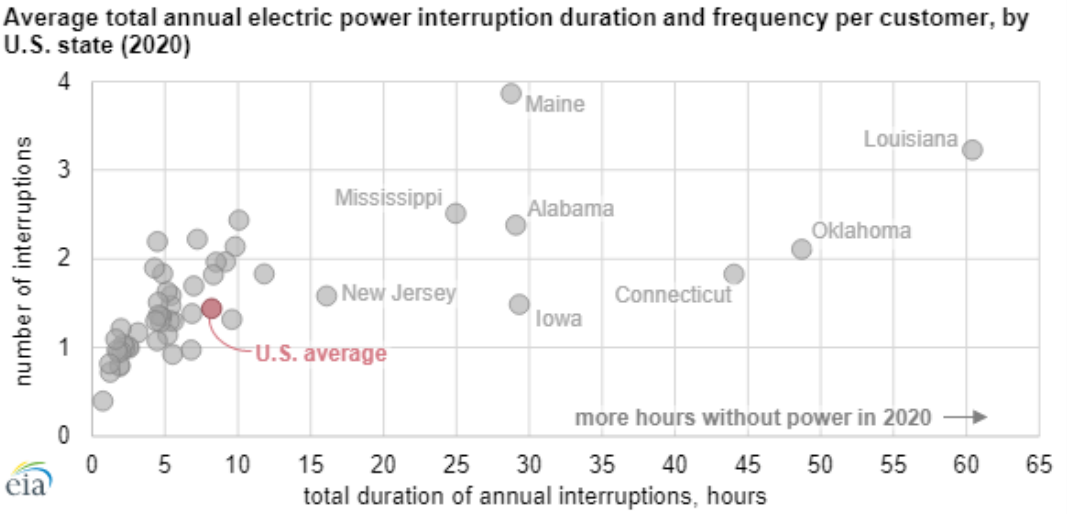


Fig.1.6 Average total annual electric power interruption duration and frequency per customer, by U.S. state (2020).

Source: U.S. Energy Information Administration, *Annual Electric Power Industry Report*

According to the BP Statistical Review of World Energy, the years of fossil fuel reserves left accounted for in 2020 are 139 years for coal, 54 years for oil, 49 years for gas, and 70 years for uranium[13], [14].

Besides their depletion, fossil fuel reserves are not equitably distributed over the world's continents giving rise to a disparity in extraction, sales, and consumption potentials. For instance, 50% of world natural gas reserves are uniquely located in three countries (Russia: 37.39 trillion m^3, Iran: 32.1 trillion m^3, and Qatar: 24.67 trillion m^3) respectively account for 19.88%,17.07%, and 13.12% of the world's total gas reserves. Likewise, two-thirds of the world's coal reserves are sited in four countries: the U.S., Russia, Australia, and China respectively account for 23.26%, 15.16%, 14.04%, and 13.38% of the world's total coal reserves[15]. As a result, these countries, as main producers, and exporters of fossil fuel sources, monopolize the reserves and so, arguably control the prices, and the access to electricity of importing countries. The latest example is the rising European energy crisis under the Russian gas cut-off to the European Union. Under a worst-case scenario, European ministers predict that electricity could have to be rationed for up to six million homes in 2023's winter, mostly at peaks in the morning and evening. As well, the shortage in gas supply to Europe drastically impacts energy prices and household utility bills which are skyrocketing[16], [17]. As distributed energy sources can accommodate a larger range of fuel than a centralized generation, they are proposed as alternatives to central power plants to diversify away from coal, fuel, natural gas, and nuclear fuel, and ensure sufficient and affordable power electricity to customers[18].

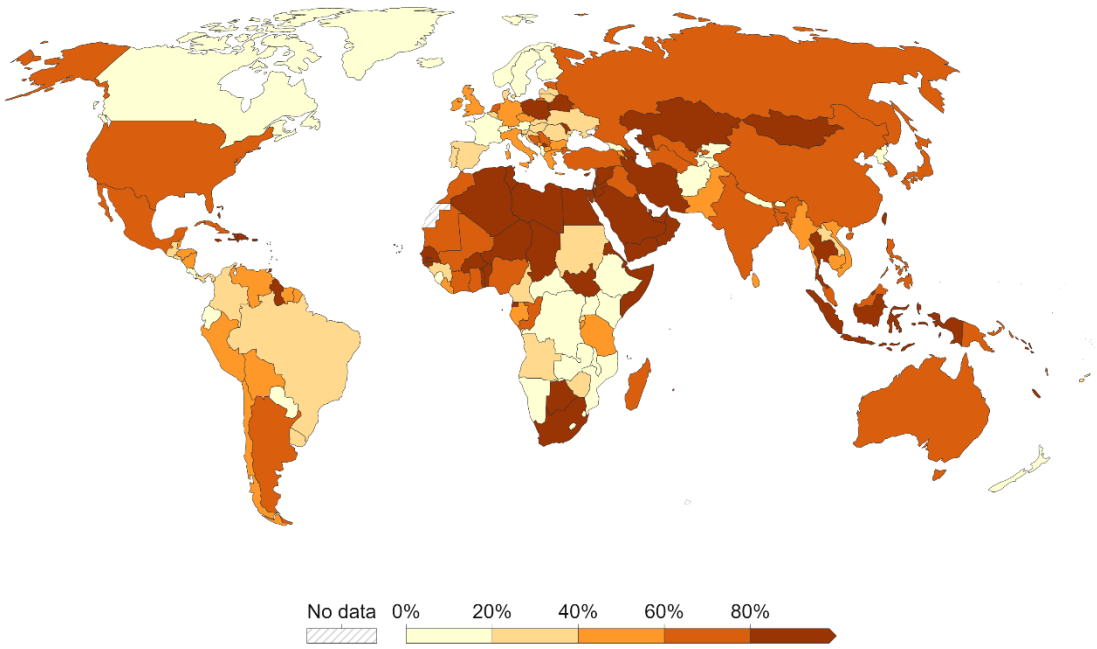


Fig.1.7 Share of electricity production from fossil fuels, 2021.

Source: Our World in Data based on BP Statistical Review of World Energy (2022); Our World in Data based on Ember's Global Electricity Review (2022); Our World in Data based on Ember's European Electricity Review (2022), OurWorldInData.org/energy • CC BY.

1.2 Distributed energy sources as alternatives to centralized energy generation

As detailed in the first section, several technical drawbacks posed by central energy generation, in terms of grid resiliency, security, reliability, efficiency, etc., expedited the diversion from the centralized generation approach to the distributed one. Hence, distributed energy sources are advanced as alternatives and back-ups to the traditional grid capable of overcoming its main downsides and offering ancillary services.

On the other hand, climate change and the need to integrate clean energy sources were instrumental drivers and catalysts to distributed energy sources. The earth's global average surface temperature has roughly increased one degree Celsius since the preindustrial era (1880-1900). According to the National Oceanic and Atmospheric Administration's (NOAA's) 2021 annual climate report, the combined land and ocean temperature has increased at an average rate of 0.08 degrees Celsius per decade since 1880 however, this rate of increase has outstripped the double since 1981 (0.18 degrees Celsius). Moreover, based on NOAA's temperature data, 2021 was the sixth's-warmest year on record for the globe with a temperature of 0.84°C above the 20th-century average, and the years 2013–2021 all rank among the ten warmest years on record. As a result of the increase in the global earth's average temperature, many other aspects of the global climate are changing. Several

kinds of research documented changes in surface, atmospheric, and oceanic temperatures; melting glaciers; diminishing snow cover; shrinking sea ice; rising sea levels; ocean acidification; and increasing atmospheric water vapor[19]. Carbon dioxide emissions and other greenhouse gases have been the dominant cause of recorded warming since the mid-20th century. In the majority, these emissions come from burned fossil fuels. A substantial increase in global carbon dioxide emissions from fossil fuels was noted with 6 billion tons of CO_2 emissions in 1950, and 34.81 billion tons in 2020[29]. The sharp rise in CO_2 emissions during the last 70 years, is strongly related to and initiated the increasing rate of the average temperature per decade. Referring to the Climate Analysis Indicators Tool (CAIT) of Climate Data Explorer via Climate Watch, the sector that produces the highest CO_2 emissions is the electricity and heat sector with 15.76 billion tons for 2019 followed by the transportation sector with 8.22 billion tons. Fig.1.8 shows the world map of greenhouse gases emitted per unit of electricity produced, measured in grams of CO_2-equivalents per kilowatt-hour of electricity. Comparing Fig.1.7 to Fig.1.8, it can be inferred that countries with high shares of electricity production from fossil fuels have a higher carbon intensity of electricity such as the U.S., China, Russia, India, Saudi-Arabia, etc. To alleviate this critical risk and impact, nearly 200 nations committed to holding the average earth temperature to well below 2 degrees Celsius in the 2015 Paris Climate Agreement. This is being realized by setting net-zero emissions targets for countries.

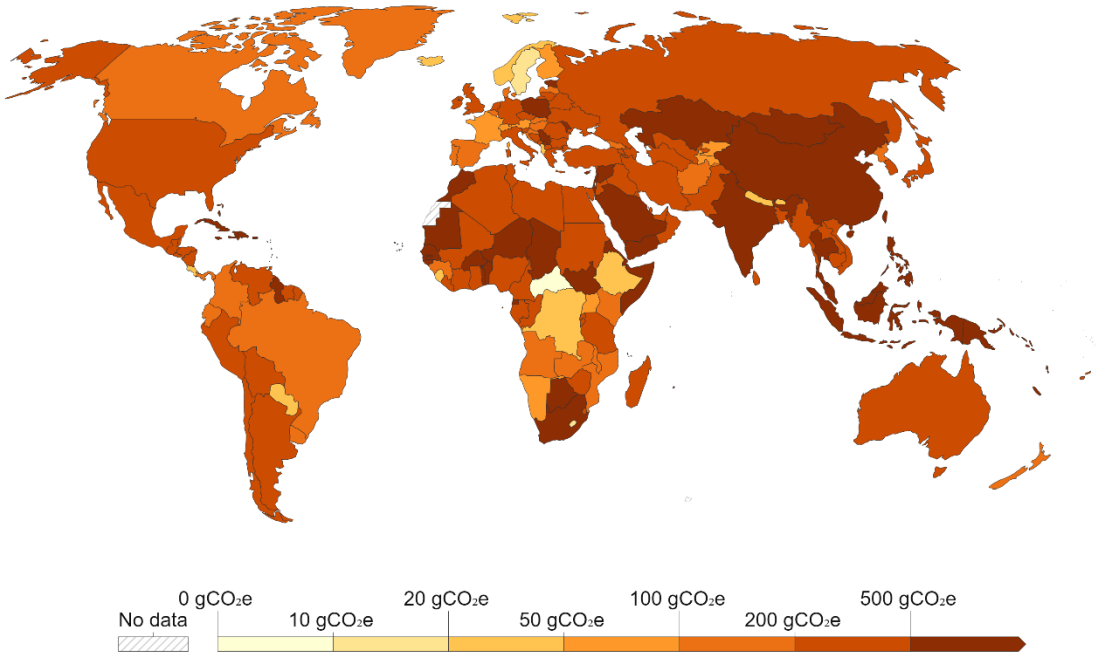


Fig.1.8 Carbon intensity of electricity for 2021.

Source: Ember Climate (from various sources including the European Environment Agency and EIA) OurWorldInData.org/energy • CC BY

that have pledged to achieve this target in future years. Lately, in November 2021, countries participating in major UN climate talks (COP26) in Glasgow, Scotland, are announcing more ambitious plans for slashing their emissions for the next decade. In this context, The G20 Energy and Climate Ministerial's Communiqué emphasized the importance of clean distributed energy resources (DERs) for addressing decarbonization and climate change. According to the IEA, about 179 GW of distributed solar was added globally from 2017 to 2020[21]. In their short-term energy outlook, IEA forecasts a rise in U.S. electricity generation from renewable energy sources (RESs) such as solar and wind, and a reduction in generation from fossil fuel-fired power plants over the next two years as seen in Fig.1.9. A forecast share of generation for the U.S. solar and wind (RES)s grows from 13% in 2021 to 17% in 2023. Additionally, it's shown in Fig.1.9 that the rapid expansion of renewable energy resources over the past years yielded a significant shift in the U.S. electricity generation mix. This shift will engender a large reduction in fossil fuel energy generation, and then a major step toward decarbonization.

Meanwhile, the European Union (EU), setting a binding target to achieve climate neutrality by 2050, has further raised its 2030 climate ambition beyond the target agreed upon in 2018, committing to cutting greenhouse gas emissions by at least 55% by 2030 under the so-called "Fit for 55" package. "Fit for 55" is a set of proposals to revise, and update EU legislation, and bring it in line with the 2030 goal.

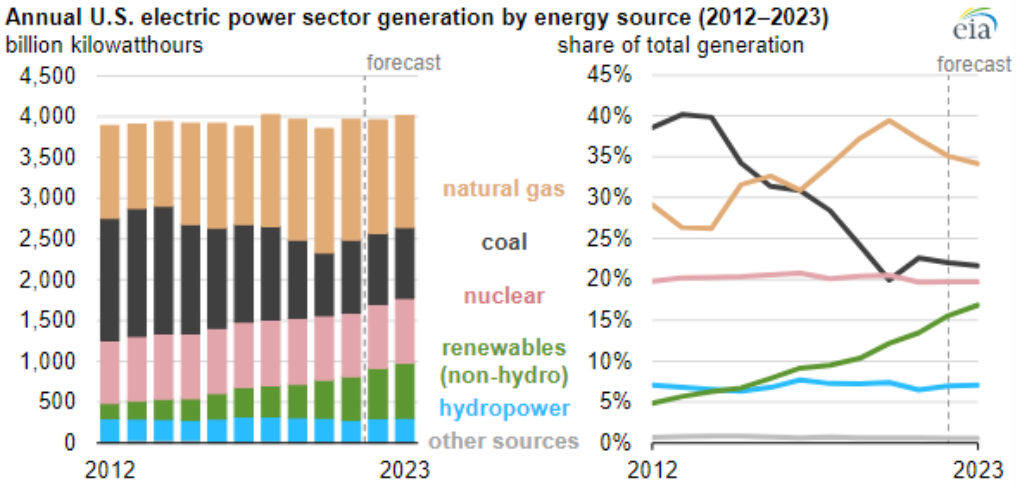


Fig.1.9 Annual U.S. short-term energy outlook for electric sector generation by energy source (2012-2023).

Source: U.S. Energy Information Administration, Short-Term Energy Outlook, January 2022

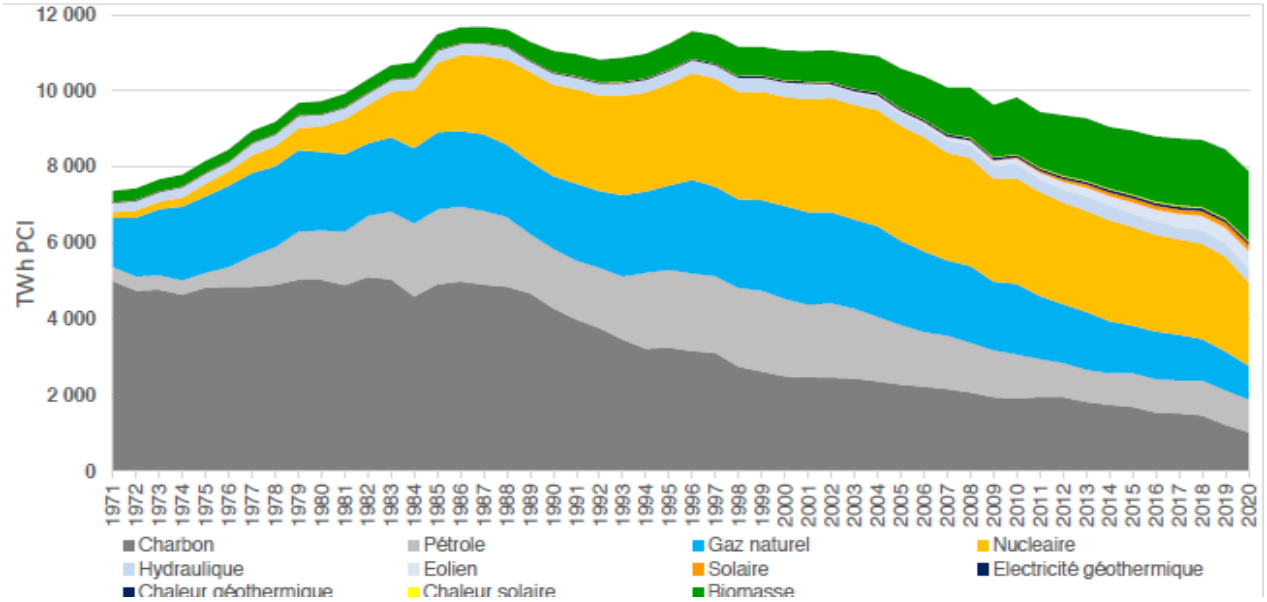


Fig.1.10 Primary energy production of EU28 (1970-2020).

Source: Enerdata, 2022

Besides energy efficiency and taxation, EU emissions trading system, CO2 emissions standards for cars and vans, carbon border adjustment mechanism, social climate fund, refuel EU aviation and fuel EU maritime, alternative fuels infrastructure, efforts sharing regulation, land use, and forestry legislations, the EU plans to boost the share of renewable energy of the total energy mix to 40% by 2030 (double 2020's share of 22,1%) [22].

The EU's shift towards (RESs) took place progressively throughout the years as shown in Fig.1.10, where 90% of energy production was from fossil fuels at the beginning of 1970th, remained at 63% in 2000, and only represented 35% of the EU energy production in 2020. However, for the first time in 2020, (RESs) share of the total energy mix surpassed that of fossil fuel by 2% (37% share of the EU primary energy mix)[23]**.**

1.3 Microgrid concept and advantages of DC over AC microgrids

As a definition, the grid architecture that manages the integration of several distributed energy sources of different types, the electricity generation, and the load demand, in sub-sections of the grid, and can be isolated from the larger grid and provide critical services in case of any grid failure, is called a "microgrid"[24]. The microgrid term was originally proposed at the beginning of the 21st century and is found in the literature with many other definitions and functional classification schemes. Another detailed and intelligible definition proposed by the Microgrid Exchange Group, an ad hoc group of research and deployment experts to the U.S. Department of Energy reads as follows: ''A microgrid is a group of interconnected loads and distributed energy resources within clearly defined electrical boundaries that acts as a single controllable entity to the grid. A microgrid can connect and disconnect from the grid to enable it to operate in both grid-

connected or island mode [25].” As seen from the definition, there are no specifications for the size of the distributed energy sources nor the type of technologies that should be applied. Thus, a microgrid can include (DERs) of utility-scale delivering power ranging from MW to GW (e.g. the 35-MW microgrid project in Gonzales, California, built by Concentric power, which delivers 14.5 MW-AC of solar, 10 MW/27.5 MWh of battery energy storage system (ESS), and 10 MW of flexible thermal generation[26]) as well as small-scale (DER)s, known as “behind the meter”, located at houses, industries, or businesses providing electrical power of tens and hundreds of KWs.

Since microgrids are advanced as supplements or alternatives to the centralized traditional grid, the main challenges addressed in earlier applications, were the seamless transition between grid-connected and islanded modes, energy management, active and reactive power, voltage, and frequency control, etc. Hence, enhancing the reliability, controllability, and minimizing the operational costs of the microgrid were the prime concerns of research programs rather than, the reduction of greenhouse gas emissions, and energy losses [24]. While all microgrids share similar challenges on a macro level, the control and functionality of each depend, essentially, on the type of voltage in the point of common coupling (PCC) of connection from which AC, DC, and hybrid AC-DC microgrid’s connection types can be distinguished. In an AC, DC-type microgrid, (DERs) are interconnected, through converters, respectively to a common AC, and DC bus meanwhile, both types of buses exist in a hybrid AC-DC microgrid connection[27]. Thanks to the predominance of AC-type power electricity transmission, and the maturity of AC-standardized technology, most of the research was centered on AC microgrids that prevail and captivated the attention more than DC microgrids. Studies focused on voltage and frequency regulation, active and reactive power control, energy management strategy, seamless connection between grid-connected and islanded modes, uninterruptible supply for critical loads, the capability of black start in case of grid failure, etc.[28]. However lately, the relative merits of AC and DC microgrids are again vulnerable to controversy, and DC-type microgrids are regaining an increased interest in the research field and are advanced in several applications over their AC counterparts[29]. There are several grounds for the shift from AC to DC-type microgrids which can be summarized as follows:

- The proliferation of renewable energy sources including photovoltaic generation, that are inherently DC supplies, eased the connection of these resources to a DC bus rather than an AC bus which requires at least one DC-to-AC conversion stage (in many applications an AC-to-DC back again conversion is required) inducing higher conversion losses ranging from 5% to 15% of power generation depending on the number of conversion stages[30], [31].
- Energy storage systems (ESSs) such as batteries and fuel cells are DC by nature, which poses the same hurdle of conversion losses and efficiency if these units are connected to an AC bus. In this context, the direct connection of the battery stack to a common DC bus has been historically a popular structure for practical applications due to the high

capacitance of the battery stack that assures the dynamic stability of the system[32]. However, connecting the battery stack to the common DC bus through a bidirectional DC-to-DC converter is a widely used configuration that increases the flexibility and controllability of the system with limited conversion losses (a DC-to-DC conversion stage results in 2% losses of generated power)[33].

- The increasing number of DC-type loads such as electric vehicles (EVs) which can act as loads as well as power sources with the grid under the well-known vehicle-to-grid (V2G) and grid-to-vehicle (G2V) applications, portable electronic devices such as laptops, computers, phone devices, etc., home appliances such LED lighting, routers, chargers[34]. Energy efficiency is highly increased when these DC-type loads are directly coupled to the common DC bus voltage with a minimal number of energy conversions. In [35], Bosh developed a DC microgrid, compared it to a traditional AC microgrid, and found that the DC system is 6 to 8 % more efficient than the AC one due to the reduced energy conversion stages.
- The ease of control of a DC microgrid in which the regulation of the common DC bus voltage is the main control priority. Issues of synchronization, harmonic distortion, reactive power flow, frequency regulation, and power quality, that exist in AC systems are all alleviated[36].

Yet, AC transmission systems still have many merits over DC ones, especially, the ease of voltage transformation with which voltage can be elevated, transmitted over long distances, and then lowered again near end users. Another advantage of AC systems is the maturity of circuit protection which benefits from periodic zero voltage crossing to extinguish naturally a fault current within the half cycle after tripping whereas, existent fuses and circuit breakers of DC systems inherently introduce large time constants and time delays before activation and trip the current from its steady-state value. While tripping, the arc occurrence presents a dangerous condition from the safety point of view, shortens circuit breakers' lifetime, and increases maintenance costs[37]. Finally, DC microgrids lack standardization as they are still considered emergent technologies. Several organizations are reviewing and developing practical standards for DC microgrids such as European standard ETSI EN 300 132-3-1 which discusses the low-voltage dc systems[38], and IEEE standards for DC microgrids[39]. Knowing this rapid advancement and expansion, DC microgrids have become vital subjects in the research field that will shape the future of small (DER) systems. This can justify the study of a DC microgrid in the context of this thesis. The applied DC microgrid consists of a PV and WT as RESs, a (DG) as a traditional pollutant source, a residential-type load, and an energy storage system that enables energy management and control. The DC microgrid can operate in an islanded or grid-connected mode which offers an additional degree of freedom to manage the energy mix in the system following predefined control objectives.

1.4 Control and energy management techniques in DC microgrids

1.4.1 Three-level hierarchical control

In a DC microgrid, the prime control priority is the regulation of the common DC bus voltage to which (DERs) are connected through local converters. To achieve this, one of the most applied techniques is droop control which ensures the common DC bus voltage stabilization and power sharing among existing sources without digital communication links (DCLs)[40]. In its conventional form, droop control degrades the current-sharing accuracy and lacks robust voltage regulation. As a result, improved versions of droop control were proposed in the literature such as virtual-resistance-based droop, adaptive droop control, mode adaptive droop, and intelligent techniques-based droop to overcome the drawbacks of the basic droop technique[41]. However, to achieve additional control functionalities and global management objectives, a hierarchical control approach is adopted. Traditionally proposed to control AC microgrids, the three-level hierarchical control is applied to control and manage the power flow in DC microgrids with a difference in the control approach and controlled variables. Fig.1.11 illustrates the hierarchical control in a DC microgrid.

The primary level consists of current, voltage, droop control, and source-dependent functions, e.g., maximum power point tracking (MPPT) for photovoltaic modules and wind turbines[42], [43], or state of charge (SOC) estimation for ESS[44].

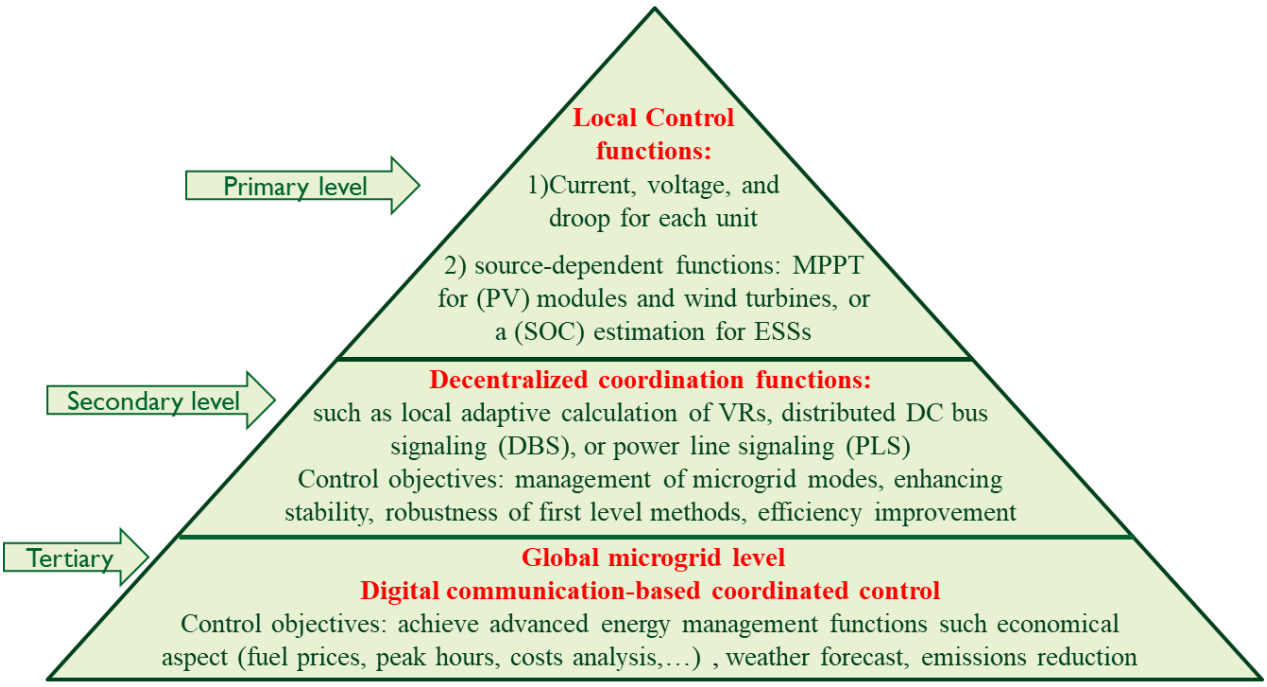


Fig.1.11 Hierarchical control of a DC microgrid.

On the secondary level, decentralized coordination functions exist such as local adaptive calculation of virtual resistances in which the robustness and stability of the primary control level are enhanced [45], [46]. Another function is the DC bus signaling (DBS) method which uses the DC bus voltage level as an information carrier to control power and switch between different operating modes[47]. A third decentralized function at the secondary level is the Power Line Signaling (PLS) method in which the units inject sinusoidal signals of specific frequency into the common DC bus voltage to communicate with each other and manage ESS and RESs[48]. Hence, secondary control is applied to enhance primary control level methods and manage the operating modes of the microgrid.

However, at a global microgrid level, the tertiary control level achieves advanced energy management functions such as the optimization of the DC microgrid performance by reducing the operation and maintenance costs, the carbon emissions, improving the battery lifetime, converters' efficiency, etc. Other functionalities can be included such as fuel and electricity prices, weather predictions… At this level, a digital communication-based coordinated control is required to monitor and manage all operating units[49].

Besides the difference in functionalities in each of the three levels of hierarchical control, the objectives to be achieved are from different time scales[50]. Correspondingly, the primary and secondary levels have the highest control speed as they take charge of current, frequency, voltage, and power factor regulations. Oppositely, the tertiary control level has a slower dynamic as it targets slower variables. While the primary control level is installed locally at each converter, secondary and tertiary control levels can be implemented in a centralized, decentralized, or distributed fashion[51]. They are classified based on the digital communication links (DCLs) which only exist in the centralized and distributed approach and are used as data carriers between all operating controllers. The sole difference between both approaches is that a central control (CC) unit collects, processes, and sends back data to all operating units in the centralized control, although (CC) doesn't exist in a distributed control and units only communicate with their neighbors to make decisions[52]. The centralized approach offers higher monitoring over the whole system and facilitates the function of global regulation and optimization. However, it requires extensive communication infrastructure which leads to an increased cost and lower reliability. Moreover, the system can be abruptly stopped because of a single-point failure in the (CC) or (DCL)s. On the other hand, a distributed control strategy offers better reliability and expandability of the system but sacrifices the overall system security because of lack of robust centralized supervision. Moreover, a consensus algorithm, also named multi-agent system, is needed to perform the decision making and a much challenging control is required to achieve a global optimization goal[53].

1.4.2 Tertiary control level to achieve smart energy management in DC microgrids

As the safe operation of DC microgrid in all modes, stable, and robust performance in response to transients and disturbances are substantial prerequisites, most of the research addressed first the primary and secondary control levels to ensure microgrid voltage regulation, load-sharing, stable and reliable performance, power management, and seamless transition between different operation modes [54]–[59]. Lately, the tertiary control level is gaining an increased interest in achieving energy management and optimization functionalities on a global microgrid level as the environmental, energy efficiency, and operation and maintenance (O&M) cost minimization aspects are becoming prime concerns of the world energy policies[60]. Hence, several objectives can be accomplished simultaneously, by formulating an optimization problem and solving it using deterministic, heuristic, or metaheuristic methods such as simulated annealing (SA)[61], genetic algorithm (GA) [62], particle swarm optimization (PSO) [63], pattern search (PS)[64], polar bear optimization (PBO)[65], etc. The selection of the optimization method is instrumental in finding the optimal solution, it is hinged on several factors as the type of microgrid planning problem to be addressed, the number of objectives to be achieved, and the constraints to be considered[66]. The application of different optimization methods and the pros and cons of each are detailed in the next section. Once found, the optimal solutions are applied to the power control of operating converters as optimal power references in the outer loop, while the primary and secondary control levels are executed in inner loops with faster dynamics.

As previously stated, the tertiary control level can be applied either in a centralized or distributed manner. Several works in the literature have investigated tertiary control functionalities in a centralized or distributed control strategy. Due to the diversity of control objectives and the wide range of their time scales, it is practically complex to represent and cover the entire hierarchical control in one research study and mathematical model, especially if targeted objectives of the tertiary control level span over long periods e.g., days, weeks, months, or years. This major difference between control levels made most researchers set apart the primary and secondary control levels from the third one either by centering their studies on the first two levels or by targeting the tertiary control level using simplified static models in steady-state. By this, variables of primary and secondary control levels with fast dynamics are excluded from the model to reduce complexity, and inner control loops are considered as established. Thence, the tertiary control level is investigated apart in most scopes of works, global management functionalities are accomplished through optimization problems and are validated without a direct referral to the hierarchical control. However, one can find in the literature several studies that execute tertiary control level functionalities such as multi-objective optimization in the scope of the hierarchical control and matches between optimality and synchrony in one framework[67]. It is frequently found in distributed control strategies with consensus algorithms and adaptive droop-based optimization problems. For instance, in [67] a distributed controller is proposed to simultaneously optimize the power-sharing among sources of an islanded DC microgrid and stabilize the common DC bus

voltage. An economic dispatch problem is solved to minimize the total generation cost and consensus protocols on incremental costs of DC resources are applied and networked on a communication graph. A distributed control methodology for both distributed feeder current balancing and power loss reduction is introduced in[68]. It modifies the weighted and constrained consensus control to include multi-objective optimization. The results are verified with an adequate selection of the weight coefficient. In [60], an optimization method is implemented on the tertiary control level. An optimization problem is formulated to minimize converters' losses and solved using (GA) which outputs optimal virtual resistances (VRs) to local controllers. The adaptive (VR) technique is applied at the primary level. A distributed control is selected based on a consensus algorithm in each local agent to obtain global information. Two consensus algorithms running in parallel are proposed in [69] to solve the economic power dispatch with transmission line losses and generator constraints. The first one is used to reach a consensus on the Lagrange multiplier, while the second one estimates the power mismatch in the system. Droop control-based techniques were introduced in [70]–[72] to optimize defined objectives. In [70], a tertiary-level optimization control is implemented, and (GA) is used to search the global efficiency optimum by minimizing the losses of operating converters. (VRs) are set as decision variables for adjusting the output power from converters and so improving their efficiencies. A similar approach is adopted in [71] to minimize the total operation cost by considering the real-time pricing in DC microgrids. All generation resources are modeled in terms of operation cost and (GA) is selected as a heuristic method to solve the optimization problem.

1.5 - Optimal sizing and optimal power scheduling of a DC Microgrid

On the other hand, the literature addresses predominantly the tertiary control level as a single entity and research topic, apart from the hierarchical control. In this context, the DC microgrid planning problem can be divided into three main categories according to Carlos Gamarra and Josep M. Guerrero[66]: power generation mix selection and sizing, siting problem, and operation scheduling. However, problems that address the optimal sizing and the optimal power scheduling of a DC microgrid are frequently found[73], [74]. Both approaches were largely investigated by researchers, optimization problems are formulated and solved using several optimization techniques.

1.5.1 - Optimal sizing of a DC Microgrid

Though the optimal sizing of a DC microgrid is out of the scope of this work, we start by citing some interesting examples found in the literature. In [75], a hybrid Particle Swarm Optimization - Grey Wolf Optimizer (PSO-GWO) technique is implemented to optimize the planning of a microgrid taking a case of three locations in the Indian state of Bihar. The microgrid consists of solar, wind, and bio-generator energy generation units, diesel generators, and a battery for energy storage. Cost of Electricity (COE) and Deficiency of Power Supply Probability (DPSP) factors are integrated into the objective function with a bound of Renewable Factor (RF). To prove the

effectiveness of the proposed hybrid algorithm, it is compared with other various algorithms. A multi-objective optimization algorithm is proposed in [76] to optimally size a DC microgrid including solar PV, wind generation units, and an energy storage system. Two criteria are taken into consideration in the decision-making: the total cost per year including the initial cost and (O&M) cost of each of the operating units and the availability of energy. Two objective functions, corresponding to each of the two criteria, are formulated and a Non-dominated Sorting Genetic Algorithm II (NSGA -II) is adopted as a search method to find a Pareto frontier of the solution. In [63] a (PSO) algorithm is applied to calculate the optimal sizing of a grid-connected DC microgrid. The on-grid price and the operating status of the grid-connected converter are considered in the objective functions and constraints on the battery state of charge (SOC), loss of power supply probability, and renewable energy efficiency are included. The optimal sizing targets the lowest annualized capital cost and (O&M) cost. Another optimization study is performed in [77] to optimally size rural applications in India. Two economic elements, the total Net Present Cost (NPC) and the Levelized Cost Of Energy (LCOE) are considered in the optimization problem along with constraints on grid power supply availability. Finally, multi-objective design optimization of a microgrid is developed in [78]. The microgrid consists of PV, wind, diesel, hydrogen, and battery systems. Three different goals are set for the optimal sizing (i.e., minimizing the Net Present Cost (NPC) of the system, the pollutant Emissions (E), and the Unmet Load (UL)), and established in three different objective functions. The Multi-Objective Evolutionary Algorithm (MOEA) and the (GA) are run in parallel as evolutionary algorithms to solve the optimization problem and return a set of non-dominated solutions.

1.5.2 -Optimal scheduling of a DC Microgrid

As previously stated, the optimal sizing of the DC microgrid is out of the scope of this thesis whose main target is the optimal power management of an existing DC microgrid configuration with a predefined power capacity and generation limits. Accordingly, this section highlights in detail the research work achieved in the optimal energy management of DC microgrids as well as the applied optimization techniques. One can identify two optimization approaches in the search for optimal energy management: offline and online optimization. Based on the microgrid configuration and the optimization target, the offline optimization approach relies on predicted data such as the ambient temperature, solar irradiance, wind speed, etc. to guess power generation profiles of RESs, economic data such as the energy market price, and load demand over a defined time horizon (i.e., mainly for 24 hours). These predicted profiles serve as input variables to the optimization problem. Mostly, system equations are discretized with a selected sampling time, and constraints and objective functions are evaluated at each sampling period. An optimization technique is applied to find the minimum total cost function which corresponds to the sum of the objective function at each time step over the whole-time horizon. The problem outputs the optimal power references of dispatchable units as a set of vectors to be applied in the next 24 hours.

1.6 - Offline optimization based on heuristic, metaheuristic, and deterministic methods

1.6.1 - Heuristic and metaheuristic methods

Heuristic and metaheuristic optimization techniques are commonly used in the energy management system (EMS) of microgrids[27]. Heuristic optimization methods are proposed as alternatives to classic optimization techniques as they are designed to find an optimum solution among a large set of feasible solutions with less computational effort[79]. Besides heuristic, metaheuristic methods are applied to find an optimum solution from a discrete search space, they can combine two heuristic methods to solve the optimization problem. As stated in [66], metaheuristic optimization methods can be classified into three main categories:

- Trajectory metaheuristics: Modify and improve one single candidate during the search process and output a single optimized solution. Examples of this category are Simulated Annealing (SA), Tabu search (TS), Variable Neighborhood Search (VNS), etc.
- Population-based metaheuristics: Modify and improve a population of solutions during a prefixed number of iterations and output a population of solutions when the stopping criterion is fulfilled. GA and PSO are the most popular algorithms in this category.
- Bio-inspired metaheuristics are based on the principles and inspiration of the biological evolution of nature for solving optimization problems. Examples of this category are Grey Wolf Optimization (GWO), Butterfly Particle Swarm Optimization (BPSO), Whale Optimization Algorithm (WOA), etc.

GA, PSO, SA, and game theory methods were recursively applied to find optimal solutions in microgrid power scheduling problems [80]–[82]. A multi-objective PSO (MOPSO) technique is presented in [83] to minimize the operation cost of a microgrid, fluctuation in generated power, uncertainty in power demand, and change in utility grid market prices. The microgrid consists of PV, wind, fuel cells, and battery units. A single combined weighted objective function is applied to aggregate all defined objectives. The (MOPSO) algorithm is validated through experimental results and compared to other metaheuristic techniques such as the GA and bee colony. In [62], a GA-based multi-objective optimization method is proposed to optimally control the power flow in a microgrid. Economic and environmental costs are chosen as objective functions. A nonlinear constrained multi-objective optimization problem is formulated in [84] to determine the optimal operation operating strategy of a microgrid. A game theory method is selected to achieve two objectives: minimizing the (O&M) cost and reducing the emissions of NO_x, SO_2, and CO_2. Another bio-inspired optimization technique, the vaccine-AIS, is adopted in [85] to take care of microgrid load dispatch and network reconfiguration. Despite their capability of solving multi-objective optimization problems for the whole-time horizon, heuristic and metaheuristic optimization methods are time-consuming in problems with a high number of decision variables

and do not guarantee the global optimal solution since the obtained results highly depend on initial guesses.

1.6.2 - Deterministic methods

Besides metaheuristic methods, several deterministic optimization techniques are proposed such as non-linear programming (NLP) methods (e.g., Sequential Quadratic programming (SQP), mixed-integer nonlinear programming (MINLP), etc.). For instance, SQP and mesh adaptive direct search methods are applied in [86] to solve a nonsmoothed optimization problem. The cost function includes the costs of emissions, the start-up cost, and the (O&M) costs to optimally schedule the operation of a microgrid. In [87], a DC microgrid comprised of a PV, fuel cell, microturbine, diesel generator, and ESS units is optimally dispatched. Two objectives are set: the reduction of the generation cost and the emissions. To solve the problem which includes nonlinear equations and integer variables, a (MIMLP) algorithm, the branch and reduced optimization navigator (BARON), is selected and tested in a multi-objective scenario.

Having the same starting point and algorithm parametrization, these algorithms lead to a single result and are generally based on gradient-descent methods that gradually improve an initial solution. These methods are faster than heuristic ones but can converge into local minimums because they tackle solutions in a concentrated space of research. Therefore, they favor the exploitation of known solutions (intensification) over the exploration of the field of study (diversification)[88].

Besides, there are deterministic techniques that require a certain modification of the problem structure such as dynamic programming (DP), linear programming (LP), mixed integer linear programming (MILP), etc. For instance, the problem is divided into successive discrete states to find the global optimum in a DP algorithm. At each calculation step, the algorithm considers all meshed decision variables and calculates the least costly transitions according to a criterion to optimize[89]. The DP is applied in [90] to optimally schedule a grid-connected microgrid integrating solar PV and ESS. The total cost function corresponds to the sum of the operation cost of each operating unit including the grid. DP algorithm is applied in this thesis as a deterministic optimization method along with other metaheuristic optimization techniques. The optimization of the DC microgrid and the applied algorithms are detailed in Chapter 3. Yet, if the cost functions and constraints can be expressed in linear expressions as a function of optimization variables, the LP method can be selected to find the global optimum of the problem. Dual Simplex and interior point are the most commonly used algorithms to solve LP optimization problems[91]. In addition, integer and binary variables can be added to the linear problem to further express a logic status in the microgrid (e.g., turn on/off a diesel generator, connect/disconnect the microgrid to/from the grid, etc.). In such cases, the optimization problem is formulated as a MILP problem, and the Branch and Bound algorithm is adopted to find the optimal solution[91]. A MILP optimization problem is formulated in [92] to optimally schedule the power in a microgrid. The optimization aims to minimize operating costs and promote self-consumption. The objective function is written

as a function of regular variables and a binary one named "*status*" which indicates whether ESSs work in a grid-interactive mode. The main drawback of LP and MILP is that they cannot include any nonlinear behavior of the system in the problem formulation.

1.7 - Online optimization techniques

The above-stated techniques are offline optimization methods that find a global optimum for the whole-time horizon based on generation, load profiles, and pool price predictions. However, prediction errors in RESs, load power, and pool price always exist and lead to a suboptimal solution if the optimal power references set by the offline optimizer are not updated through ongoing online optimization. The principle online optimization techniques are cited in this paragraph.

Model Predictive Control (MPC), also known as Receding Horizon Control (RHC)[93], the based optimization approach is one of several online optimization techniques that is gaining increased interest and is widely applied in the EMS of microgrids.

A general definition of MPC is "*a set of control approaches that take full advantage of the system model under specific constraints to gain the control signals or commands through minimizing predefined cost functions or objective targets*[93]*".* Another definition of the MPC optimization technique is proposed in [94]: "*MPC is an optimal control method that converts an infinite long open-loop optimization into a limited long closed loop at each sample time using the receding horizon strategy and considering the dynamic performance of the system, the control objectives, and the constraints".*

Fig.1.12 shows a basic simplified diagram example of an MPC method in which $X = [P_{grid}, P_{ESS}]$ are the problem variables and outputs, $SOC(t_k)$ is a state variable calculated from the discrete state equation : $SOC(t_{k+1}) = f(SOC(t_k), P_{ESS}(t_k))$, $J_t(X)$ is the total cost function to minimize, and $g(X)$ is the constraint of the problem. As seen, at each sampling step a selected optimization algorithm is executed for the whole-time horizon $[t_k = t_0, t_{k+N}]$.

For each possible transition between the SOC state variable, and over the whole-time horizon, constraint and cost function equations are evaluated to find the best route. Finally, the trajectory that complies with predefined constraints and corresponds to the minimum total cost function is retained. Only the optimal schedule of t_1 time interval is applied, the time horizon moves forward by one time interval, and the optimization algorithm is executed again for the whole new time horizon $[t_1, t_{k+N+1}]$ and so forth. The MPC-based optimization approach was applied in [95] to find the ideal power scheduling of a microgrid consisting of solar, ESS, loads, and utility grid by minimizing the total energy cost of the entire system.

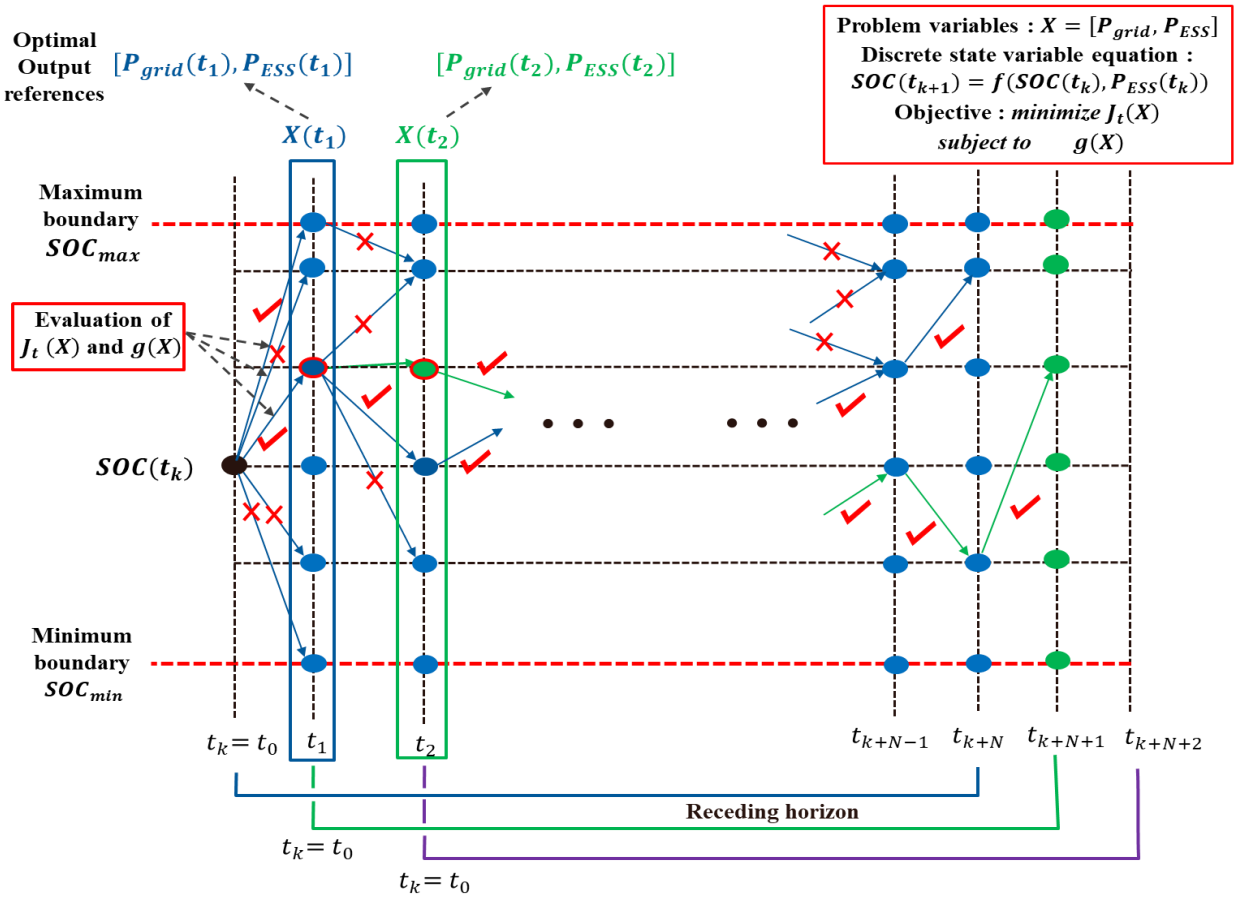


Fig.1.12 A basic simplified diagram example of an MPC-based optimization technique.

The continuous state space of the controlled model is discretized, and a graph-search algorithm is adopted. The proposed model uses a 24-hour prediction horizon and a 15-minute control horizon, it is compared to four optimization methods GA, PSO, QP, and SQP to prove its effectiveness. In [96], an MPC strategy is applied in a DC microgrid including RESs, a DG, and an ESS to minimize the operational cost. The optimization problem is formulated as a (MILP) and solved for a 48-hour time horizon with a sampling step of 15 minutes for the rolling horizon. Wind and solar energy forecasting models and neural networks for two-day-ahead electric consumption forecasting are also designed with updated data. To prove the viability of the proposed EMS MPC-based approach, it was compared to the traditional optimization method. An abundant number of MPC-based optimization technique articles are found in the literature, for further information and examples one can refer to [93].

Therefore, the MPC-based optimization technique with a rolling horizon made possible the real-time management of energy and so, the compensation of mismatches between predicted RESs, load profiles, and energy market prices and real values. Yet, if existent mismatches occur with faster dynamics than the sliding window of the receding horizon, the grid operates as a slack bus for the corrective action needed to compensate for the uncertainties. This solution may not be

optimal especially, at high pool prices. Moreover, reducing the sampling step of the receding horizon would require high computational servers to rapidly solve the optimization problem at each sampling step then, the cost of the system increases. To overcome this obstacle, many authors have included an additional internal optimization stage to the standard MPC technique or a feedback correction loop with faster dynamic to further reduce any mismatches between predicted and real-time data. In [97], an MPC-based economic scheduling problem of a DC microgrid is formulated. Two solvers are applied: the first named (E-solver) solves the economic scheduling problem formulated as a MILP for a 24-hour time horizon and a sampling step of 15 minutes for the rolling horizon. The second named (L-solver) solves the transmission loss problem formulated as an NLP and is executed at each one-minute interval. By this, the L-solver improves the model accuracy by adding the transmission losses, minimizing them, and assuring fast real-time control. A two-level optimization algorithm is proposed in [98] to minimize the total operating cost of the microgrid and the pollutant gas emissions. The optimization problem is formulated as a MILP framework and the MPC rolling horizon is established to schedule the operation for a 24-hour time horizon with a time step of 15 minutes. A feedback intrasample correction part is introduced to adjust the output of the units and balance the difference between the forecast values and the actual values at each one-minute intrasample. The feedback correction was expressed as a new optimization problem that minimizes the prediction error while taking into consideration only the present state of the system.

Several authors have included an online correction stage to the offline day-ahead optimization problem without applying the receding horizon strategy and yielded in turn efficient results. For example, supervisory control is applied in [92] to compensate for mismatches between scheduled values and real ones. The day-ahead optimization problem is formulated as a MILP to minimize the operating cost and maximize self-consumption with a sampling step of one hour. The supervisory control consists of two fuzzy interference systems with integral action. In [88], a tolerance band method is proposed as an online correction part to compensate for errors between predicted and real scheduled power references. The tolerance band online regulation approach is expressed as a new optimization problem and solved using SQP.

1.8 - Applied optimization strategy and main outcomes of this thesis

Research works on microgrid optimization are peaking since the last decade where a total of 1394 papers related to microgrid optimization have been published between (2014-2021) according to [99]. Besides, the fastest growth rate in journal publications addressing microgrid optimization was in 2017 with a growth rate of 30.64%. Among journals on microgrid optimization, the most cited one is “ A Model Predictive Control Approach to Microgrid Operation Optimization”, with a total of 345 citations [99]. As seen, recent research works are focused on the tertiary control level of DC microgrids especially, the optimal energy scheduling of DC microgrids. More specifically, the MPC-based optimization approach with the receding horizon is predominantly applied, and 2) the comparison between different optimization algorithms, in terms of complexity, convergence

speed, global versus local optimum finding, single versus multi-objective achievement, algorithms hybridization, etc., is in turn frequently addressed.

Considering the foregoing, this thesis tackles the problem of DC microgrid optimization from a different perspective. While most optimization approaches prioritize the optimization techniques and their results at the expense of the model precision, this thesis emphasizes the modeling accuracy of a DC microgrid without compromising the multi-objective optimization part. It considers three major modeling drawbacks that are rarely treated in the literature but highly influence the results of the optimization problem and the EMS:

1. Elimination of primary and secondary control level techniques such as MPPT control: Since the MPPT technique is seated at a higher level than the optimization control level, it is not considered in most of the studies, and instead simplified mathematical expressions are used [81], [98] [73] to express the outputted power of PV and wind turbine energy sources when formulating the optimization problem. These simplified expressions induce output power prediction errors that directly influence the decision-making of the optimizer. To handle this hurdle, modeling strategies are proposed in this thesis to include the MPPT control to the RESs without applying a detailed electrical model.
2. Complexity reduction by omitting nonlinear behavior and prominent variables from the system: The nonlinear behavior of many sources is frequently omitted by applying linearized expressions in the problem formulation either to reduce the problem complexity, increase the solver speed, or formulate the optimization problem as a MILP (a decent example is the adoption of the linear state space model of the battery in [95], [98], [100]). This linearized version implies that the voltage of the battery is always constant whereas, it has an exponential characteristic that largely impacts the real computed power. A precise battery model is established in Chapter 2, and the temperature effect is included in the model as an additional variable that highly affects the performance of the storage system.
3. Model simplification of power electronic devices by applying constant converters' efficiencies: In most research, the converters' efficiencies are not addressed or considered constant for all operating converters regardless of their types or the transited power [88], [101]. A major outcome of this thesis is the precise modeling of converters' losses based on their types (DC/DC, AC/DC), the selection of switching frequency, and the modulation technique. This accurate model is applied to the optimization problem in which the minimization of converters' losses is one of the predefined objectives.

Besides the minimization of converters' losses, the minimization of the total operating cost of the DC microgrid, and the reduction of the pollutant gas emissions are the main objectives of the optimization problem. Several constraints are introduced to guarantee the safe operation of the battery and emulate a real test scenario. Based on the load, solar irradiance, wind speed, temperature, and electricity purchase price input data that are partially known through predicted

profiles, two optimizations are accomplished. The first denoted offline optimization is accomplished the day ahead based on the predicted profiles and outputs the optimal power references of dispatchable sources for the next 24 hours. A second online optimization stage is added to update the optimal power references due to the mismatches between predicted and actual profiles.

In addition to this first chapter which represents the state of the art in the DC microgrid control and management, the manuscript includes four additional chapters. Chapter 2 introduces the DC microgrid configuration, size, and 24-hour modeling strategy. The 24-hour model is derived from two mathematical models: the average and the instantaneous microgrid models which are set out in Chapter 2. The offline optimization problem for the day ahead is formulated and solved in Chapter 3. However, the online optimization stage which consists of a feedback correction part is applied and detailed in Chapter 4. Finally, chapter 5 concludes the thesis.

1.9 -Conclusion

After a predominantly century of centralized energy generation, the distributed generation approach is taking the lead due to several motives such as the ease of rural electrification, the reduction of transmission and distribution losses, and maintenance costs, the higher immunity against energy security problems, cyber and physical attacks, cascading outages, etc. Besides technical catalysts, natural phenomena such as the depletion of fossil fuel, which are the main origin of energy generation in centralized power plants, climate change, and the urgent need to integrate RESs were decisive grounds to endorse a distributed generation strategy.

With the proliferation of distributed generation and renewable energy sources, the microgrid concept was proposed at the beginning of the 21st century as a group of interconnected sources and loads that act as a single controllable entity to the grid. Thanks to their maturity and standardization, AC microgrids first prevailed and captivated the attention more than DC microgrids. Since the last decade, DC microgrids have regained an increased interest in the research field and are advanced in several applications over their AC counterparts due to the surge in integrated RESs from which several are of DC nature such as solar panels, the DC-nature of most of the ESSs such as batteries, and fuel-cells making the connection to a common DC bus more efficient than an AC one, the increasing number of DC-type loads, and the ease of control of a DC microgrid.

Thereupon, a DC microgrid configuration consisting of RESs, traditional pollutant sources, loads, and an ESS is studied in the context of this thesis. To control a DC microgrid, the three-level hierarchical control is applied of which droop control is one of the most used techniques on the primary control level that ensures proper load sharing and common DC bus voltage stabilization. Having redundant research on the primary and secondary control levels, lately, the tertiary control

level has been increasingly investigated. At this level, the energy management system of the DC microgrid is addressed by formulating an optimization problem with predefined objectives, and constraints. The optimization problem is solved using metaheuristic or deterministic techniques. Besides offline optimization, online optimization methods are proposed in the literature to compensate for any mismatch between predicted and real data.

The MPC, or receding horizon control, is predominantly used as an online optimization technique that yields good results if the sliding window of the receding horizon is fast enough to compensate for all mismatches between predicted and real data. This requires high-performing servers or simplified mathematical models in the formulation of the optimization problem.

In this thesis, the optimization problem is tackled from another perspective which is the accurate modeling of a multi-objective optimization problem. Precise dynamic models, nonlinear behavior, and MPPT techniques are added to the optimization problem and shown how highly they affect the optimization results. Three objectives are selected based on the actual international energy policies: the minimization of the total operating cost, the reduction of pollutant gas emissions, and the improvement of converters' efficiency by minimizing converters' losses. The secure operation of the battery and limits on purchased/sold energy from/to the grid are considered. The optimization problem is solved using metaheuristic and deterministic techniques, and an online optimization stage is added to further refresh outputted optimal power references.

Chapter 2 : Modeling of the 24-hour DC Microgrid

2.1 Introduction

In this chapter, the configuration, sizing, and modeling of the 24-hour DC microgrid are set out. The 24-hour modeling of the DC microgrid constitutes a major challenge to address as all the simulations are performed on a standard core i7 computer processor (2630QM CPU @ 2.00GHz) with an 8.00 Gb installed RAM. In the absence of any high-performant server with a high processor and installed memory capabilities, the modeling of a detailed 24-hour DC microgrid model that includes fast dynamics, transient states, switching devices, and current and voltage loops is practically impossible. The main barrier to surmount when modeling a 24-hour DC microgrid on a standard PC is the limited memory and CPU performance. The inclusion of all dynamic phenomena with fast variables imposes a small calculation step size of the simulation. As all system equations are evaluated at each calculation step size, the duration of the simulation is highly affected by the selection of the calculation step size. Smaller calculation step sizes induce slower simulations and vice-versa[102]. Moreover, the complexity of the problem and memory usage rise with the increasing number of variables and equations to solve at each calculation step size. Therefore, simulating the detailed DC microgrid model with all fast dynamics over a 24-hour simulation will result in an extensive duration of the simulation. Besides, it incurs an excessive usage of the computer CPU and memory which leads inevitably to full capacity attainment and so an unresponsive program behavior and a blocked simulation.

To overcome this obstacle, most of the researchers that work on standard computers apply when formulating the optimization problem, a much simpler DC microgrid model that relies on simplified mathematical equations relating the generated DER power to natural variables such the solar irradiance, temperature, wind speed, etc.[81], [98] [102]. However, electrical variables with fast dynamics such as the current, frequency, and voltage are excluded from the model and considered as established[99]. Though this approach is instrumental in facilitating the solution of the optimization problem and remains upheld as the targeted control horizon and objectives of the optimization problem are much slower than electrical variables, it might induce sub-optimal results when applying the EMS on a real DC microgrid. Power computing errors result from the difference between the applied simplified model which doesn't accurately emulate the real characteristics of operating units and the real microgrid model. This issue is rarely addressed in the literature because of the existent segregation between the optimal control and the modeling of a DC microgrid.

In this context, this chapter addresses this problem and proposes several mathematical techniques to overcome the 24-hour modeling hurdle. It presents several averaging techniques, look-up tables, and curve-fitting methods to reach an intelligible trade-off between model accuracy and simulation speed to make the 24-hour model a feasible matter[102]. The trade-off is reached by omitting irrelevant fast variables and phenomena from the model which enables the increase of the

calculation step size while maintaining the essential ones that impact the accurate power calculation of all sources.

Two main objectives are accomplished through the applied modeling strategy. All operating sources, especially the RES which are the main energy source contributors to the DC microgrid, are precisely modeled. This results in accurate power-computed values that serve as data inputs to the optimization controller presented in the next chapter. In turn, the results of the optimization problem are directly affected by the precision of the collected data. Hence, by providing precise power value inputs to the optimization problem, the obtained results wouldn't present any mismatches when applied to a real DC microgrid model. Second, all variables that are subject to constraints in the optimization problem or are directly targeted in the optimization goals are maintained and represented in the model. Consequently, the proposed 24-hour model represents the closest emulation of DC microgrid characteristics that can be achieved on a standard computer CPU and memory.

Next in each section of this chapter, the energy conversion chain of each unit is presented separately. The mathematical model of each source, the converter type, and the control strategy are detailed. Finally, the 24-hour model of the whole assembled DC microgrid is presented through a simulation test that validates all advanced modeling techniques in this chapter.

2.2 Configuration, energy management problem formulation, and sizing of the DC microgrid

2.2.1 DC microgrid configuration

The applied configuration is shown in Fig.2.1. It consists of a PV array and a wind turbine as RESs, a diesel generator (DG) as a traditional pollutant source, an ESS consisting of a lithium-ion battery, a residential-type load, and the microgrid can operate in islanded or in grid-connected mode. The selected topology is a single-bus topology, commonly used in DC microgrid applications[103], in which all units are connected to the common DC bus through local converters. Each operating unit, its proper converter type, and control technique are detailed separately in this chapter. As a general EMS strategy, the PV and WT are always functioning in MPPT mode since they generate clean energy, and one has an interest in continuously extracting the maximum available power. This management strategy of RESs is mostly found in DC microgrids' optimal EMS[81], [83], [99]. Then, the output power of RESs is non-dispatchable and is applied as input to the offline optimization problem in addition to the load power profile. The dispatchable sources which are the battery, the (DG), and the grid represent the decision variables of the optimization problem. Once solved, the offline optimization problem set the power references of the battery, the DG, and utility grid converters denoted respectively P_{batt_ref}, P_{DG_ref}, and P_{grid_ref}, for the next 24 hours. As seen in Fig.2.1, arrows are used to indicate the power flow direction in the microgrid. Single

arrows indicate a unidirectional power flow such the ones of the PV, WT, and DG which operate invariably as sources so, the arrow's direction is outward. The generated power of these sources passes through unidirectional local converters to reach the common DC bus. Same for the DC residential load which always receives the required power through its unidirectional local converter and so the arrow's direction is inward. Since the power flow in the PV, WT, DG, and load is unidirectional the power signs P_{PV}, P_{WT}, P_{DG}, and P_{load} are conventionally greater or equal to zero. Contrarily, a double arrow is used to indicate the bidirectional power flow in the battery, and the grid converters.

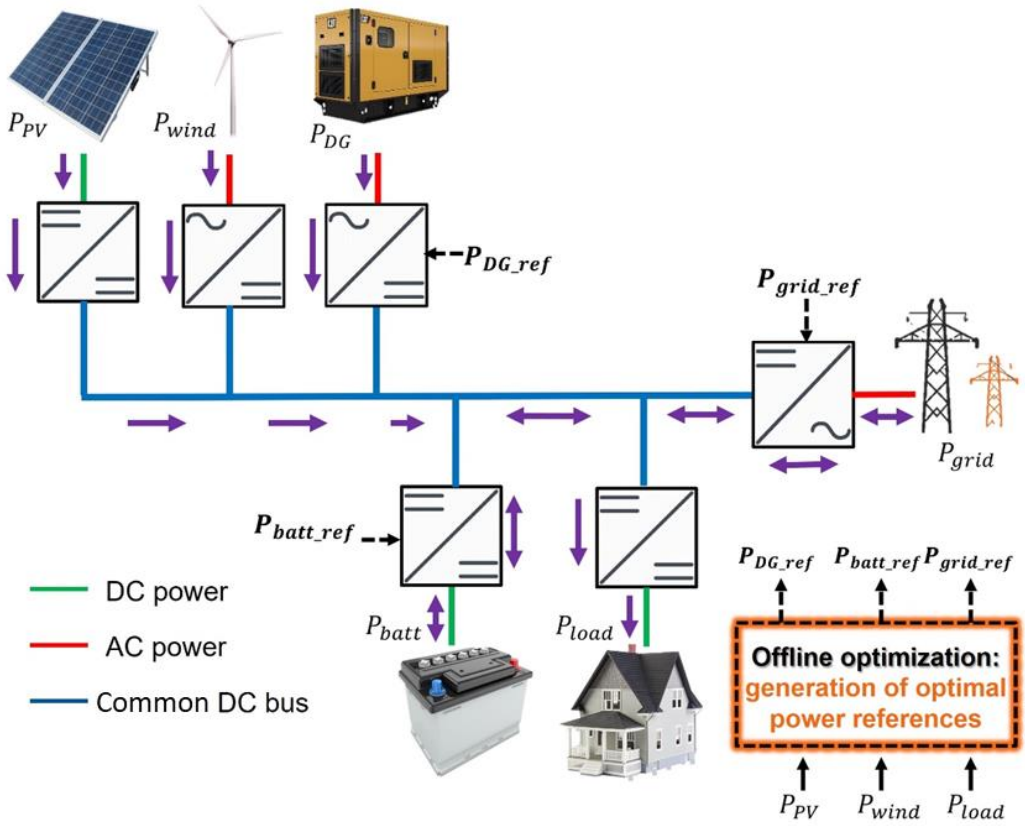


Fig.2.1 DC microgrid applied configuration.

If the battery is in charge mode, the power transits from the common DC bus to the battery and vice-versa in discharge mode. As convention, $P_{batt} > 0$ when the battery is discharging and $P_{batt} < 0$ when it is charging. This convention is widely used in the literature [104]. Similarly, if the power is purchased from the grid, conventionally, $P_{grid} > 0$ while, if it is sold to the grid $P_{grid} < 0$.

2.2.2 Energy management problem formulation

As stated before, the optimal sizing of DC microgrid units is out of the scope of this thesis without overlooking its crucial impact on the decision-making of the optimal EMS. Accordingly, the size of each operating unit in the microgrid will directly impact the amount of delivered/absorbed

power and so the goal, frequency, and continuity of interventions of all operating units. Hence, the problem should be positioned in a way that establishes a sort of competitiveness between the operating units on the predefined optimization goals. Otherwise, the solution to the optimization problem may become trivial or unfeasible[73]. From here, the problem should be defined as follows: In a DC microgrid, a specific load demand should be covered over 24 hours by existing energy sources consisting of RESs, DG, utility grid, and battery with the object of reducing the total O&M cost of the microgrid, the pollutant gas emissions, and the overall losses of converters. The highest priority in feeding the load demand is attributed to the RESs as they produce clean energy at near zero cost per kWh. Yet, if the load demand surpasses the RESs generation the DG, the ESS, and the utility grid take charge of covering the unmet load. To further identify the general EMS strategy of the microgrid, Fig.2.2 shows a brief flow chart of possible encountered scenarios. First, as defined above, the main objective is to cover the load demand so, that available RES power (P_{RESs}) is evaluated and compared to the load power (P_{load}), two possible cases come across.

1. $P_{load} < P_{RESs}$: the generated power exceeds the load demand then, all the load is fed by RESs, and the remaining power is entirely sold to the grid if the battery is fully charged (the negative grid power ($P_{grid} < 0$) implies that the power is sold to the grid). Yet, if the battery is not fully charged, the exceeding RES power can be utilized to either charge the battery and sell the remaining power to the grid simultaneously or accomplish uniquely one of the two operations (this can be expressed as $P_{grid} \leq 0$ and $P_{batt} \leq 0$). The decision-making in such a case is assigned to the optimizer which outputs the battery and grid power references (P_{grid_ref} and P_{batt_ref}). The DG is always turned off in this scenario.
2. $P_{load} > P_{RESs}$: the generated power is less than the load demand then, RES generated power is insufficient to meet the total load demand. The unmet load should be covered by existing DERs based on the optimizer's decision. Two subsections are identified depending on the battery's state of charge. If the battery is fully discharged, the utility grid and the DG may intervene simultaneously or separately to essentially feed the unmet load and potentially charge the empty battery if the optimizer requests that (this subsection is expressed as $P_{grid} \geq 0$, $P_{DG} \geq 0$, and $P_{batt} \leq 0$). However, if the battery is not fully discharged, it may be in charge or discharge mode based on the optimizer's preference. If in discharge mode, the battery may intervene solely to cover the unmet load or contribute fractionally to the power mix with the utility grid and/or the DG (this can be expressed as $P_{batt} \geq 0$).

As seen from the general EMS strategy, several scenarios can be encountered, and here lies the instrumental significance of the optimization process in finding the best combination of operating DERs that meets the load demand regarding the predefined constraints and objectives.

Once the EMS strategy, the possible scenarios, and the objectives of the optimization are defined, the sizing hurdle of the DC microgrid is overcome.

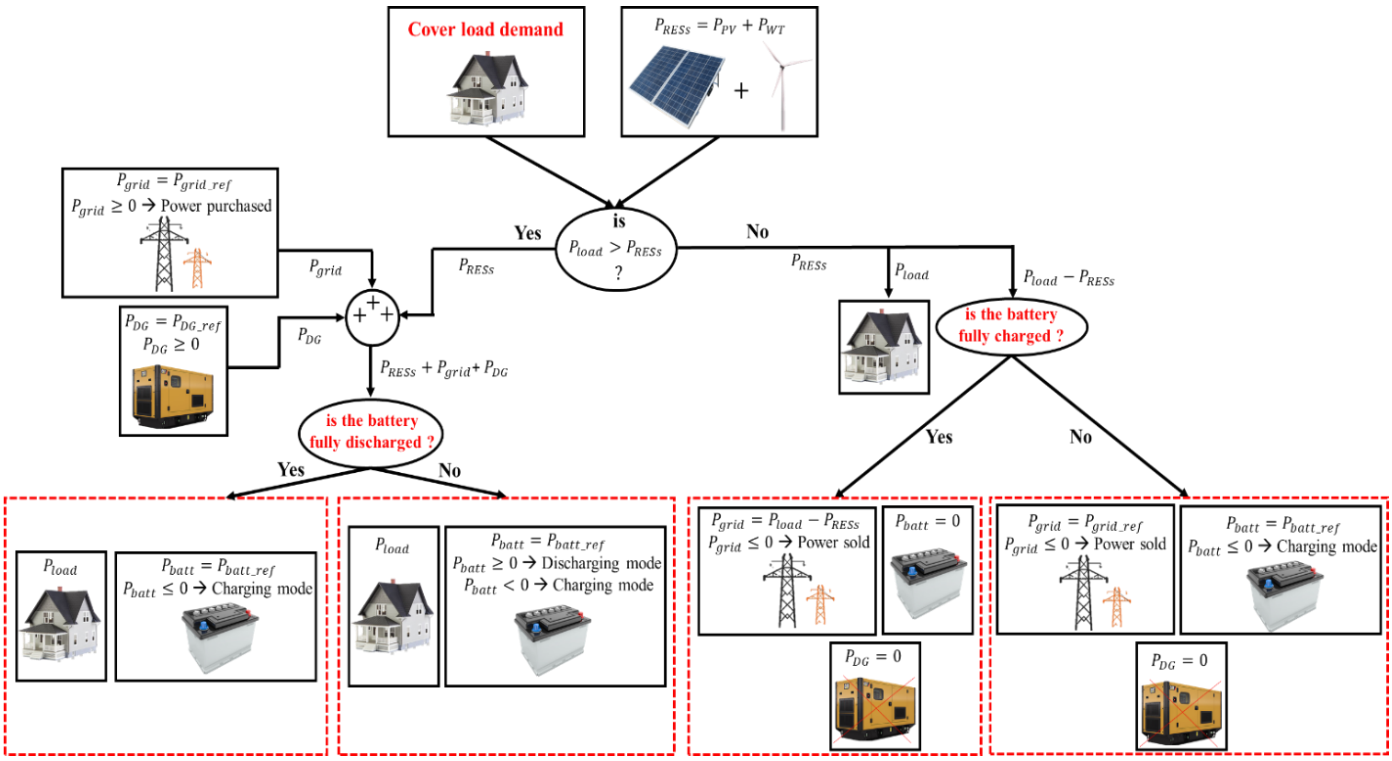


Fig.2.2 Flow chart of the general EMS strategy.

Yet, particular attention should be paid when sizing the microgrid to prevent any oversize or undersize of DERs that impact tremendously the EMS strategy and the solution of the optimization problem. For instance, a load demand that always exceeds the RES production implies a high reliance on the grid and the DG to directly feed the load, a restricted role of the battery, and an abstraction of the scenario of excessive energy production. While, if RESs are oversized this may restrict the role of the grid, the DG, and the battery. The same impacts result oppositely if the load is oversized or undersized. Besides, an oversized ESS will automatically release the constraints on the battery whose SOC remains high. In that case, the role of the DG is canceled which may intervene when the load demand exceeds RES production, the battery is discharged, and the pool prices are high. Contrarily, lower and higher bounds of the battery's state of charge are quickly reachable in an undersized ESS which may incur excessive usage of the battery, increased daily number cycle of the battery, and so a shortened battery lifetime[105]. The DG size has a minor impact on the EMS strategy when compared to the RESs, battery, and load since it operates as a backup energy source at high pool prices. Lower and higher Bounds of DG-produced power and purchased/ sold power from/ to the grid are fixed when formulating the optimization problem in the next chapter.

2.2.3 Sizing of the DC microgrid

As for this study, a low-voltage DC microgrid (LVDC) application for residential load is adopted with a rated power of 50 kW, and a common DC bus voltage of 800 V. Based on IEEE standards 1709-2010, the recommended DC bus voltage shouldn't exceed 1.5 kV for LVDC

microgrids[106]. Similar demonstration projects are found worldwide for LVDC microgrids, for instance, the FREEDM project in Raleigh, USA proposed in 2011 to a factory for DC lighting, and DC building load with a rated power of 100 kW and a 400 V DC bus voltage[107]. Another project is the Office building of Nanjing Guochen Co., Ltd. Located in Nanjing, China, proposed in 2018 for an EV charging pile, lighting, and DC appliances of an office, with a rated power of 74 kW and a 600 V common DC bus rated voltage[108]. A third demonstration project is the Suzhou Tongli integrated energy service center in Suzhou, China suggested in 2018 for lighting, and air conditioning load with a rated power of 300 kW and three different DC bus voltage levels of 750/540/220 V[108]. Further applications for LVDC microgrids can be found in [109]. In this thesis, the selected load is a cluster of small DC-type residential loads then, a DC/DC buck converter is required to decrease the voltage from 800 V to a safer lower level as shown in Fig.2.1. According to IEC 60038 [110] and IEC 61140 [111], LVDC voltage level can be divided into two ranges, including the range from 120 V to 1.5 kV, and the range bellow 120 V. The 120 V voltage level is defined by IEC as the upper boundary of extra low-voltage, which is a low risk under dry conditions [112], [113]. Meanwhile, the voltage level of a low-voltage DC distribution network should not exceed 400 V [114]. As a result, the 120 V voltage level can be used as a DC distribution network for the cluster of DC residential loads. Given that the precise modeling of the cluster of DC residential loads is out of the scope of this work, a simplified model through a standard unified residential load profile is applied. As a result, the DC residential load and its corresponding DC/DC converter appear as a single entity throughout the load profile.

Table 2.1 summarizes the size of each DER of the microgrid. As seen, the PV array and WT have almost nearby rated powers of 50 KW, knowing that they won't practically operate simultaneously and continuously at their maximum rated power. The DG generates 55 KW as nominal power with a 50 Hz nominal frequency and the rated power of the utility grid is 100 KVA with a 50 Hz nominal frequency. Concerning the battery capacity, a minimum of 3 to 4 hours of battery backup should be provided for the load in the presence of the backup diesel generator which can be automatically turned on in case of a full discharge of the battery. This ratio (3 to 4 hours) of battery backup is found in IEEE standards for traditional telecommunication sites[115] and represents a reasonable selection for the ESS capacity in residential applications, where other DERs are capable of intervening to feed the unmet load. The battery is generally sized under constant load during a predefined period then, an average constant load of 30 KW is chosen and a ratio of 4.16 hours is obtained by dividing the battery-rated energy (W_{batt_r} = battery rated capacity (Ah) × battery rated voltage (V) = $250 \times 500 = 125\ KWh$) over the constant load value (30 KW). We take note that this ratio only represents an estimation criterion that helps size the battery meanwhile, the actual value of backup hours might differ as the full capacity of the battery cannot be exploited due to the boundaries on the state of charge and the discharged power won't remain constant over the discharging hours. By this, a typical LVDC microgrid application with a tangible and realistic sizing approach is applied and can be controlled optimally based on predefined objectives.

Common DC bus, rated voltage		800 V
Wind turbine maximum rated power and efficiency (%)		55 KW- 92.8%
PV array maximum rated power		50 KW
(DG) rated parameters	Power (KW) frequency (Hz)	55 KW - 50 Hz
Utility grid-rated parameters	Power (VA) - frequency (Hz)	100 KVA - 50 Hz
Battery-rated capacity and voltage		500 Ah – 250 V

Table 2.1 Sizing of DC microgrid principal units.

2.3 Instantaneous and 24-hour DC microgrid modeling

Once a new EMS strategy for DC microgrids is proposed by researchers, it is usually validated through experimentation on a real DC microgrid or through a Hardware-in-the-loop (HIL) verification in which the real dynamic characteristic of a DC microgrid is emulated[83], [92], [98]. In this thesis, a theoretical study on an offline multi-objective optimization of a DC microgrid followed by an online optimization stage is addressed. Certainly, the experimental and the (HIL) validation of the EMS strategy on a real DC microgrid or a real-time simulator would be interesting meanwhile, the two options weren't available during the accomplishment of the thesis. Thus, apart from the offline and online EMS strategy, a 24-hour DC microgrid model is developed. The effectiveness and viability of the EMS are validated through the 24-hour DC microgrid model. For this study, MATLAB/Simulink was selected as an engineering software tool to model and optimize the DC microgrid. Three modeling approaches were applied in MATLAB/Simulink to yield the 24-hour DC microgrid assembled model:

1) The detailed microgrid model is built in the Simscape library of Simulink using the specialized power systems from the electrical toolbox. Simscape library was chosen for the detailed modeling as it represents all microgrid units with accurate mathematical models including all electrical and mechanical equations and transients in the system. Besides, the Simscape model reveals real physical connections between DERs, converters, and loads. The high accuracy of this model imposes a reduced calculation step size and so a slowed simulation, an extensive computational burden, and memory usage. Accordingly, this model can only be run for a several-second simulation on a standard computer. However, being the most accurate, the detailed model serves as a reference model for the proposed averaging ones to assess their precision.
2) The 24-hour DC microgrid is uniquely built on Simulink as all electrical and mechanical equations of the system are reestablished and new simplified modeling techniques are advanced. These assumptions mainly target the calculation step size of the simulation model that is increased without compromising the model's accuracy.
3) The script format, including .m files and MATLAB functions, is utilized to add several averaging and curve-fitting techniques and to formulate the offline and online optimization EMSs that are presented in the next chapters.

As a result, the overall assembled 24-hour DC microgrid model is built using Simulink and the script format consisting of .m files and MATLAB function files. A simulation test of the obtained 24-hour model is revealed at the end of this chapter. Finally, we take note that the developed model isn't advanced as an alternative to the HIL real-time simulators which remain the most accurate emulators of any system characteristics convenient for long and real-time simulations. Next, the detailed model of each source along with its converter and strategy of control are presented first as reference models then, the simplifying strategies are advanced, and newly obtained models are compared to the detailed ones in terms of precision and simulation speed.

2.4 PV energy conversion chain

As depicted in Fig.2.3, the PV array conversion chain consists of a PV array block connected to the common DC bus through a DC/DC boost converter which functions in MPPT mode to extract maximum available power. The boost is controlled throughout firing pulses denoted u.

2.4.1 PV array

To model the PV array, the *"PV Array" "SimScape"* library block is selected. The block models an array built of strings of modules connected in parallel, each string consisting of modules connected in series[116]. The block has two input parameters as seen in Fig.2.3: the irradiance denoted S expressed in (W/m^2), and the cell temperature denoted T expressed in (°C). The electrical circuit of the PV array includes a light-generated current source denoted I_{Light}, a diode denoted d, a series and a shunt resistance denoted respectively R_s and R_{sh}expressed in (Ω), as shown in Fig.2.4. The P-*V* characteristic is defined by equations (II.1) and (II.2):

$$P_{PV} = I_{PV} \times V_{PV} \quad \text{(II.1)}$$

$$P_{PV} = V_{PV} \times I_{Light} - V_{PV} \times I_d - V_{PV} \times I_{sh} \quad \text{(II.2)}$$

Where $I_{PV}, I_{Light}, I_d,\ I_{sh}$, and V_{PV} are respectively: PV current (A), light generated current(A), diode current (A), shunt resistance current (A), and PV voltage (V). The diode current and the light-generated current are expressed as follows:

$$I_d = I_0\left[exp\left(\frac{V_d}{V_T}\right) - 1\right] = I_0\left[exp\left(\frac{V_{PV}+R_s.I_{PV}}{V_T}\right) - 1\right] \quad \text{(II.3)}$$

$$I_{Light} = \left(\frac{S}{S_{ref}}\right) \times \left[I_{Light_ref} + \alpha_{i_{sc}}(T_K - T_{ref_K})\right] \quad \text{(II.4)}$$

Where $I_0, V_d, V_T,\ S_{ref}, I_{Light_ref}, \alpha_{i_{sc}}, T_K$ and T_{ref_K} are respectively: diode saturation current (A), diode voltage (V), diode temperature voltage of the array (V), reference irradiance at standard test conditions (STC)s ($1000\,W/m^2$), reference light-generated current (A), temperature coefficient of short-circuit current ($A/°C$), cell temperature in Kelvin ($T_K = T + 273.15$),

reference temperature at (STC)s in Kelvin ($25°C \rightarrow 298.15$ K). All module data and numeric values of parameters are found in Appendix A.1.

This model representation of the PV array is the most accurate as it computes the output power as a function of the electrical components V_{PV} and I_{PV}: $P_{PV} = f(V_{PV}, I_{PV})$. As the mathematical equations of the PV array (II.1, II.2, II.3, and II.4) do not include fast variables requiring any restriction of the calculation step size, the same model is kept for the 24-hour simulation.

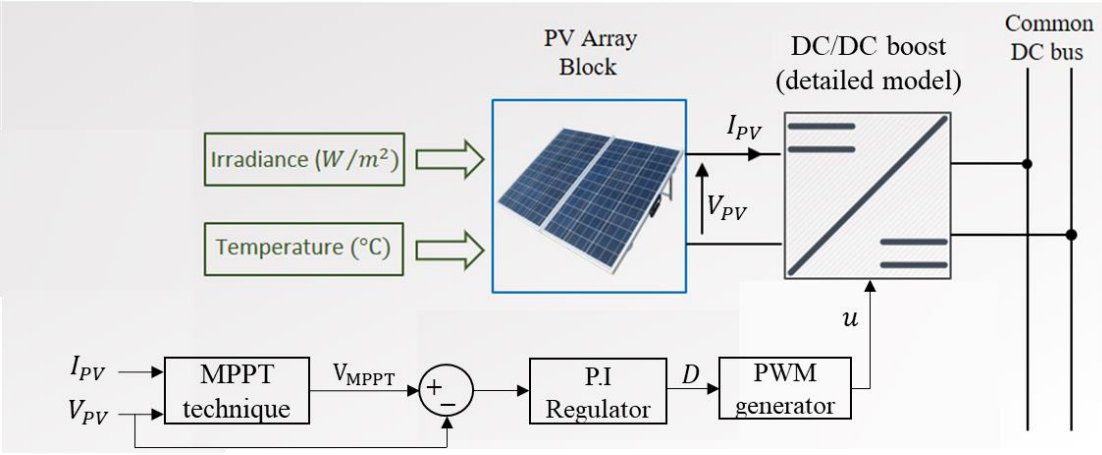


Fig.2.3 PV array conversion chain.

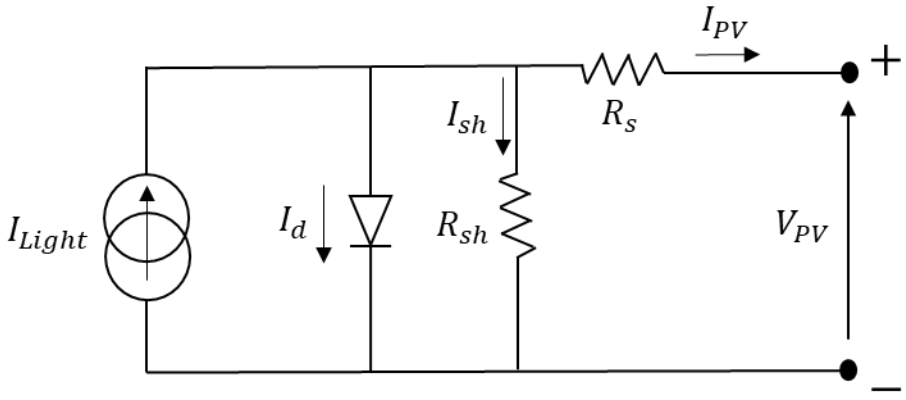


Fig.2.4 PV array electrical circuit.

2.4.2 DC/DC boost converter

2.4.2.1 Detailed model

The electrical circuit of the DC/DC boost detailed model is represented in Fig.2.5. This model is the most accurate as it includes the real electrical components (switching device, diode, filtering inductor, and capacitor). IGBT switches are chosen as switching devices for all operating converters as they highly comply with such applications and offer a reasonable trade-off between switching speed and maximum admissible power[117]. The IGBT is controlled by firing pulses, denoted u (Fig.2.3), with a fixed switching frequency $f_{sw_PV} = 20\ KHz$. The selected switching

frequency lies within the standard range of IGBT operating frequencies[117], [118]. As seen in Fig.2.5, the PV array model of Fig.2.4 is represented by a variable current source that should be connected to the DC/DC boost inductor considered, in turn, as a current source in Simscape/Simulink. To enable the connection of the PV current source with the DC/DC boost, and to access the PV voltage V_{PV}, a capacitor C_{in} is placed in parallel to the PV array block as seen in Fig.2.5. By applying Kirchhoff's current law, the equation bellow is stated, and V_{PV} can be obtained by integrating it:

$$C_{in}.\frac{dV_{PV}}{dt} = I_{PV} - I_L \tag{II.5}$$

To derive the boost equations the binary variable u (i.e., the firing pulses variable) is introduced which is equal to zero if the IGBT is OFF and one otherwise. Based on the electrical circuit of Fig.2.5, the boost equations can be expressed as follows:

$$\begin{cases} V_{PV} = R_L.I_L + L.\frac{dI_L}{dt} + (1-u).V_{BUS} \\ I_D = (1-u).I_L \\ (1-u).I_L = C_{bus}.\frac{dV_{BUS}}{dt} + I_{out} \end{cases} \tag{II.6}$$

Where R_L, I_L, L, u, V_{BUS}, u, I_D, C_{bus}, and I_{out} are respectively the inductor resistance (Ω), the inductor current (A), the filtering inductor (H), the firing pulses, the common DC voltage (V), the diode current (A), the common DC bus capacitor (F), and the output current (A).

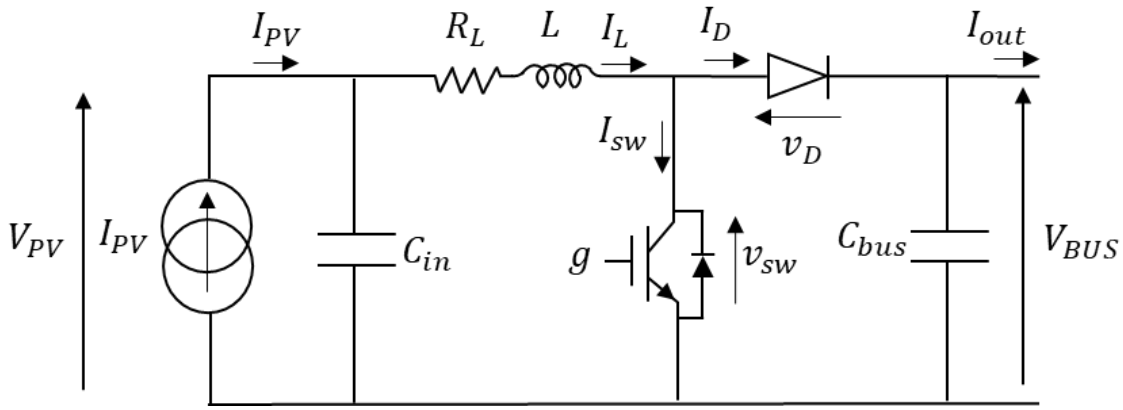


Fig.2.5 Electrical circuit of the DC/DC boost converter (detailed model).

2.4.2.2 Average model:

Based on the Nyquist-Shannon sampling theorem, which states:" to accurately reproduce a pure sinewave measurement or sample, the rate must be at least twice its frequency[119]", the maximum allowable step size of simulation can be determined. By evaluating the equations of the detailed boost model, one can identify that the highest frequency limiting the step size of the simulation is the switching frequency ($f_{sw_{PV}} = 20\ KHz$). To simulate the detailed model, and by applying the

Nyquist-Shannon theorem, a maximum allowable calculation step size of: $T_{step_det} = \frac{1}{2 \times f_{sw_{PV}}} = 2.5 \times 10^{-5}$ s is required, otherwise erroneous results may be obtained. Additionally, to get well-shaped curves of current, voltage, and power, the required ratio between the step size and the switching period has to be at least equal to 1/100 [120], [121]. Consequently, the calculation step size cannot exceed in this case $T_{step_det} = \frac{1}{100 \times f_{sw_PV}} = 5 \times 10^{-7}$ s $= 0.5\,\mu s$. As the switching characteristic with the real switches devices has the fastest dynamic in the system and is not targeted as an optimization objective in the EMS strategy, it can be considered as established. Thence, the real switches can be omitted, and the converter can be directly controlled by the duty cycle instead of the firing pulses. This model representation is known as the average converter model[122], [123]. The electrical circuit of the DC/DC boost average model is shown in Fig.2.6, it includes a controlled voltage source denoted V_L and controlled current source denoted I_{PV_out}. From Fig.2.6, the equations of the average model can be expressed as follows:

$$\begin{cases} V_L = (1 - D_{PV}).V_{BUS} \\ V_{PV} = R_L.I_L + L.\frac{dI_L}{dt} + V_L \\ I_{PV_out} = \frac{I_L.V_L}{V_{BUS}} \\ I_{PV_out} = C_{out}.\frac{dV_{BUS}}{dt} + I_{out} \end{cases} \quad \text{(II.7)}$$

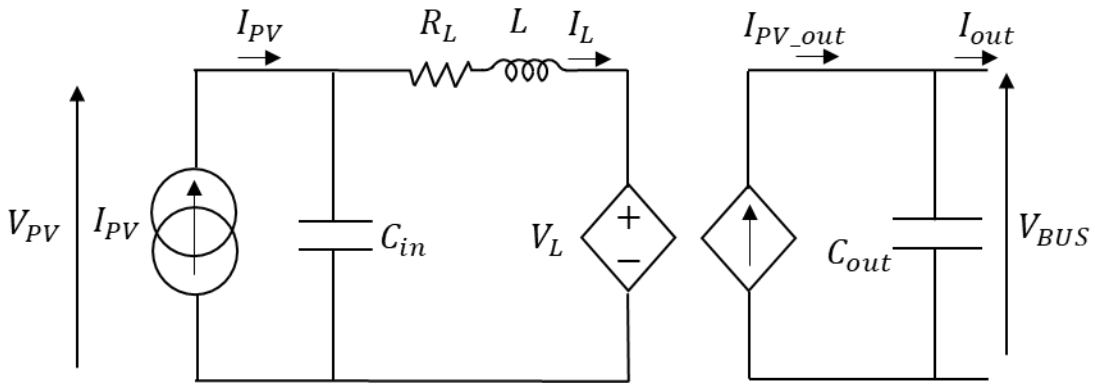


Fig.2.6 Electrical circuit of the DC/DC boost converter (average model).

Where V_L, D_{PV}, I_{PV_out} are respectively the converter-controlled voltage source (V), the duty cycle ratio of the PV, and the converter-controlled current source (A). To validate this model, it is compared to the detailed one in a simulation test. Both converters' models are simulated for one second using the same solver and the following parameters:

$R_L = 5\,m\Omega$, $L = 5\,mH$, $C_{in} = 6\,mF$, $C_{out} = 0.1\,mF$, and a simple load consisting of a resistor, connected in parallel to C_{out}, is applied with the value $R = 25\,\Omega$. A constant PV current source is selected: $I_{PV} = 64\,A$ and the following duty cycle ratio function is applied:

$$\begin{cases} D_{PV} = 0.5 & 0s \leq t < 0.5s \\ D_{PV} = 0.6 & 0.5s \leq t < 1s \end{cases}$$

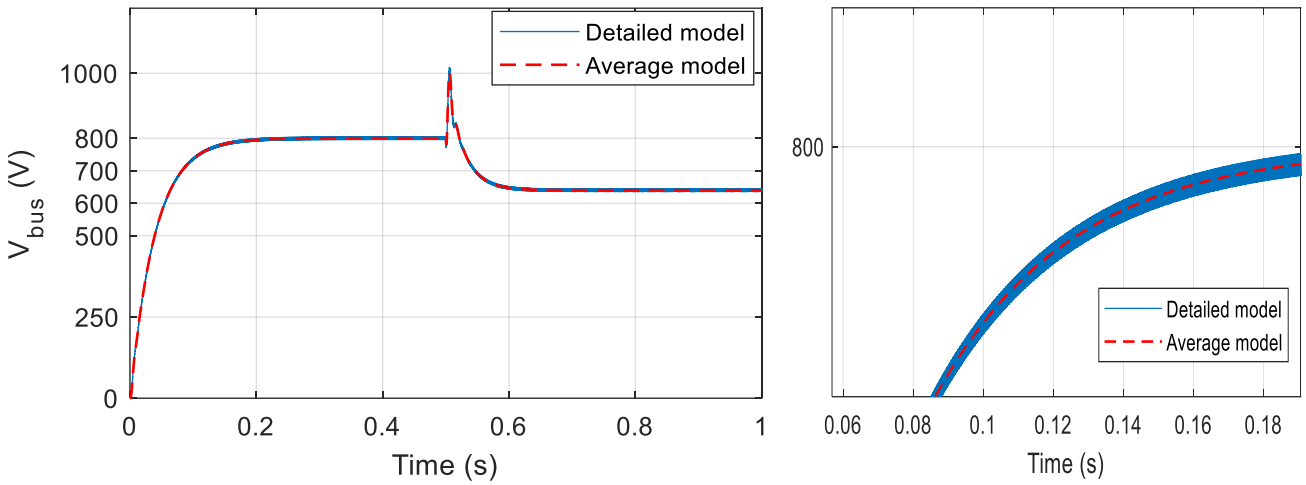


Fig.2.7 DC bus voltage of the DC/DC boost in the detailed and average model representations (on the left side: the whole curves over the full-time simulation, on the right side: a zoom over the transient state)

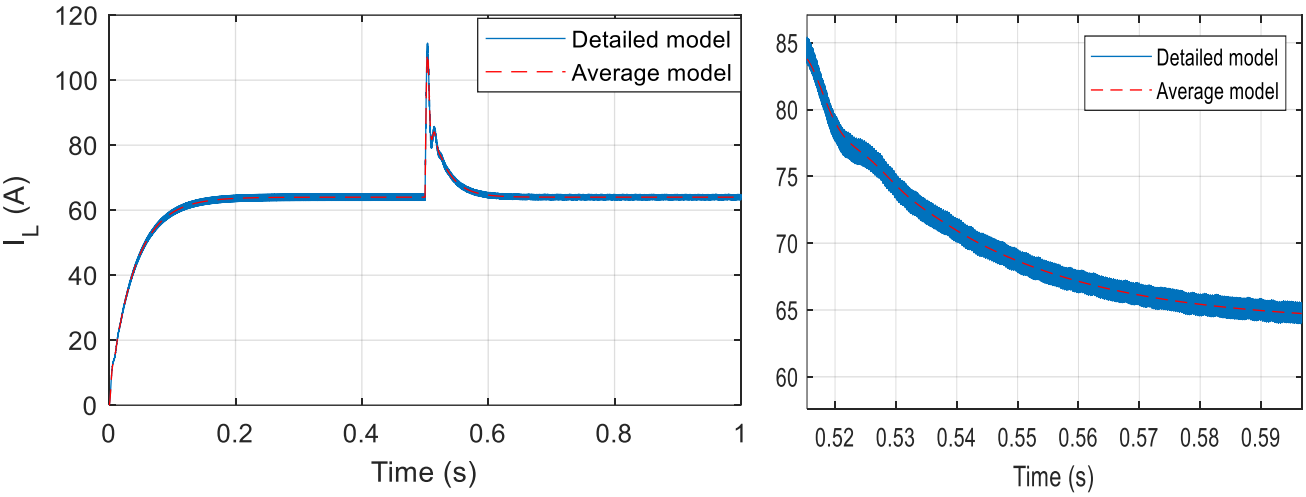


Fig.2.8 Inductor current of the DC/DC boost in the detailed and average model representations (on the left side: the whole curves over the full-time simulation, on the right side: a zoom over the transient state).

The step size calculation of the detailed model is set to: $T_{step_det} = 0.5\ \mu s$ as the switching frequency of the IGBT is set to: $f_{sw_PV} = 20\ KHz$. A step size calculation of the average model equal to $T_{step_av} = 50\ \mu s$ is chosen. The obtained simulation results are depicted in Fig.2.7 and Fig.2.8 in which the inductor current I_L and the DC bus voltage V_{BUS} are shown. It can be seen how accurately the average model curves follow the detailed model ones in transient and steady state. By applying the average model, the new calculation step size can increase at least 100 times compared to the detailed model ($T_{step_avr} \geq 100. T_{step_det}$). This assumption highly reduces the duration of the simulation as the calculation step size is increased, and the complexity of the model is reduced without compromising the accuracy of the model which always includes the dynamics of the electrical components. We take note that the above-selected values of R_L, L, and C_{in} are applied to the PV conversion chain for the rest of this thesis study, whereas the values of C_{out} and R were utilized only for the comparison between the detailed and average converters' models.

2.4.2.3 DC/DC boost losses:

Though power electronic devices are rapidly developing, and converters' efficiencies are unceasingly increasing, the reduction of converters' power losses plays a key role in the overall system efficiency improvement. By optimizing the converters' efficiency, the operating cost of the DC microgrid is reduced as well and the energy consumption decreases on a macro-level which complies with international energy policies[23]. While most DC microgrid applications neglect the converters' losses by considering a unit conversion ratio equivalent to 100% efficiency, others include the converters' efficiency in their models as a constant ratio by referring to figures provided by converters' manufacturers[88], [98]. In general, DC/DC conversion stages have higher efficiencies ranging between 98% and 99.7% compared to DC/AC conversion stages with a range between 95% and 97%[124]. In this study, converters' losses are modeled and added to the average model presented in Fig.2.6. The first losses that were already included in the DC/DC boost average model are the inductor copper losses which are modeled by a resistor, denoted R_L, placed in series with the inductor L. The second source of power loss in a converter is the conduction loss caused by semiconductor device forward voltage drops. The forward voltage drops in the diode and the IGBT can be modeled by a voltage source, denoted respectively V_{D0} and V_{IGBT0}, in series with an on-resistance denoted respectively R_D and R_{IGBT}[125]. Then, the IGBT and diode voltage sources and on-resistances are placed on the inductor branch side as seen in Fig.2.9. By referring to [125], V_{D0}, V_{IGBT0}, R_D, and R_{IGBT} can be expressed as follows:

$$\begin{cases} V_{D0} = (1 - D_{PV}).V_{f0} \\ V_{IGBT0} = D_{PV}.V_{IGBT_CE0} \\ R_D = (1 - D_{PV}).R_{D_f} \\ R_{IGBT} = D_{PV}.R_{IGBT_on} \end{cases} \quad \text{(II.8)}$$

where D_{PV}, V_{f0}, V_{IGBT_CE0}, R_{D_f}, and R_{IGBT_on} are respectively the duty cycle ratio of the converter, the diode forward voltage source (V), the IGBT forward voltage source (V), the diode forward resistance (Ω), and the IGBT on-resistance (Ω). All these parameters are defined based on the selection of each component and by referring to the manufacturer's datasheet. The detailed calculation of conduction loss parameters of the DC/DC boost can be found in Appendix B.1.

The last major source of losses in any converter is switching losses. These losses occur during the turn-on and turn-off transitions of semiconductor devices that require times of tens of nanoseconds to microseconds. Although these switching times are short, the resulting power-switching loss is significant[125]. Many techniques are proposed in the literature to model the switching losses. For instance, in [122], two terms corresponding to the change of the average voltage and current across the electronic switch due to the switching transients are introduced and added to the usual duty cycle ratio. Accordingly, the DC/DC boost converter equations are modified, and the included switching losses are revealed. Meanwhile, a simpler method, to estimate the switching losses, is proposed in [126], and is adopted in this study. The method introduces an equivalent resistance

that can dissipate the same heat as that produced by the switching loss. The switching losses equivalent resistance denoted R_{sw}, is placed in series with the inductor branch and the conduction losses' equivalent model as seen in Fig.2.9.

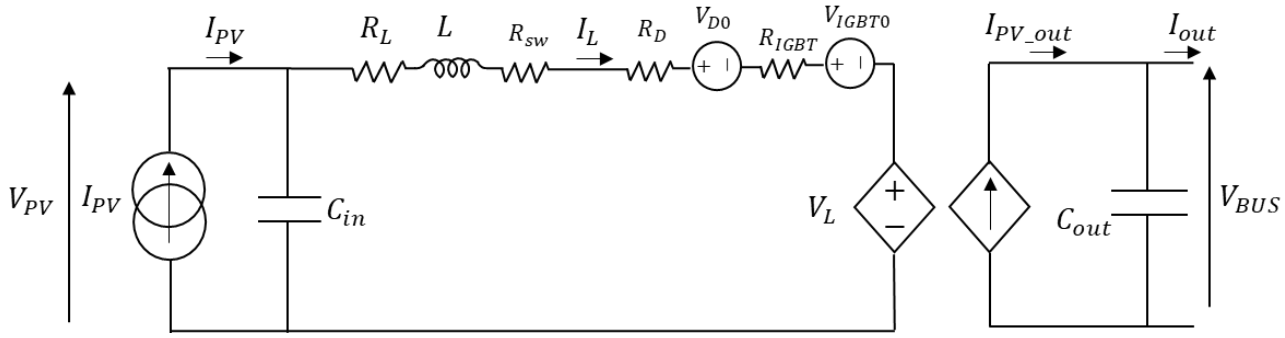


Fig.2.9 Electrical circuit of the DC/DC boost converter including the conduction and switching losses.

To compute the switching losses, the approximations of IGBT voltage V_{CE}, and current I_C waveforms are represented during the switching transition phases in Fig.2.10 (a) This switching losses calculation method is named the transition power loss method and is widely applied in the literature[126], [127]. As seen in Fig.2.10 (a), a linear approximation of the IGBT current and voltage waveforms is applied, and the below equations are derived during turn-on time (t_{on_IGBT}):

$$\begin{cases} V_{CE} = -\frac{V_{CE_max}}{t_{on_IGBT}} t + V_{CE_max} \\ I_C = \frac{I_{C_max}}{t_{on_IGBT}} t \end{cases} \quad \text{(II.9)}$$

Where V_{CE_max}, t_{on_IGBT}, and I_{C_max} are respectively the maximum switch voltage (V), the turn-on delay time (s), and the maximum switch current (A).
Using equations (II.9), the power loss in the turn-on interval can be written as:

$$P_{CE_t-on} = V_{CE}.I_C = -\frac{V_{CE_max}I_{C_max}}{t_{on_IGBT}^2} t^2 + \frac{V_{CE_max}I_{C_max}}{t_{on_IGBT}} t \quad \text{(II.10)}$$

The time-averaged power loss in the IGBT in the turn-on interval is obtained by integrating equation (II.10) over the switching period T_{sw}, which yields:

$$P_{CE_t-on} = \frac{1}{T_{sw}} \int_0^{t_{on_IGBT}} V_{CE}.I_C.dt = \frac{f_{sw} \cdot V_{CE_max} \cdot I_{C_max} \cdot t_{on_IGBT}}{6} \quad \text{(II.11)}$$

Following the same calculation steps, the time-averaged power loss in the IGBT in the turn-off interval can be expressed as follows:

$$P_{CE_t-off} = \frac{1}{T_{sw}} \int_0^{t_{off_IGBT}} V_{CE}.I_C.dt = \frac{f_{sw} \cdot V_{CE_max} \cdot I_{C_max} \cdot t_{off_IGBT}}{6} \quad \text{(II.12)}$$

Where t_{off_IGBT} is the turn-off delay time (s).

Thus, the total average power loss in the IGBT during the switching transitions is:

$$P_{CE} = P_{CE_t-on} + P_{CE_t-off} = \frac{f_{sw} \cdot V_{CE_max} \cdot I_{C_max}}{6}(t_{on_IGBT} + t_{off_IGBT}) \quad \text{(II.13)}$$

A last included source of switching power loss in the DC/DC boost is the turn-off losses of the power diode. The main cause of this power loss is the reverse recovery current of the diode which is normally accompanied by a large reverse voltage and can lead to substantially enhanced power loss at high switching frequencies[127]. As seen in Fig.2.10 (b), a segment approximation of the diode reverse recovery current and voltage figuring in several studies[127]–[129] is adopted. Hence, the diode current I_D and voltage V_D equations during the reverse recovery period are represented as follows:

$$\begin{cases} V_D = -\frac{V_{R_D}}{t_{f_D}} t \\ I_D = \frac{I_{RM_D}}{t_{f_D}} t - I_{RM_D} \end{cases} \quad \text{(II.14)}$$

Where V_{R_D}, I_{RM_D}, and t_{f_D} are respectively the peak reverse voltage (V), the peak reverse recovery current (A), and the time interval required by the reverse recovery current to fall from its negative value ($-I_{RM_D}$) back to zero (s).
By following the same calculation steps of equations (II.9), (II.10), and (II.11), the average reverse recovery power loss in the diode during the turn-off transitions, and over the switching period T_{sw} is:

$$P_{rr_D} = \frac{f_{sw} \cdot V_{R_D} \cdot I_{RM_D}}{6} . t_{f_D} \quad \text{(II.15)}$$

Thus, the total time-averaged switching power loss in the DC/DC boost can be expressed as:

$$\begin{aligned} P_{sw_boost} &= P_{CE} + P_{rr_D} \\ &= \frac{f_{sw_PV}}{6} \times [V_{CE_max} . I_{c_max} . (t_{on_IGBT} + t_{off_IGBT}) + (V_{R_D} . I_{RM_D} . t_{f_D})] \end{aligned} \quad \text{(II.16)}$$

Since the switching-loss resistance (r_{sw}) is placed at the PV source side of the converter in series with the inductor, as seen in Fig.2.9, the time-averaged switching power loss can be written as:

$$P_{sw_boost} = r_{sw} I_{L_RMS}^2 \approx r_{sw} I_L^2 \quad \text{(II.17)}$$

Where I_{L_RMS} is the inductor's current RMS value (A). This assumption is valid since the DC/DC boost is always operating in continuous conduction mode (CCM) where $I_{L_RMS} \approx I_L$. By equalizing equations (II.16) and (II.17), the time-average switching power loss can be expressed as:

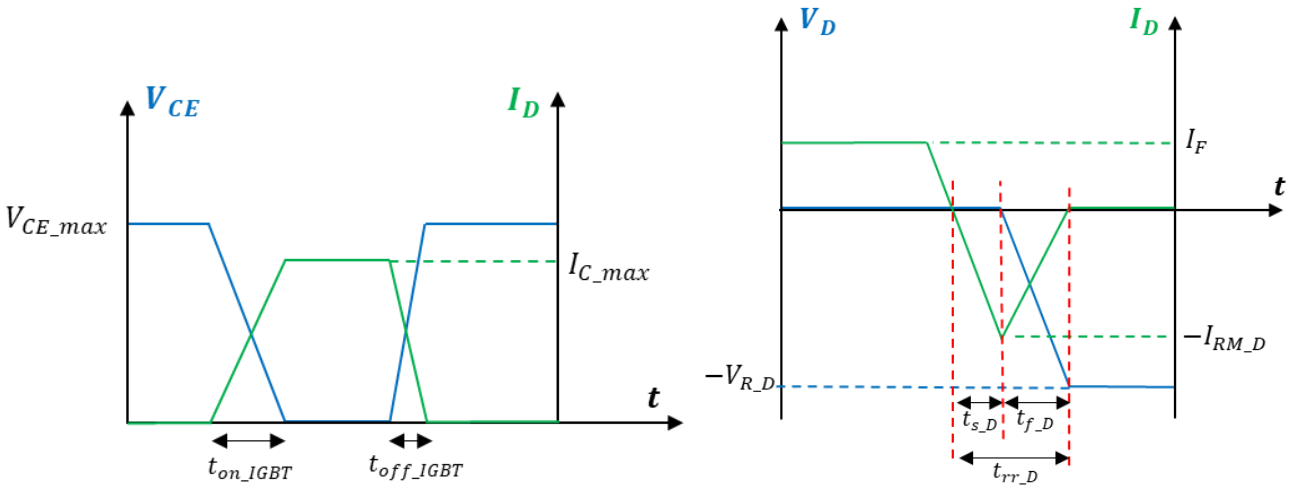
$$r_{sw} = \frac{f_{sw_PV}}{6I_L^2} \times [V_{CE_max}.I_{c_max}.(t_{on_IGBT} + t_{off_IGBT}) + (V_{R_D}.I_{RM_D}.t_{f_D})] \quad \text{(II.18)}$$

By referring to the detailed model of the DC/DC boost (Fig.2.5), when the IGBT is turned off, V_{CE_max}=V_{BUS}, and when it is on I_{c_max}=I_L. Similarly, the diode forward current (I_F) is equal to I_L when the diode conducts, and when it is blocked $V_D = -V_{R_D} \approx -V_{BUS}$. Thus, equation (II.18) can be written as:

$$r_{sw} = \frac{f_{sw_PV}.V_{BUS}}{6.I_L} \times (t_{on_IGBT} + t_{off_IGBT} + \frac{I_{RM_D}.\ t_{f_D}}{I_L}) \quad \text{(II.19)}$$

Appendix B.2 can be invoked for detailed information on parameter values and the method applied to find the peak reverse recovery current (I_{RM_D}).

Using the adapted electrical circuit of Fig.2.9 which includes the conduction and switching losses, the total losses in the DC/DC boost (P_{boost_losses}) can be represented as a function of the PV array current I_{PV}, the duty cycle ratio D_{PV} of the converter, and the DC bus voltage V_{BUS}.



(a) (b)

Fig.2.10 Approximation of (a) IGBT voltage and current, (b) diode reverse recovery current and voltage during the switching time interval.

In normal operating conditions $V_{BUS} = 800\ V$ is always constant and I_{PV} is a function of the irradiance S and the cell temperature T inputs (equations (II.2) and (II.4)). To simplify the analysis and the representation of the total losses, fixed irradiance, and temperature are selected to plot the losses curve as a function of the duty cycle ratio ($P_{boost_losses} = f(D_{PV})$). Fig.2.11 (a) and (b) show the PV array characteristics under fixed irradiance and temperature conditions: $S = 1000\ W/m^2$ and $T = 25°C$. The chosen PV module manufacturer and the corresponding module data can be found in Appendix A.1. As seen, the PV array voltage minimum value V_{PV_min} is null and corresponds to the short-circuit state, whereas the maximum value corresponds to the open-

circuit state $V_{PV_max} = 511.8\,V$. Fig.2.11 (c) represents V_{PV} as a function of D_{PV}, it can be seen that $V_{PV} = f(D_{PV})$ is a decreasing linear function since V_{PV} and D_{PV} are inversely proportional:

- $V_{PV_max} = 511.8\,V$ corresponds to $D_{PV_min} = 0.362$.
- $V_{PV_min} = 8.2\,V$ corresponds to $D_{PV_max} = 1$.

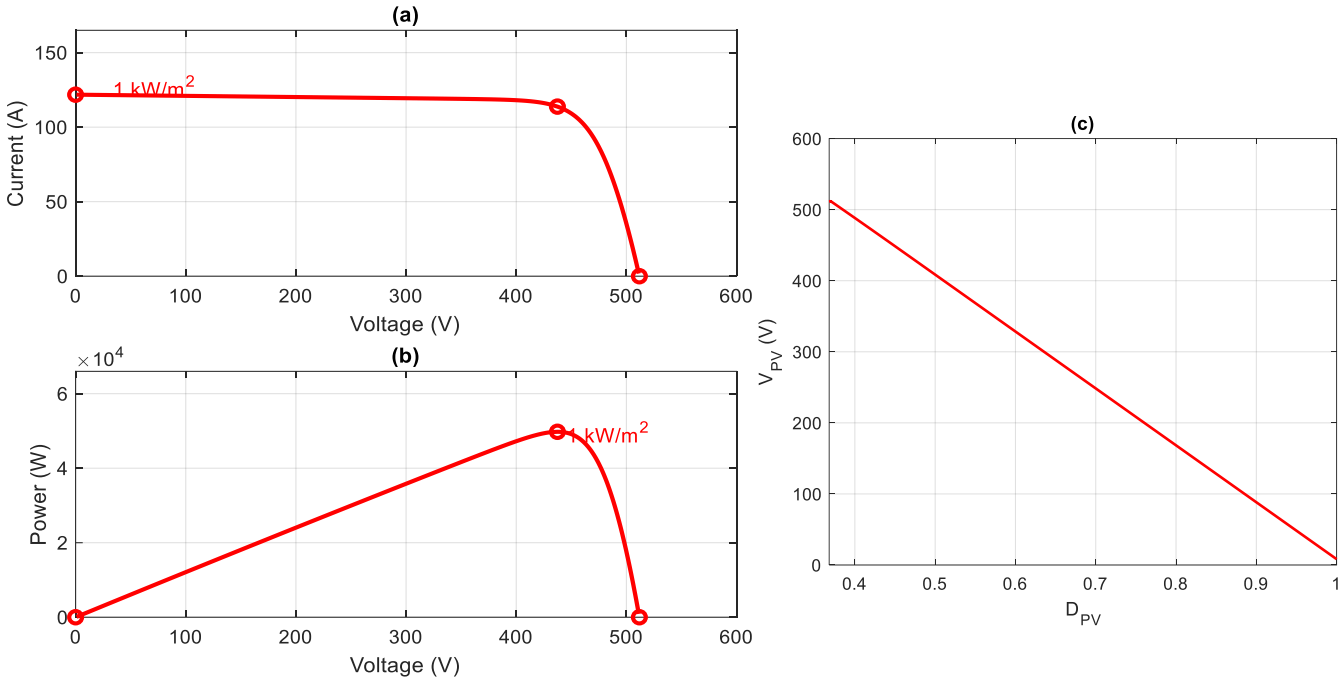


Fig.2.11 PV array characteristics ($S = 1000\,W/m^2, T = 25°C$) (a) $I_{PV} = f(V_{PV})$, (b) $P_{PV} = f(V_{PV})$, and (c) $V_{PV} = f(D_{PV})$.

Finally, the total losses, the conduction losses, and the switching losses are plotted in Fig.2.12 as functions of V_{PV}. The boost converter's efficiency denoted η_{boost}, can be expressed as follows:

$$\eta_{boost}(\%) = 100\left(1 - \frac{P_{boost_looses}}{P_{PV}}\right) = 100\left(1 - \frac{P_{boost_looses}}{I_{PV}V_{PV}}\right) \quad \text{(II.20)}$$

$\eta_{boost} = f(V_{PV})$ is represented in Fig.2.13.

The obtained results show that:

- The total losses increase gradually with the voltage and reach a maximum of 1015 W at $V_{PV} = 364.23\,V$, then decrease sharply for $V_{PV} \in [450,\ 511.8\,]$.
- The total losses correspond to the sum of the conduction and switching losses. The switching losses represent around 75% of the total losses.
- Though increasing when V_{PV} increases, the total losses remain low and relatively constant compared to P_{PV} which rises gradually to reach its maximum as seen in Fig.2.11 (b). As a result, the term P_{boost_looses} over P_{PV} figuring in equation (II.20) decreases when V_{PV} increases and so η_{boost} increases. Hence, the boost's efficiency increases with the PV voltage and reaches 98% at MPPT corresponding to $V_{PV_MPPT} = 437.4\,V$ (appendix A.1)

We take note that all obtained results correspond to a fixed irradiance of 1000 W/m^2 and cell temperature $T = 25°C$. For each irradiance and temperature corresponds to different losses and efficiency curves.

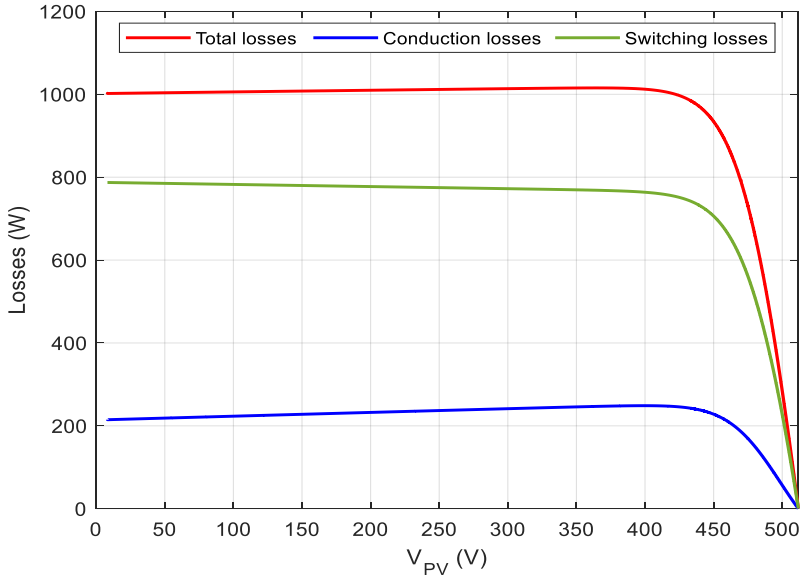


Fig.2.12 The total losses, the conduction losses, and the switching losses as functions of V_{PV}.

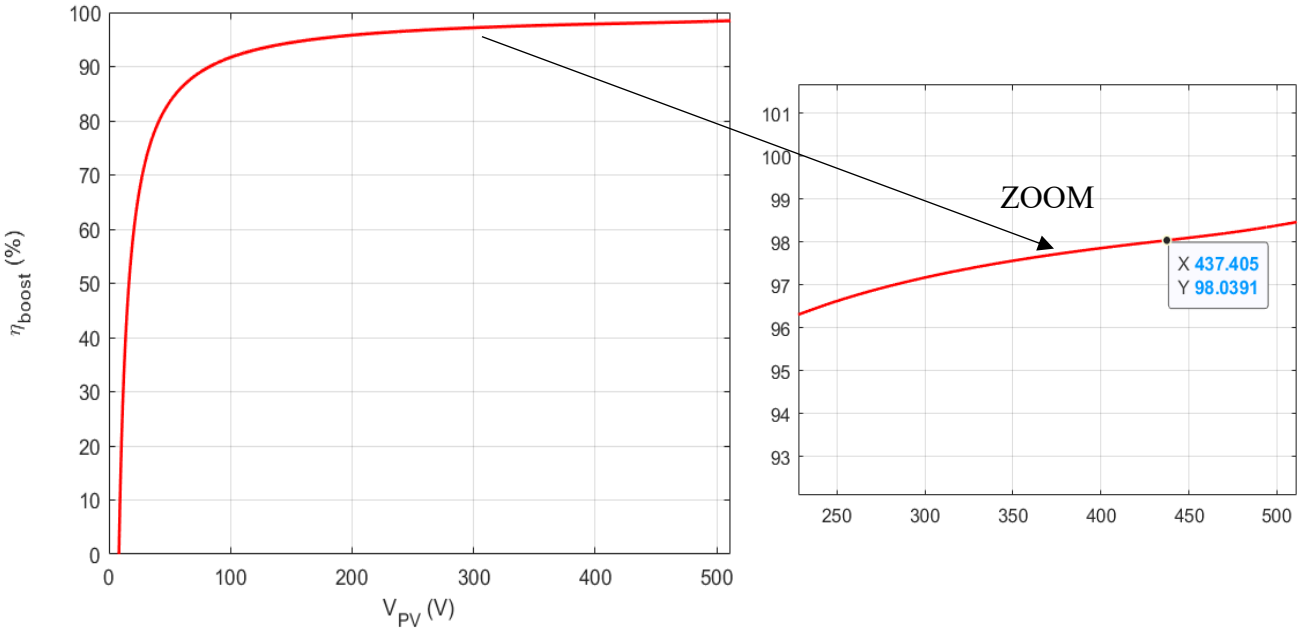


Fig.2.13 Boost converter efficiency in (%) as a function of V_{PV}.

2.4.3 DC/DC boost control strategy

As previously stated, the DC/DC boost is continuously operating in MPPT mode to extract the maximum available solar power. Several MPPT techniques are found in the literature and can be divided into two main categories: conventional and soft-computing algorithms[130]. Among the

conventional techniques, we cite the perturb and observe (P&O), the incremental conductance, the fractional short-circuit current (FSCC), the fractional open-circuit voltage (FOCV), etc. Yet, fuzzy logic control (FLC), artificial neural network (ANN), genetic algorithm (GA), and other optimization-based algorithms are the main soft-computing MPPT techniques[131]. As the analysis of each of the existing techniques is out of the scope of this thesis, incremental conductance, mostly applied in the literature, is selected as a conventional MPPT technique for this study [132]. Further information on MPPT techniques can be found in [130], [131].

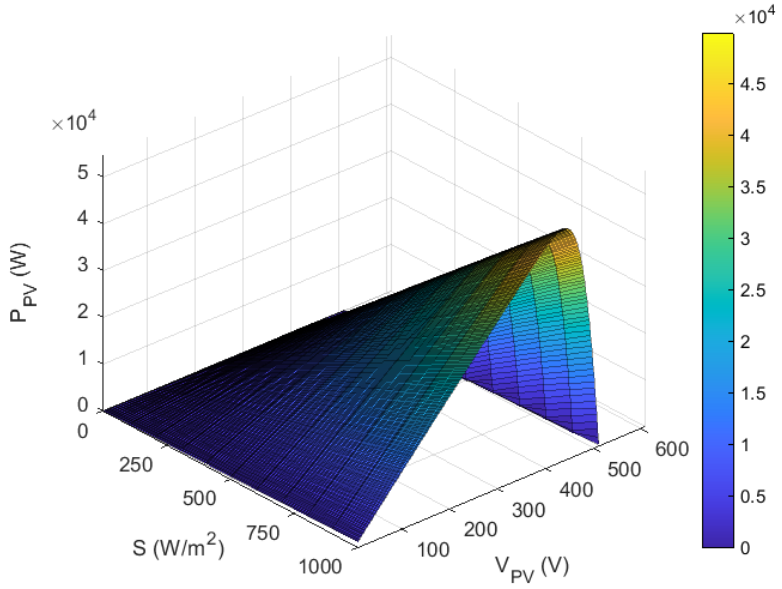


Fig.2.14 $P_{PV} = f(V_{PV}, S)$ characteristic for a constant temperature ($T = 25°C$).

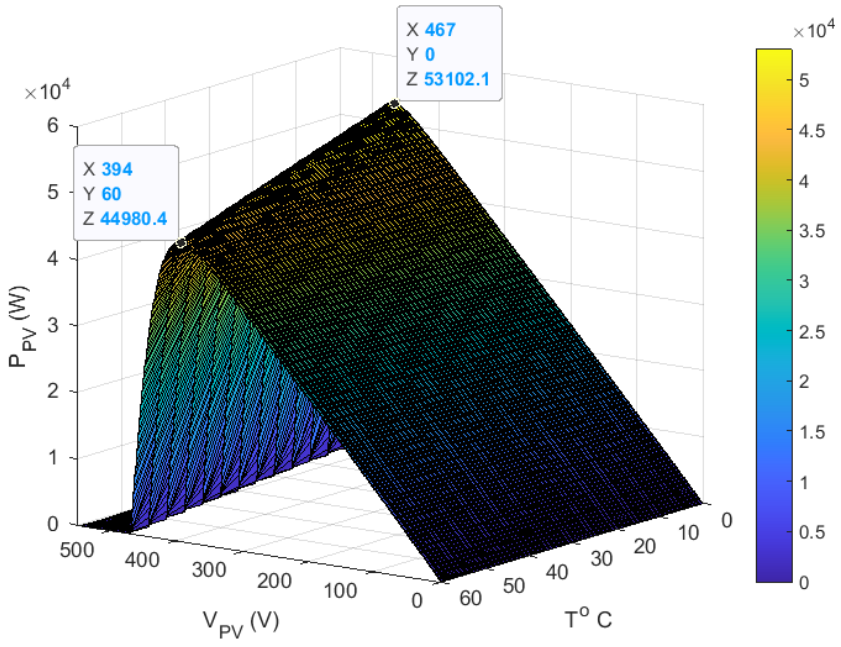


Fig.2.15 $P_{PV} = f(V_{PV}, T)$ characteristic for a constant irradiance ($S = 1000\ W/m^2$).

The incremental conductance MPPT technique is detailed in Appendix A.2. The incremental conductance and the above-cited techniques require small calculation step sizes to yield accurate results corresponding to the maximum available power. In our case, the step size named the sliding time window of the MPPT control is $T_{MPPT} = 0.2\ ms$ (appendix A.2). Higher values of T_{MPPT} speed up the simulation but leads to mistaken values.

The $P_{PV} = f(V_{PV})$ characteristic is plotted for each irradiance and temperature combination input, and then the maximum power is found and stored in a look-up table. Fig.2.14 and Fig.2.15 show respectively the PV output power as a function of the PV voltage and irradiance for a constant temperature $T = 25°C$, ($P_{PV} = f(V_{PV}, S)_{T=25°C}$), and the PV output power as a function of the PV voltage and temperature for a constant irradiance $S = 1000\ W/m^2$, ($P_{PV} = f(V_{PV}, T)_{S=1000\ W/m^2}$). As shown in Fig.2.14, the PV output power is proportional to the irradiance and the highest power curve corresponds to the highest irradiance value of $S = 1000\ W/m^2$. Contrarily, the efficiency of the PV array drops with the temperature as the highest power curve is obtained for the lowest temperature $T = 0°C$, and the lowest power curve for the highest plotted temperature $T = 60°C$ (Fig.2.15). To fill the MPPT lookup table, the irradiance and temperature data are sampled with a 0.5 W/m^2 and 0.5 $°C$ step sizes and all corresponding maximum PV power values are stored in a matrix. As seen in Fig.2.16, the MPPT lookup table block has the irradiance S (W/m^2) and the cell temperature $T(°C)$ as inputs and the reference MPPT voltage as output.

The reference MPPT voltage is compared to the actual PV voltage and the resulting error is minimized through a P.I. regulator (the system is speeded up 3 times, then $k_{mppt} = 3$). The regulator output is added to the initial duty cycle ratio ($D_{PV_init} = 0.5$) to form the duty cycle (D_{PV}) of the DC/DC boost converter.

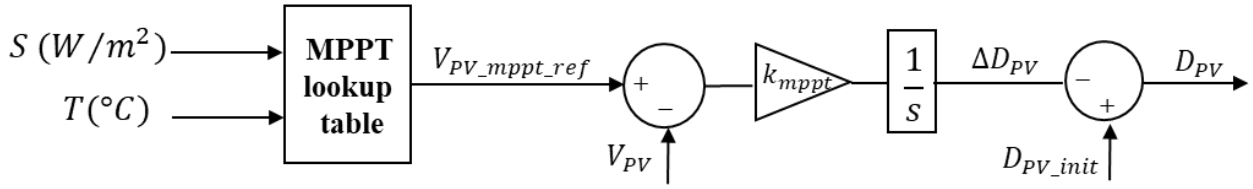


Fig.2.16 Block diagram of the lookup table MPPT control.

To validate the proposed MPPT technique, it is compared to the incremental conductance MPPT technique in a simulation test. Variable temperature and irradiation inputs are applied, and the results are shown in Fig.2.17. The incremental conductance simulation is run with a calculation step size $T_{step_IC} = \frac{T_{MPPT}}{100} = 2\ \mu s$, whereas the lookup table method is run with a calculation step size $T_{step_LT} = T_{MPPT} = 200\mu s$. Both, incremental conductance, and lookup table methods yield the same power curves in transient as well as in steady state (the power curve corresponding to the incremental conductance is denoted P_{inst}, and the one corresponding to the lookup table is denoted P_{24h}).

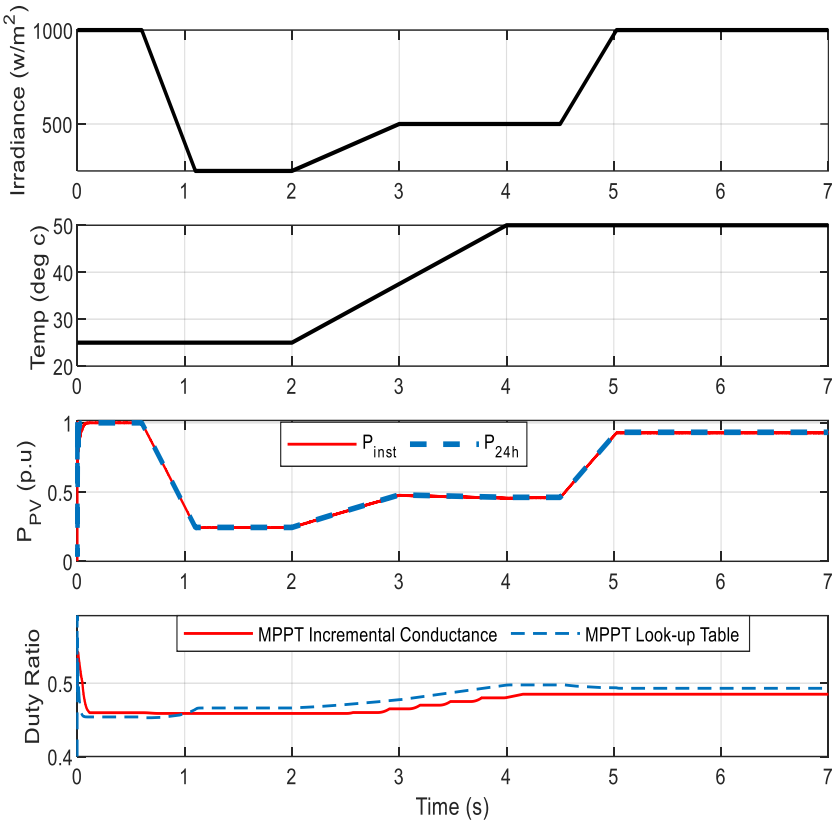


Fig.2.17 Comparison between the proposed lookup table and incremental conductance MPPT techniques.

Based on the duty cycle ratio plots, the MPPT proposed look-up table keeps a good accuracy (Maximum error of 3.4% in the duty cycle ratio and 0.2% in the power curve) compared to incremental conductance. Furthermore, the simulation speed is highly increased as the calculation step size ratio between the incremental conductance and lookup table technique is $T_{step_LT}/T_{step_IC} = 100$.

2.5 Wind turbine energy conversion chain

The wind turbine energy conversion chain is represented in Fig.2.18. It consists of a wind turbine model, a pitch angle controller, a permanent magnet synchronous machine (PMSM), and a 3ϕ rectifier to convert the AC output power to DC. The 3ϕ rectifier is continuously functioning in MPPT mode to extract the maximum available wind power.

2.5.1 Wind turbine model

The wind turbine block model in MATLAB/Simulink is applied to express the wind power characteristics. The output power of the turbine is given by the following equation:

$$P_{wind_m} = c_p(\lambda, \beta)\frac{\rho A}{2}v_{wind}^3 \quad \text{(II.21)}$$

Where P_{wind_m}, c_p, ρ, A, v_{wind}, λ, and β are respectively the wind mechanical output power (W), the performance coefficient of the turbine, the air density (Kg/m^3), the turbine-swept area (m^2), the wind speed (m/s), the tip speed ratio of the rotor blade tip speed to wind speed, and the blade pitch angle (degree). Equation (II.21) can be normalized, this yields the below equation in $p.u$:

$$P_{wind_m_pu} = k_{wind_p}.c_{p_pu}v_{wind_pu}^3 \quad \text{(II.22)}$$

where, $P_{wind_m_pu}$, c_{p_pu}, v_{wind_pu}, and k_{wind_p} are respectively the wind mechanical output power in $p.u$ for particular values of ρ and A, the performance coefficient in $p.u$ of the maximum value of c_p, the wind speed in $p.u$ of the base wind speed, and the power gain for $c_{p_pu} = 1$, and $v_{wind_pu} = 1$. The MATLAB block uses a generic equation to model the performance coefficient of the turbine c_p, based on the modeling turbine characteristics of [133]. $c_p(\lambda, \beta)$ is expressed as follows:

$$c_p(\lambda, \beta) = c_1(c_2/\lambda_i - c_3\beta - c_4)e^{-c_5/\lambda_i} + c_6\lambda \quad \text{(II.23)}$$

With: $\frac{1}{\lambda_i} = \frac{1}{\lambda+0.08\beta} - \frac{0.035}{\beta^3+1}$

$c_1 = 0.5176$, $c_2 = 116$, $c_3 = 0.4$, $c_4 = 5$, $c_5 = 21$, and $c_6 = 0.0068$.

The maximum value of c_p ($c_{p_max} = 0.48$) is obtained for $\beta = 0°$, and $\lambda = 8.1$.This value of λ is defined as the nominal value λ_{nom}.

As seen in Fig.2.18, the wind turbine model block has as input the wind speed (m/s), the generator speed (w_r) in $p.u$, and the regulated pitch angle (β in degrees) and outputs the mechanical torque T_m ($p.u$) applied to the generator shaft. The tip speed ratio λ is computed in $p.u$ of λ_{nom} as follows:

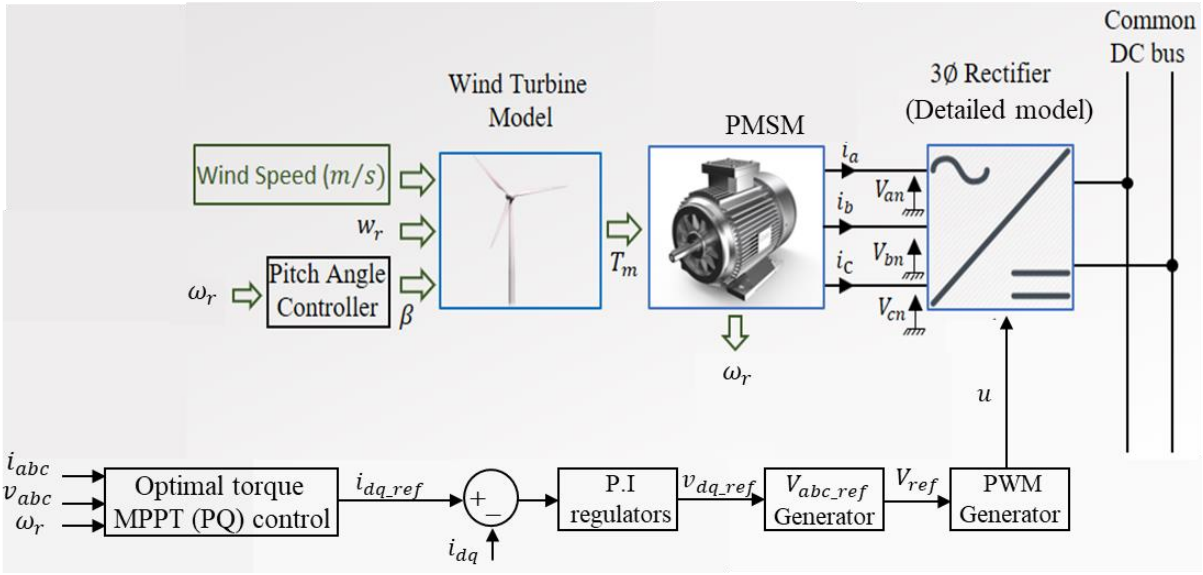


Fig.2.18 Wind turbine energy conversion chain.

$$\lambda = \frac{w_r/w_{r_base}}{v_{wind}/v_{wind_base}}\lambda_{nom} \quad \text{(II.24)}$$

Where, w_{r_base}, and v_{wind_base} are respectively the base rotational speed ($p.u$ of base generator speed equal to 1 $p.u$ in this case), and the base wind speed (equal to 12 m/s in this case). Using equation (II.22), c_p is calculated in $p.u$ of c_{p_max}, then the mechanical output power of the turbine, $P_{wind_m_pu}$, is computed in $p.u$. To obtain the real mechanical output power in $p.u$, $P_{wind_m_pu}$ is multiplied by the coefficient factor k_{w_pu}:

$$k_{w_pu} = \frac{P_{wind_base_pu}P_{wind_m_n}}{P_{PMSM_base}} \quad \text{(II.25)}$$

Where, $P_{wind_base_pu}$, $P_{wind_m_n}$, and P_{PMSM_base} are respectively the maximum power at base wind speed in $p.u$ of nominal mechanical power (equal to 0.9 $p.u$ in this case), the nominal mechanical output power (W), and the base power of the electrical generator (W). In this case, $P_{wind_m_n} = P_{PMSM_base} = 55\ KW$. As a result, the maximum available wind power at $v_{wind_base} = 12\ m/s$ is $P_{wind_m_pu} = 0.9P_{wind_m_n} = 49.5\ KW$. Finally, the mechanical torque $T_m\ (p.u)$ is obtained by dividing $P_{wind_m_pu}(p.u)$ by $w_r\ (p.u)$. Fig.2.19 represents the turbine power characteristics in $p.u$ of nominal mechanical power as a function of the turbine speed in $p.u$ of the turbine speed for different wind speeds. As seen, each curve, corresponding to a specific wind speed, has a point of maximum output power. Moreover, the maximum power at base speed $v_{wind_base} = 12\ m/s$ and for $\beta = 0°$ corresponds to $P_{wind_m_pu} = 0.9\ p.u$, and $w_r = 1\ p.u$ as mentioned above. By applying an MPPT technique to control the 3ϕ rectifier, each maximum power point corresponding to a specific wind speed value is pinpointed which enables the WT to continuously produce the maximum available wind power.

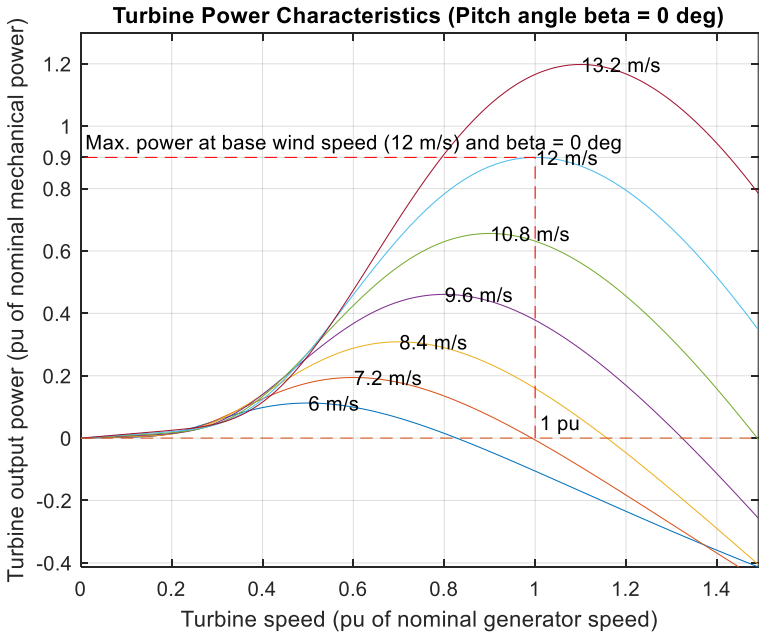


Fig.2.19 Turbine power characteristics as a function of the turbine speed for different wind speeds.

2.5.1.1 Pitch angle controller:

The pitch angle controller block controls the blade pitch angle β to limit the generator speed w_r $(p.u)$ to the base rotational speed w_{r_base} $(p.u)$. The control diagram of the pitch angle controller is shown in Fig.2.20. The actual generator speed is compared to the base one and the error is regulated by a proportional gain ($k_\beta = 500$), then the output pitch angle β is limited between minimum and maximum admissible values ($\beta_{min} = 0, \beta_{max} = 45°$). Additionally, a rising and falling slew rate of β equal to 2° is set.

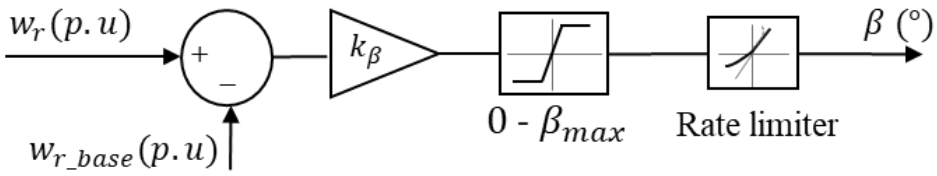


Fig.2.20 Simulink Block diagram of the pitch angle controller.

2.5.2 Permanent magnet synchronous machine

To model the generator, a permanent magnet synchronous machine (PMSM) is selected. The PMSM is generally popular in newer smaller-scale turbine types (utility-scale turbines home in size from 50 to 750 KW[132]) since it offers a variety of advantages such as reliability, compact size, loss reduction, higher power density, and optimal efficiency[134]. Though applied in the simulation model, the detailed electrical and mechanical equations of the PMSM are not revealed in the manuscript in order not to add technical content that is far from the thesis objective but can be reviewed in detail in[135].

Hence, in the rest, the PMSM is seen as a power conversion black box that converts mechanical power into electrical power without addressing the machine's internal electrical and mechanical variables. The PMSM block built in Simulink has as inputs the mechanical torque T_m, and the three-phase voltages across the stator windings V_{abc}. The outputs of the PMSM bloc are the rotor mechanical rotational speed w_r in (rad/s), the rotor mechanical angle θ_r in (rad), the three phases' currents flowing in the stator windings I_{abc}, and the electromechanical torque T_e in $(N.m)$. The PMSM parameters and manufacturer's datasheet can be found in Appendix C. Thus, the modeling of the PMSM aims to retrieve the actual efficiency of the electrical generator at each wind speed value, and then the actual value of the generated electrical power. As a result, the generated wind electrical power is expressed as follows:

$$P_{wind_elec} = \eta_{PMSM} P_{wind_m} \quad \text{(II.26)}$$

Where, P_{wind_elec}, η_{PMSM}, and P_{wind_m} are respectively the generated wind electrical power (W), the PMSM efficiency, and the wind mechanical output power (W). The efficiency curve of the

PMSM is shown later in Fig 2.31 after presenting the whole conversion chain and the control strategy of the 3ϕ rectifiers.

2.5.3 3ϕ Rectifier

2.5.3.1 Detailed model

Fig.2.21 shows the detailed electrical circuit of the 3ϕs rectifier. The equivalent circuit for the stator windings of the PMSM consists of a three-phase wye connection. Each phase consists of a voltage source in series with the equivalent resistance of each stator winding R_s, and the stator self-inductance per phase L_s. As seen, this model is the most accurate as it includes the IGBT/diode pairs controlled by firing pulses produced by a PWM generator. To model the firing pulses, binary variables u_1, u_2, and u_3 are introduced, and control respectively the switches S_1, S_2, and S_3. $u_{i=1,2,3}$ is equal to 1 when the corresponding switch is closed and 0 otherwise. Knowing that two switches of the same arm ($S_{i=1,2.3}$ and $S'_{i=1,2,3}$) cannot be closed simultaneously, their operating state should be complementary. Accordingly, the firing pulses of the switches S'_1, S'_2, and S'_3 are respectively $\overline{u_1}$, $\overline{u_2}$, and $\overline{u_3}$, where $\bar{u}_{i=1,2,3} = 1 - u_{i=1,2,3}$.

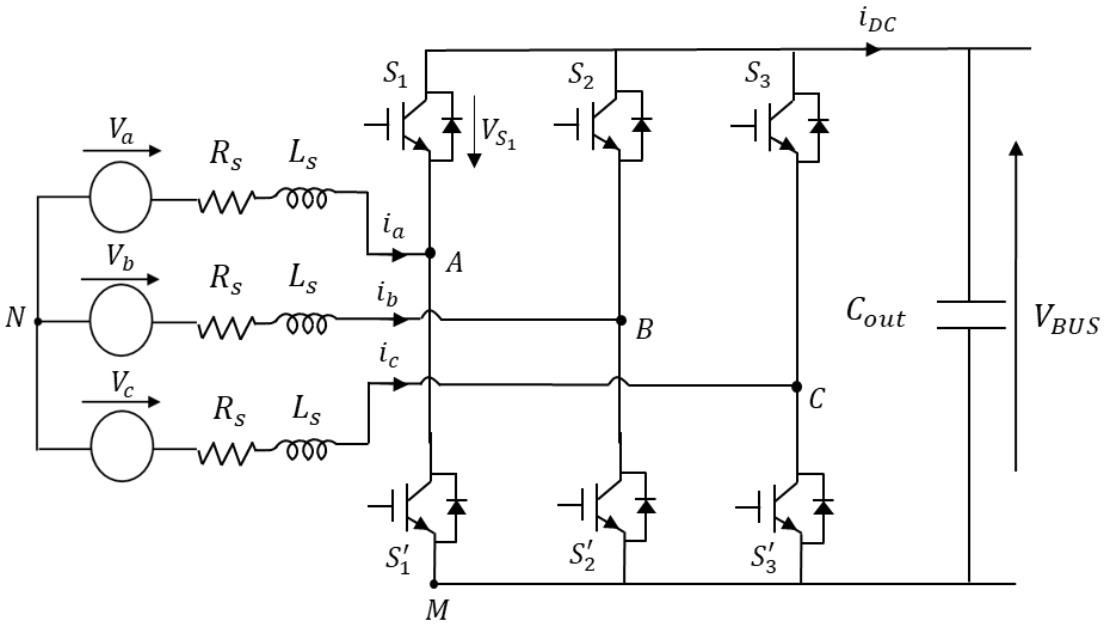


Fig.2.21 Electrical circuit of the 3ϕs rectifier (detailed model).

Then, V_{AM}, V_{BM}, and V_{CM} can be computed as follows:

$$\begin{cases} V_{AM} = u_1 V_{BUS} \\ V_{BM} = u_2 V_{BUS} \\ V_{CM} = u_3 V_{BUS} \end{cases} \quad \text{(II.27)}$$

Applying Kirchhoff's voltage low to the electrical circuit in Fig.2.21, the below equations are retrieved:

$$\begin{cases} V_a = R_s i_a + L_s \frac{di_a}{dt} + V_{AM} + V_{MN} \\ V_b = R_s i_b + L_s \frac{di_b}{dt} + V_{BM} + V_{MN} \\ V_c = R_s i_c + L_s \frac{di_c}{dt} + V_{CM} + V_{MN} \end{cases} \quad \text{(II.28)}$$

The PMSM electrical model is considered a three-phase balanced system, then:

$V_a + V_b + V_c = 0$, $L_s \frac{di_a}{dt} + L_s \frac{di_b}{dt} + L_s \frac{di_c}{dt} = 0$, and $R_s i_a + R_s i_b + R_s i_c = 0$

Thus, $V_{AM} + V_{BM} + V_{CM} + 3V_{MN} = 0$ then,

$$V_{MN} = -\frac{V_{BUS}}{3}(u_1 + u_2 + u_3) \quad \text{(II.29)}$$

Having,

$$\begin{cases} V_{AN} = V_{AM} + V_{MN} \\ V_{BN} = V_{BM} + V_{MN} \\ V_{CN} = V_{CM} + V_{MN} \end{cases} \quad \text{(II.30)}$$

Finally, the 3ϕs rectifier voltages' equations can be expressed as functions of u_1, u_2, u_3, and V_{BUS} as follows:

$$\begin{bmatrix} V_{AN} \\ V_{BN} \\ V_{CN} \end{bmatrix} = \frac{V_{BUS}}{3} \begin{bmatrix} 2 & -1 & -1 \\ -1 & 2 & -1 \\ -1 & -1 & 2 \end{bmatrix} \begin{bmatrix} u_1 \\ u_2 \\ u_3 \end{bmatrix} \quad \text{(II.31)}$$

And the DC-current i_{DC} is expressed as a function of the three-phase currents i_a, i_b, i_c, u_1, u_2, and u_3 as follows:

$$i_{DC} = 2u_1 i_a + 2u_2 i_b + 2u_3 i_c \quad \text{(II.32)}$$

2.5.3.2 Average model

Though the detailed model of the 3ϕs rectifier is the most accurate, it presents the same hurdle as the detailed DC/DC boost converter model in terms of the limitation of calculation step size. For instance, if the same switching frequency of the DC/DC boost is selected for the IGBTs of the 3ϕs rectifier ($f_{sw_WT} = f_{sw_PV} = 20\ KH$), the maximum allowable calculation step size is $T_{step_det} = 0.5\ \mu s$. To further increase the simulation speed, reduce the model complexity, and maintain a decent accuracy, an average model of the 3ϕs rectifier is applied in which the real IGBT switching devices are omitted, and controlled voltage and current sources are utilized instead. By this, the 3ϕs rectifier can be directly controlled through the voltage references V_{abc_ref} (Fig.2.18) with no need for the PWM block.

The electrical circuit of the average model of the 3ϕs rectifier is shown in Fig.2.22. As seen, on the AC side each switching device is replaced by a controlled voltage source, having a rhombus shape with a positive and negative sign inside. The imposed voltages are denoted $V_{S_{i=1,2,3}}$ and $V_{S'_{i=1,2,3}}$. A diode is connected in series with each controlled voltage current. The diodes at the top of the three arms of the rectifier, denoted $D_{S_{i=1,2,3}}$, allow only the flow of the positive part of the alternating currents i_a, i_b, and i_c. Meanwhile, the bottom diodes, denoted $D_{S'_{i=1,2,3}}$ circulates the negative part of the three phases alternating currents. This also can be deduced by applying Kirchhoff's current law to the first arm as an example: $i_a = i_{S_1} - i_{S'_1}$.

On the DC side, three controlled current sources are placed and have a rhombus shape with an arrow inside to define the directions of circulating currents. The imposed currents are denoted $i_{DC_{i=1,2,3}}$.The equations of the detailed model are all valid and used to compute the instant values of the controlled voltages and currents' sources. Only, the firing pulses $u_{i=1,2,3}$ are replaced by α_{a_ref}, α_{b_ref}, and α_{c_ref}, where α_{a_ref}, α_{b_ref}, and α_{c_ref} are expressed as :

$$\begin{cases} \alpha_{a_ref} = 0.5(1 + V_{a_ref}) \\ \alpha_{b_ref} = 0.5(1 + V_{b_ref}) \\ \alpha_{c_ref} = 0.5(1 + V_{c_ref}) \end{cases} \quad \text{(II.33)}$$

V_{a_ref}, V_{a_ref}, and V_{c_ref} are the voltage references in $p.u$ of the PMSM stator base voltage outputted from the V_{abc_ref} generator block (Fig.2.18).

Using equation (II.27) and Kirchhoff's voltage law:

$$\begin{cases} V_{S_1} = -V_{S'_1} = V_{AM} = \alpha_{a_ref} V_{BUS} \\ V_{S_2} = -V_{S'_2} = V_{BM} = \alpha_{b_ref} V_{BUS} \\ V_{S_3} = -V_{S'_3} = V_{CM} = \alpha_{c_ref} V_{BUS} \end{cases} \quad \text{(II.34)}$$

Hence, the 3ϕs rectifier voltages' equations can be expressed as functions of V_{S_1},V_{S_2},V_{S_3} as follows:

$$\begin{bmatrix} V_{AN} \\ V_{BN} \\ V_{CN} \end{bmatrix} = \frac{1}{3} \begin{bmatrix} 2 & -1 & -1 \\ -1 & 2 & -1 \\ -1 & -1 & 2 \end{bmatrix} \begin{bmatrix} V_{S_1} \\ V_{S_2} \\ V_{S_3} \end{bmatrix} \quad \text{(II.35)}$$

The output DC-current is the sum of the three controlled current sources:

$$i_{DC} = i_{DC_1} + i_{DC_2} + i_{DC_3} \quad \text{(II.36)}$$

To compute i_{DC_1}, i_{DC_2}, and i_{DC_3}, the law of power conservation is applied, these yields:

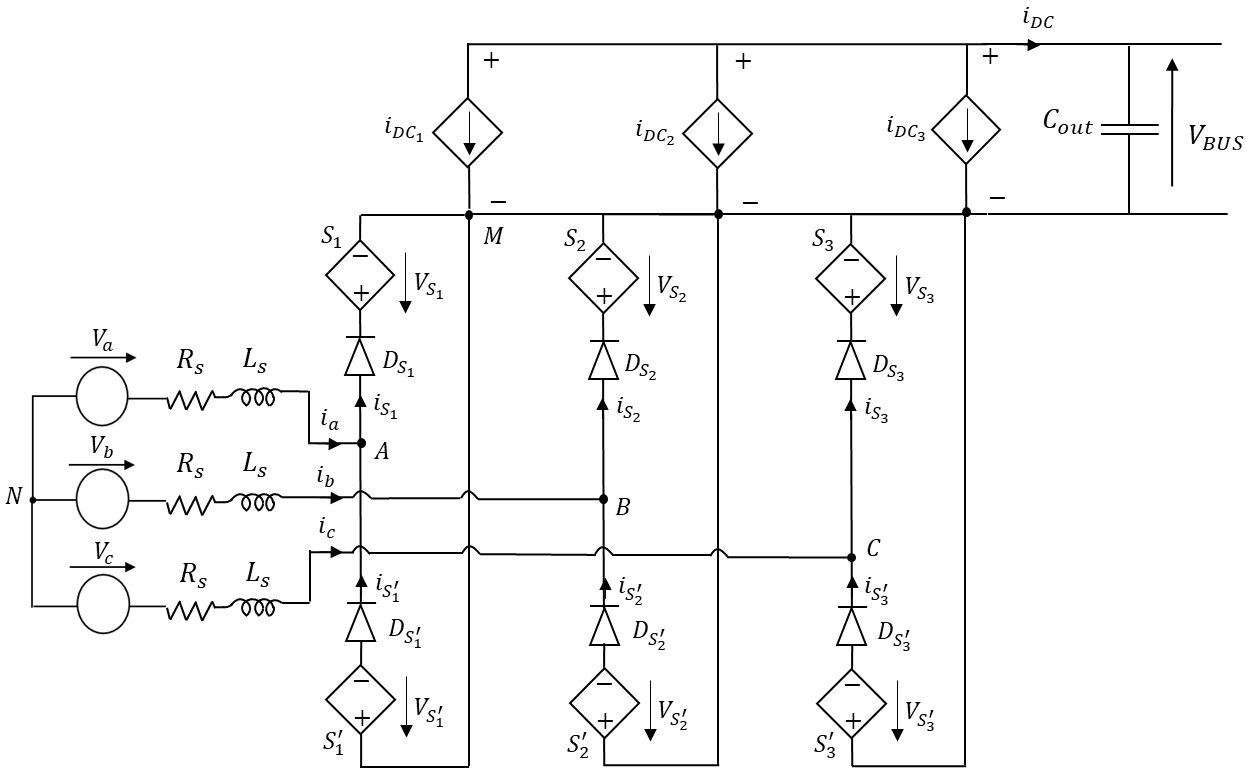


Fig.2.22 Electrical circuit of the 3ϕs rectifier (average model).

$$\begin{cases} i_{DC_1} = -V_{s_1} i_a / V_{BUS} \\ i_{DC_2} = -V_{s_2} i_b / V_{BUS} \\ i_{DC_3} = -V_{s_3} i_c / V_{BUS} \end{cases} \quad \text{(II.37)}$$

Applying the average model, the switching function is removed, and the new calculation step size can increase at least 100 times compared to the detailed model ($T_{step_avr} \geq 100.T_{step_det}$), same as the DC/DC boost converter simulation. However, additional variables limit the increase of calculation step size when modeling all AC nature sources of the DC microgrid (i.e., the WT, the DG, and the utility grid in this case). The limitation comes from the sinusoidal waveforms of the three-phase electrical components V_{abc}, and i_{abc}. As stated in the DC/DC boost average model, the required ratio between the calculation step size and any periodic signal with a defined period must be at least equal to 1/100 to precisely represent this signal and obtain flawless results. Applying this strategy to the three-phase sinusoidal currents and voltages which have a rated frequency: $f_n = 100\,Hz$ (Appendix C), and so a rated period: $T_n = 10\,ms$, the calculation step size cannot exceed $100\,\mu s$ to accurately represent the sinewave forms. Moreover, at higher operating frequencies smaller calculation step sizes are required.

Hence, the calculation step size is limited by the period of the sinewave signals: $T_{step_avr} \leq 100T_{sinewave}$. Given that a variable step solver is selected in Simulink to simulate the microgrid, the maximum calculation step size is limited to $T_{step_avr_max} = 100T_{sinewave}$ which always slows down the simulation and obstructs the 24-hour modeling goal on a standard computer.

Therefore, a third assumption method is applied to further simplify the model and increase the calculation step size.

2.5.3.3 Phasor model

The last averaging technique applied to the wind turbine conversion chain is the phasor modeling technique. The phasor notation transforms the real part of a sinusoidal function from the time domain into the complex number domain, also called the frequency domain. Fig.2.23 shows the three-phase voltages of a balanced system in the time and phasor domain:

$$\text{Time domain:}\begin{cases} V_a(t) = V_n\sqrt{2}\sin(w_n t) \\ V_b(t) = V_n\sqrt{2}\sin(w_n t - 120°) \\ V_c(t) = V_n\sqrt{2}\sin(w_n t + 120°) \end{cases} \rightarrow \text{Phasor domain:}\begin{cases} V_a = V_n\sqrt{2}e^{j0} \\ V_b = V_n\sqrt{2}e^{-120°j} \\ V_c = V_n\sqrt{2}e^{+120j} \end{cases}$$

Where, w_n is the electrical nominal pulsation ($w_n = 2\pi f_n$ in rad/s).

The phasor solution is applied to study the electromechanical oscillations of power systems consisting of large generators and motors and the transient stability of machines. Besides, it can be implemented in any linear circuit where the main interest is only the changes in magnitude and phases in all voltages and currents when switches are closed or open[136]. The only drawback of the phasor notation is that it gives the solution only at a particular frequency while the remaining harmonics of the signal cannot be spotted. Accordingly, the phasor notation offers an adequate solution in this case study since:

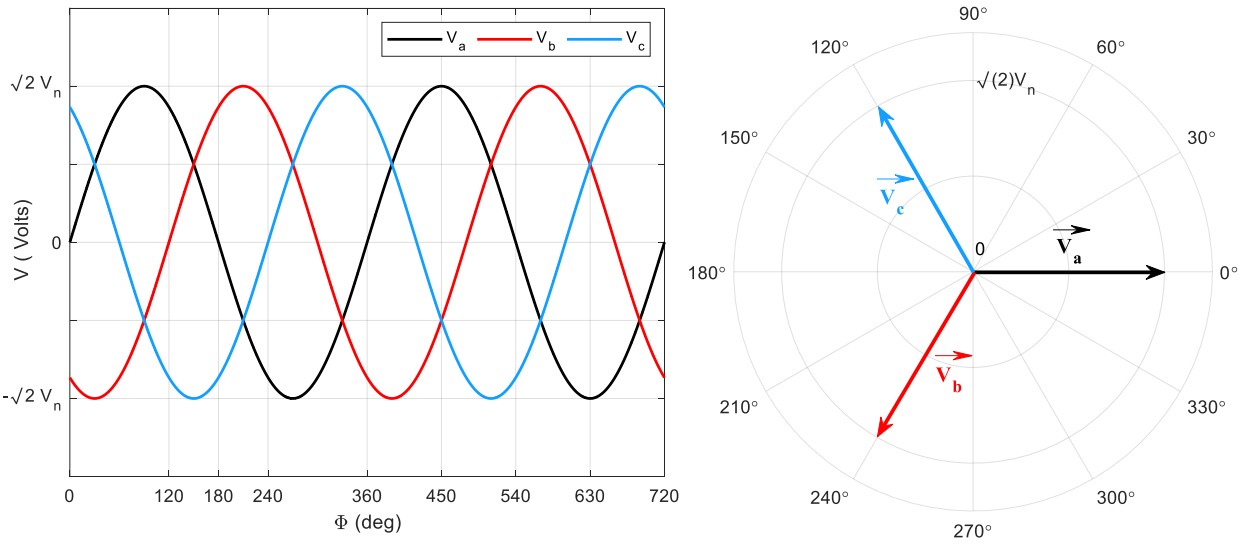


Fig.2.23 Three-phase voltages representation in the time domain (on the right) and phasor domain (on the left).

1. The electromechanical oscillations and transient stability of the PMSM are always modeled, then the power efficiency curve of the PMSM remains accurately represented.
2. The instantaneous changes in magnitude and phases in all voltages and currents are revealed, thus the precise calculation of the generated electrical/mechanical power, and converter losses are still valid.
3. The representation of the whole frequency spectrum of the sinusoidal electrical components is irrelevant as none of the predefined objectives in this study target the harmonics of the electrical signals.

Applying the phasor domain to the WT conversion chain represented in Fig.2.19, the WT model block and the pitch angle controller are unchanged. Meanwhile, instead of all $(abc) \rightarrow (\alpha\beta) \rightarrow (dq)$ transformations and their inverses, the rotation operator a is introduced to compute the positive sequence component from which the (dq) are retrieved. Then, the following transformations are applied : $(X_{abc}) \rightarrow X_1 \rightarrow (X_d, X_q)$ and $(X_d, X_q) \rightarrow X_1 \rightarrow (X_{abc})$ where, X_{abc}, X_1, X_d, and X_q are respectively the complex three-phase components, the positive sequence component, the $d-$axis, and the $q-$axis components.

The rotation operator a is defined as: $a = e^{j\frac{2\pi}{3}}$, and $1 + a + a^2 = 0$

X_1 is computed from the X_{abc} components using the equation below (X could be a three-phase current or voltage):

$$X_1 = \frac{1}{3}(X_a + aX_b + a^2X_c) \tag{II.38}$$

Then, the (dq) components can be retrieved from the positive sequence component and correspond to real and imaginary parts of X_1 : $X_1 = X_d + jX_q$

The inverse transformation from the positive sequence component to the (abc) complex domain is performed as follows:

$$\begin{cases} X_a = X_1 \\ X_b = a^2X_1 \\ X_c = aX_1 \end{cases} \tag{II.39}$$

Therefore, the phasor domain keeps an accurate representation of all variables in the (dq) frame. Knowing that the PMSM electromechanical model is established in the (dq) frame[135], the PMSM block isn't affected by the phasor representation and is kept the same as the detailed model. Same for the MPPT control which is performed in the (dq) frame, all the control strategy and blocks are kept impact. The MPPT control is detailed in the next section. Yet, a simpler model of the 3ϕ rectifier, compared to the average one, is applied. Since the sinusoidal representation of the three-phase voltages and currents isn't explicit in the phasor domain, the average model of Fig.2.22 can be modified to a much simpler model. In the control of the detailed and average circuit models, the three-phase sinusoidal voltage references are generated in the V_{abc_ref} generator block

(Fig.2.18), instead a complex (dq) voltage reference is generated to control the converter in the generator block of the phasor domain: $V_{ctrl_dq_ref} = V_{ctrl_d_ref} + jV_{ctrl_q_ref}$. Then, equation (II.33), and (II.34) of the average model can be merged in the following updated equation:

$$V_{1_3\phi_rec} = \frac{V_{ctrl_dq_ref} V_{BUS}}{2} \tag{II.40}$$

Where, $V_{1_3\phi_rec}$ is the positive sequence component of the 3ϕ rectifier voltage.

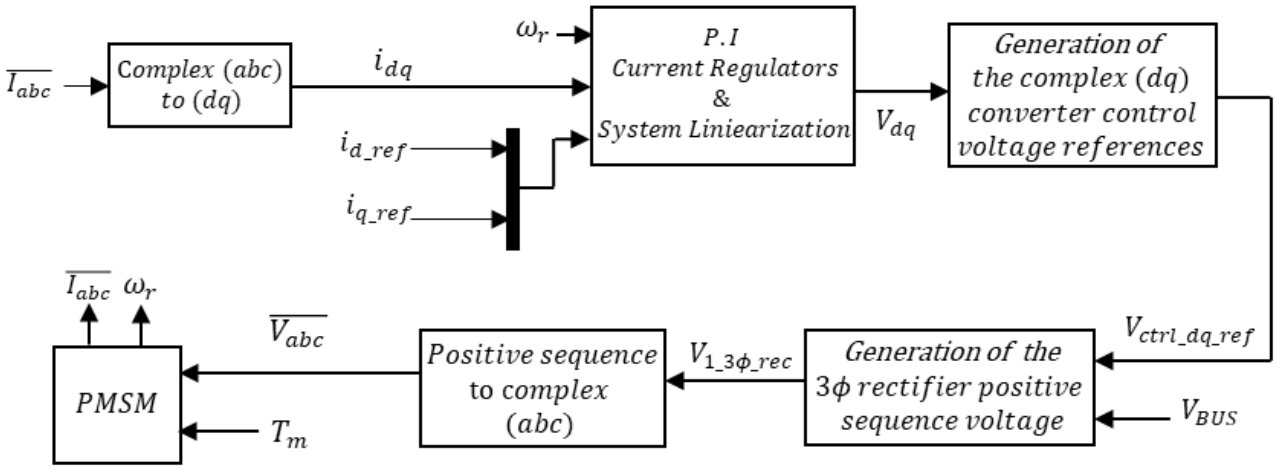


Fig.2.24 Block diagram of the complex (dq) and positive sequence power control.

Finally, the 3ϕ rectifier complex voltages can be expressed as functions of $V_{1_3\phi_rec}$ and a in the phasor domain as follows:

$$V_{abc} = \begin{cases} V_a = V_{1_3\phi_rec} \\ V_b = a^2 V_{1_3\phi_rec} \\ V_c = a V_{1_3\phi_rec} \end{cases} \tag{II.41}$$

The detailed block diagram of the complex (dq) and positive sequence power control is shown in Fig.2.24.

2.5.3.4 Simulation test of the detailed, average, and phasor models

To prove the viability of the phasor solution, it is compared to the average, and the detailed model under the same conditions and using the same parameters. In the three models, the PMSM is modeled by a three-phase balanced system in a wye connection. Each phase consists of a voltage source in series with a resistance R_s and an inductance L_s same as Fig.2.21 and 2.22 (R_s and L_s are given in Appendix C). A load consisting of a simple resistance R_{load} is applied, and a capacitor denoted $C_{out} = 0.1\ mF$ is connected in parallel to R_{load} on the DC side. For the three models, the (dq) control strategy represented in Fig.2.24 is applied. As prementioned, the block diagrams of the instantaneous and average (dq) control strategies differ from the phasor one in the generation

of the three-phase voltage references. In the phasor domain, the positive sequence voltage reference is generated, and complex three-phase voltage references ($\bar{V}_{abc}$) are applied. However, in the instantaneous and average models, a block that generates the three-phase sinusoidal waveform voltage references is required instead. Besides, a three-phase PWM generator block is added in the instantaneous model to control the real switching devices through firing pulses. As a principle, the active power is controlled through the d-axis component, and the reactive power through the q-axis. For the active power reference, three steps are imposed on the d-axis:

$$P_{ref} = \begin{cases} 20KW & t < 1s \\ 30KW & 1s \leq t < 2s \\ 10KW & t \geq 2s \end{cases} \quad \text{(II.42)}$$

However, Q_{ref} is always set to zero to absorb zero reactive power. The three models are simulated for 3 seconds each. P.I. controllers are utilized in the three simulations to control the d and q-axis current components. The same P.I. is applied to control d and q-axis in the three simulations and has the following expression: $R_{WT}(p) = k_{p_WT}\frac{k_{i_WT}\,p+1}{k_{i_WT}\,p}$ where, k_{p_WT} and k_{i_WT}, are respectively the proportional and the integral parameters of the regulator, and p is the Laplace operator. All the parameters are listed in Table 2.2. Fig.2.25, 2.26, and 2.27 show the obtained results. The active and reactive powers are shown in Fig.2.25. As seen, the active power (Fig.2.25 (a)) follows its reference in the three models, and the phasor curve accurately represents the active power in transient and steady states. The same results are obtained for the reactive power (Fig.2.25 (b)) which always follows its reference and is equal to zero in the three models. The current phase i_a is shown in Fig.2.26 (a) and (b). The current magnitude (black line) and the phase shift (golden yellow line) are plotted in the phasor simulation meanwhile, the sinusoidal waveforms appear in the detailed and average models. The waveforms of the detailed model (blue line) are thicker than the average ones (red line) because of the existence of the switching frequency in the detailed rectifier model. Fig.2.26 (b) shows that all variations in current magnitude including the steepest ones resulting from a step change in the power reference are accurately tracked in the phasor representation. Same for the phase voltage V_{AN}, plotted in Fig.2.27 (a), the full sinewave forms are observed in the detailed and the average models, while the phasor model is represented by the magnitude (black line) that is always equal to $V_{AN_max} = \sqrt{2}V_n$, and the phase shift is null (golden yellow line) as the system is a three-phase balanced one.

Hence, the precise calculation of active and reactive power is always maintained when adopting the phasor approach. Finally, the DC bus voltage represented in Fig.2.27 (b), varies conveniently with the active and reactive power references as the (dq) current components are used to control the active and reactive power in the circuit and not to stabilize the DC bus voltage. The three models have the same DC bus voltage curves in all operating states, then the phasor representation maintains the accuracy in modeling the electrical AC and DC components. To highlight the significance of the phasor model, Table 2.3 summarizes the simulation duration and the calculation step size of each of the three models. The calculation step size highly increases when

applying the phasor approach where an average value of $T_{step_Ph} = 17.8\,ms$ is obtained. This corresponds to a ratio of 356 of T_{step_Ph} to T_{step_avr} and 35600 of T_{step_Ph} to T_{step_det}.

Nominal voltage (phase to neutral) (V)	$V_n = 206.7\,V$
Operating frequency (Hz)	$f_n = 100\,Hz$
Switching frequency (detailed model) (Hz)	$f_{sw} = 20\,KHz$
Load resistance (Ω)	$R_{load} = 50\,\Omega$
P.I regulators parameters (all models)	$k_{p_WT} = 32,\ k_{i_WT} = 0.0032$

Table 2.2 Parameters of the three models.

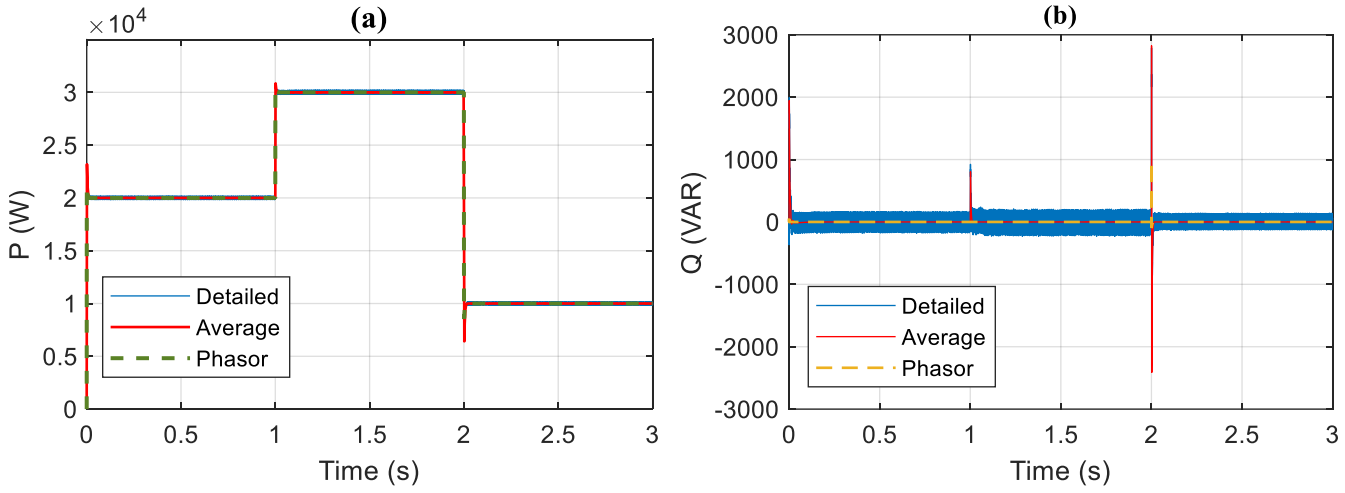


Fig.2.25 (a) Active, and (b) reactive power curves of the three models.

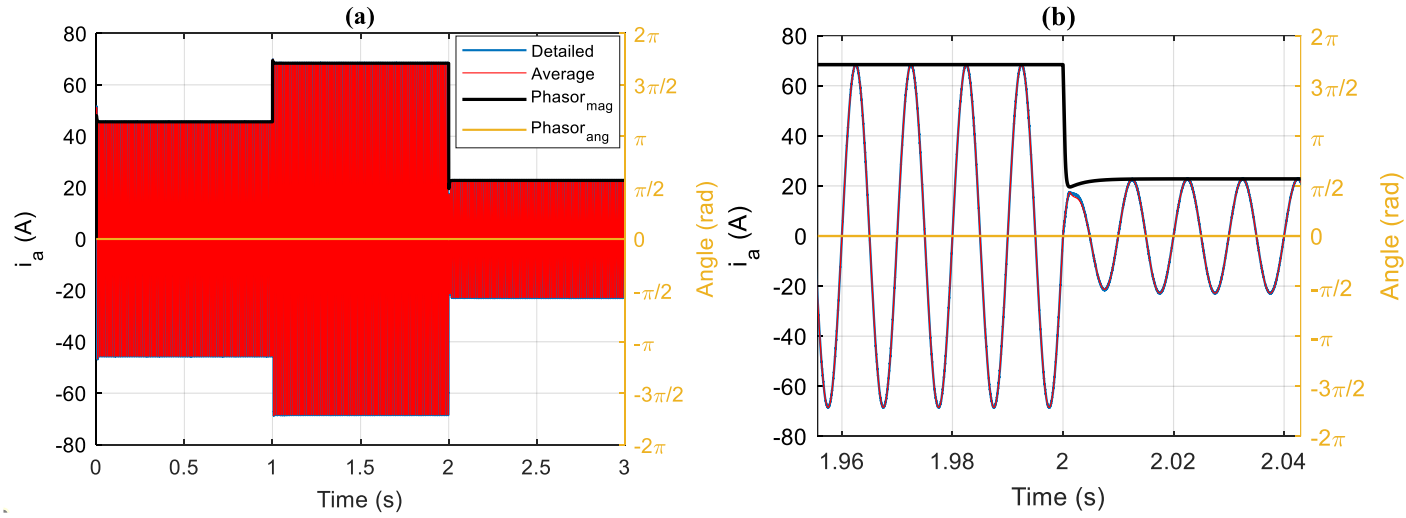


Fig.2.26 (a) current waveforms of $i_a(t)$ in the detailed and average models, the magnitude, and phase shift of i_a in the phasor model (b) A zoom of i_a curves of the three models ($1.96s \leq t \leq 2.04s$).

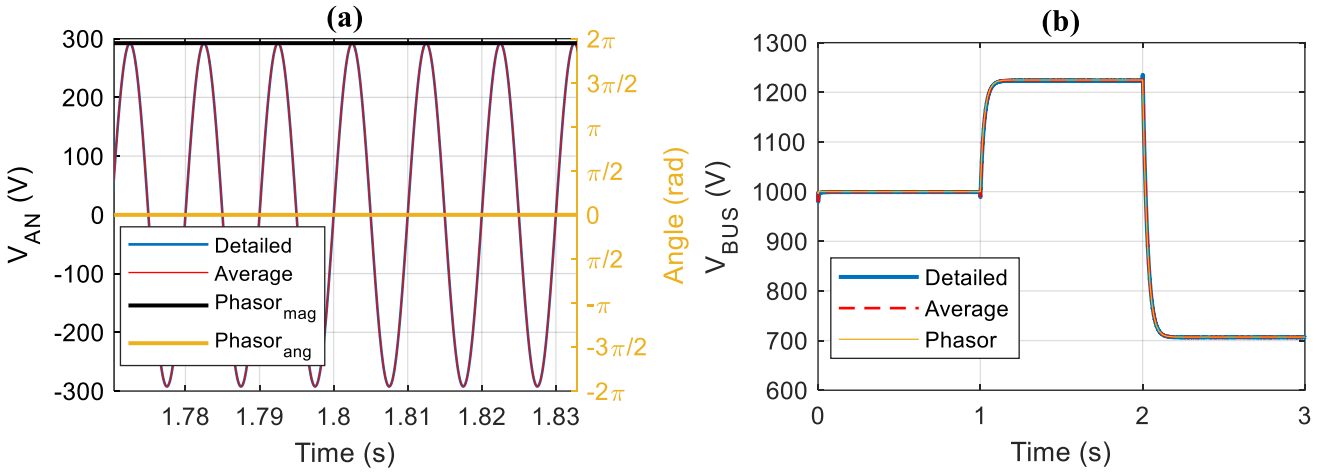


Fig.2.27 (a) A zoom on the phase to neutral voltage V_{AN} waveforms of the detailed and average models, the magnitude, and phase-shift of V_{AN} in the phasor model ($1.78s \leq t \leq 1.83s$), (b) common DC bus voltage (V_{BUS}) of the detailed, average, and phasor models.

The high increase in calculation step size and the reduction in system complexity result in a faster simulation of the phasor model (the simulation speed ratio of the average to the phasor model is 26 and 880 of the detailed to the phasor model). As a result, the phasor notation can reduce the model complexity by omitting the time domain representation of all sinusoidal electrical components and increasing the calculation step size while maintaining accurate modeling of the WT conversion chain. Next, the phasor domain is applied to all operating AC units including the utility grid and the DG.

Model	Duration of the three seconds simulation	calculation step size
Detailed	7 min 20 s	0.5 μs
Average	13 s	50 μs
Phasor	0.5 s	17.8 ms

Table 2.3 Comparison of simulation duration and calculation step size in the detailed, average, and phasor models.

2.5.3.5 Conduction and switching losses

To retrieve the efficiency of the 3ϕ rectifier, the converter losses should be evaluated and added to the proposed rectifier model. Knowing that the conduction and the switching losses account for a major part of the existing losses, they are investigated in detail in this study while other sources of power loss are neglected. First, the switching losses are modeled based on the expression proposed in [137] as follows:

$$P_{sw_3\phi_rec} = \frac{6}{\pi} f_{sw}\left(E_{on_IGBT} + E_{off_IGBT} + E_{off_diode}\right)\frac{V_{BUS}}{V_{ref}} \cdot \frac{\hat{\imath}_l}{i_{ref}} \quad \text{(II.43)}$$

Where,

- f_{sw} is the switching frequency in Hz ($f_{sw} = 20\ KHz$)
- E_{on_IGBT}, E_{off_IGBT}, E_{off_diode} are respectively the turn-on and turn-off energy losses of the IGBT, and the turn-off energy losses of the diode due to the reverse recovery charge current (mJ) (Appendix C)
- V_{BUS} is the DC bus voltage in (V) ($V_{BUS} = 800\ V$)
- $\hat{\imath}_l$ is the peak value of the AC load sinusoidal current (in this case, $\hat{\imath}_l$ corresponds to the d-axis current component i_d of the phasor model as $i_q = 0$)
- V_{ref} and i_{ref} are respectively the voltage and current references under which the switching losses are given (Appendix C)

Unlike the switching losses, the conduction losses are directly dependent on the modulation function such as the sinusoidal PWM, suboptimal space vector, etc.[138]. In this study, the selected modulation function is the sine triangular PWM. Accordingly, the conduction losses of a single IGBT and a single diode are expressed as follows[139]:

$$\begin{cases} P_{cond_IGBT} = \frac{V_{CE,0}\hat{\imath}_l}{2\pi}\left(1 + \frac{M\pi}{4}\right) + \frac{r_{CE}\hat{\imath}_l^2}{2\pi}\left(\frac{\pi}{4} + \frac{2M}{3}\right) \\ P_{cond_diode} = \frac{V_{F,0}\hat{\imath}_l}{2\pi}\left(1 - \frac{M\pi}{4}\right) + \frac{r_F\hat{\imath}_l^2}{2\pi}\left(\frac{\pi}{4} - \frac{2M}{3}\right) \end{cases} \quad \text{(II.44)}$$

Where, P_{cond_IGBT}, P_{cond_diode}, $V_{CE,0}$, r_{CE}, $V_{F,0}$, r_F, and M are respectively the conduction losses of a single IGBT (W), the conduction losses of one diode (W), the IGBT's threshold voltage (V), the IGBT's differential resistance (Ω), the diode's threshold voltage (V), the diode's differential resistance (Ω), and the modulation index.

Hence, the total conduction losses can be deduced from equation (II.44) as the sum of P_{cond_IGBT} and P_{cond_diode} times the number of total IGBTs and diodes of the rectifier:

$$P_{cond_3\phi_rec} = 6(P_{cond_IGBT} + P_{cond_diode}) \quad \text{(II.45)}$$

Finally, the total power losses in the 3ϕ rectifier can be expressed as follows:

$$P_{losses_3\phi_rec} = P_{sw_3\phi_rec} + P_{cond_3\phi_rec} \quad \text{(II.46)}$$

Next, the conduction, the switching, and the total losses are plotted as functions of the input variables which are M, $\hat{\imath}_l$, and V_{BUS}:

- As the WT and PV are continuously functioning in MPPT mode, the remaining converters of the DC microgrid take charge of stabilizing the common DC bus voltage then, V_{BUS} is considered constant equal to its reference value $V_{BUS} = 800V$.
- The modulation index M imposes the three-phase voltages of the PMSM (V_{abc}), then the (dq) axes components in the phasor domain: V_{dq}

- The peak value of the AC sinusoidal current $\hat{\imath}_l$ corresponds to i_d in the phasor domain as i_q is set to zero.

Yet, the input electrical power of the 3ϕ rectifier corresponds to the electrical active power generated by the PMSM (P_{PMSM}) and is computed as a function of V_{dq} and i_{dq} as follows:

$$P_{elec_3\phi_rec} = P_{PMSM} = \frac{3}{2}(V_d i_d + V_q i_q) \tag{II.47}$$

Thus, the losses can be simply represented as a function of $P_{elec_3\phi_rec}$ instead of M and $\hat{\imath}_l$. Referring to Fig.2.19, the maximum wind mechanical power at base speed is $P_{wind_m} = 0.9P_{PMSM_base} = 49.5\,KW$, and the nominal efficiency of the PMSM is $\eta_{n,G} = 92.85\,\%$ (Appendix C). Hence, the maximum generated electrical power is $P_{elec_3\phi_rec_max} = 0.9285P_{wind_m} = 45.96\,KW$. Fig.2.28 (a) shows the conduction, switching, and total losses curves as a function of $P_{elec_3\phi_rec}$. It is seen that around 80% of the total losses account for the switching losses. In addition, the 3ϕ rectifier power efficiency, $\eta_{3\phi_{rec}}$, is expressed as:

$$\eta_{3\phi_rec} = 1 - \frac{P_{losses_3\phi_rec}}{P_{elec_3\phi_rec}} \tag{II.48}$$

$\eta_{3\phi_rec} = f(P_{elec_3\phi_rec})$ curve is depicted in Fig.2.28 (b). It shows that the converter's efficiency increases with the input power and reaches a maximum of $\eta_{3\phi_rec} = 97.3\%$ at $P_{elec_3\phi_rec_max}$.

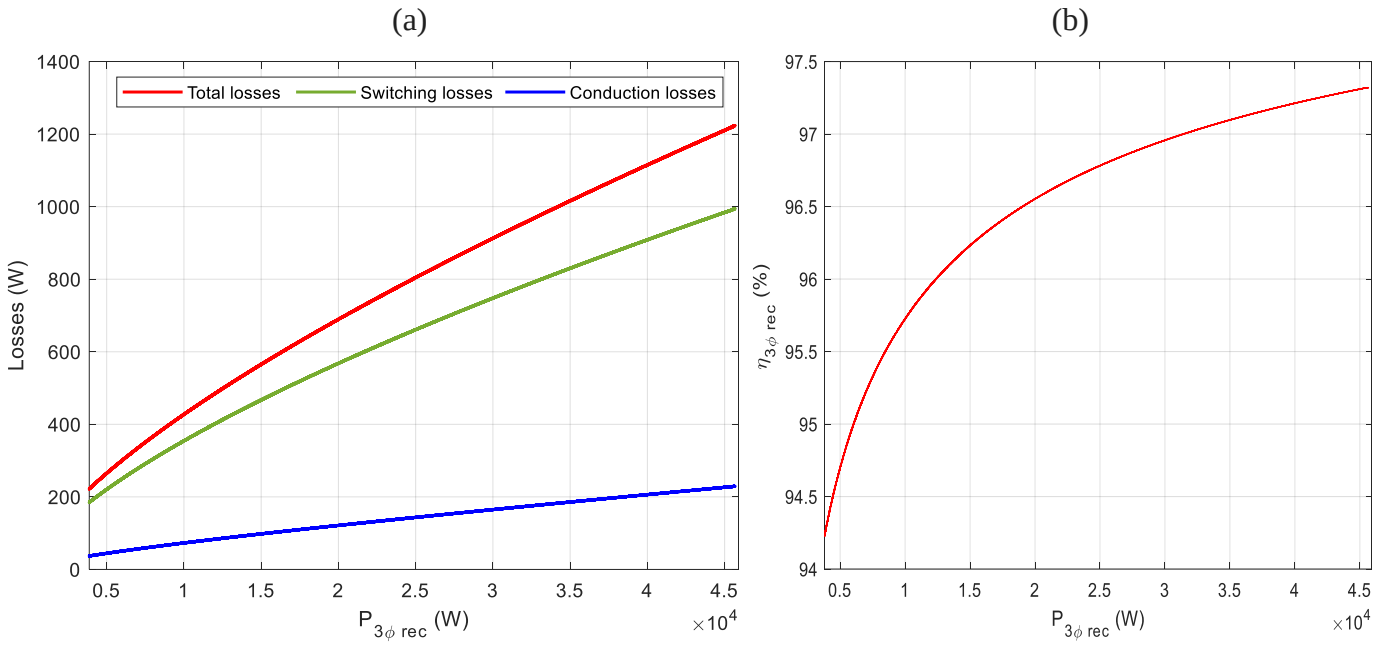


Fig.2.28 (a) 3ϕ rectifier losses as a function of the input electrical power, (b) efficiency of the 3ϕ rectifier losses as a function of the input electrical power.

2.5.3.6 3ϕ rectifier control strategy

To continuously extract the maximum available wind power, an MPPT technique is applied as a control strategy of the 3ϕ rectifier. Among several MPPT techniques found in the literature such as the tip speed ratio control, the optimal torque control, the power signal feedback control, the perturb and observe control, etc. the optimal torque control is applied in this study. For further information on the MPPT techniques, it can be referred to [42]. The block diagram of the (WT) (dq) frame control with the optimal torque technique in the phasor domain is represented in Fig.2.29. The branch colored in light blue corresponds to the optimal torque MPPT technique and is detailed in Appendix C. Fig.2.30 shows the MPPT characteristic in a blue dashed line as a function of the turbine speed for different wind speed values.

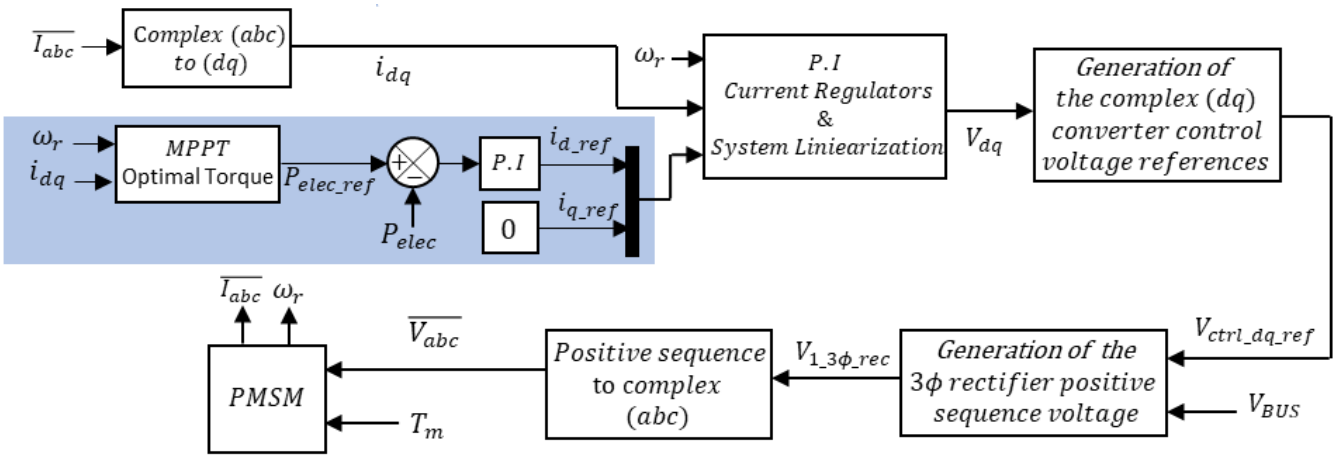


Fig.2.29 Block diagram of the (WT) (dq) frame control in the phasor domain.

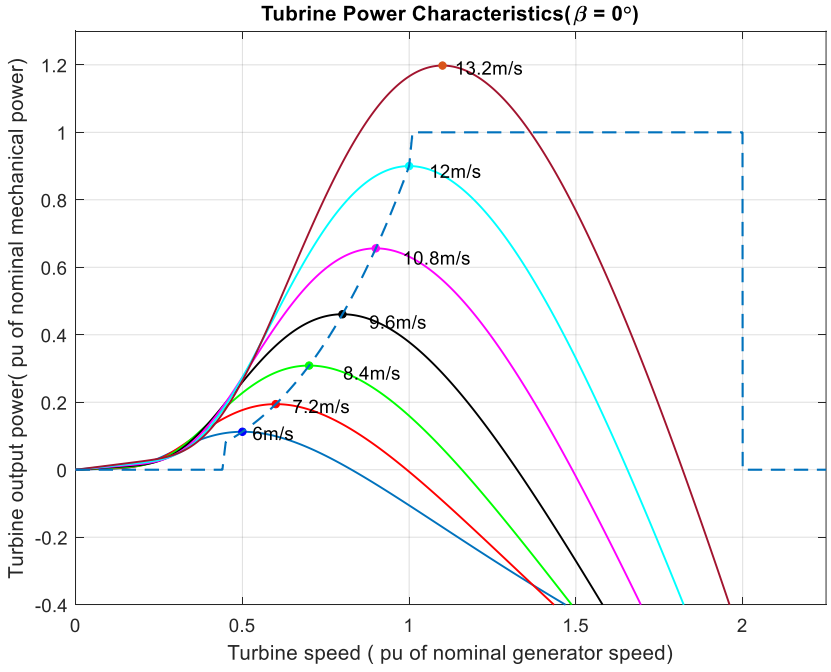


Fig.2.30 MPPT characteristic for different wind speed values.

To test the validity of the proposed MPPT, the wind conversion chain is simulated under variable wind speeds. The mechanical wind power P_{wind_m} is plotted as a function of the wind speed in p.u of the nominal wind speed in Fig.2.31. The obtained curve (solid blue line) is the same as that plotted of the MPPT characteristic in Fig.2.30 and the six different operating zones are identified (Appendix C). Besides, the electrical power generated by the PMSM denoted P_{wind_elec} (dashed red line), and the outputted power from the 3ϕ rectifier denoted $P_{wind_3\phi_out}$ (black line),are represented in the same plot of P_{wind_m}. The cumulative losses resulting from the conversion of the mechanical power to electrical across the PMSM and the conversion of the AC power to DC through the 3ϕ rectifier are tangibly identified in Fig.2.31.

This can be seen by P_{wind_elec} curve plotted bellow P_{wind_m} curve, same for $P_{wind_3\phi_out}$ curve which is situated below P_{wind_elec} curve. At last, the power efficiency of the PMSM, η_{PMSM} (eq.II.26), is plotted in (%) as a function of the wind mechanical power in Fig.2.32. By this, the 3ϕ rectifier output power can be computed for each wind speed input correspondingly:

$$P_{wind_3\phi_out} = \eta_{PMSM}\eta_{3\phi_rec}P_{wind_m} \quad \text{(II.49)}$$

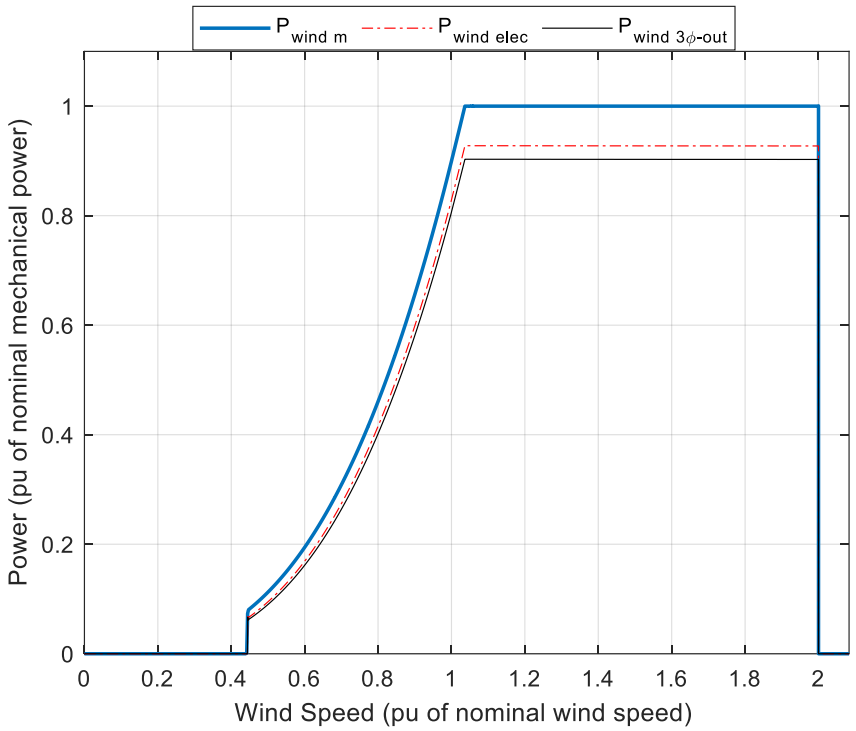


Fig.2.31 The mechanical and electrical wind power, and the 3ϕ rectifier power output as functions of the wind speed.

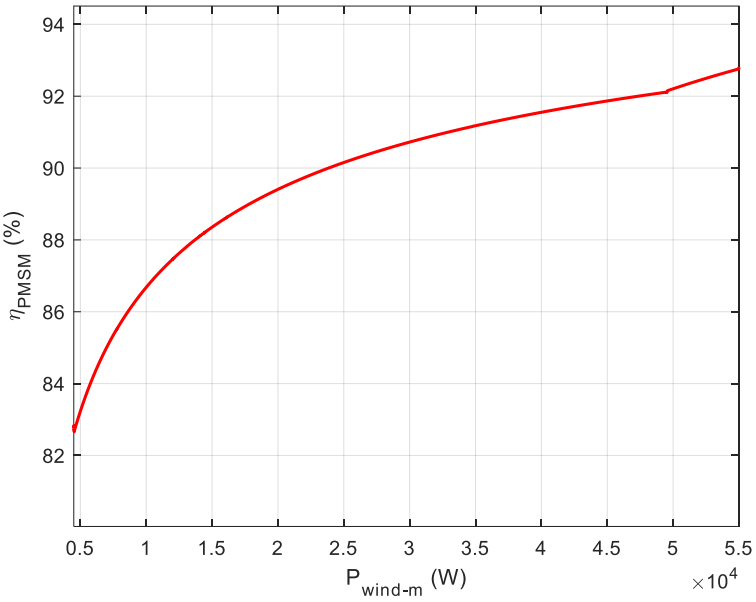


Fig.2.32 The PMSM power efficiency in (%) as a function of the mechanical wind power.

2.6 Diesel generator and utility-grid energy conversion chains

The (DG) and the utility grid are additional AC sources that are connected to the common DC bus voltage of the DC microgrid. Their connection to the microgrid, the amount of generated power from the DG, and the purchased/ sold power from/to the utility grid are subject to the decision of the optimizer controller detailed in the next chapter. Hence, the power references of the (DG) and the utility grid are imposed by the optimization problem: P_{DG_ref} and P_{grid_ref}. The detailed study and analysis of each component from the energy conversion chain of the (DG) and utility grid are out of the scope of this thesis. In other words, the (DG) and the utility grid are regarded as potential AC sources or loads that interact with the DC microgrid and can generate or absorb an instantaneous amount of power set by the optimization problem. Accordingly, all phenomena such as the thermal/mechanical, the mechanical/electrical energy conversions in the combustion engine of the (DG), the power line losses, the voltage drop, the harmonic distortions in the utility grid, etc. are not detailed in this thesis. Although, to include the (DG) and the utility grid units in the 24-hour DC microgrid simulation model, the averaging techniques applied to the (WT) conversion chain were included as follows:

- Three-phase sources: As the (DG), and the utility grid are of AC type, they were simply modeled by a three-phase voltage source forming a direct balanced system, in series with a resistance, and an inductor. The system was modeled in the phasor domain detailed in the previous section.
- 3ϕ rectifiers: The (DG) and the utility grid are connected to the common DC bus through a 3ϕ rectifier that is modeled similarly to the (WT) rectifier. For the utility grid, the same converter operates as a rectifier when the power is purchased from the grid and as an inverter when the power is sold to the grid.

- (dq) frame control in the phasor domain: To control the 3ϕ rectifiers of the (DG) and the utility grid, the (dq) control technique applied to the (WT) rectifier is adopted (Fig.2.24). The active power is controlled through the d-axis current component, P_{DG_ref} and P_{grid_ref} are the d-axis active power references. However, the q-axis reference of both rectifiers is always set to zero to absorb zero reactive power.
- IGBTs, diodes selection, and loss modeling: By referring to Table 2.1 at the beginning of Chapter 2, the rated power of the (DG) is equal to the one of the (WT) $P_{DG_r} = P_{WT_r} = 55KW$. As to the utility grid, the maximum allowable purchased/sold power is set in the next chapter to $P_{grid_max} = 60\ KW$. Hence, the power rates of the (DG) and utility grid 3ϕ rectifiers are the same as the (WT). Besides, the same switches and diodes can be selected as:
  1) For the (DG), the alternator has the same rated power as the (WT) PMSM, and then the (DG) outputted voltage and current are in the same range as the (WT).
  2) for the utility grid, having a standard voltage rating of 380-400V- 3ϕ (RMS phase to phase), this leads to a maximum grid current of $I_{grid_max} \approx \pm 90A$.

  As a result, and without loss of generality, the same 3ϕ Rectifier of the (WT) can be selected for the (DG) and the utility grid, and the conduction and switching losses are always computed following the same approach of the (WT). Next, the modeled losses of the (DG) and utility grid 3ϕ Rectifiers will account for the total converters losses to be minimized as one of the optimization goals.

2.7 ESS conversion chain

The proposed DC microgrid includes an energy storage system consisting of a lithium-ion battery. The lithium-ion battery has several merits over Nickel Metal Hybrid (Ni-MH) and lead-acid

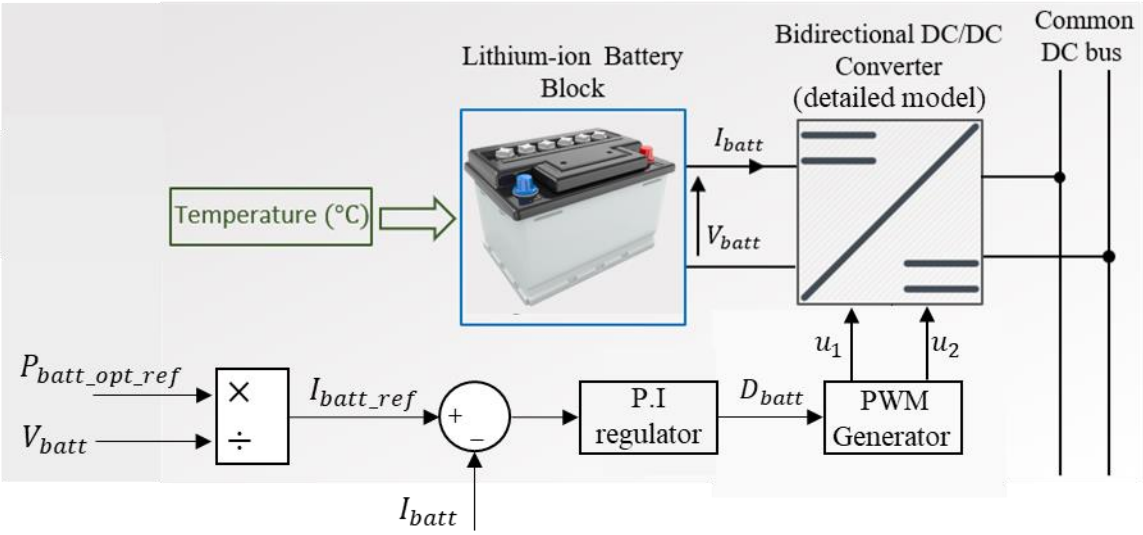


Fig.2.33 ESS conversion chain.

batteries in terms of higher energy density (75-200 Wh/Kg), low self-discharge (1%/day), absence of memory effect, better power output, better cycle-life, and higher coulomb efficiency (~98%)[140], [141]. Besides lithium-ion batteries which are the most used in electrical vehicles (EVs) are replaced when their capacity reaches 80% of the original value. These used EV batteries are largely applied in residential applications as ESSs which offer a better life span, and a shorter payback time for residential use[142]. For the above-mentioned reasons, the selected ESS is a lithium-ion battery with a rated capacity of 500 Ah, and a rated voltage of 250 V. The ESS energy conversion chain is shown in Fig.2.33. It consists of a lithium-ion battery connected to the common DC bus through a bidirectional DC/DC converter.

2.7.1 Lithium-ion battery model

Several microgrid optimization studies that include an ESS consisting of a battery adopt a linear state space model of the battery [95], [98], [100]. A discrete version representing the battery State of Charge (SOC) at the instant $(k+1)$ as a function of the SOC, the battery charge and discharge power at the instant (k) is utilized. The expression is the following:

$$SOC(k+1) = SOC(k) + \frac{\eta_{ch} P_{ch}(k) T_s}{E_{batt}} + \frac{\eta_{dis} P_{dis}(k) T_s}{E_{batt}} \quad \text{(II.50)}$$

Where η_{ch}, η_{dis}, E_{batt}, $P_{ch}(k)$, $P_{dis}(k)$, and T_s are respectively the charge efficiency, the discharge efficiency, the maximum battery energy (Wh), the battery charging power (W), the battery discharging power (W), and the sampling period (s). In this mathematical representation, the maximum battery energy is given as a constant and can be expressed as:

$$E_{batt} = Q_{batt} V_{batt} \quad \text{(II.51)}$$

Where, Q_{batt} and V_{batt} are respectively the maximum battery capacity (Ah) and the battery voltage (V). Standardly, the maximum battery capacity is a constant given by the manufacturer, then the battery voltage is considered constant and equal to its nominal value regardless of the battery SOC. The problem lies in this assumption as the battery voltage has a nonlinear characteristic that largely depends on the SOC value [143]. Thus, the consideration of a constant battery voltage leads to inexact SOC deduction which impacts the whole results of the optimization problem. Hence, a precise model of the lithium-ion battery dynamics proposed by Tremblay and adopted in Simulink is applied[143]. The model represents accurately the battery voltage dynamics including all nonlinear zones. The applied battery voltage curve is represented as a function of the SOC (%) in Fig.2.34. Three different sections are identified:

1. The first section represents the exponential voltage drop when the battery is fully charged.
2. The second section represents the nominal area where the battery voltage is approximately equal to its nominal value. This section ends when the voltage drops below the battery's nominal voltage.

3. The third section represents the total discharge of the battery when the voltage drops rapidly.

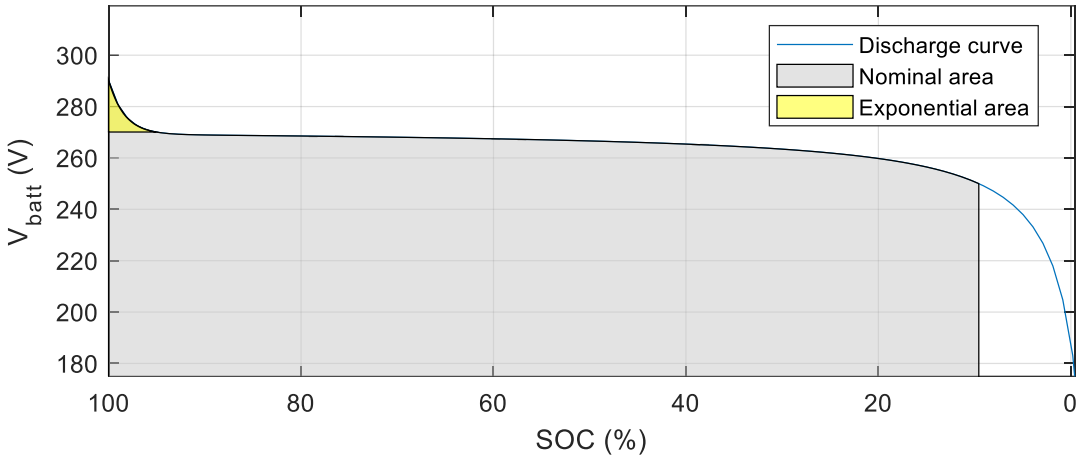


Fig.2.34 The battery voltage discharge curve as a function of the SOC at $0.43C$ ($217.4\ A$).

Hence, the detailed battery model proposed by Tremblay and represented in MATLAB/Simulink in the "generic battery model" block is applied. Besides the detailed modeling of the battery dynamics, another crucial factor that substantially impacts the battery performance and is rarely addressed in optimization problems is the temperature effect.

Nowadays, lithium-ion batteries are widely favored as ESS in DC microgrid applications worldwide. Moreover, increasing areas around the world are witnessing high differences in temperature seasonally and even daily due to climate change. Therefore, the temperature effect is included in Tremblay's standard equations, and the thermal impact on the battery's performance is assessed. Based on[144] [145], the battery's charge and discharge equations become the following:

Discharge model ($I_{batt} > 0$):

$$\begin{cases} f_1(it, I^*_{batt}, I_{batt}, T, T_a) = E_0(T) - K(T).\frac{Q(T_a)}{Q(T_a)-it}(I^*_{batt} + it) + Ae^{-B.it} \\ V_{batt}(T) = f_1(it, I^*_{batt}, I_{batt}, T, T_a) - R(T).I_{batt} \end{cases} \quad \text{(II.52)}$$

Charge model ($I_{batt} < 0$):

$$\begin{cases} f_1(it, I^*_{batt}, I_{batt}, T, T_a) = E_0(T) - K(T).\frac{Q(T_a)}{it+0.1Q(T_a)}I^*_{batt} - K(T).\frac{Q(T_a)}{Q(T_a)-it}it + Ae^{-B.it} \\ V_{batt}(T) = f_1(it, I^*_{batt}, I_{batt}, T, T_a) - R(T).I_{batt} \end{cases} \quad \text{(II.53)}$$

Where,

- it is the extracted capacity, in Ah.
- I^*_{batt} is the low-frequency current dynamics, in A.
- I_{batt} is the battery current, in A.
- T is the cell temperature, in K.

- T_a is the ambient temperature, in K.
- $E_0(T)$ is the constant voltage expressed as a function of the cell temperature, in V.
- $K(T)$ is the polarization resistance expressed as a function of the cell temperature, in **Ω**.
- $Q(T_a)$ is the maximum battery capacity expressed as a function of the ambient temperature, in Ah.
- A is the exponential voltage, in V.
- B is the exponential capacity, in Ah^{-1}.
- $R(T)$ is the internal resistance expressed as a function of the cell temperature, in **Ω**.

As I^*_{batt} is the low-frequency current dynamics, it is modeled by a first-order low-pass filter and can be expressed as a function of I_{batt} as follows:

$$I^*_{batt} = \frac{I_{batt}}{\tau_{batt} p + 1} \tag{II.54}$$

Where, τ_{batt}, and p are respectively the time constant of the low-pass filter, and the transfer function object.

The SOC of the battery is calculated as:

$$SOC = 100\left(1 - \frac{1}{Q(T_a)}\int_0^t I_{batt}(t)dt\right) \tag{II.55}$$

The expressions of $E_0(T)$, $K(T)$, $Q(T_a)$, $R(T)$, T, and additional battery parameters can be found in Appendix D.

To validate the battery dynamic model, the battery discharge characteristics are plotted for different constant discharge currents at 25°C and for different different temperatures at a constant current $1C$ $(500A)$.

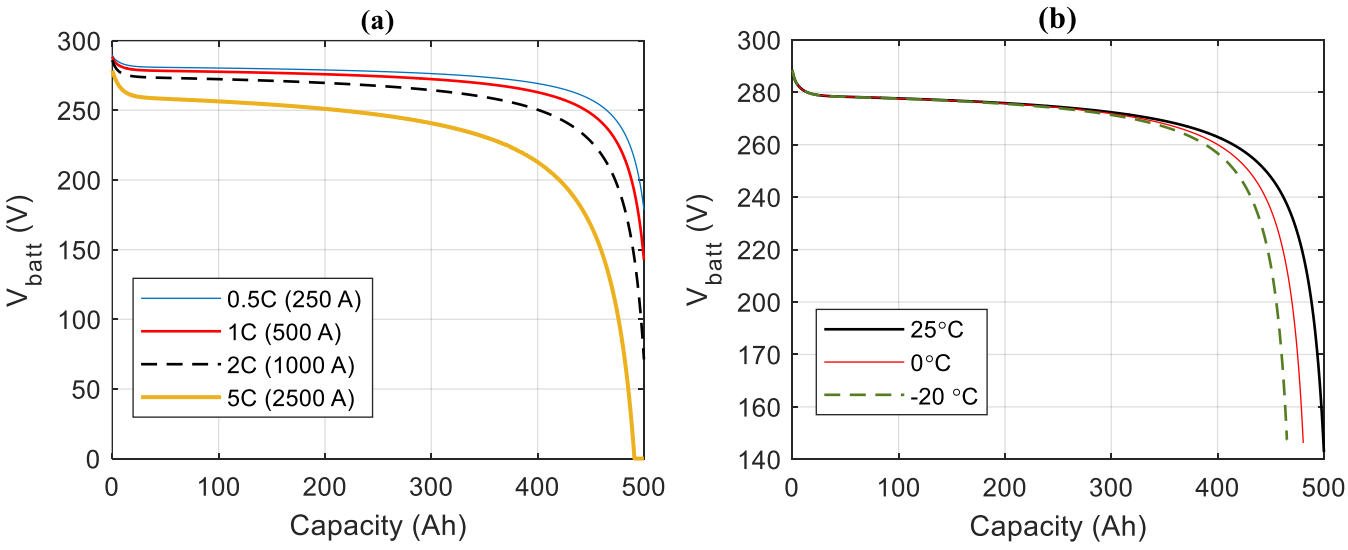


Fig.2.35 (a) Battery voltage discharge characteristic for different constant discharge currents at 25°C, (b) voltage discharge characteristic at a constant current of $1C$ $(500A)$ for variable temperatures.

Fig.2.35 (a) shows the battery voltage discharge characteristic as a function of the capacity (Ah) for $0.5C$, $1C$, $2C$, and $5C$ constant discharge currents. The obtained curves show that the battery voltage curve is highly impacted by the discharge current. The nominal area in which the battery voltage is practically equal to its nominal value narrows when the discharge current increases (the steepest curve is the $5C$ discharge curve in gold color). Fig.2.35 (b) shows the results of the discharge characteristic with a constant current of $1C$ $(500A)$ for variable temperatures.

The maximum battery capacity decreases when the temperature drops and loses respectively 4% and 7% at $0°C$ and $-20°C$ from its nominal value at $25°C$. The nominal area of the voltage curve is negligibly impacted by the temperature effect at high battery SOCs ($SOC > 30\%$), whereas for lower SOCs the battery voltage drops faster at low temperatures.

2.7.2 Bidirectional DC/DC converter

Bidirectional DC/DC converters are widely applied to connect ESSs of a DC nature to a common DC bus to assure voltage matching. These converters are predominantly found in new energy electric vehicles, they assure the power conversion between newly equipped hybrid ESSs such as the fuel-cell, batteries, supercapacitors, and the vehicle bus[146]. Existing in several isolated and non-isolated topologies, a basic non-isolated bidirectional DC/DC boost topology is applied in this study. The electrical circuit of the bidirectional DC/DC converter is shown in Fig.2.36. Operating in continuous mode, the converter functions separately in two different modes:

- Boost mode: The boost mode is enabled when the battery is in discharge mode ($I_{batt} > 0$). The switch $sw1$ is active and $sw2$ is inactive. The diode of the $sw2$, denoted D_{sw2}, allows the current flow to the common DC bus when $sw1$ is off. In this operating mode, the voltage is stepped up from around $V_{batt_n} = 250V$ to $V_{BUS} = 800V$.
- Buck mode: The buck mode is enabled when the battery is in charge mode ($I_{batt} < 0$). The switch $sw2$ is active and $sw1$ is inactive. The diode of the $sw1$, denoted D_{sw1}, allows the current flow of I_{batt} when $sw2$ is off. In this operating mode, the voltage is stepped down from $V_{BUS} = 800V$ to around $V_{batt_n} = 250V$.

The IGBTs $sw1$ and $sw2$ are controlled by firing pulses, denoted respectively u_1 and u_2 with a fixed switching frequency $f_{sw_batt} = 20\,KHz$. In boost mode $I_{batt} > 0$, the mathematical equations of the converter are the following:

$$\begin{cases} V_{batt} = (R_{batt} + R_{L_batt})I_{batt} + L_{batt}.\frac{dI_{batt}}{dt} + (1-u_1).V_{BUS} \\ I_{D_{sw2}} = (1-u_1).I_{batt} \\ (1-u_1).I_{batt} = C_{out}.\frac{dV_{BUS}}{dt} + I_{out} \end{cases} \quad \text{(II.56)}$$

Where, R_{batt}, R_{L_batt}, L_{batt}, and $I_{D_{sw2}}$ are respectively the battery's internal constant resistance ($R_{\text{batt}} = R|_{T_{ref}}$) (Ω), the inductor resistance (Ω), the filtering inductor (H), and the current flowing in the diode of $sw2$ (A).

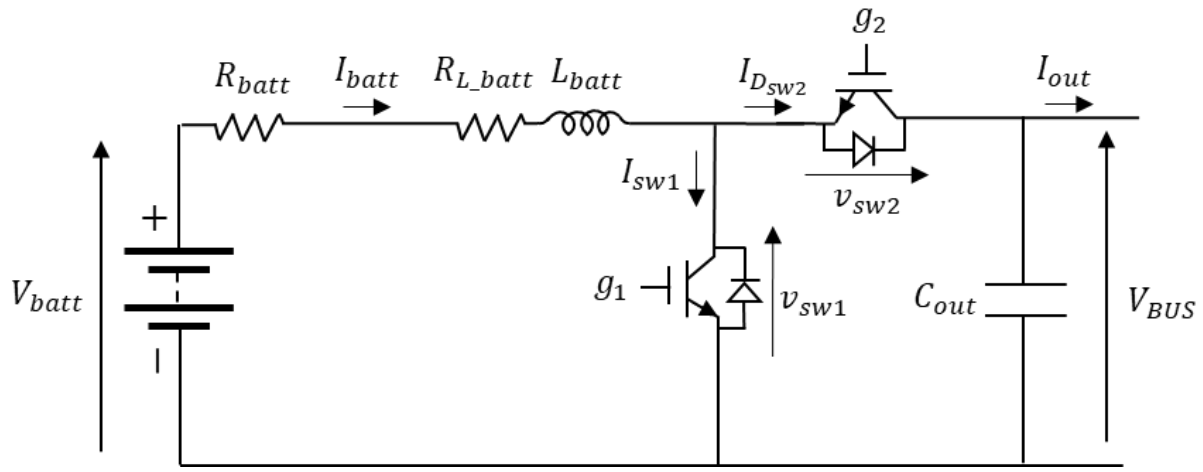


Fig.2.36 Electrical circuit of the bidirectional DC/DC converter (detailed model).

By always setting $u_2 = \bar{u}_1 = 1 - u_1$, and taking into account that I_{batt} and I_{out} have opposite signs in the buck mode operation, it can be seen that the bidirectional DC/DC converter keeps the same equations of the boost mode (II.56) in the buck mode. The buck equations are then expressed as:

$$\begin{cases} V_{batt} = -(R_{batt} + R_{L_batt})I_{batt_buck} - L_{batt}.\frac{dI_{batt_buck}}{dt} + u_2.V_{BUS} \\ I_{sw2} = u_2.I_{batt_buck} \\ -u_2.I_{batt_buck} = C_{out}.\frac{dV_{BUS}}{dt} - I_{out_buck} \end{cases} \quad \text{(II.57)}$$

Where, $I_{batt_buck} = -I_{batt}$, $I_{out_buck} = -I_{out}$, and $I_{sw2} = -I_{\text{D}_{\text{sw2}}}$. As a result, if $u_2 = \bar{u}_1 = 1 - u_1$ is always imposed by the PWM pulses generator of the control loop, and the opposite signs of currents are considered in the mathematical modeling, the bidirectional DC/DC converter can be simply modeled by the DC/DC boost equations (II.56). Consequently, the same approach of averaging technique and losses modeling of the DC/DC boost is applied to the bidirectional DC/DC converter. Omitting the switching devices and introducing the controlled current and voltage sources to derive the average model, the same electrical circuit of the DC/DC boost average model of Fig.2.6 is obtained. The resulting converter equations are the same as the ones obtained in (II.7), and the bidirectional DC/DC converter is directly controlled by the duty cycle ratio, denoted D_{batt}, instead of the firing pulses u_1 and u_2. As for the switching and the conduction losses, the same modeling strategy is put in. This leads to the same electrical circuit of Fig.2.9 with the same expression of the switching losses as only one switch and one diode are active during a switching period in the boost as well in buck mode ($sw1$ & D_{sw2} in boost mode, and $sw2$ & D_{sw1} in buck mode). Hence, the switching-loss resistance (r_{sw}) can be expressed similarly to equation (II.19) as:

$$r_{sw} = \frac{f_{sw_batt}.V_{BUS}}{6.I_{batt}} \times \left(t_{on_IGBT} + t_{off_IGBT} + \frac{I_{RM_D}.\ t_{f_D}}{I_{batt}}\right) \quad \text{(II.58)}$$

However, as detailed before, variable voltage sources and on-resistances are utilized to model the conduction losses. These voltage sources and on-resistances are expressed as functions of the duty cycle ratio (equation II.8). Knowing that in both modes, the on-resistances and equivalent voltage sources are placed on the inductor branch side (L_{batt}) same as in Fig.2.9. The equivalent on-resistances and voltage sources have different expressions in boost and buck modes. In boost mode, they are expressed as:

$$\begin{cases} V_{D0_sw2} = (1 - D_{batt}).V_{f0_sw2} \\ V_{0_sw1} = D_{batt}.V_{CE0_sw1} \\ R_{D_sw2} = (1 - D_{batt}).R_{D_f_sw2} \\ R_{sw1} = D_{batt}.R_{on_sw1} \end{cases} \quad \text{(II.59)}$$

Where,

- V_{D0_sw2} is the conduction loss equivalent voltage source of D_{sw2}, in (V).
- V_{f0_sw2} is the D_{sw2} forward voltage source, in (V).
- V_{0_sw1} is the conduction loss equivalent voltage source of $sw1$, in (V).
- V_{CE0_sw1} is the $sw1$ forward voltage source, in (V).
- R_{D_sw2} is the conduction loss equivalent resistance of D_{sw2}, in (Ω).
- $R_{D_f_sw2}$ is the D_{sw2} forward resistance, in (Ω).
- $R_{sw1}$is the conduction loss equivalent resistance of $sw1$, in (Ω).
- R_{on_sw1} is the $sw1$ on-resistance, in (Ω).

If the same switch from the same manufacturer is selected for $sw1$ and $sw2$, the equivalent on-resistances and voltage sources in buck mode are expressed as:

$$\begin{cases} V_{D0_sw1} = D_{batt}.V_{f0_sw2} \\ V_{0_sw2} = (1 - D_{batt}).V_{CE0_sw1} \\ R_{D_sw1} = D_{batt}.R_{D_f_sw2} \\ R_{sw2} = (1 - D_{batt}).R_{on_sw1} \end{cases} \quad \text{(II.60)}$$

Where,

- V_{D0_sw1} is the conduction loss equivalent voltage source of D_{sw1}, in (V).
- V_{0_sw2} is the conduction loss equivalent voltage source of $sw2$, in (V).
- R_{D_sw1} is the conduction loss equivalent resistance of D_{sw1}, in (Ω).
- R_{sw2} is the conduction loss equivalent resistance of $sw2$, in (Ω).

It can be referred to Appendix D.2 for detailed information on parameter values. The losses in the DC/DC bidirectional converter are represented as functions of the charged/discharged battery power in Fig.2.37 (a) and (b). The maximum charged/discharged battery power is fixed at 0.434C ($I_{batt_max} = \pm 217A$) which yields: $P_{batt_max} = I_{batt_max}V_{batt_n} = \pm 217 \times 250 = \pm 54250\ W$. The conduction, the switching, and the total losses for the boost and buck modes are

represented respectively in Fig.2.37 (a) and (b). As seen, the total losses in both operating modes are proportional to the charged/discharged battery power and are almost equal. The switching losses account for around 60% of the total losses in the two operating modes.

Fig.2.38 shows the efficiencies of the two operating modes as a function of the charged/discharged battery power.

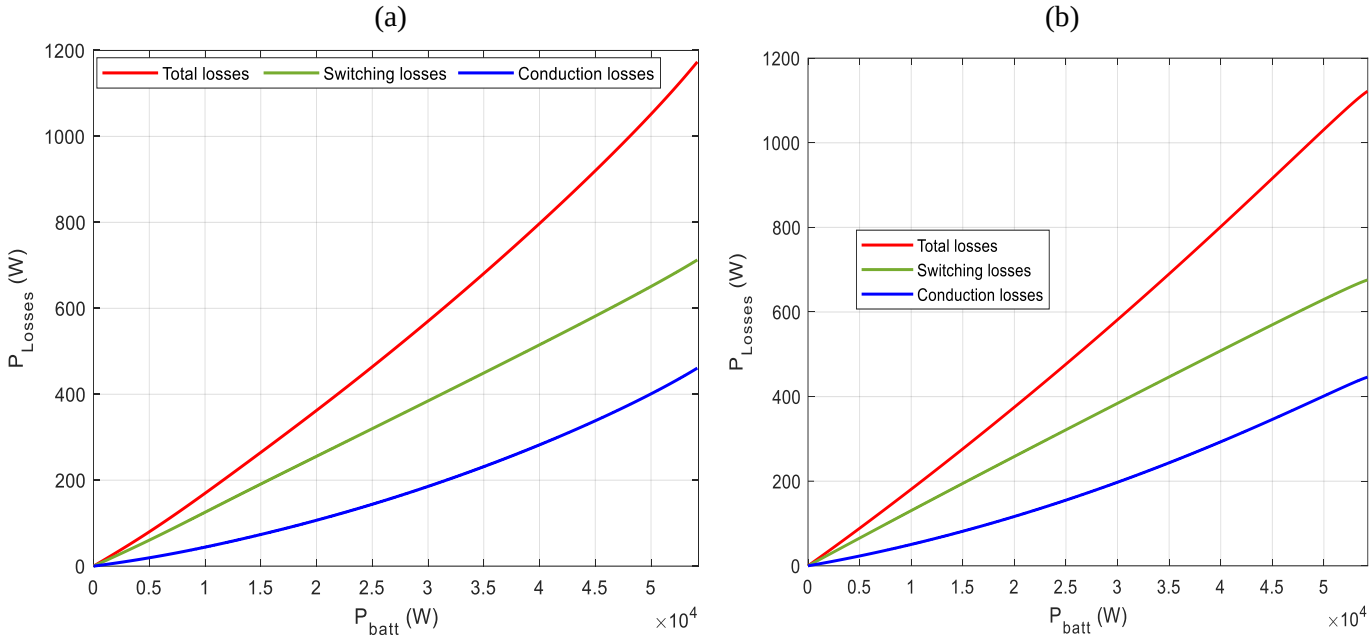


Fig.2.37 (a) Bidirectional DC/DC converter total losses, conduction, and switching losses in boost operating mode (b) in buck operating mode.

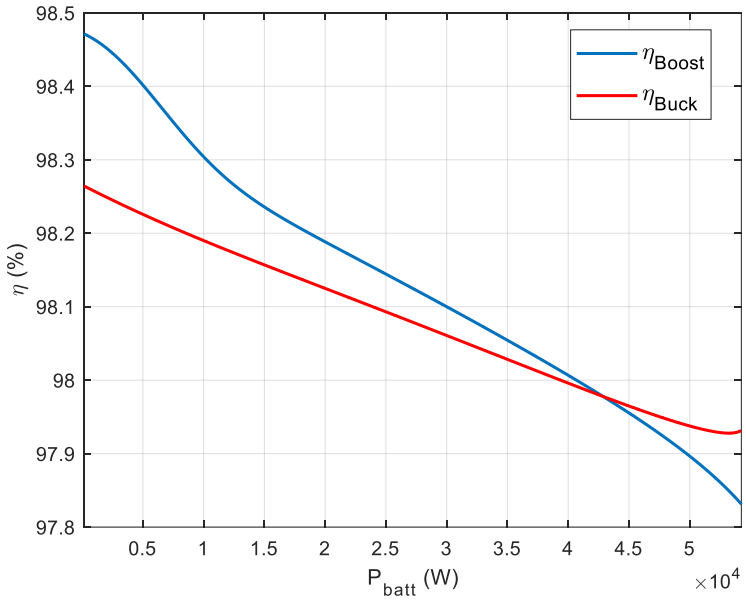


Fig.2.38 Bidirectional DC/DC converter power efficiencies curves in boost and buck operating modes.

Both efficiencies' curves slightly drop with the increase of charged/discharged power, and the boost curve shows a larger variation margin than the buck curve. However, in both operating modes, the efficiency almost stays constant at 98% for the whole power charge/discharge interval.

2.8 Simulation test of the 24-hour assembled DC microgrid

2.8.1 Applied EMS strategy

In this section, the 24-hour assembled DC microgrid model is validated through simulation tests with variable input profiles. A simple EMS strategy that allows the share of all energy sources to the overall power mix is applied. The applied EMS strategy assures two prior objectives, the fulfillment of the load demand and the stabilization of the common DC bus voltage at each instant of the overall 24-hour horizon. Moreover, it guarantees the battery's proper operation and prevents its excess discharge and overcharge by limiting the battery state of charge (SOC) within minimum and maximum admissible values[102]. The flow chart of the applied EMS strategy is depicted in Fig.2.39. As a principle, the RESs are continuously operating in MPPT mode to extract the maximum available power and the applied MPPT techniques are the ones detailed in sections 2.4.3 and 2.5.3.6. The RES and load power profiles are known for the whole time horizon and the battery, (DG), and grid are the dispatchable sources whose power references are imposed by the EMS. Two cases can be differentiated following the difference between the load demand and the generated RES power that is evaluated at each calculation step size.
If the generated power exceeds the load demand, then the SOC variable is evaluated, and one of the two operating modes is selected:

Mode 1 ($SOC < SOC_{max}$): The battery stabilizes the DC bus voltage by charging the surplus of unused power, the (DG) and the grid aren't connected to the microgrid which is operating in islanded mode.
Mode 2 ($SOC \geq SOC_{max}$): The battery has already reached its higher admissible energy charging threshold, so it switches to a floating mode ($I_{batt} = 0$), and the surplus of unused power is sold to the grid. By this, the battery SOC is fixed on its maximum threshold and the grid converter takes charge of stabilizing the DC bus voltage.
On the other hand, if the load consumption is higher than power production then, the SOC variable is compared to its minimum threshold, and one of three operating modes is selected:
Mode 3 ($SOC > SOC_{min}$): The battery stabilizes the DC bus voltage by discharging and supplying the load with the unavailable needed power. The (DG) and gird are disconnected from the microgrid which is operating in islanded mode.
($SOC \leq SOC_{min}$): The power deficit can either be covered by the (DG) or the utility grid as the battery operates in a floating mode ($I_{batt} = 0$). Standardly, DGs operate in a margin of around 25% to 100% of their nominal power[98].

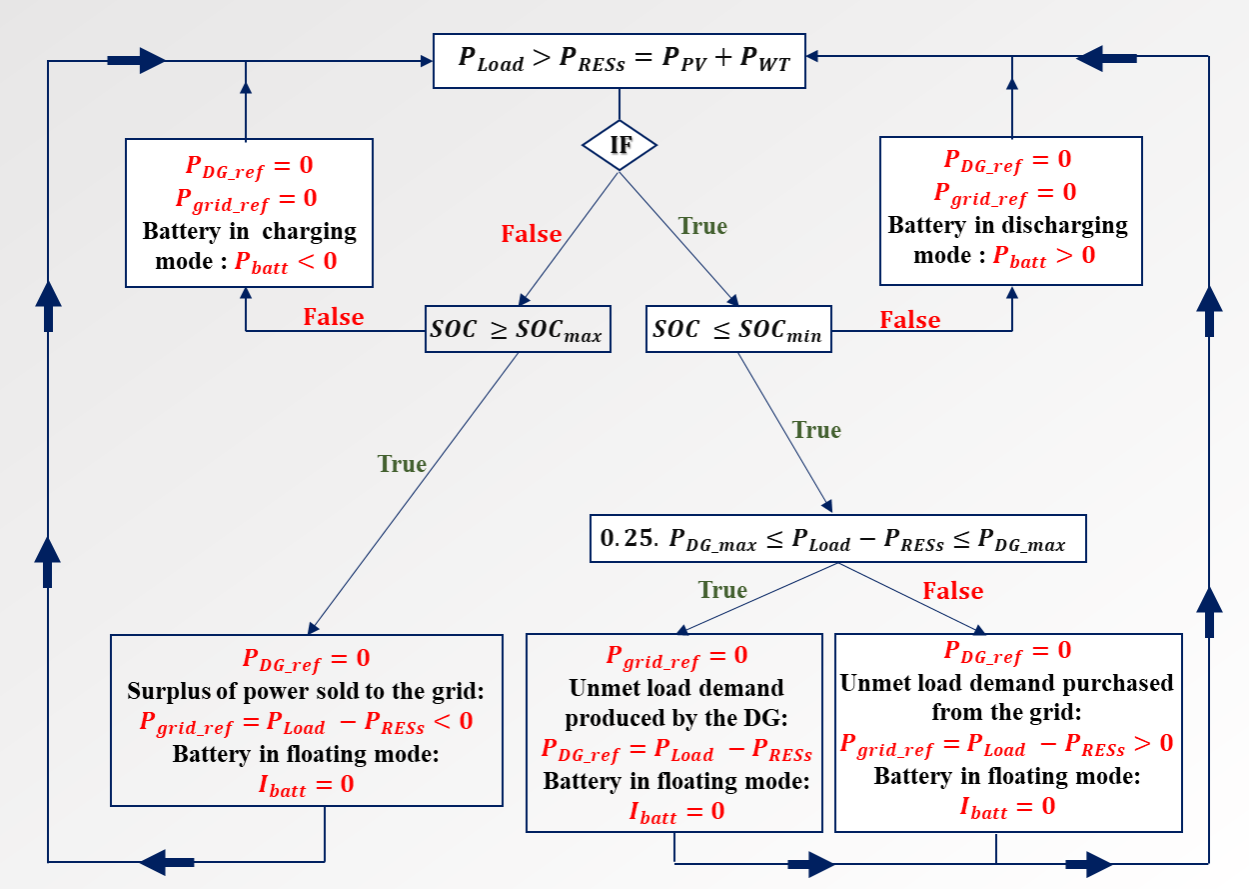


Fig.2.39 Flow chart of proposed EMS strategy.

As a result, the existing power deficit is compared to the minimum and maximum admissible (DG) power generation limits and two operation modes can be encountered:

Mode 4: The required power value is within the admissible power limits of the (DG). Thus, the (DG) is turned on, connected to the microgrid, and generates the remaining unavailable power to cover the load demand. By this, the (DG) rectifier stabilizes the common DC bus voltage. However, none of the power deficit is purchased from the grid.

Mode 5: The power deficit value is not within the (DG) allowable power operating range. Therefore, the required power is uniquely purchased from the utility grid and the (DG) is turned off. By this, the utility grid converter takes charge of stabilizing the DC bus voltage and the microgrid operates in grid-connected mode.

Finally, the same control steps are restarted again at each calculation step size. As the applied EMS strategy does not consider or include any of the optimization goals in the decision-making, it is not advanced as an optimal one. Instead, it is only adopted to test the viability of the overall 24-hour DC microgrid model. However, the application of an optimal EMS with predefined objectives and constraints requires the formulation of an optimization problem that is detailed in the next chapter.

2.8.2 EMS control parameters and 24-hour variable input profiles

The control strategies of the RESs operating in MPPT mode and corresponding regulators' parameters were detailed in sections 2.4.3 and 2.5.3.6 so, they are not recalled in this paragraph. Moreover, the active and reactive power of the (DG) and utility grid are imposed through the (dq) frame control represented in the phasor domain (Fig.2.24). The active power is imposed through the $d-$axis component while the reactive power is always set to zero through the $q-$axis component to absorb zero reactive power. The error between (dq) axes components and their corresponding references are minimized by P.I. regulators for both (DG) and utility grid.
For the (DG), the same P.I. is applied to control d and q-axis components and has the following expression: $R_{DG}(p) = k_{p_DG}.\frac{k_{i_DG}.p+1}{k_{i_DG}.p}$ where, k_{p_DG} and k_{i_DG}, are respectively the proportional and the integral parameters of the (DG) regulator, and p is the Laplace operator. The same for the utility grid regulators which have the following expression: $R_{grid}(p) = k_{p_grid}.\frac{k_{i_grid}.p+1}{k_{i_grid}.p}$ where, k_{p_grid} and k_{i_grid}, are respectively the proportional and the integral parameters of the grid regulator. The parameters of the applied regulators of the (DG) and utility grid are all listed in Table 2.4.

Following the proposed EMS strategy, a voltage and current cascaded loop regulation technique is adopted to control the bidirectional DC/DC converter of the battery. The block diagram of the cascaded control loop is depicted in Fig.2.40. As seen, P.I. regulators are adopted to regulate the common DC bus voltage (V_{BUS}) and the battery current (I_{batt}), respectively. k_{pv_batt}, k_{pc_batt}, k_{iv_batt}, and k_{ic_batt} are respectively the proportional and the integral parameters of the DC bus voltage and battery current regulators. All these regulators' parameters can be found in Table 2.4.
A PWM generator block is required in the instantaneous model to control the real switching devices through the firing pulses, u_1 and u_2 (Fig.2.36 and equations II.56 and II.57). As stated before, the PWM generator block is omitted in the 24-hour DC microgrid model, and the bidirectional DC/DC converter average model is directly controlled by the duty cycle ratio, D_{batt}.
All P.I. regulators of all operating units are equipped with wind-up systems. Finally, we take note that the battery-cascaded loop control is only applied for the above proposed EMS strategy to validate the 24-hour DC microgrid model. Consequently, in the upcoming chapters, the adopted control block diagram of the bidirectional DC/DC converter of the battery is the one represented in Fig.2.33.

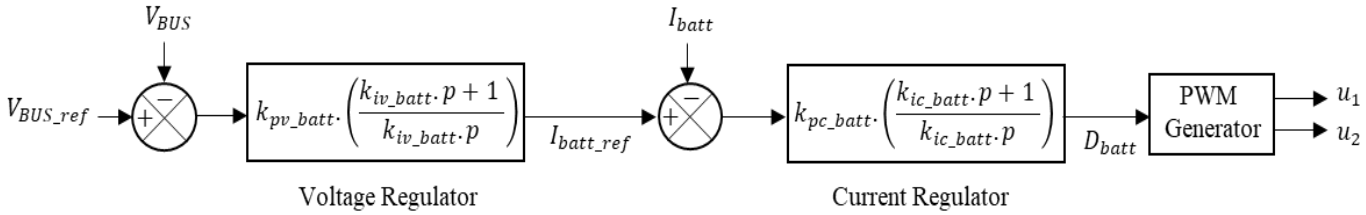


Fig.2.40 Battery-cascaded loop control.

Common DC bus voltage	Rated voltage: $800V$	
	Allowable voltage continuous deviation: $\pm 10\% \leftrightarrow 80\ V$	
	Allowable voltage fluctuation: $\pm 5\% \leftrightarrow 40\ V$	
Lithium-ion Battery	$SOC_{min} = 20\%$ - $SOC_{max} = 90\%$ Initial state of charge: $SOC_{init} = 70\%$	
	$k_{pv_batt} = 3.14 \times 10^{-4}$	$k_{iv_batt} = 0.0628$
	$k_{pc_batt} = 6.2832$	$k_{ic_batt} = 1.25 \times 10^{4}$
(DG)	$P_{DG_min} = 13.75\ KW$ - $P_{DG_max} = 55\ KW$	
	$k_{p_DG} = 8.68$	$k_{i_DG} = 1.82 \times 10^{4}$
Utility-grid	$k_{p_grid} = 9.93$	$k_{i_grid} = 3.12 \times 10^{4}$

Table 2.4 EMS and regulators control parameters.

Next, variable input profiles are applied when simulating the 24-hour DC microgrid model. The applied inputs consisting of variable irradiance (W/m^2), air temperature (°C), wind turbine speed (m/s), and residential load demand (W) 24-hour profiles are represented in Fig.2.41 (a), (b), (c), and (d), respectively. The shown variable profiles are not extracted from a real database and are only adopted to validate the 24-hour DC microgrid model under variable input profiles.

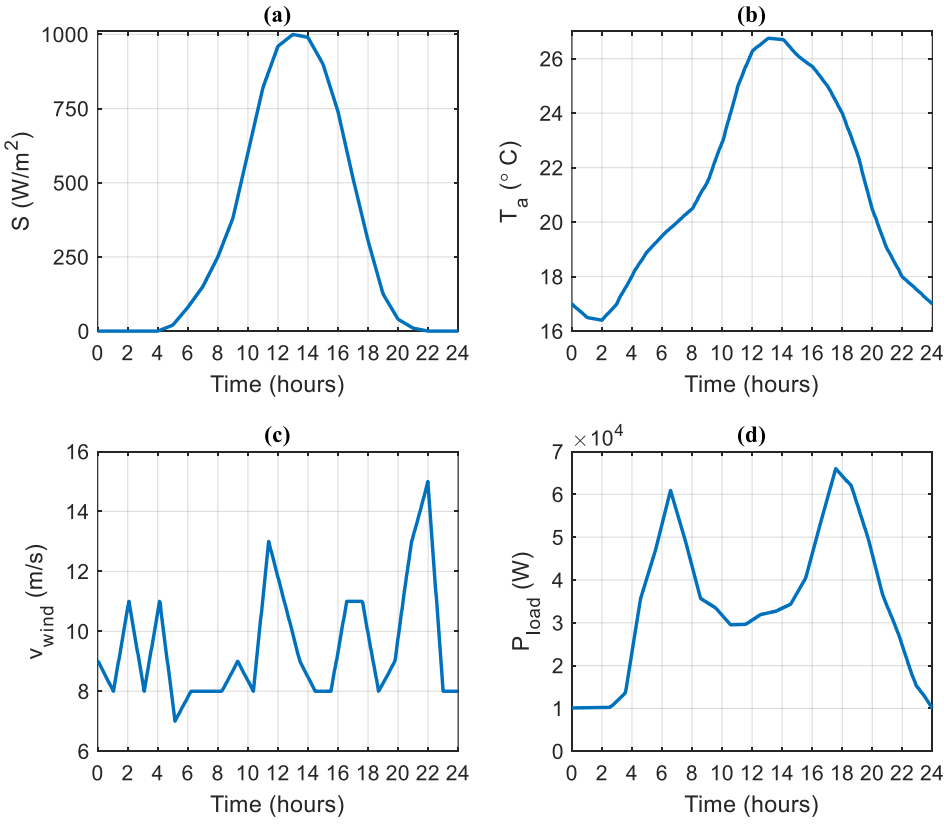


Fig.2.41 Variable Input profiles: (a) Irradiance (W/m^2), (b) Temperature (°C), (c) Wind speed (m/s), and (d) residential load demand (W).

Yet, the shape and dynamics of all profile curves are realistic. For instance, the irradiance profile has a bell shape (Fig.2.41 (a)) with a peak at noon and null values at night. The residential load profile has two peaks corresponding to the surges in load demand in the morning and the evening (Fig.2.41 (d)). Finally, we take note that a real reference location point for the DC microgrid and real discrete profile inputs collected from specific databases are introduced in the next chapter to emulate a real case study.

2.8.3 Simulation tests

Test 1:

To validate the 24-hour DC microgrid model, two simulation tests are conducted. In the first, the 24-hour DC microgrid model is simulated separately with the variable input profiles of Fig.2.41. The simulation results over the 24 hours are shown respectively in Fig.2.42, 2.43, and 2.44. The power flow of all operating units is represented in Fig.2.42. As seen, (RESs) generated power curves have the same form as their input profiles. The PV is operating in MPPT mode and reaches its maximum power generation: P_{PV_max}= 49.4 KW corresponding to $S = 1000\ W/m^2$ value at 12:30 P.M. (light green curve). However, for the WT, the maximum wind power is reached at $V_{wind} = 12\ m/s$ corresponding to ($0.9 \times P_{wind_m_n} = 49.5\ KW$). In turn, the wind turbine pitch controller intervenes when the wind speed exceeds 12.12 m/s to limit the generated power to its allowable maximum rate $P_{wind_m_n} = 55\ KW$. Thus, for higher wind speed values the wind power is limited at $P_{wind_m_n}$ (dashed red cuve). Yet, the power of dispatchable sources is defined following the proposed EMS strategy.

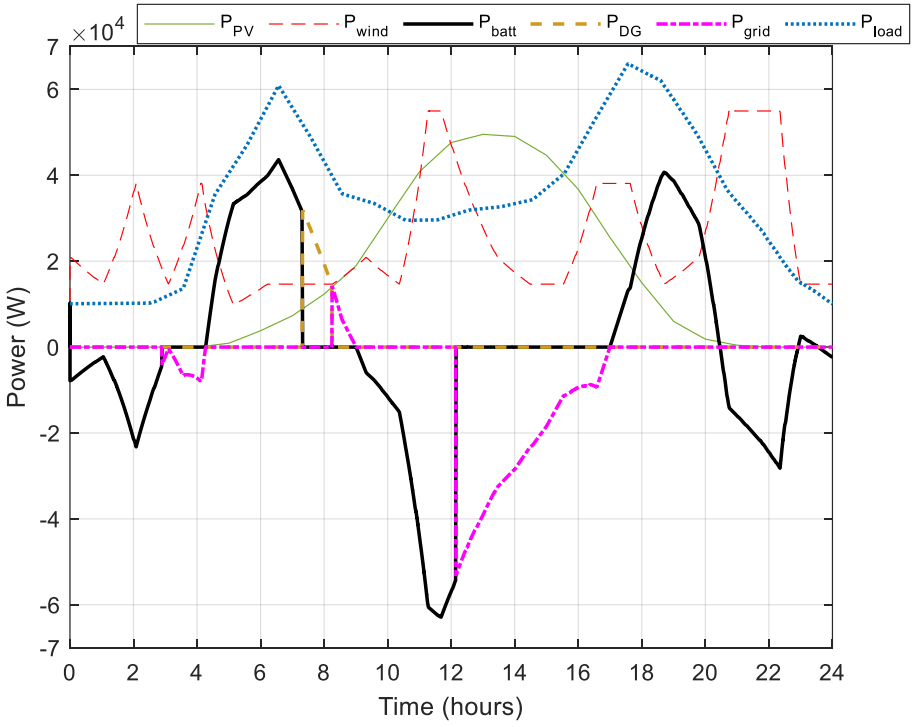


Fig.2.42 Power flow of all operating units of the 24-hour DC microgrid model in (W).

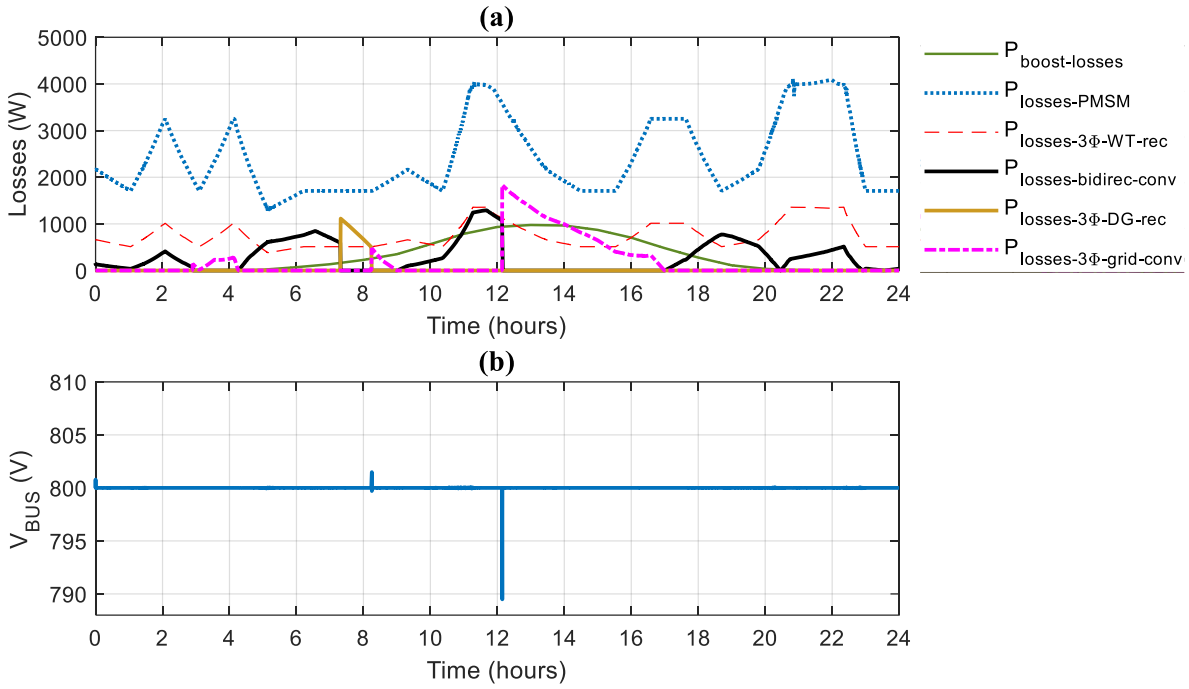


Fig.2.43 (a) Losses in all operating converters in (W) and (b) Common DC bus voltage in (V).

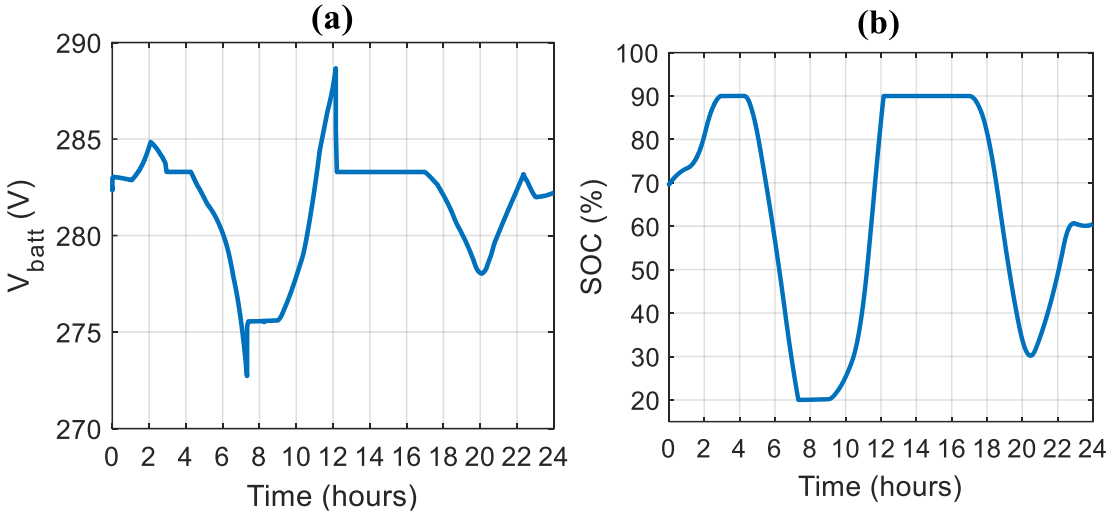


Fig.2.44 (a) Battery's voltage (V) and (b) SOC (%).

The operating modes stated above can be identified in the power flow plot. For instance, the (DG) (dashed gold curve) generates power within its allowable limits when there is a power deficit in the microgrid, and the battery is entirely discharged (operating mode 4: between 7:00 and 8:00 A.M.). The utility grid is connected to the microgrid (long dash-dotted magenta curve) when the battery is entirely discharged, and the power deficit is outside the (DG) allowable boundaries (operating mode 5: between 8:00 and 9:00 A.M.). Besides, the power excess between 12:00 and 5:00 P.M. is sold to the utility grid when the battery is charged totally (operating mode 2). The losses in all operating converters are shown in Fig.2.43 (a). All losses' curves have the same shape

as their corresponding input power as they are proportional. Losses of the WT energy conversion chain are the highest as they include in addition to the converter losses the PMSM losses (dotted blue curve) which are the highest among all converters' losses. The common DC bus voltage is depicted in Fig.2.43 (b), it is stabilized on its referenced value and does not exceed its allowable limits in transient and steady state. Hence, a seamless transition between different operating modes is stated. Finally, Fig.2.44 shows the battery's voltage and state of charge. Battery SOC curve (Fig.2.44 (b)) shows convenient results in terms of modes transition, battery stability, and safe operation. Practically, the battery operates within the predefined admissible SOC boundaries 20% $\leq SOC \leq$ 90%. Furthermore, in Fig.2.44 (a), a maximum variation of 16 V in the battery voltage is noted (between 273 V and 289 V) which highlights the necessity of including the nonlinear zones of the battery voltage in the dynamic model.

Test 2:

In the second simulation test, the accuracy of the 24-hour DC microgrid model is assessed. For that, the detailed DC microgrid model built on Simscape and the 24-hour proposed model are both simulated over 15 minutes. The selection of the simulation time for both models is chiefly restricted by the detailed model which cannot be simulated over 24 hours as stated at the beginning of this chapter. As a solution, the same variable input profiles of test 1 are applied in this test but with a much faster dynamic. A ratio of simulation time reduction equal to 100 is chosen.
By this, the same input profile curves of Fig.2.41 are applied in this test over 864 seconds which accounts for one-hundredth of the 24 hours (i.e., 86400 seconds). Considering the increased dynamic of the system the above-proposed EMS strategy is no longer applicable in this test. Instead, the (DG) and utility grid power references are set equal to the power curves obtained in Fig.2.42 (long dash-dotted magenta and dashed gold curves). However, the battery always stabilizes the common DC bus voltage in this test. As a result, the dynamic of all variables is increased 100 times which constitutes an even worse-case scenario to test the accuracy of the 24-hour model compared to the detailed one.

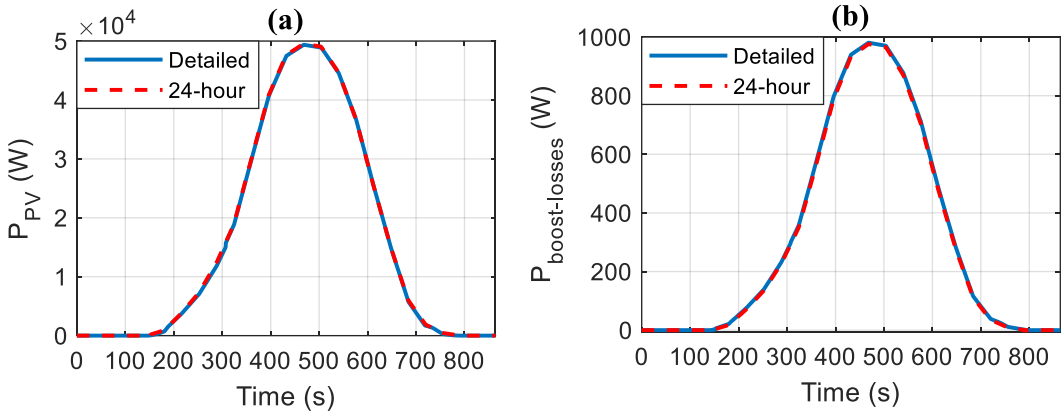


Fig.2.45 Obtained PV (a) power and (b) boost-losses of the detailed and 24-hour models.

The results of each energy source for both models are shown separately. In all figures, the detailed and 24-hour model plots correspond to the blue and dashed-red curves, respectively. The results of the PV energy conversion chain are represented in Fig.2.45. As seen, the power and losses in the boost converter curves are perfectly merged. A maximum error of 5.3 % is noted between the two models at low irradiance values (lower than 320 W/m^2), whereas the error drops to 0.4% at the maximum irradiance value ($S = 1000\ W/m^2$).

Fig.2.46 shows the results of the WT energy conversion chain. The mechanical and electrical power curves are merged for both models. The mechanical power curves are slightly higher than the electrical ones because of the losses in the PMSM. The (dq) axes' current components for both models are the same. The d- component has the same shape as the wind power curve since the MPPT technique is applied on the d-axis, while the q component is always null for both models

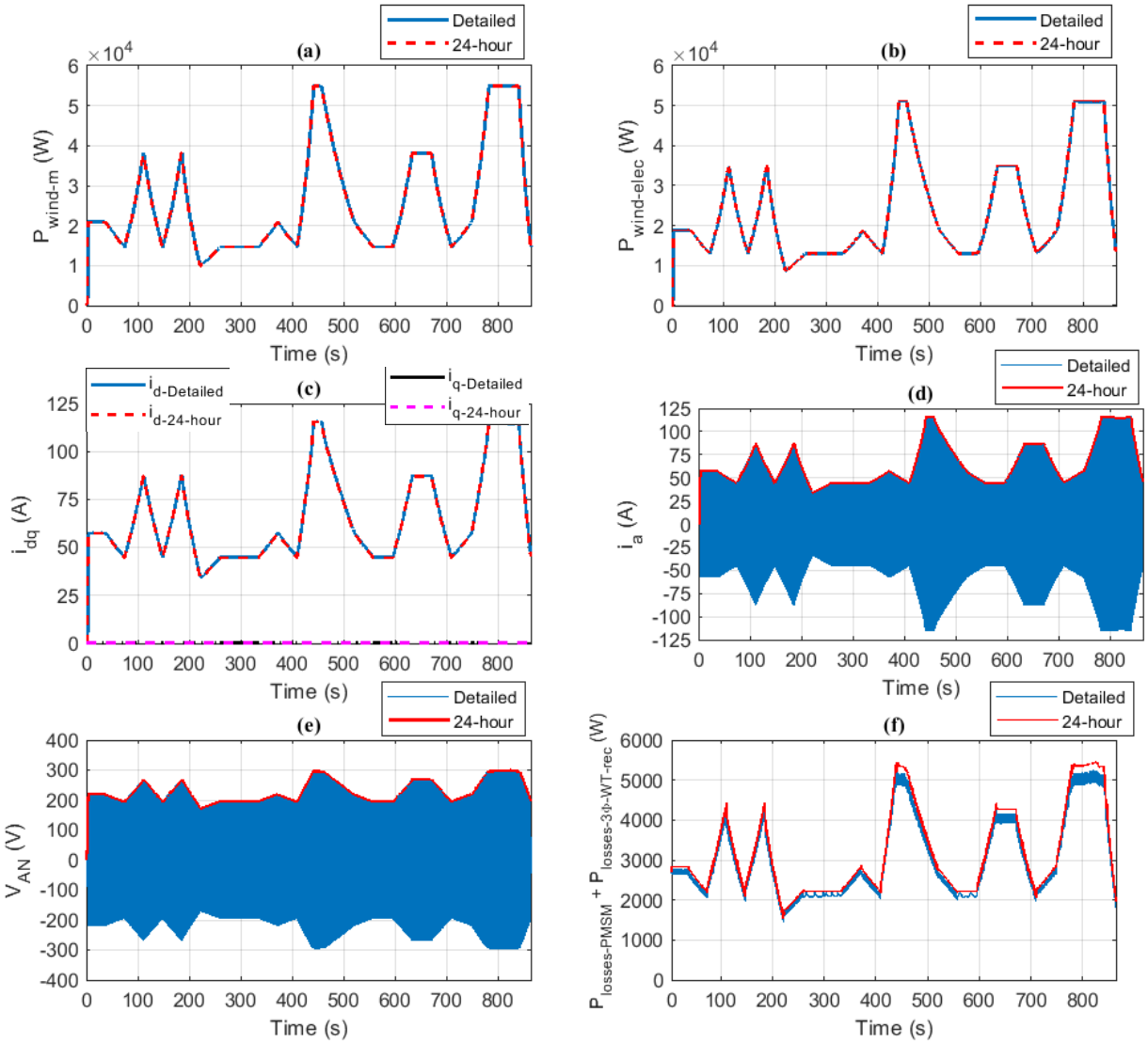


Fig.2.46 WT (a) mechanical power, (b) electrical power, (c) (dq) current components, (d) phase A current, (e) phase A to neutral voltage, and (f) losses in PMSM and 3Φ rectifier of the detailed and 24-hour models.

to absorb zero reactive power. Fig.2.46 (d) and (e) show the phase A current and the phase A to neutral voltage, respectively. As seen, the plotted magnitude of i_a and V_{AN} of the 24-hour model accurately follow the plots of i_a and V_{AN} of the detailed model. Hence, the phasor approach accurately tracks the real magnitudes of the alternating current and voltage in transient and steady states which maintain the precise power computing. Fig.2.46 (f) represents the losses in the PMSM and the 3Φ rectifier. The curves of both models have the same shape with a maximum error of 5.8% at 600 s.

Fig.2.47 shows the results of the (DG) energy conversion chain. The power, (dq) current components, and losses in the 3Φ rectifier for both models are merged which validates the accuracy of the 24-hour model in computing the power in transient and steady states. A maximum error of 1% is noted between P_{DG} curves and 3% between the losses of the two models. The results of the utility grid energy conversion chain are depicted in Fig.4.48. The 24-hour model curves accurately follow the detailed model ones in transient and steady states. Similarly, the (dq) axes' current components curves are merged in the two models. The d- axis current curve has the same shape as the power curve since the grid power reference is set through the d-axis, while the q- axis is null to absorb zero reactive power. Besides, Fig.4.48 (d) and (e) shows how the phasor approach tracks the real current magnitude during the whole simulation.

Fig.2.49 shows the results of the lithium-ion battery which stabilizes the common DC bus voltage. Fig.2.49 (a) shows the power curves of the two models that are merged. The same for the battery voltage curves which are the same in both models.

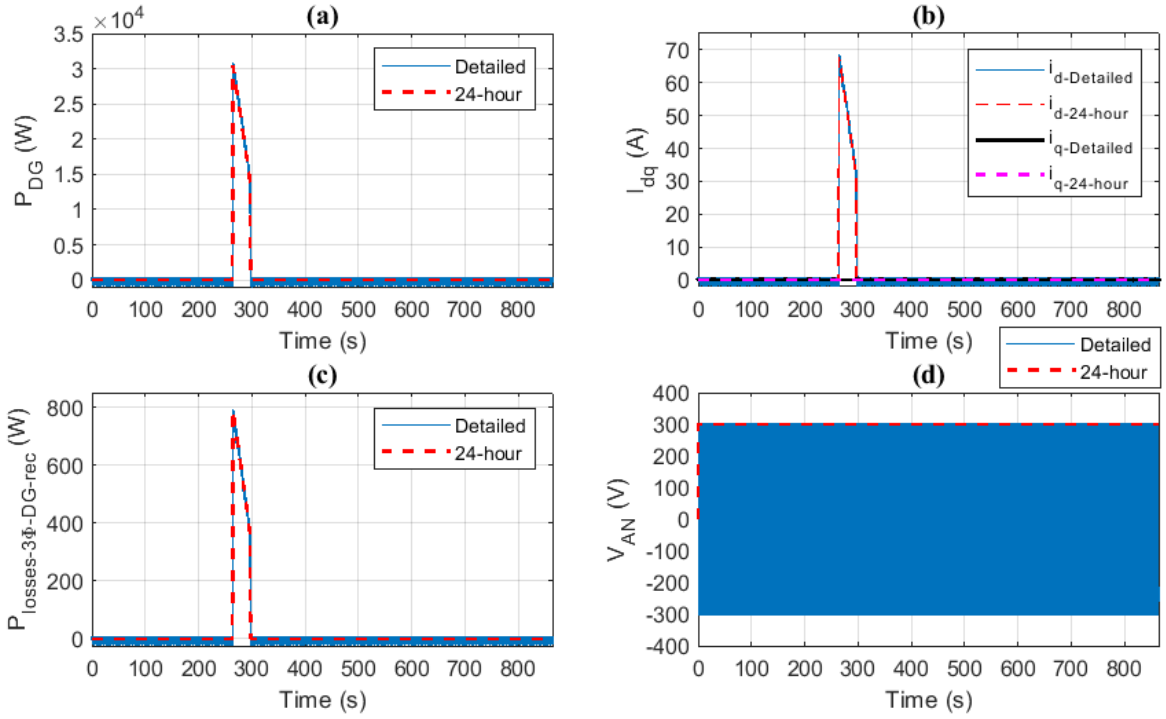


Fig.2.47 DG (a) power, (b) (dq) axes current components, (c) losses in 3Φ rectifier, and (d) phase A to neutral voltage of the detailed and 24-hour models.

Fig.2.49 (c) shows the losses in the bidirectional DC/DC converter which have the same curve shapes in the two models and are proportional to the battery charged/discharged power. The SOC curves of the two models are represented in Fig.2.49 (d) and are the same. A maximum variation of 1% in the battery's SOC is noted as the simulation time is reduced to 864 seconds (SOC varies between 69.2% and 70.2%). Though the limited variation in the battery's SOC, the battery voltage plots in Fig.2.49 (b) show a maximum variation of $5V$ (between 281V and $286V$) which highlights the necessity of including the nonlinear zones of the battery voltage in both models.

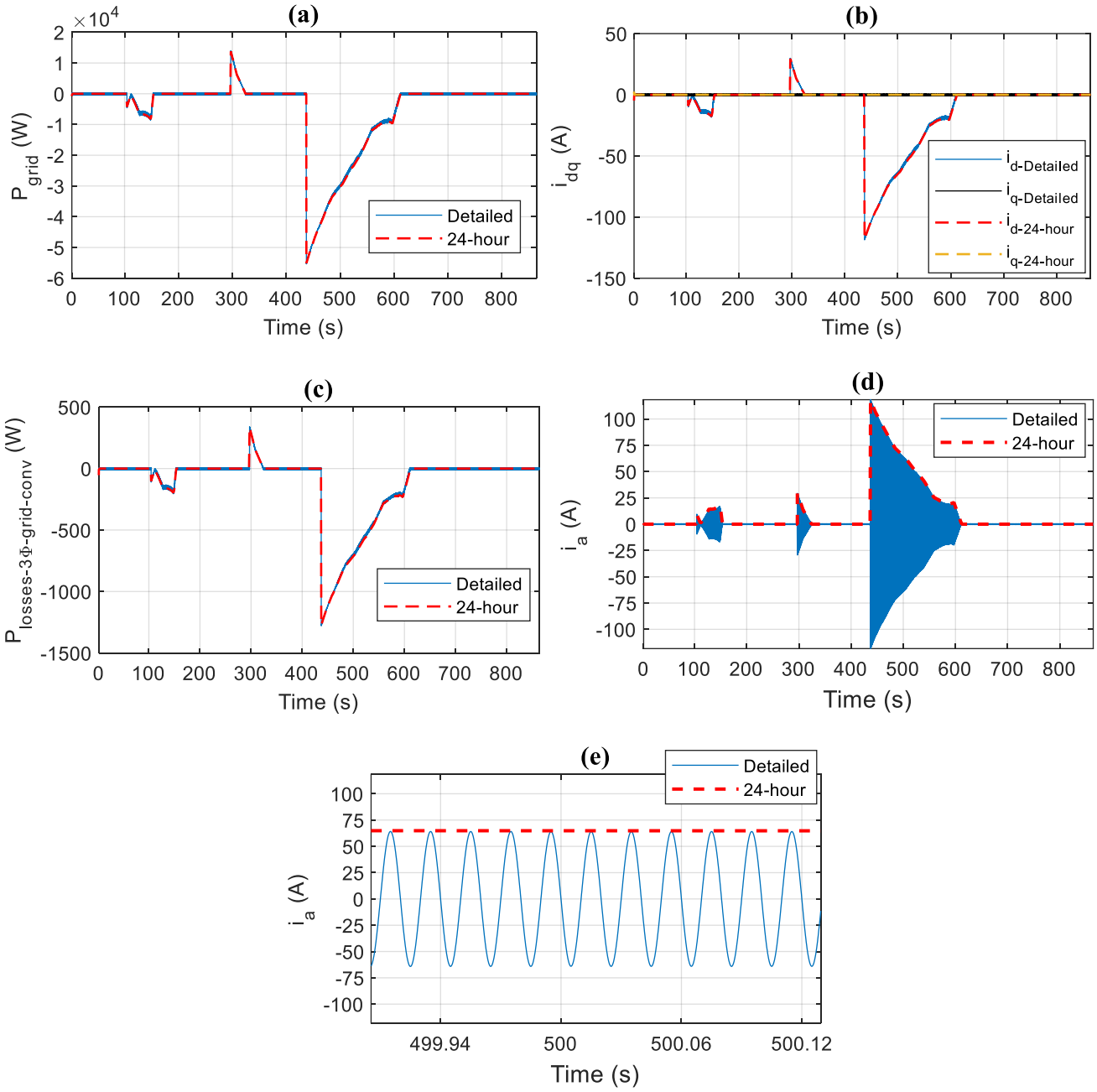


Fig.2.48 Utility grid (a) power, (b) (dq) current components, (c) losses in 3Φ converter, (d) Phase A current, and (e) Zoom on phase A current of the detailed and 24-hour models.

Fig.2.49 (e) represents the common DC bus voltage of the models which are stabilized on their referenced value (800 V) and do not exceed the allowable limits in transient and steady states. The detailed model shows additional fluctuations in V_{BUS} as the switching devices of operating converters exist. Meanwhile, these fluctuations disappear in the 24-hour model as the switching devices are omitted. The cell temperature curves are shown in Fig.2.49 (f), the two curves are merged and present a maximum variation of 1.25 ℃ during the simulation. The cell temperature varies slowly compared to the ambient one as the battery thermal time constant is equal to 1800 s (Appendix D).

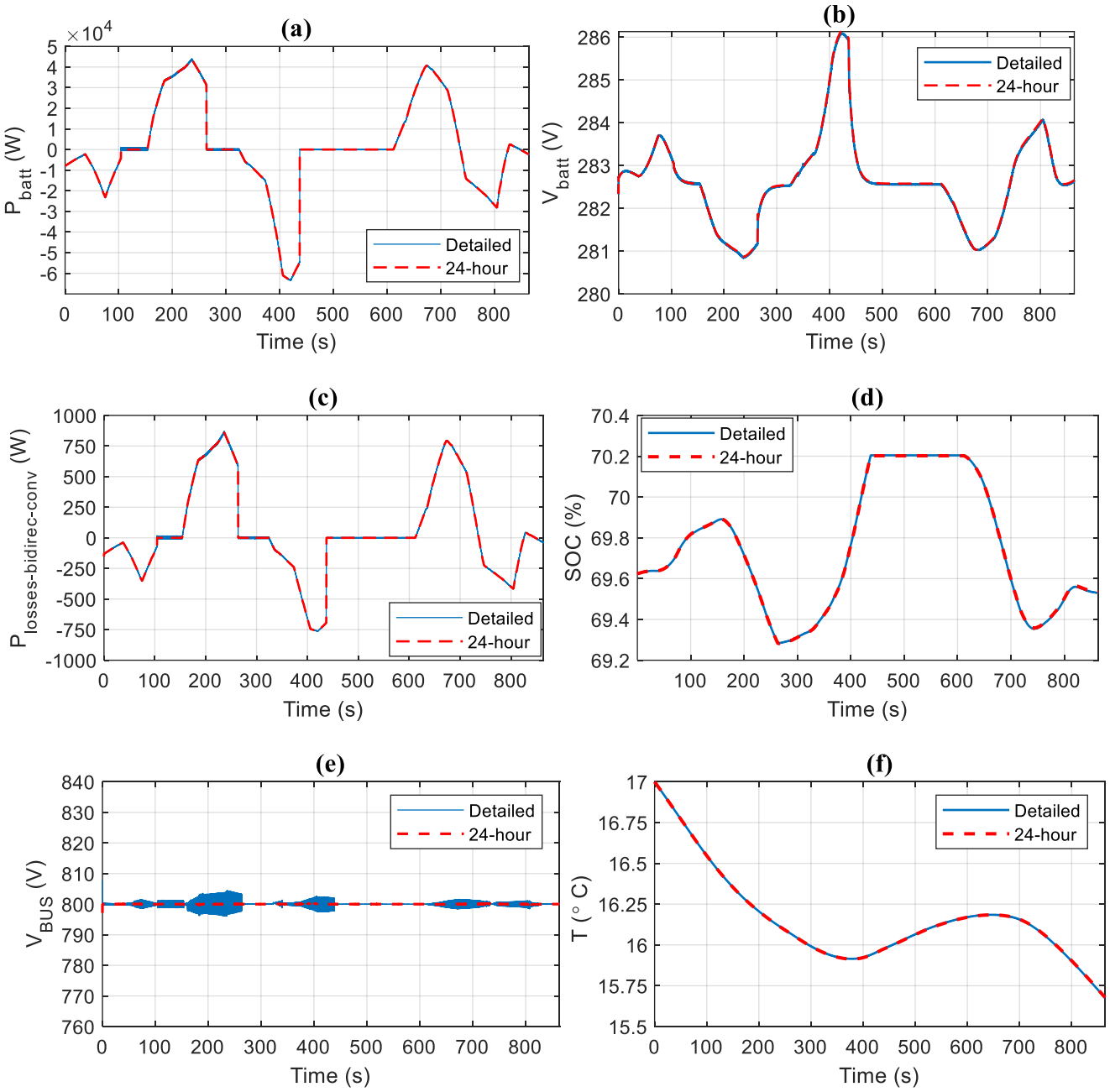


Fig.2.49 Battery (a) power, (b) voltage, (c) losses in the bidirectional DC/DC converter, (d) SOC, (e) common DC bus voltage, and (f) cell temperature of the detailed and 24-hour models.

Finally, we take note that a fixed-step solver is selected to simulate the DC microgrid detailed model with a calculation step size equal to 1 μs, while the 24-hour model is simulated with a variable-step solver with an average step size of 8.3 ms. Hence, the calculation step size is increased 8300 times when moving from the detailed to the 24-hour model which made the modeling of the DC microgrid over 24 hours a viable solution.

2.9 Conclusion

In this chapter, the configuration and sizing of the DC microgrid were presented. The hurdle of 24-hour modeling was confronted as the simulations were conducted on a standard computer with limited CPU performance and memory. To overcome this problem, new averaging techniques were advanced for each operating unit at different energy conversion levels. A trade-off between model precision, complexity, and simulation speed was created. For instance, in all operating units, average converter models were applied in which the switching devices were omitted to increase the calculation step size of the simulation. To prove the viability of the average model, it is compared to the detailed one in terms of accuracy and calculation step size. The obtained results show that increasing the calculation step size highly speeds up the simulation while maintaining accurate voltage and current modeling in transient and steady states.

For all AC operating sources, the phasor domain was proposed to express the electrical sinusoidal components in the complex number domain. To validate the phasor mathematical representation, it is compared to the detailed time domain model in which the real sinusoidal waveforms appear and the switching devices of the 3ϕ rectifier are included. The obtained results show that this representation reduces the complexity of the problem, largely increases the calculation step size of the simulation, and keeps good accuracy as the magnitudes of all electrical components are accurately tracked in the phasor domain.

On the other hand, as the minimization of the converters' losses is one of the predefined optimization goals, the conduction and the switching losses which are the major source of losses in all operating converters were accurately modeled, and the power efficiency curves of all converters were deduced. Besides, a precise model of a lithium-ion battery including the temperature effect was presented. This model represents the nonlinear characteristic of the battery voltage considered constant in most optimization problems which may lead to erroneous power and SOC computed values.

Finally, two simulation tests were conducted to test the viability of the proposed 24-hour model. In the first test, the assembled model is simulated over 24 hours by applying a proposed EMS strategy and variable input profiles. By this, the 24-hour modeling aspect is proven. However, the second test validates the accuracy of the assembled model and compares it to a detailed one over two identical 15-minute simulations. The obtained results show that the 24-hour model maintains accurate modeling and power calculation and ensures a remarkable increase in the calculation step size with a ratio of 8300. The 24-hour DC microgrid model is adopted in the next chapters and a new optimal EMS strategy with optimization goals is advanced.

Chapter 3 : DC Microgrid Offline Optimization

3.1 Introduction

In this chapter, the offline optimization problem is formulated. Real data over 24 hours of electricity pool prices, residential load profile, solar irradiation, ambient temperature, and wind speed are applied to the DC microgrid to simulate a real case scenario study. To test the performance of the DC microgrid under extremely different weather conditions, two different scenarios corresponding to a winter and a summer day are simulated. First, the total cost functions for the two operating days in the absence of an ESS and a (DG) are computed, and then the EMS is applied to the overall DC microgrid including all units. Three distinct objectives of the EMS are set, the first is the minimization of the total operating cost of dispatchable sources comprising the utility grid, the (DG), and the ESS, the reduction of toxic gas emissions produced by the (DG), and the minimization of losses in operating converters of dispatchable sources.

An optimization problem is formulated to attain the objectives which are all included in one unified weighted objective function expressed in $. Three different weight coefficients are assigned to each of the predefined optimization goals. The representation of each optimization goal as three distinct cost functions in $ leads to a unified total energy bill. The first cost function to minimize consists of the operation cost of the overall DC microgrid in $. It includes the (O&M) cost of RESs, (DG), and ESS, and the cost of purchased/sold energy from/to the grid following the pool prices. The second cost function corresponds to the pollutant gas emissions. It is established as a penalty function, in $, proportional to the total pollutant energy produced by the (DG). Similarly, the last cost function of converters' losses is introduced as an additional penalty function, in $, proportional to the total energy loss in converters. By this, the total energy bill consists of the total (O&M) cost of the DC microgrid and two penalty factors related to the emitted toxic gas and losses in operating converters.

Besides, several constraints are defined to emulate a realistic scenario and to guarantee the safe operation of existing units. To solve the optimization problem two different algorithms are applied in this chapter, the first is a step-by-step deterministic technique named Dynamic Programming (DP) and the second is a metaheuristic method named Genetic Algorithm (GA). Based on different mathematical strategies, (DP) and (GA) require different problem shaping to yield viable results. Thus, the mathematical problem structure of each of the applied algorithms is represented in detail.

Two main outcomes are obtained in this chapter, the first is the validity of the proposed algorithms in finding a feasible solution to the EMS-posed problem and the second is the effectiveness of the sole weighted objective function in achieving a multi-objective optimization. To further validate the obtained results, a comparison between both algorithms in terms of convergence speed and ability to find a global minimum solution is conducted at the end of this chapter.

3.2 Inclusion of input data and converters' losses in the DC microgrid configuration

Having set optimization objectives for the DC microgrid over a 24-hour time horizon, real data inputs are collected and applied to emulate a practical scenario and real-case study. For this purpose, the location of the proposed DC microgrid was chosen on a reference point proposed by the WindFinder application. In this case, the reference point is Toulouse-Blagnac Airport (France) for which wind statistics are available throughout the day.

We take note that this site was chosen arbitrarily and exclusively to have real and practical data and does not reflect any theoretical study for a future project. Meteorological data such as the ambient temperature and the wind speed, solar irradiance, electricity pool price, and residential load profiles are applied for two days with extremely different weather conditions. A winter working day on 18/02/2021 and another summer working day on 16/07/2021 are chosen as the two days for the case study. The wind speed data are extracted from the WindFinder application[147]. The electricity pool prices which are the prices established on the electricity market by the stock exchange EPEX on the day (D) for the next day (D+1) are collected from the rte-France site [148]. The residential load profile data are extracted from the ENEDIS open data source[149], which consists of an anticipated dynamic profile of a residential load provided the day (D) for the next day (D+1). Lastly, the irradiance and ambient temperature data are extracted from the Solcast website [150]. All collected data are free to access and are available with different sampling periods.

To obtain a unified data format, a unified sampling period of 10 minutes, denoted T_s, was selected for all input data. The 10-minute sampling period represents a reasonable trade-off that takes into consideration the dynamics of all natural phenomena occurring during the 24-hour simulation study, and the optimization goals. Higher sampling periods won't offer a decent observation of all fast changes in load and/or sources' profiles which leads to unmatched optimization results. Meanwhile, smaller sampling periods may be impractical and irrelevant taking into consideration the slow dynamics of natural phenomena such as the variations of wind speed, temperature, and irradiation [151]. Besides, as the fixed management goals don't target fast disturbances or instantaneous faults that may occur in the system, the selection of a smaller sampling period appears inappropriate.

Hence, the sampled data inputs, and the losses in operating converters can be added to the initial DC microgrid configuration represented in Chapter 2, Fig.2.1. The final configuration is depicted in Fig.3.1 in which the 24-hour profiles of the sampled inputs are shown. v_{wind} , S, T_a , P_{load} , and δ_{grid}^{pur} are respectively the wind speed in (m/s), the irradiance in (W/m^2), the ambient temperature in $(°C)$, the residential load profile in (W), and the electricity purchase price in $(¢/KWh)$ for the whole time horizon (i.e. 24 hours). Therefore, the inputs of the optimization problem can be

regrouped in a unique matrix denoted M_{in_opt} : $M_{in_opt} = [v_{wind} \quad S \quad T_a \quad P_{load} \quad \delta_{grid}^{pur}]$, where M_{in_opt} is a $(5 \times N)$ matrix.

N is the number of total steps for the whole-time horizon and is computed as follows:

$$N = \frac{Time\ horizon\ (in\ \ hours)}{T_s\ \ (in\ hours)} = 24 \times 6 = 144 \tag{III.1}$$

Hence, the size of M_{in_opt} is (5×144).

The degree of freedom in the system, in other words, the decision variables of the optimization problem are defined based on the number of units that can be controlled. In this case, as the RESs are continuously operating in MPPT mode and the load profile is imposed by the consumers, they both cannot be considered as decision variables and serve as inputs to the optimization problem. However, the remaining units that can be controlled through the optimization process are the ESS, the DG, and the utility grid. Then, the fixed decision variables of the optimization problem are: P_{batt}, P_{DG}, and P_{grid}, and the output references can be regrouped in a unique matrix denoted M_{out_opt}, $M_{out_opt} = [P_{batt_ref} \quad P_{DG_ref} \quad P_{grid_ref}]$. As M_{out_opt} includes all the optimal reference outputs for the whole-time horizon, it has a size of (3×144). We take note that the offline optimization is carried out a day before the day targeted by the study. Knowing that all the optimal output references are based on predicted data, an online optimization process is followed the next day to adapt the optimal power references in case of any mismatches between predicted and actual data (see Fig.3.1).

3.2.1 Losses inclusion

As seen in Fig.3.1, the losses in converters are considered by adding the subscript "bus" to the initially generated/consumed power. By this, the bellow expressions are retrieved:

$$\begin{cases} P_{PV} = P_{PV_bus} + P_{boost_looses} \\ P_{wind} = P_{wind_bus} + P_{losses_3\phi_WT_rec} + P_{losses_PMSM} \\ P_{grid} = P_{grid_bus} + P_{losses_3\phi_grid_conv} \\ P_{DG} = P_{DG_bus} + P_{losses_3\phi_DG_rec} \\ P_{batt} = P_{batt_bus} + P_{losses_bidirec_conv} \end{cases} \tag{III.2}$$

Where,

- P_{boost_looses} are the losses in the DC/DC boost of the PV, in (W).
- $P_{losses_3\phi_WT_rec}$ and P_{losses_PMSM} are respectively the losses in the 3ϕ rectifier and the PMSM of the (WT), in (W).
- $P_{losses_3\phi_grid_conv}$ are the losses in the 3ϕ grid converter, in (W).
- $P_{losses_3\phi_DG_rec}$ are the losses in the 3ϕ (DG) rectifier, in (W).
- $P_{losses_bidirec_conv}$ are the losses in the bidirectional DC/DC converter of the battery, in (W).

All converters' losses are computed based on the expressions detailed in Chapter 2. Besides, as previously mentioned in Chapter 2, the load and its corresponding converter are regarded as a single entity. Thus, the overall load is simply modeled by the load profile, and so the losses in its converter are not considered in this study.

We take note that the power loss expressions of all converters are always positive. Particular attention should be given to the 3ϕ grid converter and the battery's bidirectional DC/DC converter as they are bidirectional converters.

For the battery, in charge and discharge modes, $P_{losses_bidirec_conv}$ is always positive and computed based on equation (III.1):

- In discharge mode ($P_{batt} > 0$ & $P_{batt_bus} > 0$) : $P_{batt_bus} = P_{batt} - P_{losses_bidirec_conv}$ then, $P_{batt_bus} < P_{batt}$. This implies that only a part of the battery's total discharged power reaches the common DC bus, and the rest is dissipated in the converter functioning in boost mode.

- In charge mode ($P_{batt} < 0$ & $P_{batt_bus} < 0$) : $P_{batt_bus} = P_{batt} - P_{losses_bidirec_conv}$ then, $|P_{batt_bus}| > |P_{batt}|$. This implies that only a part of the battery's power on the common DC bus side reaches the battery to charge it and the rest is dissipated in the converter functioning in buck mode.

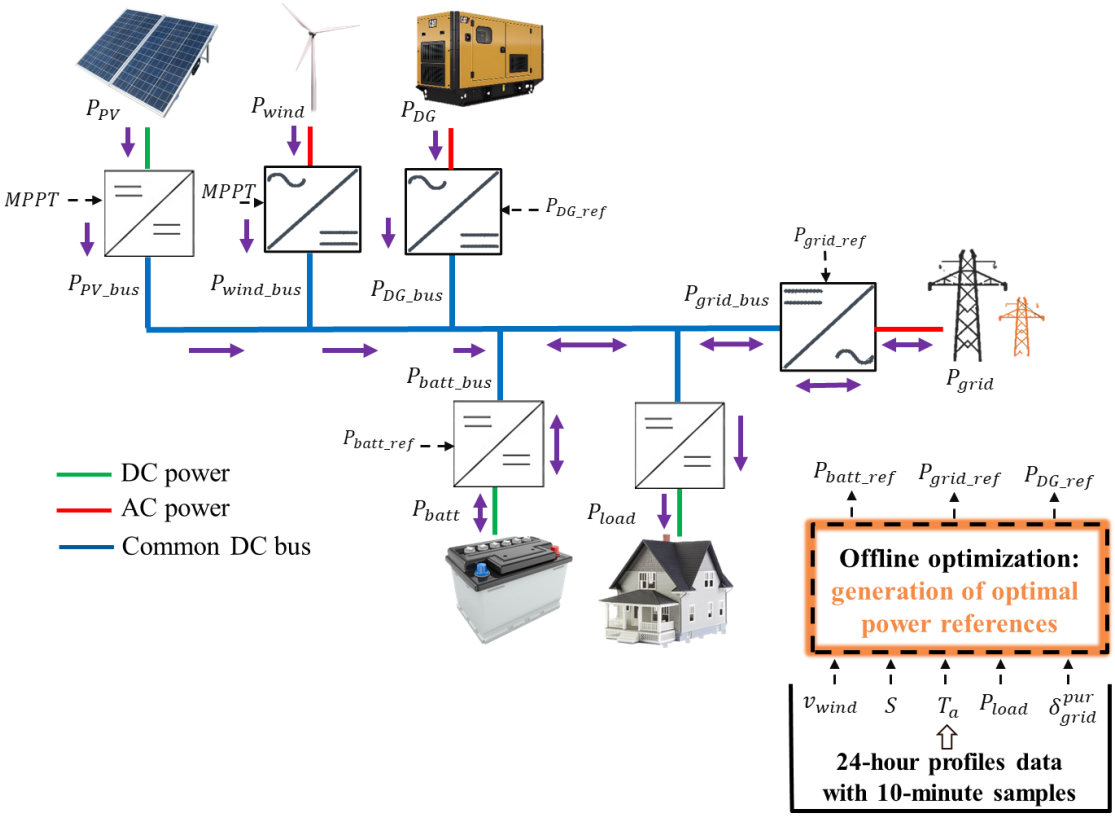
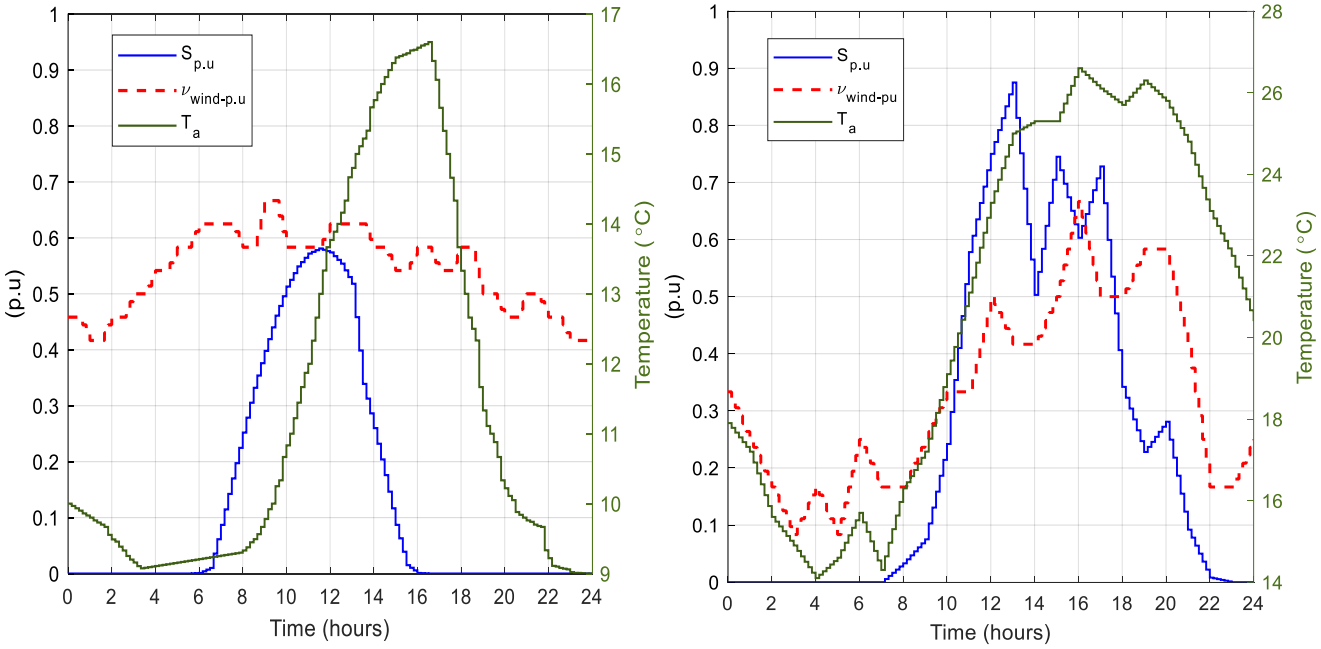


Fig.3.1 DC microgrid configuration.

The same strategy is applied to the 3ϕ grid converter. $P_{losses_3\phi_grid_conv}$ is always positive in both rectifier and inverter operating modes. P_{grid} and P_{grid_bus} are positive when the power is purchased from the utility grid and then, the converter operates in rectifier mode. P_{grid} and P_{grid_bus} are negative when the power is sold to the utility grid and then, the converter operates in inverter mode.

3.2.2 Winter and summer days scenario

The input data for the two days case study are represented in this paragraph. Fig.3.2(a) and (b) show the wind speed, v_{wind_pu} (red dashed curve), in $(p.u)$ of the wind base speed ($v_{wind_base} = 12\ m/s$), the solar irradiance, $S_{p.u}$ (blue solid curve), in $(p.u)$ of the reference irradiance at (STC) ($S_{ref} = 1000\ W/m^2$), and the ambient temperature, T_a (green solid curve), in (°C) for the winter and summer days. The winter day is represented in Fig.3.2 (a) (the left plot) and the summer day in Fig.3.2 (b) (the right plot). The PV and wind-generated power profiles on the winter and the summer days are respectively represented in Fig.3. 3 (a) and (b). PV and wind power are represented respectively in red solid and green dash-dotted lines. P_{PV_bus}, plotted in black-dashed line, corresponds to the losses in the DC/DC boost subtracted from the P_{PV}. P_{wind_bus}, plotted in purple solid line, corresponds to the sum of the losses in the PMSM and the 3ϕ rectifier subtsracted from P_{wind}. As seen in Fig.3.3 (a) and (b) the (WT) operates at low efficiency as low wind speed profiles are recorded on the two days of the case study (fig.3.2 (a) and (b)).



(a) (b)

Fig.3.2 (a) Wind speed, irradiance, and temperature profiles of the winter day (18/02/2021), (b) of the summer day (16/07/2021).

However, the efficiency of the DC/DC boost of the PV system is higher than the AC rectifier, this results in closer curves of P_{PV} and P_{PV_bus} (dashed black and solid red lines) in both winter and summer days. Almost 97% boost efficiency is recorded at peak hours production in the two operating days. Fig.3.4 shows the electricity pool price, the residential load, and the total net RESs generated power profiles on the winter day (Fig.3.4 (a)) and the summer day (Fig.3.4 (b)).

The residential load profile in the black solid line has two peaks, the first in the morning and the second in the evening which genuinely represents the residential consumption pace on winter and summer working weekdays. By referring to Fig.3.4 (b), the summer load profile curve is slightly shifted to the right as the day hours increase during the summer, and the sun sets later which keeps people active for late hours. The RES production is plotted in a red dashed line in Fig.3.4 (a) and (b), the losses in converters and PMSM for the (WT) are then taken into consideration in the plots. Finally, the electricity pool price is plotted in a green solid line and has a similar curve shape as that of the residential load profile. This can be simply justified by the fact that an increase in electricity demand leads to a surge in its price in the market. Unlike the electricity purchase price, denoted δ_{grid}^{pur}, which varies following the plots of Fig.3.4 (a) and (b), the electricity sell price is considered constant for the two operating days and equal to ($\delta_{grid}^{sold} = 6.8\ ¢/KWh$).

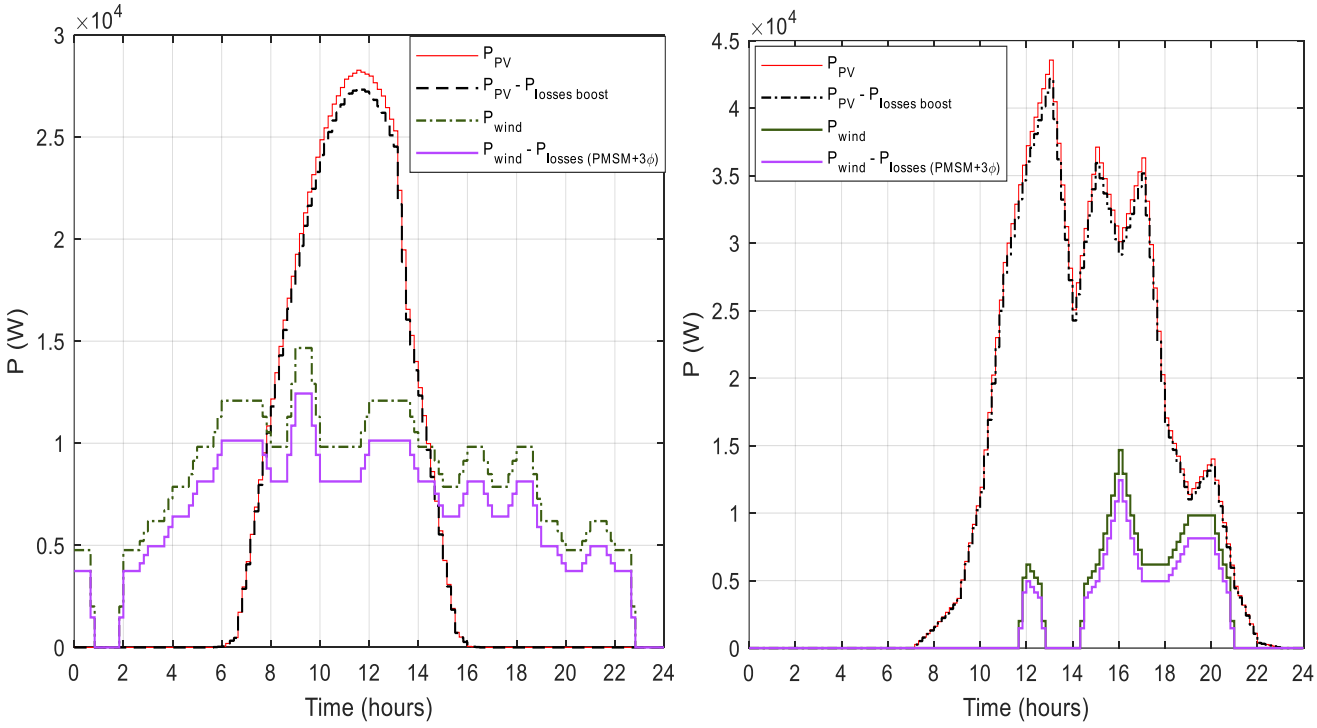


Fig.3.3 (a) The PV and wind-generated power on the winter day (18/02/2021), (b) on the summer day (16/07/2021).

3.3 The total cost function in the absence of the ESS and the DG

In this paragraph, the total cost function of the two tested days is evaluated without applying any optimization strategy and in the absence of the ESS and the (DG). In such a scenario, only two operating states are identified:

1. $P_{load} > P_{PV_bus} + P_{wind_bus}$: in this case, the load demand exceeds the RESs generated power then, the remaining unmet load power is purchased from the utility grid and P_{grid} equals $P_{load} - P_{PV_bus} - P_{wind_bus} + P_{losses_3\phi_grid_conv} > 0$.
2. $P_{load} < P_{PV_bus} + P_{wind_bus}$, in this case, the produced power from the RESs exceeds the load demand. The surplus of power is sold to the utility grid and P_{grid} equals $P_{load} - P_{PV_{bus}} - P_{wind_{bus}} + P_{losses_3\phi_grid_conv} < 0$.

As all inputs are discretized with a sampling period T_s, the total cost function corresponds to the discrete sum of the cost computed at each sampling time, k, over the whole time horizon. The total cost function over the 24-hour time horizon, denoted J_{tot}, can be expressed in $ as follows:

$$J_{tot} = J_{oc} \tag{III.3}$$

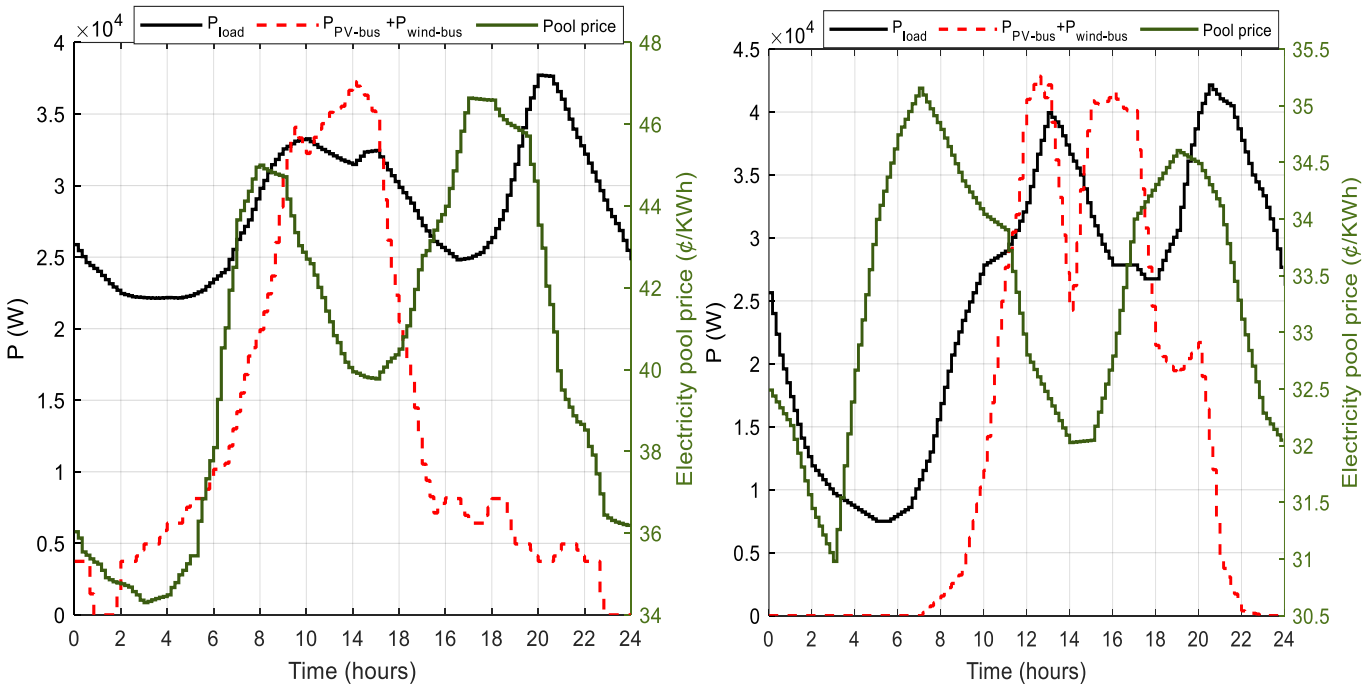


Fig.3.4 (a) The residential load, the RESs power profiles, and the electricity pool price on the winter day (18/02/2021), (b) on the summer day (16/07/2021).

Where, J_{oc} is the operating cost function over the 24-hour time horizon. J_{oc} is expressed in \$ as follows:

$$J_{oc} = J_{RESs} + J_{grid} \tag{III.4}$$

Where, J_{RESs} and J_{grid} are respectively the RESs and the utility grid cost functions. J_{RESs} is computed in \$ and expressed as follows:

$$J_{RESs} = J_{PV}^{O\&M} + J_{WT}^{O\&M} \tag{III.5}$$

Where, $J_{PV}^{O\&M}$ and $J_{WT}^{O\&M}$ are respectively the operation and maintenance cost (O&M) costs of the PV and the WT in \$. $J_{PV}^{O\&M}$ and $J_{WT}^{O\&M}$ are calculated as follows:

$$J_{PV}^{O\&M} = \sum_{k=0}^{N-1} \delta_{PV}^{O\&M} . P_{PV}(k) . T_s \tag{III.6}$$

$$J_{WT}^{O\&M} = \sum_{k=0}^{N-1} \delta_{WT}^{O\&M} . P_{WT}(k) . T_s \tag{III.7}$$

where $\delta_{PV}^{O\&M}$ and $\delta_{WT}^{O\&M}$ are respectively the (O&M) costs per KWh of the PV, and the WT ($\delta_{PV}^{O\&M} = 0.0024\ \$/KWh$, and $\delta_{WT}^{O\&M} = 0.0098\ \$/KWh$).

The utility grid cost function can be expressed as the difference between the purchased energy from the utility grid and the sold energy to the utility grid over the 24-hour time horizon.

$$J_{grid} = \sum_{k=0}^{N-1} \left(\delta_{grid}^{pur} . P_{pur}(k) - \delta_{grid}^{sold} . P_{sold}(k) \right) . T_s \tag{III.8}$$

$P_{pur}(k)$ and $P_{sold}(k)$ are respectively the purchased electricity power at time k, and the sold electricity power at time k. $P_{pur}(k)$ and $P_{sold}(k)$ are expressed as functions of the grid power $P_{grid}(k)$ at time k as follows:

$$P_{pur}(k) = P_{grid}(k) . \max(\text{sign}(P_{grid}(k)),0) \tag{III.9}$$

$$P_{sold}(k) = P_{grid}(k) . \min(\text{sign}(P_{grid}(k)),0) \tag{III.10}$$

The functions max, min, and sign are introduced in equations III.9 and III.10 to impose a unidirectionality constraint of $P_{grid}(k)$. In other terms, the utility grid power cannot be purchased and sold at the same time k.

When $P_{grid}(k)$ is positive $P_{pur}(k)$ is equal to $P_{grid}(k)$ and $P_{sold}(k)$ is null whereas, $P_{pur}(k)$ is set to zero and $P_{sold}(k)$ is equal to $-P_{grid}(k)$ when $P_{grid}(k)$ is negative.

The obtained results for the two operating days are summarized in Table 3.1 As seen the summer day has a lower total cost function compared to the winter day. As the produced solar energy increases during the summer, this results in a minor reliance on the utility grid to cover the load demand and then limited purchased energy from the utility grid (summer day: $J_{grid} = 116.67\ \$ <$ winter day:$J_{grid} = 179\ \$$). The RESs cost function is slightly higher on the winter day as it is predominantly affected by the wind turbine-produced energy (equations III.6 and III.7) which is higher on the winter day ($E_{wind} = 190.55\ KWh$ in winter versus $E_{wind} = 58.32\ KWh$ in summer). These results are obtained in the absence of the lithium-ion battery and the (DG).

Winter day (18/02/2021)	Summer day (16/07/2021)
$J_{grid} = 179\ \$$	$J_{grid} = 116.67\ \$$
$J_{RESs} = 2.25\ \$$	$J_{RESs} = 1.3\ \$$
$J_{tot} = 181.25\ \$$	$J_{tot} = 118\ \$$

Table 3.1 Cost functions for the two operating days in the absence of ESS and (DG).

3.4 Optimization objectives, cost function, and constraints

The applied microgrid configuration is that of Fig.3.1 in which all operating units are managed optimally to feed the load while maintaining a stable voltage of the common DC bus. This is considered a primary goal of the EMS that should be accomplished consistently. However, on a higher management level, the coexistence of multi-sources and ESS in one DC microgrid offers a high degree of freedom on how the load power can be shared between operating sources. To ensure a smart EMS, an optimization problem is formulated with predefined objectives, cost function, and constraints and solved using deterministic or metaheuristic algorithms. Referring to the literature and the research work on multi-objective optimization of microgrids such as in [86], [87], [90], and following the actual international energy policies, three objectives are set :

1. The minimization of the total operating cost of the DC microgrid. By setting this objective, several outcomes are derived, mainly the minimization of the electricity bill, the enhancement of energy self-sufficiency of the DC microgrid, and the reduction of the O&M costs of the ESS and the DG.
2. The reduction of pollutant gas emissions. This objective exclusively targets the (DG) as a unique traditional pollutant source in the DC microgrid producing toxic gases that are the main cause of air pollution and greenhouse gases.
3. The minimization of converters' losses. This optimization objective is rarely addressed in the literature as the detailed modeling of losses in converters requires direct access to its current and voltage components as seen in Chapter 2. Knowing that the current and voltage variables are sited in the primary and secondary control levels, unlike most optimization variables that are located at higher management levels, the losses are usually considered constant or neglected. Contrarily, the losses in the lithium-ion battery, the utility grid, and

the (DG) converters are accurately computed, included in the optimization problem, and minimized.

Once the optimization objectives are set, the optimization problem is formulated. There are several ways to formulate the optimization problem, one is to assign independent objective functions for each of the predefined optimization goals such as in [78], [152], and minimize them by finding Pareto sets. Another simple way is to scalarize the set of objectives into a single objective function by multiplying each objective by a fixed weight. This method is known as the weighted sum method and is widely used in the literature [83], [98]. Besides the reduction of the complexity of the problem, it offers the user the possibility of objectives' preference through the selected weights. Therefore, the total cost function denoted J_{tot}, expressed in equation (III.3), can now be computed in $ as the sum of the weighted cost functions of the operating cost, the pollutant gas emissions, and the converters' losses. This yields the following expression:

$$J_{tot} = \zeta_{oc}J_{oc} + \zeta_{emissions}J_{emissions} + \zeta_{conv_losses}J_{conv_losses} \quad \text{(III.11)}$$

Where, $J_{tot}, J_{oc}, J_{emissions}, J_{conv_losses}, \zeta_{oc}, \zeta_{emissions},$ and ζ_{conv_losses} are respectively the total cost function in $, the operation cost function in $, the pollutant gas emissions cost function in $, the converters losses cost function in $, the operation cost weight, the pollutant gas emissions weigh, and the converters losses weight.

3.4.1 Operating cost function

The operating cost function is the sum of the (RES)s cost function, the power grid cost function, the battery storage cost function, and the diesel generator cost function. Hence, two terms related to the battery and the DG are added to equation III.4 which becomes:

$$J_{oc} = J_{RESs} + J_{grid} + J_{batt} + J_{DG} \quad \text{(III.12)}$$

Where, J_{batt} , J_{DG} are respectively the battery and the DG cost functions. J_{RESs} and J_{grid} expressions are the ones of equations (III.5 till III.10) detailed above.

3.4.1.1 Battery cost function

The battery lifetime is represented as the number of charge and discharge cycles. Hence, to quantify the storage operating cost, one way is to divide the battery capital cost per KWh over the number of cycles to obtain the battery operating cost per cycle. In addition, the battery degradation issue is added to the operating cost function [100]. J_{batt} is expressed as follows:

$$J_{batt} = \sum_{k=0}^{N-1} \left(\frac{CC}{2.Cycles} . P_{batt}(k).T_s + \delta_{deg}.P_{batt}^2(k).T_s \right) \quad \text{(III.13)}$$

where $CC, Cycles, P_{batt}(k), \delta_{deg}$ are respectively the battery capital cost per KWh (CC=135.38 $/$KWh$), number of life cycles ($Cycles$=1000 for a depth of discharge DoD =80%), the battery power at time k, and the degradation cost (δ_{deg}=10^{-9} $/$W^2h$).

3.4.1.2 Diesel generator cost function

The (DG) total cost function J_{DG} consists of the fuel consumption cost function J_{DG}^{fuel}, the start-up cost function J_{DG}^{SU}, and the maintenance cost function J_{DG}^{M}. It can be expressed as follows:

$$J_{DG} = J_{DG}^{fuel} + J_{DG}^{SU} + J_{DG}^{M} \quad \text{(III.14)}$$

A piecewise approximation of the fuel consumption, proposed in[96], is applied. The piecewise linearized fuel consumption function is shown in Fig.3.5. For more details on the approximation method, it can be referred to[96]. Thus, the fuel consumption cost can be expressed as:

$$J_{DG}^{fuel} = \sum_{k=0}^{N-1} \lambda_{fuel}.F(k).T_s \quad \text{(III.15)}$$

where λ_{fuel}, $F(k)$ are respectively the price of diesel per liter ($\lambda_{fuel} = 1.05\ \$/L$), and the fuel consumption in L/h. Knowing $P_{DG}(k)$, $F(k)$ is determined based on the plotted curve in Fig.3.5. The constant parameters are defined in Table 3.2 The start-up cost function J_{DG}^{SU} corresponds to the fuel consumed during the start-up phase before any power production. The start-up cost is the cost per start-up ($\xi_{SU} = 0.011\ \$$) times the number of start-ups over the time horizon. This can be calculated as:

$$J_{DG}^{SU} = \xi_{SU}.\sum_{k=0}^{N-1} \sigma_{DG}^{ON}(k) \quad \text{(III.16)}$$

Where, $\sigma_{DG}^{ON}(k)$ is a binary variable that equals one if the (DG) is turned on at time k and zero otherwise. $\sigma_{DG}^{ON}(k)$ is defined as:

$$\sigma_{DG}^{ON}(k) = \max\left(\text{sign}(P_{DG}(k+1)) - \text{sign}(P_{DG}(k)), 0\right) \quad \text{(III.17)}$$

Finally, the maintenance cost depends on the operation time of the (DG). It can be calculated as the maintenance cost per hour ($\chi_M = 0.03\ \$/h$) times the total operating hours of the (DG):

$$J_{DG}^{M} = \chi_M.\sum_{k=0}^{N-1} \text{sign}(P_{DG}(k)).T_s \quad \text{(III.18)}$$

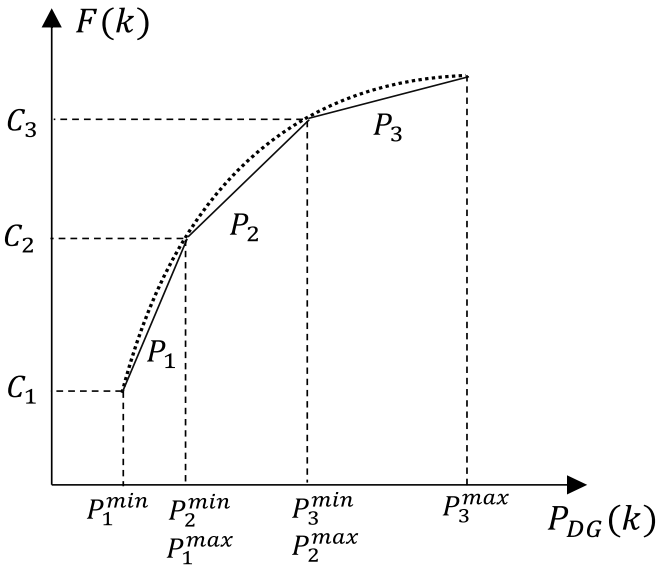


Fig.3.5 Piecewise approximation of the (DG) fuel consumption function.

3.4.2 Pollutant gas emissions cost function

Fossil fuel consumption produces toxic gases such NO_x, CO_2, CO, and SO_2. These gas emissions are the main source of air pollution and greenhouse gases. The pollution aspect can be considered by introducing the quantity of emitted toxic gases in a (DG) application, (α) expressed in (g/KWh), and the expenses related to environmental damages resulting from the pollutant gas emissions, (μ) expressed in $(\$/Kg)$[73]. All parameters' values are listed in Table 3.2. Thereby, the pollutant gas emissions cost function can be represented as:

$$\begin{cases} J_{emissions} = \beta_{emiss} \cdot \sum_{k=0}^{N-1} P_{DG}(k).T_s \\ \beta_{emiss} = 10^{-3}\left(\alpha_{NO_x}.\mu_{NO_x} + \alpha_{CO_2}.\mu_{CO_2} + \alpha_{CO}.\mu_{CO} + \alpha_{SO_2}.\mu_{SO_2}\right) \end{cases} \quad \text{(III.19)}$$

3.4.3 Converters' losses cost function

Penalty coefficients for the battery, (DG), and utility grid converters' losses are introduced and expressed in $(\$/KWh)$. The converters' losses cost function can be expressed as follows:

$$J_{conv_losses} = \sum_{k=0}^{N-1} \left(\delta_{batt}^{loss}.P_{losses_bidirec_conv}(k) + \delta_{DG}^{loss}.P_{losses_3\phi_DG_rec}(k) + \delta_{grid}^{loss}.P_{losses_3\phi_grid_conv}(k) \right).T_s \quad \text{(III.20)}$$

Where, δ_{batt}^{loss}, δ_{DG}^{loss}, and δ_{grid}^{loss} are respectively the penalty coefficients for converters' losses of the battery, the (DG), and the utility grid. As seen, the losses in the DC/DC boost of the PV, and the 3ϕ rectifier of the (WT) aren't included in equation (III.20) and so, cannot be minimized. Since the PV and (WT) are non-dispatchable sources and continuously operate in MPPT mode, their generated power is imposed by the MPPT and so are the resulting converters' losses. As a result, the losses in the DC/DC boost of the PV and the 3ϕ rectifier of the (WT) can only be included to obtain an accurate model but cannot be controlled. The penalty coefficients for converters' losses are found in Table 3.2.

3.4.4 Problem constraints

In any applied EMS, the optimal solution is usually subject to several constraints such as lower and upper bounds of the decision variables, equality, and inequality equations, etc. In this study, several constraints are imposed to emulate a realistic and practical microgrid scenario. In this paragraph, all the constraints of each microgrid unit are detailed separately.

3.4.4.1 Power balance constraint

To maintain a stable DC microgrid performance, the load demand should be covered unceasingly by existing sources for the whole operating time horizon. Adding this constraint, the stabilization of the common DC bus voltage is automatically secured. Thus, at each sampling time k, the generated power should be equal to the demanded one. This is known as the power balance equation which can be expressed as:

$$P_{PV}(k) + P_{wind}(k) + P_{batt}(k) + P_{grid}(k) + P_{DG}(k) = P_{load}(k) + \sum P_{conv_losses}(k) \quad \text{(III.21)}$$

With,

$$\sum P_{conv_losses}(k) = P_{boost_losses}(k) + P_{losses_3\phi_WT_rec}(k) + P_{losses_PMSM}(k) + P_{losses_bidirec_conv} + P_{losses_3\phi_grid_conv}(k) + P_{losses_3\phi_DG_conv}(k) \quad \text{(III.22)}$$

3.4.4.2 Utility grid constraints

Lower and upper bounds are fixed to limit the purchased/sold power from/to the utility grid. This can be represented as:

$$P_{grid_min} \leq P_{grid}(k) \leq P_{grid_max} \quad \text{(III.23)}$$

Where, P_{grid_min}, and P_{grid_max} are respectively the maximum allowable power to be sold to the utility grid and to be purchased from the utility grid. These parameters are found in Table 3.2.

3.4.4.3 Lithium-ion battery constraints

As ESS, the lithium-ion battery has an instrumental role in the DC microgrid especially in case of deficit or excess in energy production. Therefore, the safe operation of the battery must be guaranteed to extend its lifetime and optimize its performance. This can be acquired through the constraints that are defined. First, the battery power is restricted in terms of maximum charged/discharged power:

$$P_{batt_min} \leq P_{batt}(k) \leq P_{batt_max} \quad \text{(III.24)}$$

Where, P_{batt_min}, and P_{batt_max} are respectively the maximum allowable power to be charged and discharged into/from the battery. The maximum allowable charge/discharge is fixed at $0.43C$ ($217.4\ A$).
Second, the battery-safe operation is ensured by limiting its state of charge (SOC) within allowable limits. The allowable limits, defined in Table 3.2, are based on similar microgrid applications that include lithium-ion batteries [88], [153]. The SOC constraint is then expressed as follows:

$$SOC_{min} \leq SOC(k) \leq SOC_{max} \quad \text{(III.25)}$$

Lastly, the battery's initial state at the time ($k = 0$) should be retrieved at the end of the time horizon ($k = N$) to further standardize and optimize the battery performance:

$$SOC(k = 0) = SOC(N) \quad \text{(III.26)}$$

3.4.4.4 (DG) constraints

For proper and efficient operation, (DG) manufacturers define an output power range for generators. Then, when turned on, the (DG) operation is limited by lower and upper bounds (in this paper a range between 25%-100% of the rated power is applied)[98]. This can be expressed as:

$$sign\big(P_{DG}(k)\big).P_{DG_min} \leq P_{DG}(k) \leq sign\big(P_{DG}(k)\big).P_{DG_max} \quad \text{(III.27)}$$

The function sign () is introduced since the DG power is null when it is turned off and between the allowable limits when it is turned on.

Besides, and following the predefined objectives, the (DG), as a backup pollutant source, intercepts directly to feed the load in case of an energy deficit, and/or to charge the battery. Hence, at each time k none of (DG)'s produced power should be sold to the utility grid. By this, the (DG) main functionality is secured. This can be expressed as:

$$P_{DG}(k) \leq sign\big(P_{DG}(k)\big).(P_{load}(k) - P_{PV}(k) - P_{WT}(k) + P_{batt}(k)) \quad \text{(III.28)}$$

3.5 Implementation of optimization approaches

Several techniques can be used to solve the optimization problem. In this thesis, two techniques were applied: Dynamic Programming (DP) and Genetic Algorithm (GA).

(DP) is a deterministic technique that requires a certain modification of the problem structure to find the optimal solution and is based on the principle of Bellman[154]. In (DP), the problem is divided into successive discrete states to find the global optimum. At each calculation step, the algorithm considers all meshed decision variables and calculates the least costly transitions according to a criterion to optimize[89]. The total cost function corresponds to the sum of the operation cost of each operating unit for each sampled period. The DP was successfully applied in similar optimal scheduling problems of microgrids including several sources and ESS and yielded improved results in comparison to other optimization algorithms [88], [90].

(GA) is the second metaheuristic optimization method that is applied to solve the optimization problem. Unlike (DP), which is considered a "step-by-step" optimization algorithm, (GA) is an evolutionary search algorithm that is based on an analogy with the theory of the natural evolution of species. (GA) considers the problem with a set of ($N \times$ Number of decision variables = $3N$) variables for the overall time horizon planning. It has as a starting point a population composed of a set of distributed solutions (or individuals) randomly in the search space. This method is by nature stochastic so that two successive runs don't necessarily lead to the same result as different final populations can be obtained. (GA) was applied in [155] and [152] to manage and schedule the generation and consumption in a microgrid to minimize the operating cost and greenhouse gas emissions.

Battery SOC limits		$SOC_{min} = 20\%$ - $SOC_{max} = 90\%$ $SOC(1) = 50\%$
(DG) fuel consumption function parameters: $P\ (KW)$ and $C\ (L/h)$		$P_{1_min} = 13.75, P_{2_min} = 25.5$ $P_{3_min} = 37.6, P_{3_max} = 55$
		$C_1 = 6.4, C_2 = 11.41, C_3 = 15$
Utility grid power upper and lower limits (KW)		$P_{grid_min} = -30$ $P_{grid_max} = 60$
Battery power upper and lower limits (KW)		$P_{batt_min} = -54.25$ $P_{batt_max} = 54.25$
(DG) upper and lower limits when turned on (KW)		$P_{DG_min} = 13.75$ $P_{DG_max} = 55$
Emissions parameters	Emission levels (g/KWh)	$\alpha_{CO_2} = 232.037,\ \alpha_{NO_x} = 4.331$ $\alpha_{CO} = 2.32,\ \alpha_{SO_2} = 0.464$
	Cost ($\$/Kg$)	$\mu_{CO_2} = 0.0012,\ \mu_{NO_x} = 0.27$ $\mu_{CO} = 0.022,\ \mu_{SO_2} = 0.12$
Penalty coefficients for converters' losses		$\delta_{batt}^{loss} = \delta_{DG}^{loss} = \delta_{grid}^{loss} = 1.14\ \$/KWh$

Table 3.2 Optimization parameters.

The application of two different methods serves primarily as a means of comparison for validation of the obtained results. On the other hand, by choosing these two methods, the problem is tackled from two different approaches. In the first, the (DP) discretizes the decision variables and evaluates each possible transition to find the optimal route by reconstructing a trajectory vector from the last to the initial state, while the second is an evolutionary algorithm that considers the overall problem variables on the whole time horizon and produces successive generations to find the optimal solution.

3.5.1 Dynamic programming

3.5.1.1 Problem formatting

In (DP), the problem is seen as a succession in time of discrete states of the system. The outputs of the optimization problem are $\left[P_{batt_ref} \;\; P_{DG_ref} \;\; P_{grid_ref}\right]$. Referring to the problem constraints, the actual number of decision variables is two, while the third variable can be deduced from the power balance constraint (equation (III.21)). Hence, any two out of the three power reference outputs: P_{batt_ref}, P_{DG_ref}, and P_{grid_ref} can be selected as decision variables for the DP algorithm. P_{DG_ref} and P_{batt_ref} are selected as decision variables for the optimization problem. As (DP) is a step-by-step discrete algorithm, it is applied to discretized state equation systems. In the current problem, the battery SOC is considered as a state variable of the system as it can be expressed in discretized form as:

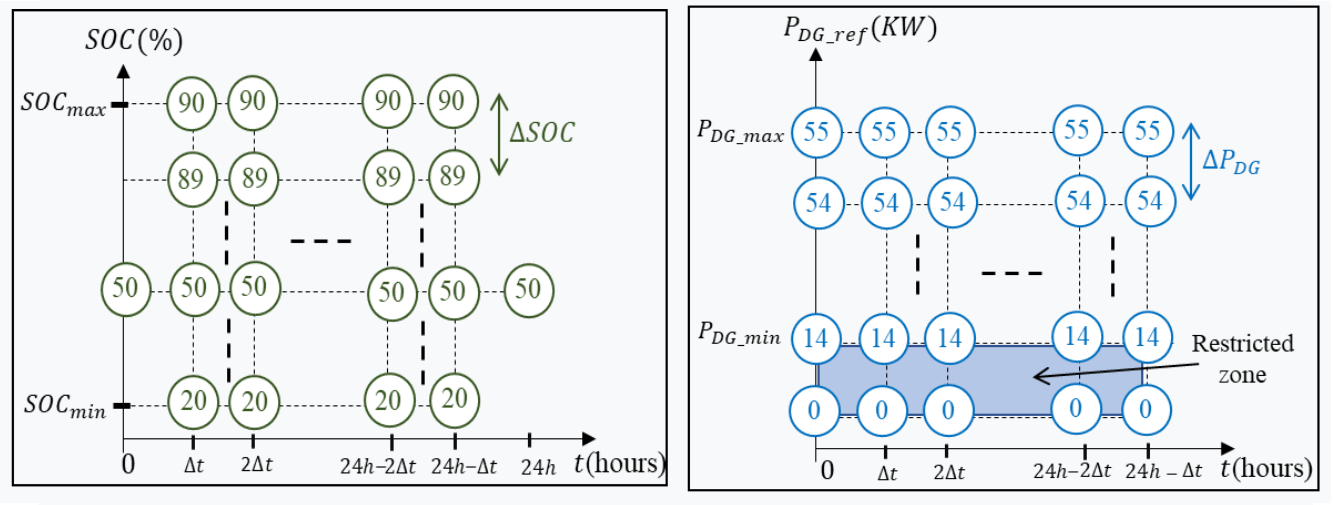
$$SOC(k+1) = f_{batt}\big(SOC(k), P_{batt}(k)\big) \tag{III.29}$$

Where, $SOC(k+1)$, $SOC(k)$, $P_{batt}(k)$, and f_{batt} are respectively the battery's SOC at time $k+1$, the battery's SOC at time k, the battery's power at time k, and the battery-discretized dynamic model. Equation (III.29) is called the state equation of the system for which SOC is the state variable, and P_{batt} is the decision variable. The battery-discretized dynamic model and the mathematical expression of f_{batt} are detailed in Appendix E. The total cost function and the constraints over the whole-time horizon are the same ones represented by equations (III.11) to (III.28).

3.5.1.2 Mesh of decision variables and state equation

In (DP), each of the selected decision variables $\{P_{batt_ref}, P_{DG_ref}\}$ is meshed. Having linked the battery's SOC to the charged/discharged power P_{batt_ref} through equation (III.29), SOC can be selected instead of P_{batt_ref} along with P_{DG_ref} as meshed variables without loss of generality. Thus, $\{SOC, P_{DG_ref}\}$ meshed variables are characterized by a time step Δt over the planning horizon and are discretized following a sampling step denoted ΔSOC and ΔP_{DG} respectively for

SOC and P_{DG_ref}. Fig 3.6 (a) and (b) represent the meshed decision variables SOC (Fig 3.6 (a)) and P_{DG_ref} (Fig 3.6 (b)).



(a) (b)

Fig.3.6 Discretization of the decision variables to states characterized by a time step Δt: (a) SOC discretized with a sampling step ΔSOC and (b) P_{DG_ref} discretized with a sampling step ΔP_{DG}.

Each decision variable is discretized at each time step Δt with a fixed sampling step. For instance, in Fig.3.6 (a) and (b), and only for illustration purposes, ΔSOC is fixed at 1% and ΔP_{DG} to 1 KW. The SOC constraints, expressed in equations (III.26) and (III.25), are considered in Fig.3.6 (a). Only one SOC value is attainable at the beginning and the end of the planning horizon and the SOC variable is discretized between its minimum and maximum admissible values, respectively $SOC_{min} = 20\%$ and $SOC_{max} = 90\%$.

Same to P_{DG_ref}, represented in Fig.3.6 (b), when the (DG) is turned on it can exclusively operate between a minimum and a maximum admissible value, denoted respectively P_{DG_min} and P_{DG_max}. P_{DG_ref} values that lie in the range of $[0, P_{DG_min}]$ aren't discretized as they belong to the restricted zone in light blue (constraint represented by equation (III.27)). To choose the time step Δt over the planning horizon and the sampling steps ΔSOC and ΔP_{DG} several factors should be considered. Knowing that all data inputs have the same sampling period $T_s = 1/6$ hour, the minimum time step for the DP algorithm, Δt_{min} is limited by T_s. Selecting values for Δt lower than T_s would irrelevantly slow down the algorithm as all inputs remain constants for a whole sampling period. On the other hand, higher values than T_s speeds up the algorithm but ends up with a suboptimal solution as several troughs and peaks of load demand or production may not be identified by the optimization problem which has a slower dynamic than the real system. Thereupon, Δt is fixed at $T_s = 1/6$ h and the time-space is divided into N points characterizing N stages of evaluation of the optimization algorithm. As $\Delta t = T_s$, N is always expressed following equation (III.1) and is equal to 144.

In turn, a trade-off is achieved when selecting ΔSOC and ΔP_{DG} as extra-small values add insignificant states to test when searching for the optimal solution which slows down the algorithm. Contrarily, though high values of ΔSOC and ΔP_{DG} speeds up the algorithm, it reduces the

resolution of the decision variables which impacts the optimal solution. After several trials with different ΔSOC and ΔP_{DG} values, the best trade-off is found for a $\Delta SOC = 0.25$ % and $\Delta P_{DG} = 0.1 P_{DG_max} = 550W$. Hence, the SOC state space is divided into $M + 1$ points separated by the fixed sampling step $\Delta SOC = 0.25\%$. M is calculated as follows:

$$M = \frac{SOC_{max} - SOC_{min}}{\Delta SOC} = \frac{90-20}{0.25} = 280 \quad \text{(III.30)}$$

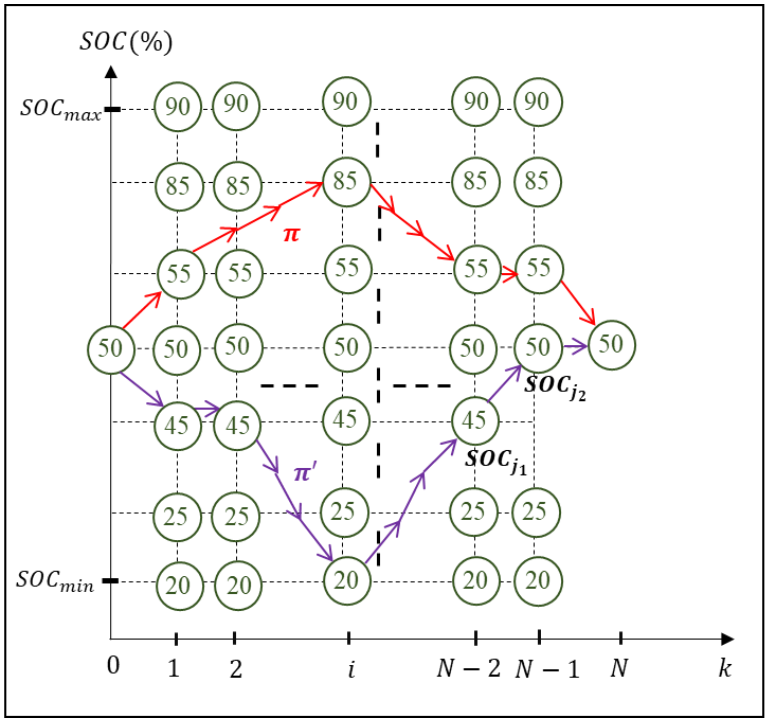
$$\text{By this, } SOC(t) \approx SOC_{min} + j \,.\Delta SOC \qquad \text{for } j = 0, \dots, M \quad \text{(III.31)}$$

Hence, the P_{DG_ref} state space is divided into $Z + 1$ points separated by the fixed sampling step $\Delta P_{DG} = 550\ W$. Z is calculated as follows:

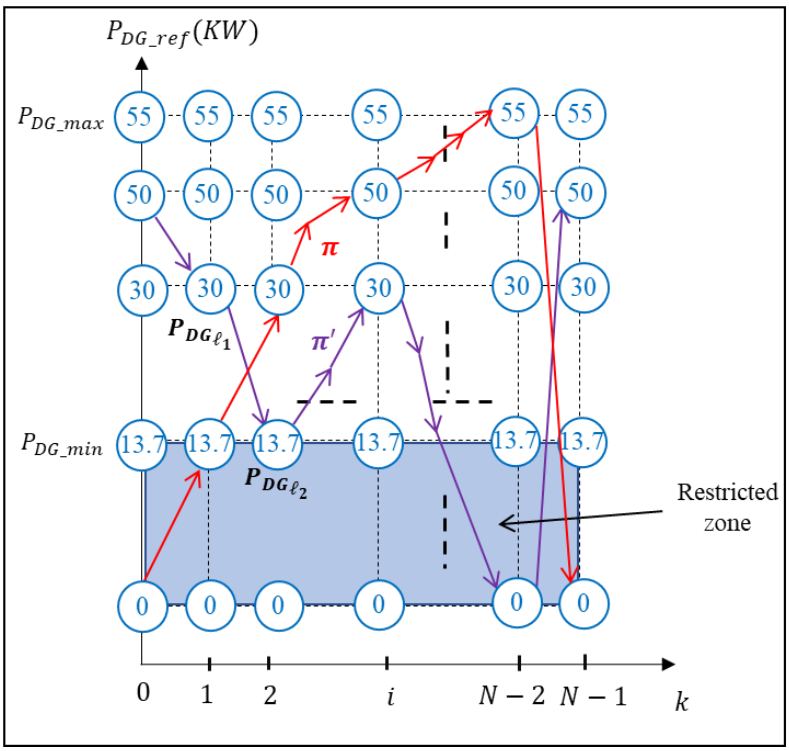
$$Z = \frac{P_{DG_max} - P_{DG_min}}{\Delta P_{DG}} = \frac{55-13.75}{550\times10^{-3}} = 75 \quad \text{(III.32)}$$

$$P_{DG_ref}(t) \approx P_{DG_min} + \ell.\Delta P_{DG} \qquad \text{for } \ell = 0, \dots, Z \quad \text{(III.33)}$$

Fig.3.7 (a) highlights two admissible control strategies denoted π (red arrows) and π' (purple arrows). These two control strategies drive the battery SOC from the initial state $SOC(1) = 50$ to



(a)



(b)

Fig.3.7 (a) Example of two admissible control strategies π and π' in the SOC state space (b) Example of two admissible control strategies π and π' in the P_{DG_ref} state space.

the final state $SOC(N) = 50$ through different admissible trajectories. The same strategies of control π and π' correspond to two different P_{DG_ref} trajectories depicted in Fig.3.7 (b). The main objective of the (DP) algorithm is to find the optimal sequence or control strategy to retrieve the optimal SOC and P_{DG_ref} states trajectories. The evolution of the SOC from a state SOC_{j_1} at time k to the state SOC_{j_2} at time $k+1$ corresponds to a value of the decision variable $P_{batt}^{j_1,j_2}$ expressed following the battery discrete function f_{batt} (Appendix E) :

$$P_{batt}^{j_1,j_2}(k) = Q(T_a).V_{batt}^{j_1,j_2}\left(\frac{SOC_{j_1}-SOC_{j_2}}{\Delta t}\right) \quad \text{(III.34)}$$

Where, $V_{batt}^{j_1,j_2}$ and $\mathrm{Q}(T_\mathrm{a})$ are respectively the battery voltage corresponding to the transition from SOC_{j_1} at time k to the state SOC_{j_2} at time $k+1$ (Volts), and the battery maximum capacity at ambient temperature (Ah).

In turn, each state $P_{batt}^{j_1,j_2}$ corresponds to a set of $(Z+2)$ P_{DG_ref} maximum possible states. After evaluating all constraints that include P_{DG_ref} variable, the number of P_{DG_ref} admissible states may vary from one, corresponding to a turned-off (DG) state ($P_{DG_ref} = 0$), to $Z+2$ for which the turned-off state and the whole interval $[P_{DG_min}, P_{DG_max}]$ are admissible.

Hence, the approach followed when applying the (DP) algorithm consists of finding the optimal evolution sequence of:

1. the battery's SOC between the initial and the final instants of the whole-time interval. From this sequence, the optimal charged/discharged battery power at each instant k is computed following equation (III.34).
2. The (DG) reference power between the initial and the final instants of the whole-time interval. The whole sequence should comply with all predefined constraints.

3.5.1.3 Algorithm implementation:

The implementation of the (DP) algorithm is initiated by creating a cost matrix $\mathbf{R} \in R^{(M+1)\times N}$. The filling of this matrix is done recursively starting from $k = N$ and returning until $k = 1$ following Bellman's principle detailed in Appendix E.2. Each element (j, k) of this matrix represents the optimal cost to go from $SOC(j)$ state at time k to the final state $SOC(j_N)$ at time N. Formally:

$$\boldsymbol{R}\,(j_N, N) = 0 \tag{III. 35}$$

$$\boldsymbol{R}\,(j, k) = \min_{j,j'} \left(\boldsymbol{R}(j', k+1) + \gamma_{tot}(k, j, j', l_{opt})\right) \qquad \text{for } k = N-1, \dots, 1 \tag{III.36}$$

Where, $\gamma_{\text{tot}}(k, j, j', \text{l}_{\text{opt}})$ represents the total cost of transition from the state SOC_j at time k to $SOC_{j'}$ at time $k+1$ for optimal (DG) operating state. l_{opt} is the index of the optimal (DG) operating state. It is equal to:

$$l_{opt} = \begin{cases} -1 & if\ (DG)\ is\ turned - off \\ \ell & if\ (DG)\ is\ turned - on \end{cases} \tag{III. 37}$$

$\gamma_{\text{tot}}(k, j, j', \text{l}_{\text{opt}})$ is expressed as:

$$\gamma_{\text{tot}}(k, j, j', \text{l}_{\text{opt}}) = \min_{\text{j,j}'} \left(\gamma_{\text{tot}}(\text{k, j, j}', -1), \gamma_{\text{tot}}(\text{k, j, j}', \ell_1), \gamma_{\text{tot}}(\text{k, j, j}', \ell_2), \dots, \gamma_{\text{tot}}(\text{k, j, j}', \ell)\right) \tag{III.38}$$

Where, $\gamma_{\text{tot}}(\text{k, j, j}', \ell)$ is the total cost of transition from the state SOC_j at time k to $SOC_{j'}$ at time $k+1$ for a (DG) operating state index ℓ. Having the index ℓ, P_{DG_ref}'s corresponding value is retrieved through equation (III.33). The maximum number of (DG) admissible states is $Z + 2$. Finally, $\gamma_{\text{tot}}(\text{k, j, j}', \ell)$ can be expressed similarly to the cost expressions from equation (III.11) to equation (III.20) except that summation over the whole time horizon is omitted in the (DP) cost equations and the symbol "γ" is adopted to express each cost function instead of the symbol "J". Hence, the new modified (DP) cost functions are:

$$\begin{cases} P_{batt}^{j.j'}(k) = Q(T_a).V_{batt}^{j.j'}\left(\frac{SOC_j - SOC_{j'}}{\Delta t}\right) \\ P_{DG}(k) = \begin{cases} 0 & if\ \ turned-off \\ P_{DG_min} + \ \ell.\Delta P_{DG} & if\ \ turned-on \end{cases} \end{cases}$$
(III.39)

$$\gamma_{tot}(k,j,j',\ell) = \zeta_{oc}\gamma_{oc}(k,j,j',\ell) + \zeta_{emissions}\gamma_{emissions}(k,j,j',\ell) + \zeta_{conv_losses}\gamma_{conv_losses}(k,j,j',\ell)$$ (III.40)

$$\gamma_{oc}(k,j,j',\ell) = \gamma_{grid}(k,j,j',\ell) + \gamma_{batt}(k,j,j',\ell) + \gamma_{DG}(k,j,j',\ell)$$ (III.41)

$$\gamma_{grid}(k,j,j',\ell) = \left(\delta_{grid}^{pur}.P_{pur}(k) - \delta_{grid}^{sold}.P_{sold}(k)\right).\Delta t$$ (III.42)

$$\gamma_{batt}(k,j,j',\ell) = \frac{CC}{2.Cycles}.P_{batt}^{j.j'}(k).\Delta t + \delta_{deg}.P_{batt}^{j.j'}(k).\Delta t$$ (III.43)

$$\begin{cases} \gamma_{DG}(k,j,j',\ell) = \gamma_{DG}^{fuel}(k,j,j',\ell) + \gamma_{DG}^{SU}(k,j,j',\ell) + \gamma_{DG}^{M}(k,j,j',\ell) \\ \gamma_{DG}^{fuel}(k,j,j',\ell) = \lambda_{fuel}.F(k).\Delta t \\ \gamma_{DG}^{SU}(k,j,j',\ell) = \xi_{SU}.\sigma_{DG}^{ON}(k) \\ \gamma_{DG}^{M}(k,j,j',\ell) = \chi_M.sign(P_{DG}(k)).\Delta t \end{cases}$$ (III.44)

$$\gamma_{emissions}(k,j,j',\ell) = \beta_{emiss}.P_{DG}(k).\Delta t$$ (III.45)

$$\gamma_{conv_losses}(k,j,j',\ell) = \left(\delta_{batt}^{loss}.P_{losses_bidirec_conv}(k) + \delta_{DG}^{loss}.P_{losses_3\phi_DG_rec}(k) + \delta_{grid}^{loss}.P_{losses_3\phi_grid_conv}(k)\right).\Delta t$$ (III.46)

We take note that:

- The RESs operating cost isn't included in the (DP) equations since their generated power serves as input to the optimization problem and not as a decision variable. Hence, the RESs operating cost is always calculated apart following equations (III.5) and (III.6).
- All constraints presented in equations (III.21) to (III.28) are kept the same when applying the (DP) algorithm as they all target the system at a specific time k and not for the whole time horizon.
- To compute the utility-grid power and the converter losses at time k, equations (III.2) and (III.21) are utilized.

The element $\boldsymbol{R}$ (j_0, 1), of the matrix $\boldsymbol{R}$, which corresponds to the initial state of charge, contains the value of the total optimal cost to move from the initial state of charge SOC_{j_0} at time $k = 0$ to SOC_{j_N} at time $k = N$. Besides, $\boldsymbol{R}$ is a sparse matrix as the elements corresponding to inadmissible SOC levels are not taken into consideration. In parallel with the construction of the cost matrix, two matrices with the same dimension denoted $\mathbf{S}^{SOC}$ and $\mathbf{S}^{P_{DG_ref}}$ are used to store respectively:

1. the index of the optimal found SOC state of the next step.

2. the index of the optimal $P_{DG_ref}(k)$ of the current step for the corresponding SOC transition SOC_j to $SOC_{j'}$.

An element $\mathbf{S}^{SOC}(j,k)$ contains the index, j', of the next step which corresponds to the optimal path starting from state $SOC(j)$ at time k towards the end of the cycle. However, an element $\mathbf{S}^{P_{DG_ref}}(j,k)$ contains the index l_{opt_k} of the current step at time k for the corresponding SOC transition SOC_j to $SOC_{j'}$.

Finally, once the matrices $\mathbf{S}^{SOC}$ and $\mathbf{S}^{P_{DG_ref}}$ are filled, an optimal path vector denoted **T** is built and corresponds to the minimum cost over the whole-time horizon.

T, which length is N, is expressed as follows:

$$\boldsymbol{T}(1) = SOC(j_0) \tag{III.47}$$

$$\boldsymbol{T}(k) = \boldsymbol{S}^{SOC}\,(\boldsymbol{T}(k-1), k-1), \qquad \text{for } k = 2, \dots, N \tag{III.48}$$

The diagram in Fig.3.8 illustrates the method followed to implement the (DP) algorithm on a representative example with a limited number of points.

3.5.1.4 Simulation results :

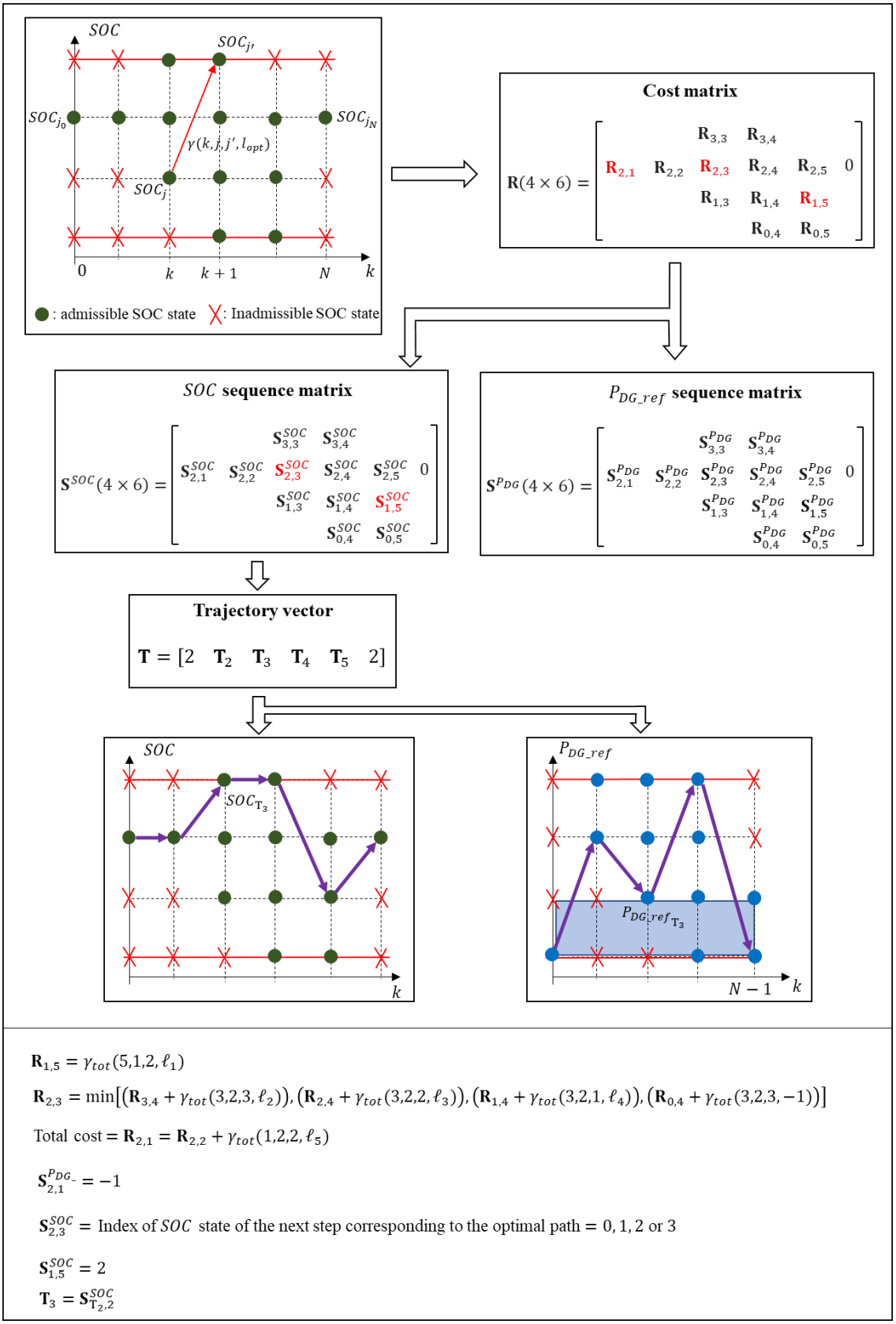
To prove the viability of the DP algorithm in solving a multi-objective optimization problem, several simulation tests are conducted. First, as mentioned before, the preference between each of the three optimization goals is accessed through the corresponding weights in the total cost function of the equation (III.11). The three weights ζ_{oc}, $\zeta_{emissions}$, and ζ_{conv_losses} are real positive values $\in [0,1]$. First, weights equal to unity are set $\zeta_{oc} = \zeta_{emissions} = \zeta_{conv_losses} = 1$ to examine the effectiveness of the DP in finding a feasible solution to the proposed problem conveniently to all imposed constraints. The simulation plot results for the two tested days are revealed in Figures 3.9, 3.10, 3.11, and 3.12. The share of the energy mix and the corresponding operating costs on the winter and the summer days are respectively summarized in Table 3.3 and Table 3.4.

The results of the winter day are shown in the left plots (Fig.3.9 (a), 3.10 (a), 3.11 (a), and 3.12 (a)), and the ones of the summer day in the right plots (Fig.3.9 (b), 3.10 (b), 3.11 (b), and 3.12 (b)). For both days, the (DP) algorithm converges and presents effective results by finding a feasible solution for the proposed problem. As seen in Fig.3.9 (a) and (b), the unmet load power is purchased from the utility grid at low pool prices (between 0:00 A.M and 6:00 A.M), while the battery and the (DG) intervene to cover the load demand at high pool prices (during the evening load peak). Besides, when turned on, the (DG) average produced power is always close to its maximum value. Hence, a low deficit in power production is covered by the battery operating in discharge mode and/or the utility grid. On the other hand, when the power deficit is high the EMS prioritizes the (DG) over the battery and the utility grid to provide the required power. All low and

upper power bounds of the (DG), the battery, and the utility grid aren't exceeded for the whole time horizon of the two tested days.

The battery's SOC optimal trajectory on the winter and the summer days are respectively represented in Fig.3.10 (a) and (b). The SOC curves of the two days lie between the minimum and maximum admissible values and the SOCs initial states at the beginning of the time horizon are equal to the SOCs at the end of the day $SOC(k = 0) = SOC(k = N) = 50\%$, conveniently to the constraint imposed in equation (III.26). Moreover, the compliance with the SOC constraint of equation (III.26) can be verified through the battery's total charged and discharged energy in Tables 3.3 and 3.4 where both quantities are almost equal for the two tested days: $E_{dis_batt} \approx E_{ch_batt}$. Hence, the initial state of the ESS is retrieved at the end of the day which verifies equation (III.26). The toxic gas emissions on the winter and the summer days are respectively represented in Fig.3.11 (a) and (b) and show higher values on the winter day. The total cumulative mass of emitted toxic gas on the winter day is almost five times greater than the summer day. The same ratio can be retrieved when evaluating the total amount of produced (DG) energy on winter and summer days. Referring to Table 3.3 and Table 3.4, $E_{DG} = 187.64\ KWh$ for the winter day and $36.4\ KWh$ for the summer day.

Therefore, the ratio between the produced energy on the winter and summer days is $E_{DG_w}/E_{DG_s} = 5.15$. Lastly, the CO_2 emissions account for 97% of the total toxic gas emissions and the rest is divided between NO_x, SO_2, and CO emissions.



$\mathbf{R}_{1,5} = \gamma_{tot}(5,1,2,\ell_1)$

$\mathbf{R}_{2,3} = \min[(\mathbf{R}_{3,4} + \gamma_{tot}(3,2,3,\ell_2)), (\mathbf{R}_{2,4} + \gamma_{tot}(3,2,2,\ell_3)), (\mathbf{R}_{1,4} + \gamma_{tot}(3,2,1,\ell_4)), (\mathbf{R}_{0,4} + \gamma_{tot}(3,2,3,-1))]$

Total cost $= \mathbf{R}_{2,1} = \mathbf{R}_{2,2} + \gamma_{tot}(1,2,2,\ell_5)$

$\mathbf{S}_{2,1}^{P_{DG}} = -1$

$\mathbf{S}_{2,3}^{SOC}$ = Index of SOC state of the next step corresponding to the optimal path = 0, 1, 2 or 3

$\mathbf{S}_{1,5}^{SOC} = 2$

$\mathbf{T}_3 = \mathbf{S}_{\mathbf{T}_2,2}^{SOC}$

Fig.3.8 Illustrative diagram of the applied DP algorithm.

(a) (b)

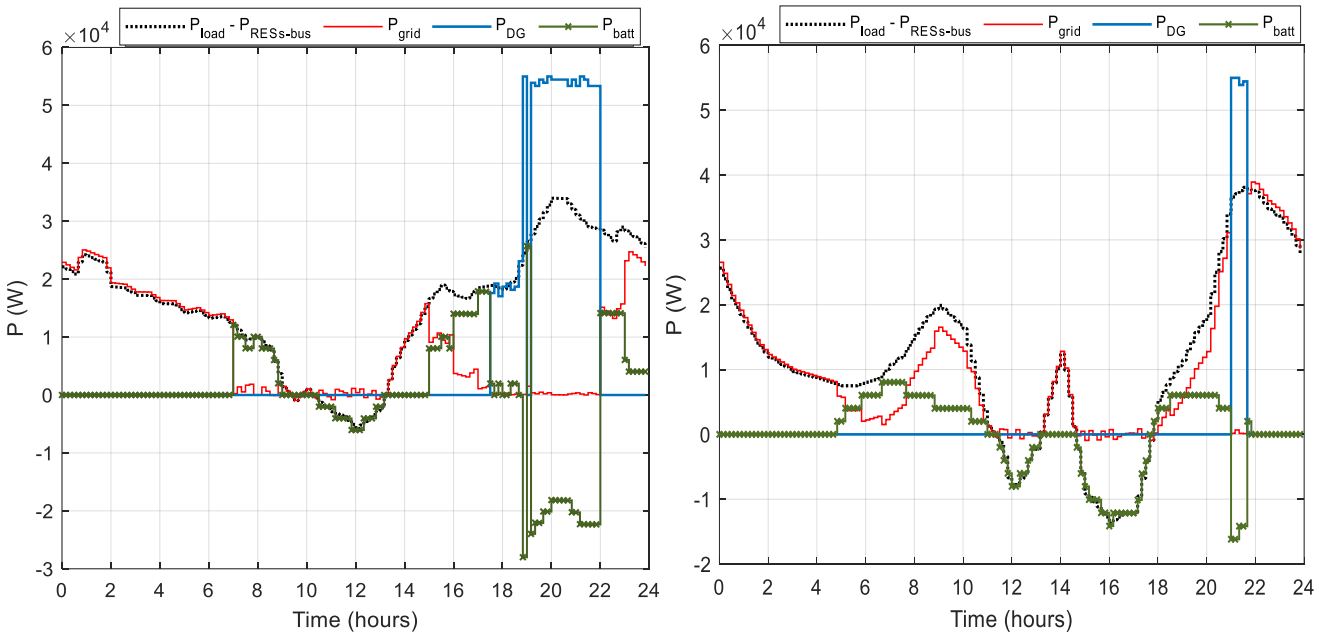


Fig.3.9 Optimal (DG), battery, and grid power references on (a) the winter day and (b) the summer day.

(a) (b)

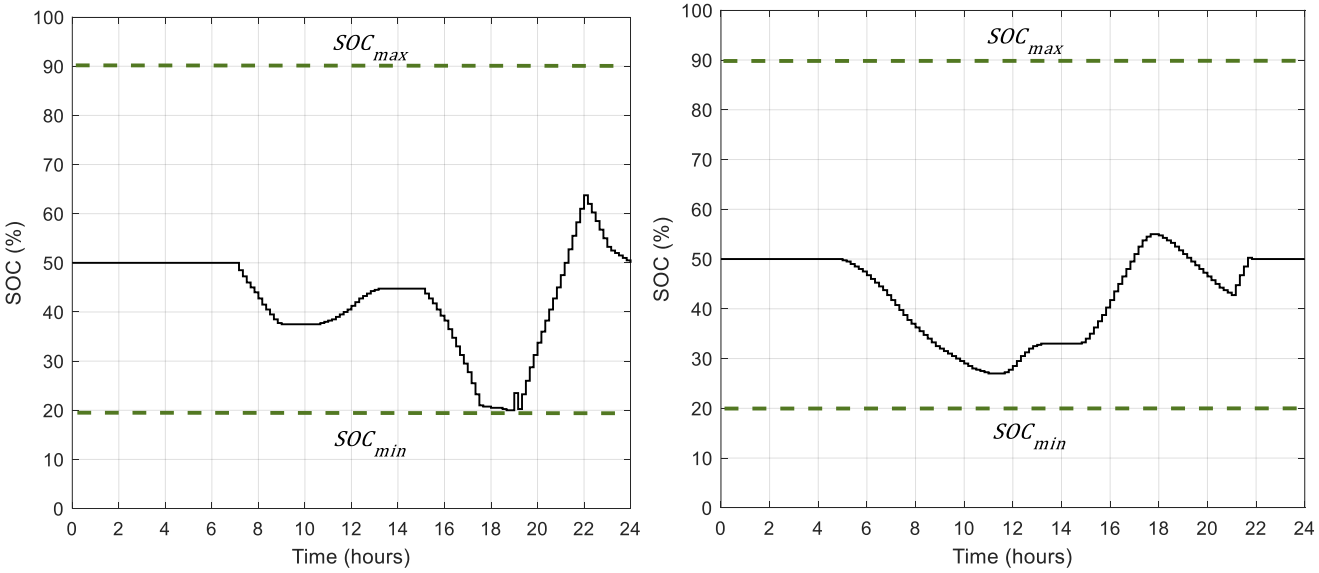


Fig.3.10 Battery's SOC optimal trajectories on (a) the winter day and (b) the summer day.

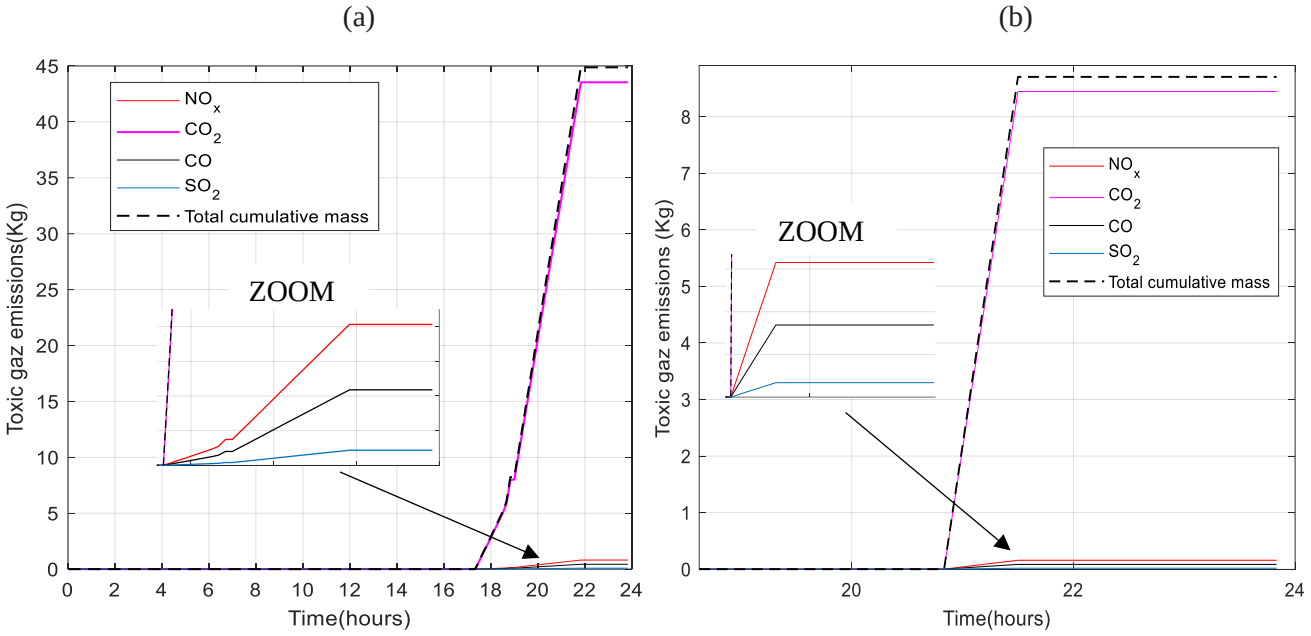


Fig.3.11 Toxic gas emissions on (a) the winter day and (b) the summer day.

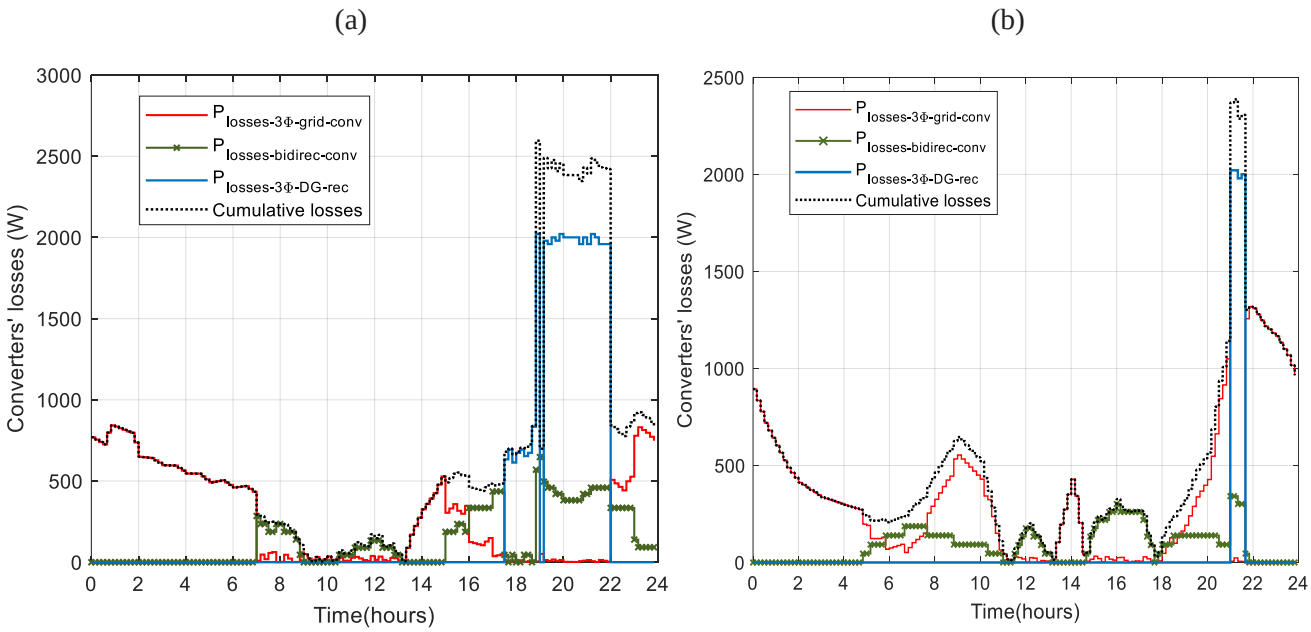


Fig.3.12 Losses in (DG), battery, and grid converters on (a) the winter day and (b) the summer day.

Fig.3.12 (a) and (b) show the losses of dispatchable converters, which are the (DG) 3ϕ rectifier, the utility grid 3ϕ converter, and the bidirectional DC/DC converter of the battery, respectively on the winter and the summer days. The losses in each converter are proportional to the power transiting from/to its corresponding unit. Referring to Tables 3.3 and 3.4, the total energy loss in dispatchable converters is higher on the winter day ($E_{loss_conv} = 16.88\ KWh$) comparing to the summer day ($E_{loss_conv} = 11.58\ KWh$) as a higher energy mix is provided from dispatchable

sources on the winter day compared to the summer day. The total energy mix of dispatchable sources denoted E_{tot_disp} , is expressed as:

$$E_{tot_disp} = E_{pur} + E_{sold} + E_{dis_batt} + E_{ch_batt} + E_{DG} \quad \text{(III.49)}$$

Referring to Tables 3.3 and 3.4, on the winter day $E_{tot_disp} = 534.53\ KWh$, and on the summer day $E_{tot_disp} = 373\ KWh$. Thus, the higher reliance on dispatchable sources during the winter day results in higher losses in the corresponding converters compared to the summer day.

Finally, a profit of 29 $ is achieved on the winter day when comparing the total operating cost ($J_{oc} = 152.29$ $) with the one obtained when the ESS and the (DG) aren't included in the DC microgrid ($J_{oc} = 181.25$ $). This profit accounts for 16 % of the 181.25 $ operating cost. For the summer day, the made profit is 18.5 $ as the actual total operating cost is ($J_{oc} = 99.51$ $), while the one with no ESS and (DG) ($J_{oc} = 118$ $). This profit accounts for 15.66 % of the 118 $ operating cost.

Winter day (18/02/2021)	
Load consumption and RESs production	- Total load energy consumption: $E_{load} = 679.11\ KWh$ - Total PV effective generated energy: $E_{PV_bus} = 152.01\ KWh$ - Total WT effective generated energy: $E_{WT_bus} = 156.9\ KWh$ - Total RESs effective generated energy: $E_{PV_bus} + E_{WT_bus} = 308.91\ KWh$
	RESs cost function: $J_{RESs} = 2.25$ $
Utility grid	- Total purchased energy: $E_{pur} = 200.62\ KWh$ - Total sold energy: $E_{sold} = 0.77\ KWh$
	Utility grid cost function: $J_{grid} = 73.89$ $
Battery	- Total discharged energy: $E_{dis_batt} = 72.96\ KWh$ - Total charged energy: $E_{ch_batt} = 72.55\ KWh$
	Battery cost function: $J_{batt} = 12.62$ $
(DG)	- Total operating time: 4 hours 20 minutes - Total number of start-ups: 2 - Total diesel consumption: 59.63 Liters - Total emitted toxic gas: 44. 9 Kg (from which 97% accounts for CO_2) - Total generated energy: $E_{DG} = 187.64\ KWh$
	(DG) cost function: $J_{DG} = 63.53$ $
Losses in dispatchable converters	Total energy loss in dispatchable converters: $E_{loss_conv} = 16.88\ KWh$
CPU time	5 minutes 14 seconds
Total operating cost function	$J_{oc} = 152.29$ $

Table 3.3 Summary of share of the energy mix and corresponding operating costs on the winter day (18/02/2021).

Summer day (16/07/2021)	
Load consumption and RESs production	- Total load energy consumption: $E_{load} = 604.17\ KWh$ - Total PV effective generated energy: $E_{PV_bus} = 292.94\ KWh$ - Total WT effective generated energy: $E_{WT_bus} = 47.56\ KWh$ - Total RESs effective generated energy: $E_{PV_bus} + E_{WT_bus} = 340.51\ KWh$
	RESs cost function: $J_{RESs} = 1.3$ \$
Utility grid	- Total purchased energy: $E_{pur} = 240.13\ KWh$ - Total sold energy: $E_{sold} = 1.18\ KWh$
	Utility grid cost function: $J_{grid} = 79.29$ \$
Battery	- Total discharged energy: $E_{dis_batt} = 47.61\ KWh$ - Total charged energy: $E_{ch_batt} = 47.74\ KWh$
	Battery cost function: $J_{batt} = 7.44$ \$
(DG)	- Total operating time: 40 minutes - Total number of start-ups: 1 - Total diesel consumption: 10.72 Liters - Total emitted toxic gas: 8.7 Kg (from which 97% accounts for CO_2) - Total generated energy: $E_{DG} = 36.4\ KWh$
	(DG) cost function: $J_{DG} = 11.48$ \$
Losses in dispatchable converters	Total energy loss in dispatchable converters: $E_{loss_conv} = 11.58\ KWh$
CPU time	4 minutes 25 seconds
Total operating cost function	$J_{oc} = 99.51$ \$

Table 3.4 Summary of share of the energy mix and corresponding operating costs on the summer day (16/07/2021).

3.5.2 Preference between optimization objectives

The minimization of the total operating cost, the toxic gas emissions, and the losses in operating converters are fixed as three distinct optimization objectives. To prioritize any of the defined objectives over the remaining ones, a higher weight should be assigned in the main objective function to the corresponding objective. As prementioned, the corresponding weights ζ_{oc}, $\zeta_{emissions}$, and ζ_{conv_losses} are real positive values $\in [0,1]$. Though the three objectives are expressed distinctly through their proper weights in the main objective function, this doesn't mean that they are practically disassociated. In other words, the achievement of any of the three objectives may foster or restrict the attainment of the remaining ones. Therefore, the impact of achieving one objective on the remaining ones should be studied apart to conveniently find the best weight combination for a specific goal.

Consequently, a Pareto of solutions exists based on the user's preferences and goals priorities. For instance, the user may select only a prime objective with no preferences between the remaining objectives, or beside the main priority goal which is assigned the highest weight out of the three, the user may set a second priority goal, etc.

For this, several simulation tests are conducted on the winter day, taken as a case study, in which one weight is set to one and the two remaining are varied to assess the impact of each of the variable weights on the total operating cost function J_{oc}, the (DG) total produced energy E_{DG}, and the total energy loss in dispatchable converters E_{loss_conv} over the 24-hour time horizon. The three variables J_{oc}, E_{DG}, and E_{loss_conv} are selected as each of them represents one of the three defined goals. By evaluating these three variables with different weight values, the impact of the weight's selection on the attainment of defined goals is revealed.

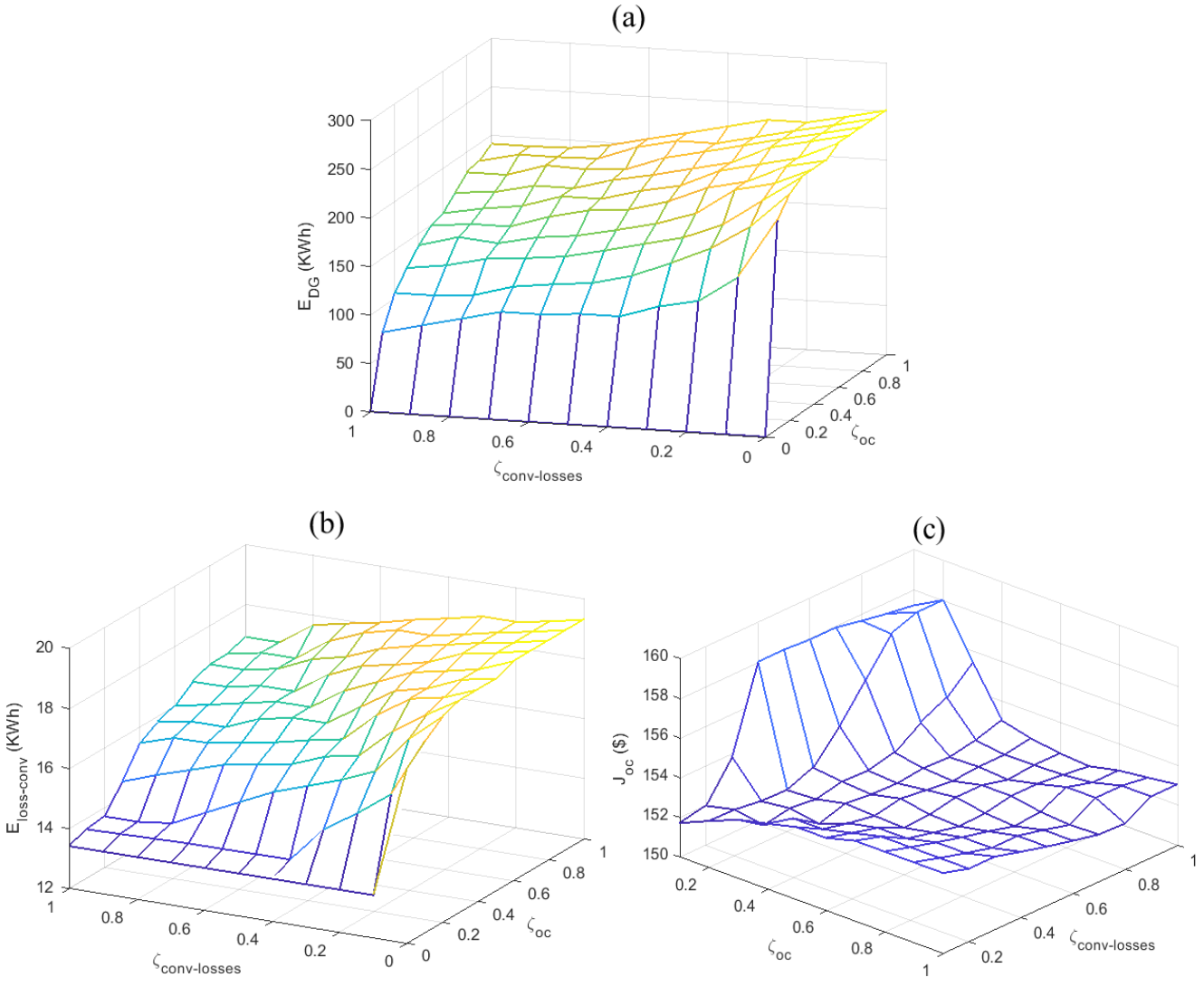


Fig.3.13 (a) E_{DG}, (b) $E_{loss-conv}$, and (c) J_{oc} as functions of ζ_{oc} and $\zeta_{conv-losses}$ for $\zeta_{emissions} = 1$.

The sampling step of variable weights is 0.1 then in each test, each of the three variables J_{oc}, E_{DG}, and E_{loss_conv} corresponds to an (11×11) matrix. To quantify all possible sets of solutions, a representation of variables E_{DG}, $E_{loss-conv}$, and J_{oc} in per unit $(p.u.)$ of their maximum range values is required. E_{DG}, $E_{loss-conv}$, and J_{oc} are respectively expressed in $(p.u.)$ as follows:

$$\begin{cases} E_{DG_p.u} = \frac{E_{DG} - E_{DG_min}}{E_{DG_max} - E_{DG_min}} \\ E_{loss-conv_p.u} = \frac{E_{loss-conv} - E_{loss-conv_min}}{E_{loss-conv_max} - E_{loss-conv_min}} \\ J_{oc_p.u} = \frac{J_{oc} - J_{oc_min}}{J_{oc_max} - J_{oc_min}} \end{cases} \quad \text{(III.50)}$$

Where all min and max subscripts correspond respectively to the minimum and maximum values of E_{DG}, $E_{loss-conv}$, and J_{oc} plotted curves for each test. By this, the three variables are now represented in $p.u.$ and by applying the "minimum" function to any of the variables, the optimal weights combination is retrieved. In the first test, the emissions weight, $\zeta_{emissions}$ is fixed at one, ζ_{oc} and ζ_{conv_losses} are variables. The plot results are depicted in Fig.3.13 (a), (b), and (c). All possible solutions based on user preferences are detailed in Table 3.5.

$\zeta_{emissions} = 1$			
Goals preferences	Optimal weights	Applied formula	Obtained Results
- Prime goal: reduction of toxic gas emissions	$\zeta_{emissions} = 1$ $\zeta_{oc} = 0$ $\forall\, \zeta_{conv_losses} \in [0,1]$	min $(E_{DG_p.u})$	$E_{DG} = 0\ KWh$ $E_{loss-conv}(KWh) \in [13.41\ , 17.85]$ $J_{oc}(\$) \in [157.7\ , 180.25]$
- Prime goal: reduction of toxic gas emissions - Second goal: reduction of losses in converters	$\zeta_{emissions} = 1$ $\zeta_{oc} = 0$ $\forall\, \zeta_{conv_losses} \in [0.1,1]$	min $(E_{DG_p.u} + E_{loss-conv_p.u})$	$E_{DG} = 0\ KWh$ $E_{loss-conv} = 13.41\ KWh$ $J_{oc} = 157.7\ \$$
- Prime goal: reduction of toxic gas emissions - Second goal: reduction of operating cost	$\zeta_{emissions} = 1$ $\zeta_{oc} = 0$ $\forall\, \zeta_{conv_losses} \in [0.1,1]$	min $(E_{DG_p.u} + J_{oc_p.u})$	$E_{DG} = 0\ KWh$ $E_{loss-conv} = 13.41\ KWh$ $J_{oc} = 157.7\ \$$
- Prime goal: reduction of emissions - Equal preferences between the reduction of the operating cost and losses in converters	$\zeta_{emissions} = 1$ $\zeta_{oc} = 0$ $\forall\, \zeta_{conv_losses} \in [0.1,1]$	min $(E_{DG_p.u} + J_{oc_p.u} + E_{loss-conv_p.u})$	$E_{DG} = 0\ KWh$ $E_{loss-conv} = 13.41\ KWh$ $J_{oc} = 157.7\ \$$

Table 3.5 Optimal weights and corresponding results for $\zeta_{emissions} = 1$ and different goals preferences.

For example, if the user selects in addition to the prime goal which is the reduction of toxic gas emission, a second goal priority corresponding to the minimization of the total operating cost, the matrices of $E_{DG_p.u}$ and $J_{oc_p.u}$ are added and the minimum of the obtained matrix corresponds to the best weights combination. It can be seen from Table.3.5 that the optimal weights for all goals' preferences cases are $\zeta_{emissions} = 1$, $\zeta_{oc} = 0$, and $\forall\, \zeta_{conv_losses} \in [0.1,1]$ giving the following results $E_{DG} = 0\ KWh$ ($E_{DG_p.u} = 0\ p.u$), $J_{oc} = 157.7\$$ ($J_{oc_p.u} = 0.21\ p.u$), and $E_{loss-conv} = 13.41\ KWh$ ($E_{loss-conv_p.u} = 0\ p.u$).

In the second test, the operating cost weight, ζ_{oc} is fixed at one, $\zeta_{emissions}$ and ζ_{conv_losses} are variables. The $p.u.$ variables are computed following equation (III.50) based on the new maximum and minimum values obtained from the new matrices E_{DG}, $E_{loss-conv}$, and J_{oc} . The plot results are depicted in Fig.3.14 (a), (b), and (c).

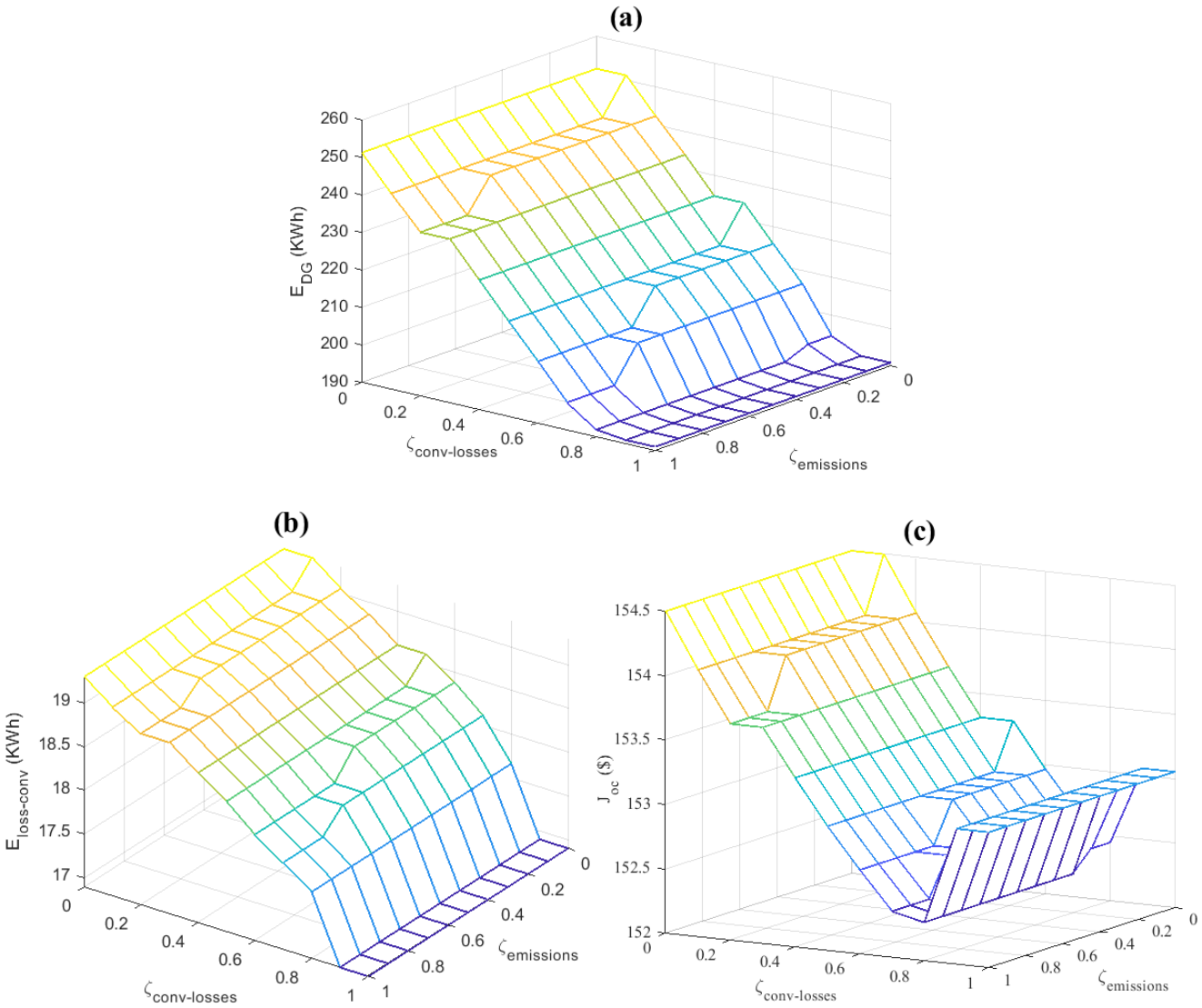


Fig.3.14 (a) E_{DG}, (b) $E_{loss-conv}$, and (c) J_{oc} as functions of $\zeta_{emissions}$ and $\zeta_{conv-losses}$ for $\zeta_{oc} = 1$.

In this case, $\zeta_{oc} = 1$, one optimal weights' combination solution is found for all possible goals' preferences. The optimal weights are $\zeta_{oc} = 1$, $\forall\, \zeta_{emissions} \in [0.2,1]$, and $\zeta_{conv_losses} = 0.8$ and yields the following results : $J_{oc} = 152.3\ \$$ ($J_{oc_p.u} = 0\ p.u$), $E_{DG} = 191.86\ KWh$ ($E_{DG_p.u} = 0.017\ p.u$), and $E_{loss-conv} = 17.66\ KWh$ ($E_{loss-conv_p.u} = 0.32\ p.u$).

In the last test, the losses in converters' weight, ζ_{conv_losses} is fixed at one, $\zeta_{emissions}$ and ζ_{oc} are variables. The plot results are depicted in Fig.3.15 (a), (b), and (c). Here two different optimal weights combination are obtained depending on the goals preferences: 1) If the reduction of converters losses is the only prime goal, 2) the reduction of converters losses is the prime goal and the reduction of toxic gas emissions is the second preferred goal, and 3) if there are equal preferences between the reduction of toxic gas emissions and operating cost as second goals one optimal weights' combination is obtained and equal to: $\zeta_{conv_losses} = 1$, $\zeta_{oc} = 0$, and $\forall\, \zeta_{emissions} \in [0,1]$.

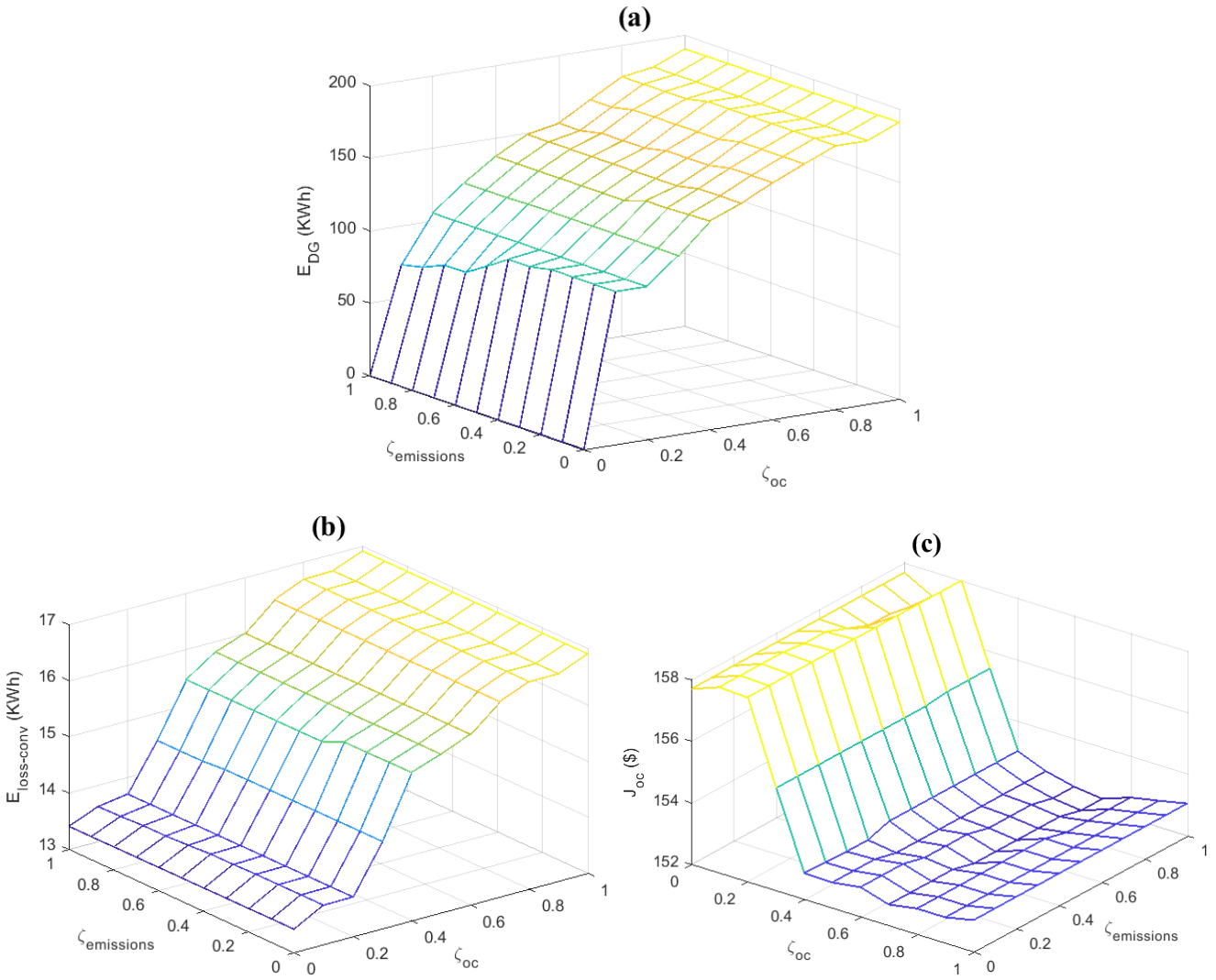


Fig.3.15 (a) E_{DG}, (b) $E_{loss-conv}$, and (c) J_{oc} as functions of ζ_{oc} and $\zeta_{emissions}$ for $\zeta_{conv-losses} = 1$.

This weights' combination yields the following results, $J_{oc} = 157.7\ \$$ ($J_{oc_p.u} = 0.94\ p.u$), $E_{DG} = 0\ KWh$ ($E_{DG_p.u} = 0\ p.u$), and $E_{loss-conv} = 13.41\ KWh$ ($E_{loss-conv_p.u} = 0\ p.u$). However, if the minimization of the operating cost is set as a second goal after the reduction of losses in converters the optimal weights' combination is : $\zeta_{conv_losses} = 1$, $\zeta_{oc} = 0.4$, and $\forall\ \zeta_{emissions} \in [0.4,1]$. This yields the following results: $J_{oc} = 153.04\ \$$ ($J_{oc_p.u} = 0.12\ p.u$), $E_{DG} = 137.41\ KWh$ ($E_{DG_p.u} = 0.72\ p.u$), and $E_{loss-conv} = 15.46\ KWh$ ($E_{loss-conv_p.u} = 0.59\ p.u$).

Finally, to highlight the impact of weights' selection in achieving each of the three optimization goals, the maximum and minimum values of $E_{loss-conv}$, E_{DG}, and J_{oc} obtained out of the three tests are summarized in Table 3.6. The corresponding weights' combinations of each minimum and maximum value are stated. As seen from the results, the attainment of any of the three goals is tremendously impacted by the selection of the three weights and not only by the one assigned to the desired goal. Hence, if any preference between the proposed goals is intended, the construction of E_{DG}, $E_{loss-conv}$, and J_{oc} matrices presented in this section and the optimal weights selection method should be conducted. The weights selection process should precede the application of offline optimization. Meanwhile, if there aren't any preferences between the defined goals, all weights are set to one.

	Minimum	Corresponding weights	Maximum	Corresponding weights
E_{DG}	$0\ KWh$	$\zeta_{emissions} = 1$ $\forall\ \zeta_{losses_conv} \in [0,1]$ $\zeta_{oc} = 0$ --- $\zeta_{losses_conv} = 1$ $\forall\ \zeta_{emissions} \in [0,1]$ $\zeta_{oc} = 0$	$251.83\ KWh$	$\zeta_{oc} = 1$ $\forall\ \zeta_{emissions} \in [0,1]$ $\zeta_{losses_conv} = 0$
$E_{loss-conv}$	$13.41\ KWh$	$\zeta_{losses_conv} = 1$ $\forall\ \zeta_{emissions} \in [0,1]$ $\zeta_{oc} = 0$ --- $\zeta_{emissions} = 1$ $\forall\ \zeta_{losses_conv} \in [0.1,1]$ $\zeta_{oc} = 0$	$19.3\ KWh$	$\zeta_{losses_conv} = 0$ $\zeta_{oc} = 1$ $\forall\ \zeta_{emissions} \in [0,1]$ --- $\zeta_{losses_conv} = 0$ $\zeta_{emissions} = 1$ $\forall\ \zeta_{oc} \in [0.6,1]$
J_{oc}	$152.3\ \$$	$\zeta_{oc} = 1$ $\forall\ \zeta_{emissions} \in [0.2,1]$ $\zeta_{losses_conv} = 0.8$	$180.25\ \$$	$\zeta_{oc} = 0$ $\zeta_{losses_conv} = 0$ $\zeta_{emissions} = 1$

Table 3.6 The minimum and maximum E_{DG}, $E_{loss-conv}$, and J_{oc} obtained results with the corresponding weights' combination.

3.5.3 Genetic algorithm

The second method applied to solve the optimization problem is an evolutionary algorithm based on the Genetic Algorithm (GA). The application of the (GA) highlights the following elements:

1. A principle of coding the population element. This step associates each of the points of the state space to a data structure. It is generally placed after the mathematical modeling phase of the addressed problem. The quality of coded data conditions the success of the (GA).
2. A mechanism for generating the initial population. This mechanism must be able to produce a non-homogeneous population of individuals that will serve as a basis for future generations. The selection of the initial population is instrumental as it can speed up or slow down the convergence to the global optimum.
3. A function to optimize, or an objective function, returns a value $\in \mathbb{R}^+$ named fitness or individual assessment function.
4. Operators for diversification of the population over generations and exploration of the state space. The crossover operator recomposes the genes of individuals existing in the population, the mutation operator aims to guarantee the exploration of space of state.
5. Sizing parameters: population size, number of total generations, stopping criteria, probability of application of crossover, mutation operators, etc.

The general principle of operation of the (GA) algorithm is shown in Fig.3.16. We start by generating a random population of individuals. To move from a generation k to a generation $k + 1$, the following steps are repeated for all elements of the population k. Each individual of the current population is given a score by computing its fitness value. These values are called the raw fitness scores. Then, the raw fitness scores are scaled to convert them into a more usable range of values. These scaled values are called expectation values. Based on their expectations, some members are selected as parents, and other individuals of the generation k that have lower fitness are chosen as Elite. These Elites are passed automatically to the next generation without being reevaluated during the reproduction phase. Meanwhile, the selected parents produce children either by making random changes to a single parent – mutation – or by combining the vector entries of a pair of parents – *crossover*. The obtained children are evaluated again and the ones with lower fitness values are selected for the next generation $k + 1$. Finally, the current population is replaced with children to form the next generation.

The algorithm generally stops as soon as one of the following conditions is met: the number of generations reaches the maximum predefined value, the amount of running time reaches a prefixed value in seconds, the value of the fitness function for the best point in the current population is less than or equal to fitness limit, the objective function is no more improving during a predefined interval of time in seconds.

3.5.3.1 Implementation of the (GA)

To implement the (GA), the "ga " function in MATLAB is applied. This function finds a minimum of an objective function using the (GA). The syntax of the "ga" function is the following:

$$x = ga\ (fun, nvars, A, b, A_{eq}, b_{eq}, lb, ub, nonlcon) \quad \text{(III.51)}$$

Where,

- x is the local minimum solution.
- fun is the objective function.
- $nvars$ is the dimension of the problem or the number of design variables.
- A and b form the linear inequalities in the problem, ga evaluates the matrix product $A.x \leq b$.
- A_{eq} and b_{eq} form the linear equalities in the problem, ga evaluates the matrix product $A_{eq}.x = b_{eq}$.

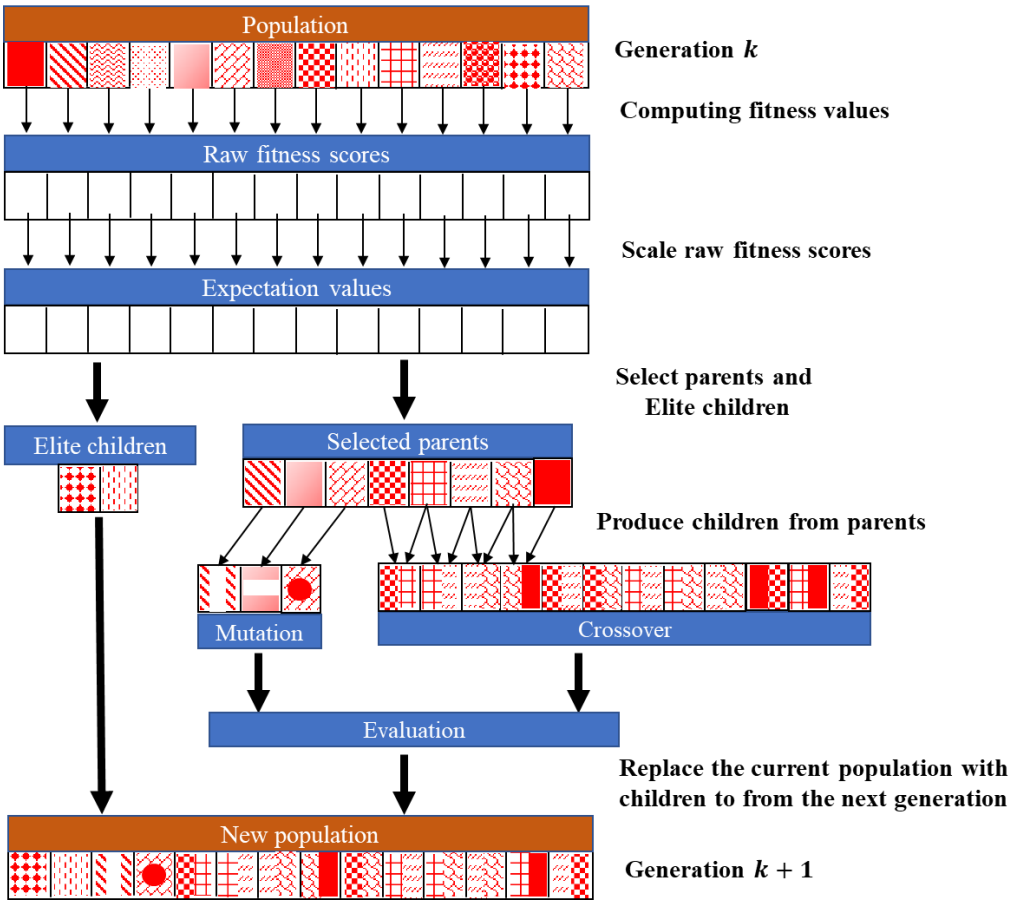


Fig.3.16 General structure of the (GA).

- lb and ub are respectively the lower and upper bounds on the design variables so that the solution is found in the range $lb \leq x \leq ub$.
- $Nonlcon$ is a function corresponding to the nonlinear constraints in the problem. It accepts x and returns vectors C and C_{eq}, representing the nonlinear inequalities and equalities respectively. ga minimizes the function such that $C(x) \leq 0$ and $C_{eq}(x) = 0$.

The flow chart showing the main steps of this algorithm is given in Fig.3.17. According to the operating principle of the algorithm, an initial population consisting of a number N_{pop} of individuals is created, each of these individuals forming a specific combination of tuning parameters to be optimized. At each step of the algorithm, the total cost function for the whole-time horizon, J_{tot}, is computed to find the fitness value of each individual. Moreover, all applied constraints are verified for each individual in the population. The next step is to select specific individuals to whom crossover and mutation operations are applied. The new individuals created in this stage are again evaluated to retain the best individuals or the individuals who adapted best to the imposed criterion. These individuals form the population of the next generation that undergoes the same process as its antecedent. The algorithm stops if the chosen stopping criteria are satisfied.

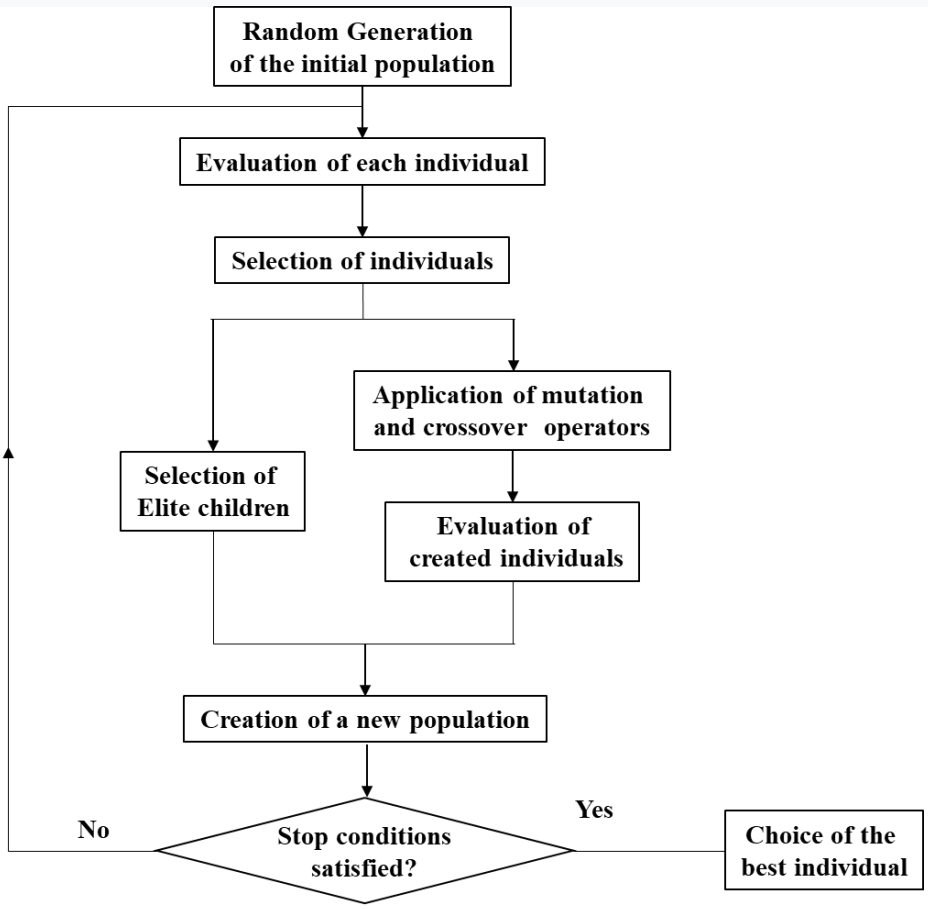


Fig.3.17 (GA) operation flow chart.

The genetic algorithm presents standard functions which are the initial population generation function, "*CreationFcn*", the selection operators of the best individuals, "*SelectionFcn*", of crossing between individuals, " *CrossoverFcn* " and mutation of an individual's genes, "*MutationFcn*". The choice of each function must be made as well as parameters or specific options for each of these functions. In this study, the standard operators given by default by the (GA) toolbox are applied.

Without revealing the operation details of these functions which can be consulted in the user manual, we simply present the functions chosen and their setting parameters in Table 3.7. Additional parameters for adjusting the functions of the genetic algorithm are given in Table 3.8. Indeed, the population size N_{pop} is set by default to 200 as the number of variables in the problem is higher than 5. The number of Elite children to be directly transferred to the next generation is specified through the "Elitecount" option parameter. In this case, the "Elitecount" is set to 10 then, 10 out of the 200 individuals of each population with the best fitness values automatically survive to the next generation. On the other hand, the "CrossoverFraction" set to 0.8 in this case, indicates that 80% of the remaining individuals after the selection of Elite children are chosen to undergo the necessary crossings. This implies that 152 individuals in our case are creating by crossing, while the rest of the population, 38 in this case, will therefore undergo a mutation in their genes to be transmitted to the next generation.

Operator type	Selected function	Description
CreationFcn	gacreationuniform	Generation function of the initial population
SelectionFcn	selectionstochunif	Selection function
CrossoverFcn	crossoverscattered	Crossover function
MutationFcn	mutationadaptfeasible	Mutation function

Table 3.7 (GA) Standard operators.

Parameter	Fixed value	Description
N_{pop}	200	Number of individuals per population
Elitecount	10	Number of Elite individuals to survive to the next generation
CrossoverFraction	0.8	Fraction of the population created by crossing

Table 3.8 Parameters for setting the (GA) functions.

3.5.3.2 Coding of individuals

Each individual in (GA) is represented by a chromosome. A chromosome is formed from a sequence of genes of a certain alphabet. This could be composed of binary digits, real numbers, integers, symbols, matrices, etc. In this case study, the chromosome consists of the decision variables $[P_{grid_ref} \;\; P_{DG_ref} \;\; P_{batt_ref}]$. Unlike the (DP) in which the number of decision variables can be reduced to two, the formulation of the problem using (GA) gets more complicated if only two variables are chosen. Hence, the three power references are included as decision variables, and the battery's SOC reference is selected instead of the battery's power reference along with the (DG) and the grid power references. The battery's SOC is always represented in discretized state form (equation III.29). Besides, the (AG) tries to find a minimum of the objective function over the whole-time horizon then, the chromosome should include the power references of the three decision variables over the 24-hours. As a result, the actual number of variables of the optimization problem, using (GA), is equal to the number of decision variables times the number of total steps for the whole time horizon, N. In the (DP) algorithm a sampling period $T_s = 1/6$ hour was selected and yielded $N = 144$, if an equal T_s is selected for the (GA) case, the number of variables increases to $nvars = 3 \times 144 = 432$. Such a high number of variables makes the mission of finding a global minimum extremely harsh and prolonged as well as reduces the convergence probability of the algorithm. Though the resolution of the optimal power samples will be reduced, the only practical and decent solution is to increase the sampling time to one hour at least and thus reduce N to 24 and $nvars$ to $3 \times 24 = 72$.

Individual or chromosome	
1	$P_{grid_opt}(0)$
2	$P_{dies_opt}(0)$
3	$SOC(1)$
4	$P_{grid_opt}(1)$
5	$P_{dies_opt}(1)$
6	$SOC(2)$
…	…
…	…
…	…
70	$P_{grid_opt}(23)$
71	$P_{dies_opt}(23)$
72	$SOC(24)$

Fig.3.18 Parameters to be optimized forming a chromosome or an individual.

Therefore, a chromosome or an individual consists of 72 genes as seen in Fig.3.18. Referring to equation (III.29), The battery's power at the time k is a function of the SOC at time k and $k+1$ then, the first battery's power reference corresponding to $(k=0)$ is a function of $SOC(0)$ and $SOC(1)$. Similarly, the last battery power reference corresponding to $(k=23)$ is a function of $SOC(23)$ and $SOC(24)$. As the battery's SOC is replacing P_{batt_ref} as decision variable in the optimization problem, the SOC vector should include $N+1$ elements from $(k=0)$ to $SOC(k=N=24)$ to be able to build P_{batt_ref} vector consisting of N elements. To simplify the formulation of the problem and by referring to equation (III.26), $SOC(0)=50\%$ then, it can be entered as a constant. By this, the SOC vector consists of 24 elements of which the first is $SOC(1)$ and the last is $SOC(24)$. On the other hand, the power reference vectors P_{grid_ref} and P_{DG_ref} consist of 24 elements or genes corresponding to the samples from the beginning of the 24-hour time horizon ($(k=0)$ till the end $(k=N-1=23)$. A population made up of N_{pop} of individuals is then created and evolves from one generation to another by adapting to an evolution criterion.

The objective function denoted fun, is the same as presented in equation (III.11) expressed as follows:

$$fun = J_{tot} = \zeta_{oc}J_{oc} + \zeta_{emissions}J_{emissions} + \zeta_{conv_losses}J_{conv_losses} \quad \text{(III.52)}$$

$J_{oc}, J_{emissions}$, and J_{conv_losses} expressions are the ones figuring in equations (III.12) to (III.20). The remaining parameters of the ga function: $A, b, A_{eq}, b_{eq}, lb, ub,$ and $nonlcon$ can be found in Appendix F.

3.5.3.3 Simulation results

To test the viability of the (GA) in finding a feasible solution to the optimization problem, it is applied to the two operating days. All weights are set to unity in both simulations, and obtained results are shown in Figures 3.19 and 3.20. The results of the winter day are shown in the left plots (Fig.3.19 (a) and 3.20 (a)) and the ones of the summer day in the right plots (Fig.3.19 (b), 3.18 (b)). The obtained results show that (GA) converges for the two tested days and finds a feasible solution to the proposed optimization problem while respecting all fixed constraints. As general EMS and referring to Fig.3.19 (a) and (b), the (GA) algorithm follows a similar strategy to (DP). Needed load energy is purchased from the utility grid at low pool prices while it is covered by the battery and the (DG) at high pool prices.

Besides, the SOC curves of the two days, represented in Fig.3.20 (a) and (b), lie between the minimum and maximum admissible values. The SOCs initial states at the beginning of the day are retrieved at the end of the day $SOC(k=0)=SOC(k=N)=50\%$ then, the battery's constraints are respected.

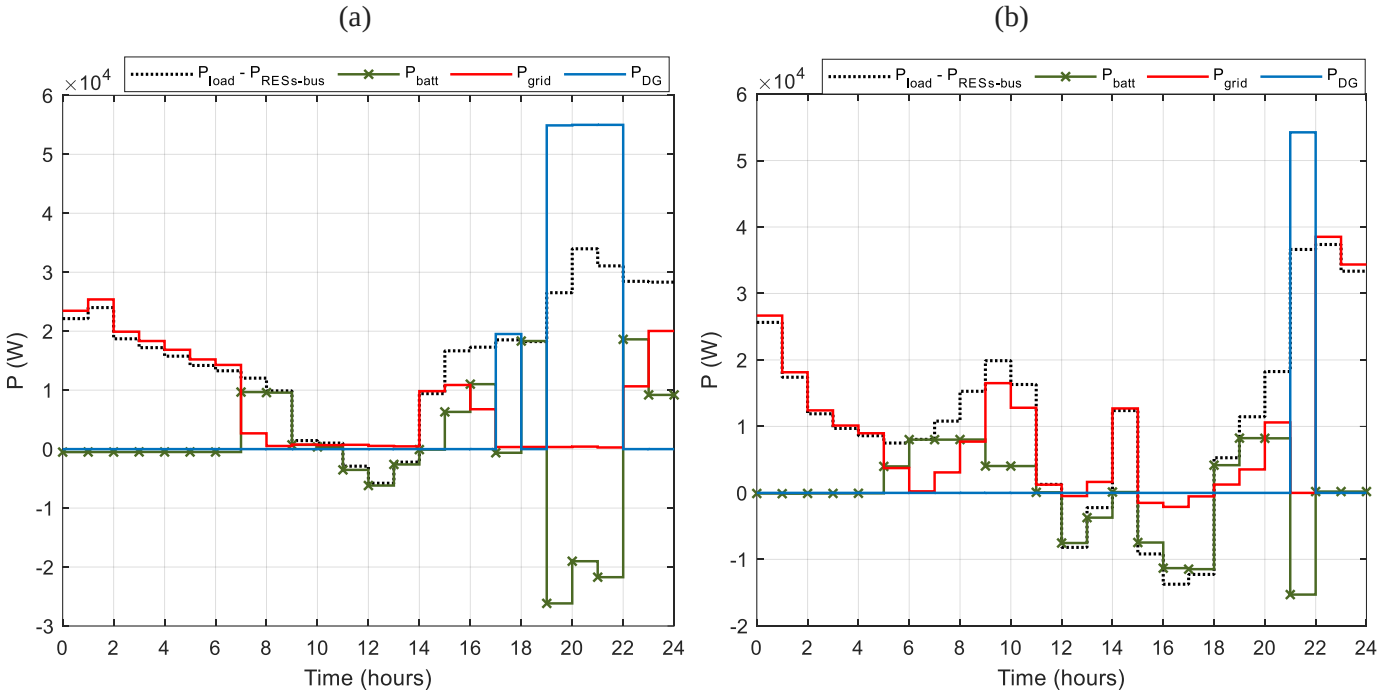


Fig.3.19 (GA) results of optimal (DG), battery, and grid power references on (a) the winter day and (b) the summer day.

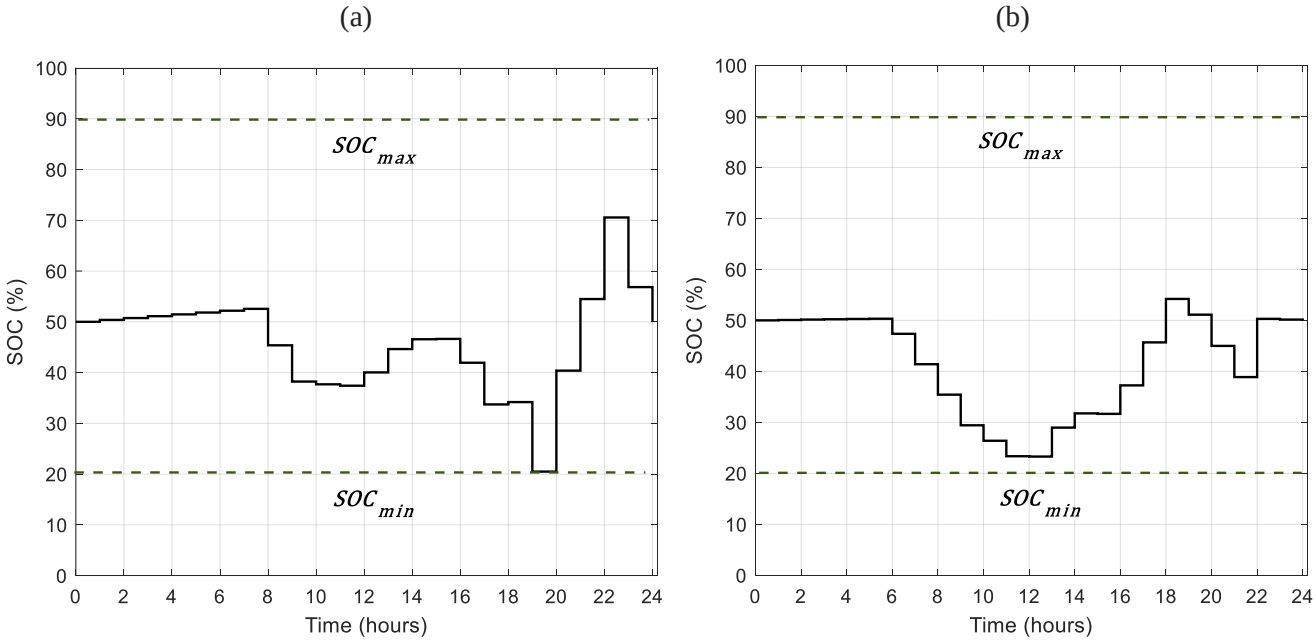


Fig.3.20 (GA) results of optimal trajectories of the battery's SOC on (a) the winter day and (b) the summer day.

Same for the (DG) and the utility-grid power curves which range between the lower and upper bounds.

The share of the energy mix and the corresponding operating costs on the winter and summer days are found in Table 3.9. Comparing, the (GA) results in Table 3.9 to the (DP) ones in Tables 3.3 and 3.4, the total operating costs values for the two days are too close meanwhile the shares of each source in the overall energy mix present slight differences especially on the summer day. Finally, to carry out a fair comparison between (DP) and (GA) algorithms, the same sampling period T_s should be selected. Knowing that diving the one-hour sampling period by x, increases the numbers of variables of (GA) to 72 times x and so the convergence time increases exponentially, a better-adapted solution is to rerun the (DP) using a sampling $T_s = 1$ hour equal to that of (GA). By this, the two algorithms can be fairly compared. The results of the comparison between (DP) and (GA) are summarized in Table 3.10. As seen, the (DP) algorithm converges much faster than the (GA), (DP) is 16 times faster than the (GA) for the winter test day and 25.5 times for the summer day. For the reduction of toxic gas emissions goal, the (GA) performs better than the (DP) and this can be seen through the emitted toxic gas and the operating cost of the (DG) which are lower on both days when applying the (GA) algorithm. On the other hand, the (DP) shows better results than (GA) regarding the reduction of converters losses on the winter and summer days.

(GA) results	Winter day (18/02/2021)	Summer day (16/07/2021)
RESs	$E_{PV} + E_{WT} = 351.7\ KWh$	$E_{PV} + E_{WT} = 361.58\ KWh$
	$J_{RESs} = 2.28\ \$$	$J_{RESs} = 1.31\ \$$
Utility grid	$E_{pur} = 200\ KWh$ $E_{sold} = 0\ KWh$	$E_{pur} = 224.27\ KWh$ $E_{sold} = 4.61\ KWh$
	$J_{grid} = 73.77\ \$$	$J_{grid} = 73.53\ \$$
Battery	$E_{dis_batt} = 83.33\ KWh$ $E_{ch_batt} = 83.83\ KWh$	$E_{dis_batt} = 57.25\ KWh$ $E_{ch_batt} = 57.34\ KWh$
	$J_{batt} = 14.54\ \$$	$J_{batt} = 9\ \$$
DG	Operating hours: 4 hours Start-ups: 2 times Diesel consumption: 57.15 Liters Emitted toxic gas: 44.1 Kg $E_{DG} = 184.44\ KWh$	Operating hours: 1 hour Start-ups: 1 time Diesel consumption: 16.05 Liters Emitted toxic gas: 13 Kg $E_{DG} = 54.24\ KWh$
	$J_{DG} = 61.18\ \$$	$J_{DG} = 17.19\ \$$
Losses in dispatchable converters	$E_{loss_conv} = 17.44\ KWh$	$E_{loss_conv} = 12.52\ KWh$
Total operating cost function	$J_{oc} = 151.77\ \$$	$J_{oc} = 101.03\ \$$

Table 3.9 (GA) summary results of the share of the energy mix and corresponding operating costs on the winter and summer days.

However, there are no intelligible preferences between the two algorithms regarding the total operating costs which are too close for the two operating days. A slightly lower operating cost is obtained in the winter while using the (GA) (difference of 0.12 $), whereas the (DP) shows a better result on the summer day (difference of 0.87 $).

As a result, both algorithms converge and find feasible solutions for the optimization problem with a similar EMS strategy. Each of the applied algorithms slightly performed better than the other in one out of the two objectives: the minimization of toxic gas emissions and losses in dispatchable converters. Yet, the total operating costs are almost equal for the two algorithms which further validates that the minimum found is a global minimum for the optimization problem. Finally, as both algorithms showed similar performance, two additional criteria may favor the (DP) over the (GA) and are the required CPU time for convergence and the sampling time of variables. Following these criteria, (DP) algorithm is selected as an offline optimization technique and its results are applied in the next chapter.

		Winter day (18/02/2021)	Summer day (16/07/2021)
CPU time	DP	12 minutes 28 seconds	8 minutes 40 seconds
	GA	3 hours 12 minutes 45 seconds	3 hours 32 minutes 29 seconds
Emitted toxic gas	DP	47.9 Kg	13.2 Kg
	GA	44.1 Kg	13 Kg
E_{loss_conv}	DP	16.9 KWh	12.10 KWh
	GA	17.44 KWh	12.52 KWh
J_{RESs}	DP	2.28 $	1.31 $
	GA	2.28 $	1.31 $
J_{grid}	DP	67.12 $	71.99 $
	GA	73.77 $	73.53 $
J_{batt}	DP	13.17 $	9.62 $
	GA	14.54 $	9 $
J_{DG}	DP	69.32 $	17.24 $
	GA	61.18 $	17.19 $
J_{oc}	DP	151.89 $	100.16 $
	GA	151.77 $	101.03 $

Table 3.10 Comparison between (DP) and (GA).

3.6 Conclusion

In this chapter, an offline optimization problem was formulated to ensure the optimal power planning of the DC microgrid for a 24-hour time horizon operation. For this, real profile data of solar irradiance, wind speed, ambient temperature, residential load profile, and electricity pool prices were applied on winter and summer days as a case study. The EMS targets three main objectives: the minimization of the total operating cost, the reduction of the toxic gas emissions produced by the (DG), and the minimization of losses in dispatchable converters. To attain these objectives, a unique weighted objective function is applied with three weights corresponding to each of the predefined objectives. Several constraints are introduced to emulate a real DC microgrid scenario consisting of lower and upper power bounds for operating units, minimum and maximum admissible SOC values to guarantee a safe operation of the ESS, etc. To solve the optimization problem, among several algorithms, two were represented and applied.

First, a deterministic algorithm called dynamic programming is applied and yields effective results. The algorithm presents fast convergence and finds a feasible solution to the optimization problem while respecting all defined constraints. A second metaheuristic algorithm, named the genetic algorithm was applied to further validate the effectiveness of (DP) obtained results. In turn, (GA) converges and finds a feasible solution to the proposed problem. A comparison between the two algorithms is conducted and the main outcomes are:

- (GA) and (DP) find close solutions for the two operating days and follow a similar EMS to optimally plan the DC microgrid sources with a slight difference in the power management of the utility grid and the (DG). Compared to (DP), (GA) relies less on the (DG) and more on the utility grid to cover the unmet load for the two tested days. (GA) slightly outperforms (DP) on the winter day and vice-versa. Then, no clear preference between the two algorithms can be made by assessing the results. However, using the two algorithms yield close results which verify that the found solution is a global minimum to the optimization problem.
- Two main criteria favor (DP) over (GA). The extremely higher convergence time of (GA) compared to (DP), a ratio of convergence time : $GA_{CT}/DP_{CT} = 15.44$ for the winter day, and 24.54 for the summer day are obtained. The second criterion is the selection of the sampling period which is restricted for (GA) to $T_s = 1$ hour in our case. Dividing T_s by n_s where $n_s \in \mathbb{Z}^+$ increases the number of variables from 72 for $T_s = 1$ hour to $72n_s$ for $T_s = 1/n_s$ hour. As the convergence time increases exponentially with the number of variables as well as the feasible solution becomes harder to find, the sampling time is limited to one hour in the (GA) case. However, (DP) is run with a sampling period of $T_s = 1/6$ hour and presents a viable solution with a limited convergence time. Hence, (DP) algorithm solves the optimization problem with a higher time resolution.

All obtained results are validated with equal weights, set to one, in the unified objective function. Hence, there are no preferences between predefined goals. Yet, if any of the three optimization goals are prioritized, the impact of weights' selection should be treated apart. For this, the weights selection problem is addressed in case of any preferences between the predefined objectives. A weights selection method is proposed to optimally find the best weights combination based on the goals' preferences. The obtained results show the impact of weights' selection on the targeted objectives.

Finally, though the offline optimization problem finds the optimal power references of the DC microgrid for the next 24 hours, this technique remains unable to adapt to any mismatches between predictions and real profile data. As a result, an online optimization stage is added in the next chapter and operates as a regulator to optimally adapt the power references.

Chapter 4 : DC Microgrid Online Optimization

4.1 Introduction

The offline optimization of the DC microgrid addressed in Chapter 3, outputs the optimal power references of the dispatchable sources consisting of the utility grid, ESS, and the (DG) for the next 24 hours. The inputs of the offline optimization problem consist of forecasted data for the next day that may be inaccurate. Thus, differences between forecasted and actual data will inevitably exist which leads to a suboptimal solution if the offline optimal power references are applied without any update. As a result, and based on the actual input data, an online optimization process is required to continuously retrieve the new optimal power references. Different online optimization strategies can be found in the literature from which Model Predictive Control (MPC), also known as Receding Horizon Control (RHC), fuzzy logic rules-based, feedback correction, etc. are the commonly used techniques.

As a concept, (MPC) carries out a first optimization for the whole-time horizon using any deterministic or metaheuristic optimization algorithm, then finds the best route for the decision variables corresponding to the minimum total cost function. Only the optimal schedule of the first-time interval is applied, the time horizon moves forward by one-time interval, and the optimization algorithm is executed again for the whole new time horizon and so forth. The (MPC) based optimization approach was successfully applied in [95], and [96] to optimally schedule microgrids including several DERs and ESS and showed effective results in response to mismatches between predicted and actual data. A sampling step for the rolling horizon of 15 minutes is selected in both studies with a 24-hour prediction horizon in [95], and 48 hours in [96]. Among the latest publications on online optimization techniques, the MPC- based optimization technique with a receding horizon is the most found [99].

In [104], a fuzzy logic rules-based online optimization technique is applied in a hybrid fuel cell vehicle to optimally ensure the required traction power while minimizing the hydrogen consumption of the fuel cell. The state of charge of the fuel cell and the required traction power are two input variables and the output variable is the power supplied by the fuel cell. The inference rules, the number, and the type of membership functions are specified based on the defined optimization objective. A genetic algorithm is applied to an offline profile over the whole-time horizon to optimally locate the characteristic points of the membership functions. MPC and fuzzy logic-based online optimization techniques were largely investigated for optimal power dispatching problems and are not applied in this thesis.

Unlike MPC and fuzzy logic-based methods which are considered stand-alone online optimization techniques, other online optimization strategies are added as an adaptive correction part to the

offline optimization problem. In such strategies, the optimal power references generated by the offline optimization problem are updated each intrasample period through an online optimization process. This allows the system to retrieve the optimal solution following the occurring mismatches between real and predicted inputs. In [88], an offline optimization is achieved the day ahead for a 24-hour time horizon to optimally dispatch power in a microgrid. An online optimization stage is added to the offline optimization problem. The online optimization problem is formulated as an SQP to optimally find the new power references for the ESS and the utility grid following an excess or deficit of power in the microgrid. As the offline optimization objectives are not included in the online optimization stage, tolerance bands, based on the offline power references, are introduced to limit the online decision variables and maintain the same trajectory pace of the offline optimization. In [98], a feedback online optimization correction part is added to an MPC to adjust the output of the units to balance the difference between the forecasted and actual values at each intra-time sample. The time step of the MPC optimization is 15 minutes while the intra-time sample of the online optimization is one minute. The adopted objectives and constraints for the online optimization problem are the same as those of the offline optimization with adequate shaping of equations.

In this chapter, an adaptive online optimization stage is applied to update the offline power references due to the occurring mismatches between predicted and actual data. The obtained results are validated through several simulation tests and compared with the offline optimization results to prove the effectiveness and viability of the online optimization stage.

4.2 Online optimization stage

The offline and online optimization block diagrams are depicted in Fig.4.1. As detailed in Chapter 3, the offline optimization is applied the day ahead for the next 24 hours. Besides, the offline optimization has a 24-hour time horizon with a sampling period $T_s = 1/6$ hour. It outputs the optimal power references of dispatchable sources which are P_{DG_ref}, P_{grid_ref}, and P_{batt_ref} for the next 24 hours. In offline optimization, the time domain is discretized at each $T_s = 1/6$ hour into ($N = 144$) total number of steps for the whole-time horizon. Any optimal power reference at time k is denoted $P_{grid_ref}\,(k)$, $P_{batt_ref}\,(k)$, and $P_{DG_ref}\,(k)$ with $k = 1, 2, \dots, N$. As stated before, these optimal power references are computed based on predicted input data denoted : v_{wind_pred}, S_{pred}, T_{a_pred}, P_{load_pred}, and $\delta^{pur}_{grid_pred}$ which correspond respectively to the predicted wind speed in (m/s), the predicted solar irradiance in (W/m^2), the predicted ambient temperature in ($°C$), the predicted residential load profile in (W), and the electricity purchased price in ($¢/KWh$) for the whole time horizon (i.e. 24 hours).

The predictions' accuracy, mathematical modeling, and correlation with actual data are separate study subjects, investigated independently in the literature, and are out of the scope of this thesis. Without loss of generality, a random deviation is added to the predicted data to simulate the mismatches between predicted and actual data. The sign and span of the deviation between the

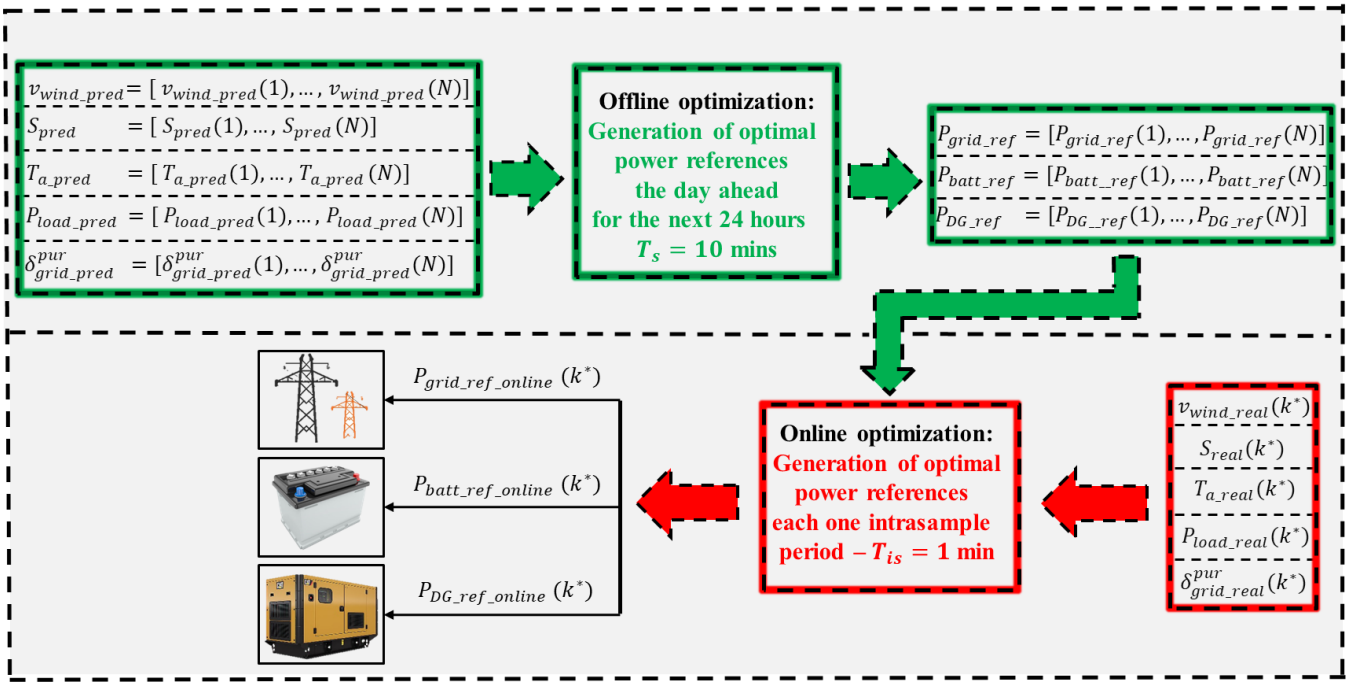


Fig.4.1 Block diagram of the applied offline and online optimization stages.

predicted and actual produced/consumed energy and purchased electricity prices are detailed in the simulation tests section. Therefore, in all that follows, there will always be mismatches between predicted and actual input data. As seen in Fig.4.1, the online optimization stage takes as inputs the offline power references and actual measured data each minute. The actual input data at the time $k^*$are denoted : $v_{wind_real}(k^*)$, $S_{real}(k^*)$, $T_{a_real}(k^*)$, $P_{load_real}(k^*)$, and $\delta^{pur}_{grid_real}(k^*)$. The online optimization stage is ten times faster than the offline optimization references, then each sampling period $T_s = 1/6$ hour is discretized in turn into several intrasample periods ($T_{is} = 1/60$ hour). The total number of intrasample periods in each sampling period equals $(T_s / T_{is}) = 10$. As a result, the total number of intrasample steps for the whole time horizon is denoted N^* and is expressed as follows:

$$N^* = N \times 10 = 1440 \quad \text{(IV.1)}$$

Thus, the optimal online power references are denoted $P_{grid_ref_online}(k^*)$, $P_{batt_ref_online}(k^*)$, and $P_{DG_ref_online}(k^*)$ with $k^* = 1, 2, \dots, N^*$.

4.2.1 The online optimization stage target

In the absence of any online optimization stage, the offline optimized power references are applied without any update. Thus, existent mismatches between actual and predicted data result in an inequality in the microgrid power balance equation. The power imbalance leads to a deviation in the common DC bus voltage causing an unstabilized operation of the DC microgrid. To overcome this hurdle, one of the operating converters of dispatchable sources always takes charge of

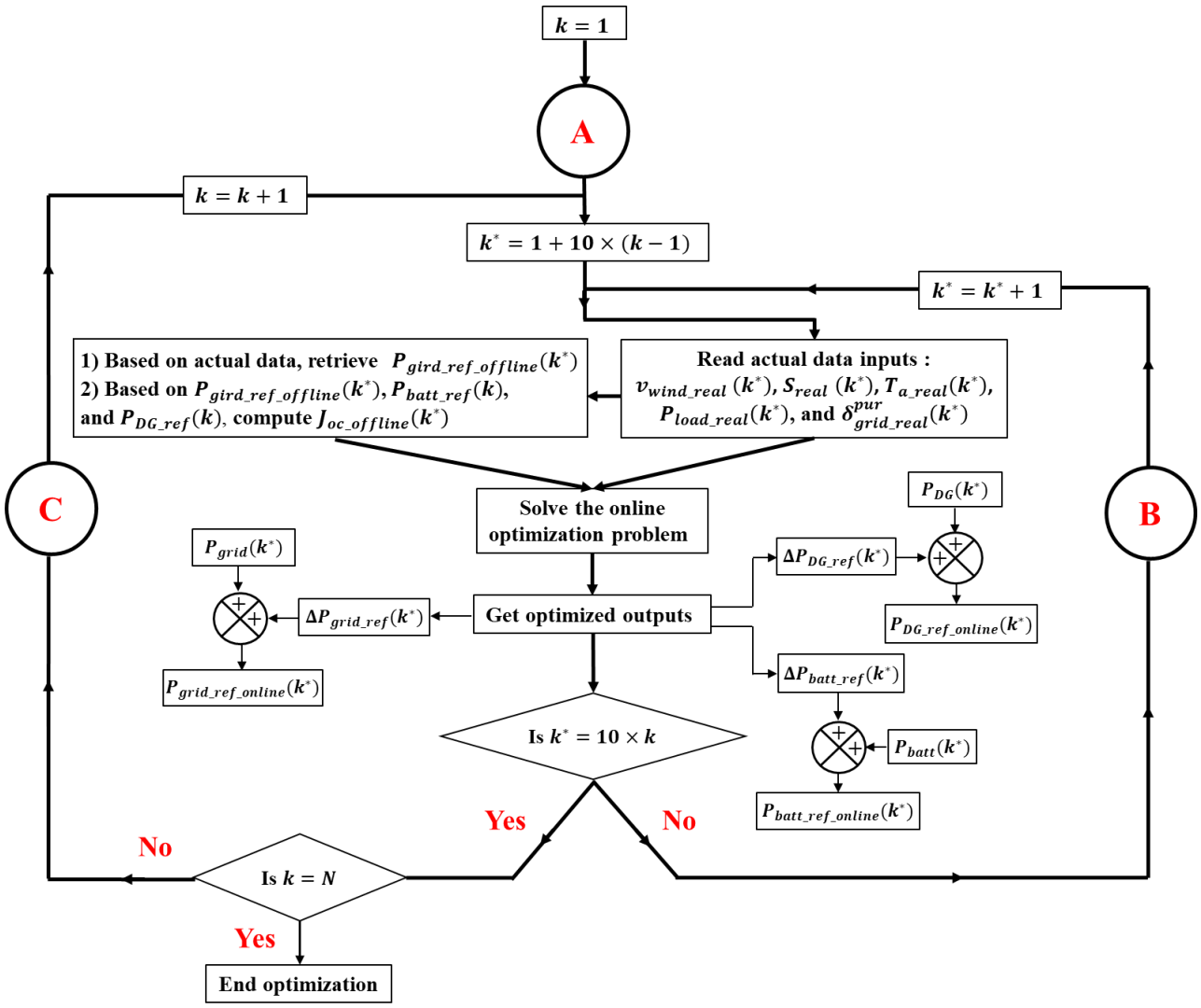
stabilizing the common DC bus voltage[156]. Thus, the selected converter compensates for the occurring power mismatches. Applications with no active online optimization controller, usually adopt the utility grid as a slack bus for the corrective action needed to compensate for the uncertainties[157]. However, this solution may not be optimal especially, at high pool prices. Besides, for time intervals where the actual pool prices are lower than the predicted ones, the optimal solution may be to purchase additional energy from the grid and rely less on the ESS or the (DG). As seen, several scenarios can be encountered in which always selecting the utility grid to compensate for the power mismatches doesn't lead to the optimal solution.

From the above, the online optimization stage should find a feasible solution following the same predefined offline objectives and system constraints. Applying the online correction part, all dispatchable sources can intervene in the new power mix through their updated reference values. The obtained solution must restore the power balance equality in case of a power imbalance and modify the power references of dispatchable sources conveniently to the actual electricity pool prices. Hence, the mission of online optimization can only be accomplished if it provides improved results over those that would be obtained in the case of offline optimization.

On the other hand, unlike offline optimization which finds the optimal path for the whole-time horizon, the online optimization correction stage is applied for one intrasample period T_{is} as seen in Fig.4.1. Although online optimization is run N^* times at the end of the time horizon and finds N^* optimal solutions corresponding to each intrasample, the obtained results do not correspond to the new optimal solution for the actual whole-time horizon.
As a result, the online optimization stage is not advanced as an alternative to offline optimization and must not rebuild the optimal path for the whole-time horizon. Besides, the SOC online trajectory should always maintain a close path and shape to the proposed offline optimal one. Otherwise, offline optimization will permanently offer the optimal solution for the whole-time horizon despite the existent mismatches. Therefore, the online optimization stage performs local optimizations at each intrasample to improve the obtained results at the end of the time horizon while maintaining the general optimal path built by offline optimization. All cited criteria and objectives are included when formulating the online optimization problem in the next paragraph.

4.3 Online optimization algorithm

The flow chart of the proposed online optimization controller is represented in Fig.4.1. As seen in the flow chart, the online optimization variables are the changes in P_{grid_ref}, SOC_{ref}, and P_{DG_ref} over one intrasample period denoted respectively ΔP_{grid_ref}, ΔSOC_{ref}, and ΔP_{DG_ref}. Thus, if the online optimization variables are stored in one vector named Δx then, Δx (k^*), at a given time k^*, corresponds to the vector $\left[\Delta P_{grid_ref}(k^*) \quad \Delta SOC_{ref}(k^*) \quad \Delta P_{DG_ref}(k^*)\right]$.



A

Based on $P_{gird_ref}(k)$, $P_{batt_ref}(k)$, and $P_{DG_ref}(k)$:
1) Set lower and upper bounds of online variables for the next step
$[\Delta P_{grid_ref}(k^*) \quad \Delta SOC_{ref}(k^*) \quad \Delta P_{DG_ref}(k^*)]$
2) Set $P_{grid}(k^*) = P_{gird_ref}(k)$, $P_{batt}(k^*) = P_{batt_ref}(k)$, and $P_{DG}(k^*) = P_{DG_ref}(k)$

B

Based on $P_{gird_ref_online}(k^*)$, $P_{batt_ref_online}(k^*)$, and $P_{DG_ref_online}(k^*)$:
1) Set lower and upper bounds of online variables for the next step:
$[\Delta P_{grid_ref}(k^* + 1) \quad \Delta SOC_{ref}(k^* + 1) \quad \Delta P_{DG_ref}(k^* + 1)]$
2) Set $P_{grid}(k^* + 1) = P_{gird_ref_online}(k^*)$, $P_{batt}(k^* + 1) = P_{batt_ref}(k)$, and $P_{DG}(k^* + 1) = P_{DG_ref_online}(k^*)$,

C

Based on $P_{gird_ref_online}(k^*)$, $P_{batt_ref_online}(k^*)$, and $P_{DG_ref_online}(k^*)$:
1) Set lower and upper bounds of online variables for the next step:
$[\Delta P_{grid_ref}(k^* + 1) \quad \Delta SOC_{ref}(k^* + 1) \quad \Delta P_{DG_ref}(k^* + 1)]$
2) Set $P_{grid}(k^* + 1) = P_{gird_ref_online}(k^* + 1)$, $P_{batt}(k^* + 1) = P_{batt_ref}(k + 1)$, and $P_{DG}(k^* + 1) = P_{DG_ref}(k + 1)$

Fig.4.2 Flow chart of the proposed online optimization controller.

For the first sampling period T_s, corresponding to $k = 1$, and the first intrasample period T_{is} corresponding to $k^* = 1$, the lower and upper bounds of online variables respectively $lb(k^*)$ and and $ub(k^*)$, are fixed based on the offline optimization references $P_{grid_ref}\ (1)$, $SOC_{ref}\ (1)$, and $P_{DG_ref}\ (1)$ as follows:

$$\begin{cases} lb\ (k^* = 1) = \left[P_{grid_min} - P_{grid_ref}\ (1) \quad SOC_{min} - SOC_{ref}\ (1) \quad - P_{DG_ref}\ (1)\right] \\ ub\ (k^* = 1) = \left[P_{grid_max} - P_{grid_ref}\ (1) \quad SOC_{max} - SOC_{ref}\ (1) \quad P_{DG_max} - P_{DG_ref}\ (1)\right] \end{cases} \tag{IV.2}$$

min and max subscripts denote respectively the minimum and maximum admissible values represented in Chapter 3.
Besides, $P_{grid}(k^* = 1)$, $P_{batt}(k^* = 1)$, $P_{DG}(k^* = 1)$ are respectively set to $P_{grid_ref}\ (1)$, $P_{batt_ref}\ (1)$, and $P_{DG_ref}\ (1)$. At any given time k^*, the outputted online optimal power references are expressed as follows:

$$\begin{cases} P_{grid_ref_online}\ (k^*) = P_{grid}\ (k^*) + \Delta P_{grid_ref}\ (k^*) \\ P_{batt_ref_online}\ (k^*) = P_{batt}\ (k^*) + \Delta P_{batt_ref}\ (k^*) \\ P_{DG_ref_online}\ (k^*) = P_{DG}\ (k^*) + \Delta P_{DG_ref}\ (k^*) \end{cases} \tag{IV.3}$$

In the next step, the actual data inputs are read and applied as inputs to the online optimization problem. Furthermore, they are utilized to compute the potential grid power value that would be obtained if no online optimization stage is applied, and the grid converter only compensates for all existing power mismatches. This grid power value at the time k^*, denoted $P_{grid_ref_offline}\ (k^*)$, is utilized along with the remaining offline optimization power references: $P_{batt_ref}\ (k)$ and $P_{DG_ref}\ (k)$ to compute the total cost function in the absence of the online optimization stage at the time k^* denoted $J_{tot_offline}\ (k^*)$. The total cost function is affected by the subscript "offline" to designate the case in which the offline optimized power references are applied without an online optimization stage. In turn, $J_{tot_offline}\ (k^*)$ is applied as input to the online optimization problem which computes the online total cost function at the time k^*, denoted $J_{tot_online}\ (k^*)$, and minimizes the difference between the two functions as follows:

$$\min_{\Delta x(k^*)} \left(J_{tot_online}\ (k^*) - J_{tot_offline}\ (k^*)\right) \tag{IV.4}$$

The offline and online cost functions and constraints' expressions are detailed in the next paragraph.

Once the online optimization problem is solved, the optimal online outputs at the time k^* which are $\left[\Delta P_{grid_ref}(k^*) \quad \Delta P_{batt_ref}(k^*) \quad \Delta P_{DG_ref}(k^*)\right]$ are retrieved. Then, the optimal online

power references $P_{grid_ref_online}\ (k^*)$, $P_{batt_ref_online}\ (k^*)$, and $P_{DG_ref_online}\ (k^*)$ are computed using the expressions of equation (IV.3).

Then $k^*$is compared to $10k$ which indicates the next sampling step as $T_s = 10.T_{is}$. As long as this condition is not fulfilled, the algorithm sets the lower and upper bounds of online variables for the next intrasample step k^*+1, denoted $\Delta x(k^*+1) = [\Delta P_{grid_ref}(k^*+1) \quad \Delta SOC_{ref}(k^*+1) \quad \Delta P_{DG_ref}(k^*+1)]$ based on the current optimal online power references: $P_{grid_ref_online}\ (k^*)$, $P_{batt_ref_online}\ (k^*)$, and $P_{DG_ref_online}\ (k^*)$ as follows:

$$\begin{cases} lb\ (k^*+1) = [P_{grid_min} - P_{grid_ref_online}\ (k^*) \quad SOC_{min} - SOC_{online}\ (k^*) \quad - P_{DG_ref_online}\ (k^*)] \\ ub\ (k^*+1) = [P_{grid_max} - P_{grid_ref_online}\ (k^*) \quad SOC_{max} - SOC_{online}\ (k^*) \quad P_{DG_max} - P_{DG_ref_online}\ (k^*)] \end{cases}$$

(IV.5)

Where $SOC_{online}\ (k^*)$, is the real online SOC value at the time k^*.

In addition, $P_{grid}(k^*+1)$, $P_{batt}(k^*+1)$, $P_{DG}(k^*+1)$, corresponding to the next step k^*+1, are respectively set to $P_{grid_ref_online}\ (k^*)$, $P_{batt_ref}\ (k)$, and $P_{DG_ref_online}\ (k^*)$.
Once k^* reaches $10k$, $P_{grid}(k^*+1)$, $P_{batt}(k^*+1)$, $P_{DG}(k^*+1)$ change respectively to $P_{grid_ref_online}\ (k^*)$, $P_{batt_ref}\ (k+1)$, and $P_{DG_ref}\ (k+1)$. Meanwhile, the lower and upper bounds of online variables for the next intrasample step are always set based on the latest online power references $P_{grid_ref_online}\ (k^*)$, $P_{batt_ref_online}\ (k^*)$, and $P_{DG_ref_online}\ (k^*)$ following equation (IV.5). These steps are all repeated until k reaches N which corresponds to the end of the 24-hour time horizon and the algorithm is terminated.

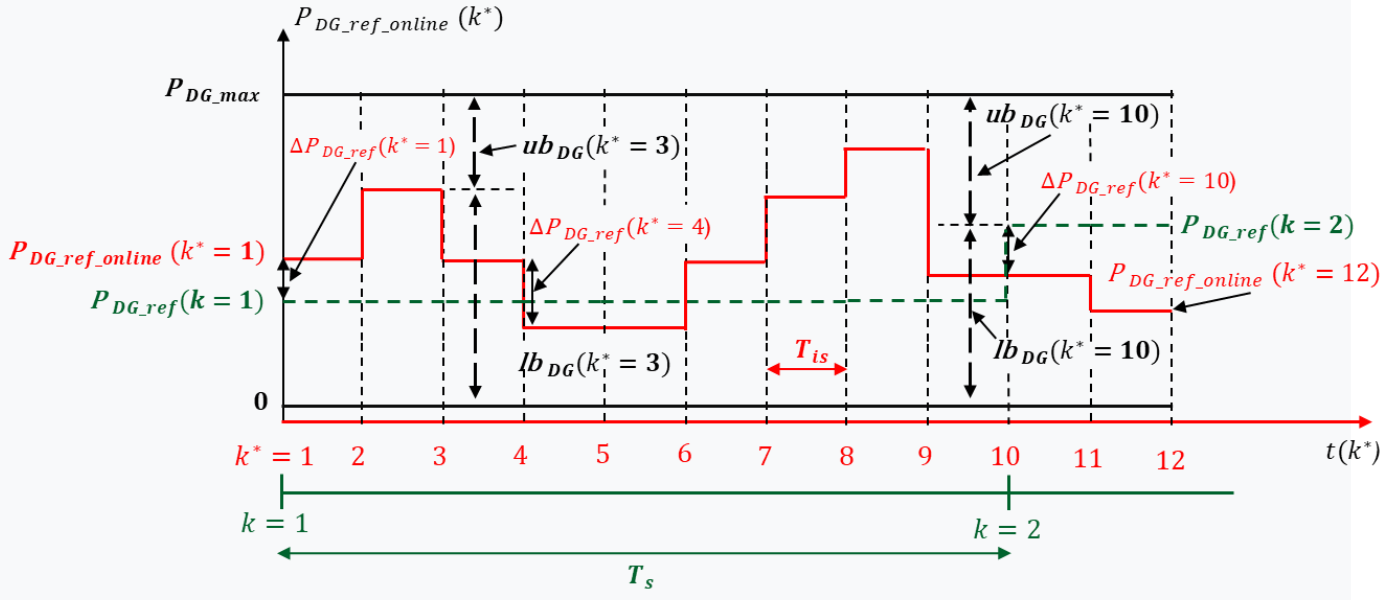


Fig.4.3 Illustrative example of $P_{DG_ref_online}\ (k^*)$ for the first and second sampling steps.

Figures 4.3 and 4.4 show an illustrative example of the proposed online optimization stage for the first and second sampling steps corresponding to $k = 1$ and 2 along with the intrasample steps $k^* = 1, 2, \dots, 12$. Fig. 4.3 shows an admissible trajectory of $P_{DG_ref_online}\ (k^*)$ in which the online variable ΔP_{DG_ref}, the lower and upper bounds respectively denoted lb_{DG} and ub_{DG}, are defined following the flow chart in Fig.4.2. The trajectory curve of $P_{grid_ref_online}\ (\mathrm{k}^*)$ can be plotted following the same strategy as the illustrative example of $P_{DG_ref_online}\ (\mathrm{k}^*)$. A slight difference is noted at each first intrasample step of a new sampling period where $P_{DG}(k^* + 1) = P_{DG_ref}\ (k + 1)$ whereas, $P_{grid}\ (\mathrm{k}^* + 1) = P_{grid_ref_online}\ (\mathrm{k}^*)$.

Fig.4.4 shows an illustrative example of an admissible trajectory of $P_{batt_ref_online}\ (k^*)$. As seen, $P_{batt_ref_online}\ (\mathrm{k}^*)$ differs from $P_{grid_ref_online}\ (\mathrm{k}^*)$ and $P_{DG_ref_online}\ (\mathrm{k}^*)$ in the expression which always equals :

$$P_{batt_ref_online}\ (k^*) = P_{batt_ref}(k) + \Delta P_{batt_ref}\ (k^*) \qquad \text{(IV.6)}$$

with $\mathrm{k}^* = 1 + 10.(k-1),\ 2 + 10.(k-1), \dots, 10 + 10\ (k-1)$ for $k = 1, 2, \dots, N$

Same for the lower and upper bounds of $\Delta P_{batt_ref}\ (k^*)$ which equal respectively $\Delta P_{batt_min} - P_{batt_ref}(k)$ and $\Delta P_{batt_max} - P_{batt_ref}(k)$. ΔP_{batt_min} and ΔP_{batt_max} are respectively the minimum and maximum allowable variations in the battery reference power.

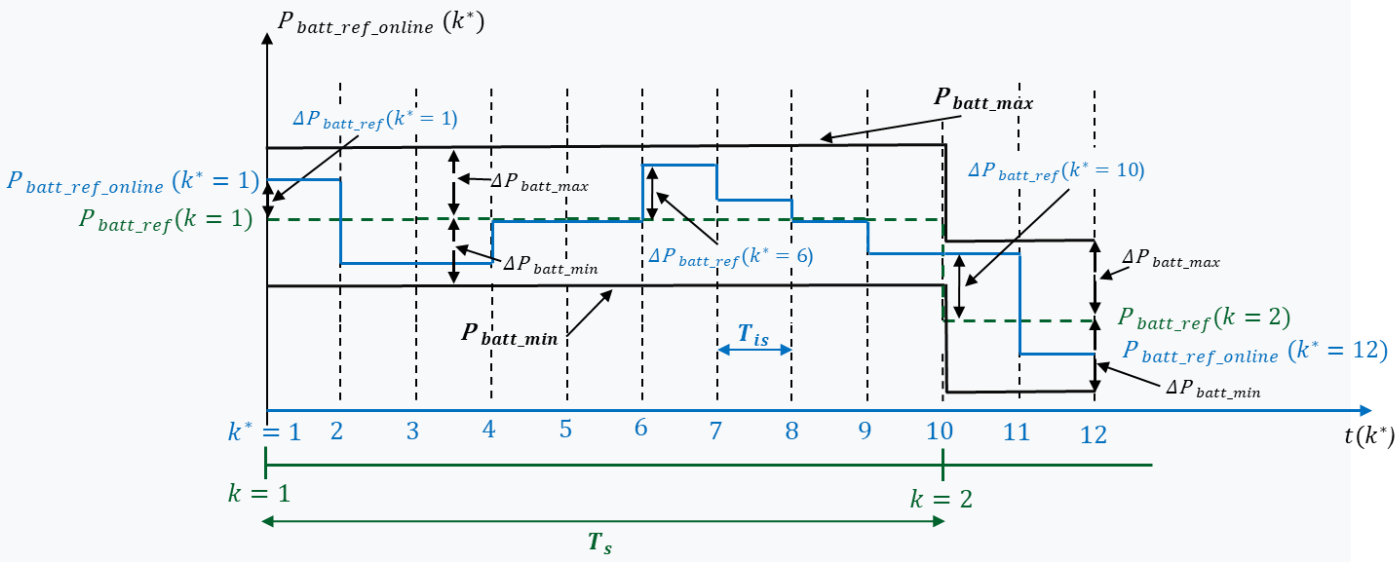


Fig.4.4 Illustrative example of $P_{batt_ref_online}\ (\mathrm{k}^*)$ for the first and second sampling steps.

4.3.1 GS algorithm

To solve the online optimization problem, an algorithm is selected based on two fundamental criteria: the convergence speed and the potential of finding a global minimum. In a real-time simulation, the optimization algorithm which is run in parallel to the DC microgrid simulation

should converge and output the optimal power references before the next intrasample time step. Besides, all obtained solutions should correspond to global and not local minima. Referring to the MATLAB Global Optimization Toolbox, several solvers are proposed to search for global solutions to problems that contain multiple maxima or minima. Among all proposed solvers, the Global Search (GS) algorithm yielded the fastest and most optimized results. As a concept, the GS algorithm starts a local solver (such as $fmincon$) from multiple start points to sample multiple basins of attraction and search for a global minimum. Next, the selected local solver and the GS algorithm's general concept are detailed.

4.3.1.1 Local solver selection

To successfully run the GS algorithm, a local solver should be selected before starting the algorithm. By referring to the MATLAB Global Optimization Toolbox, the $fmincon$ solver is suggested as a local solver when running a GS optimization problem. As a definition, $fmincon$ is a nonlinear programming solver that finds a local minimum of a constrained nonlinear multivariable function. The optimization problem is specified by the following:

$$\min_x f(x) \quad \text{such that} \quad \begin{cases} c(x) \leq 0 \\ ceq(x) = 0 \\ A.x \leq b \\ A_{eq}.x = b_{eq} \\ lb \leq x \leq ub \end{cases} \tag{IV.7}$$

Where,

- $f(x)$ is the function to minimize, named the objective function.
- $c(x)$ is the nonlinear inequality constraints' function that returns a scalar.
- $ceq(x)$ is the nonlinear equality constraints' function that returns a scalar.
- A and b are respectively the matrix and vector of the linear inequality equations.
- A_{eq} and b_{eq} are respectively the matrix and vector of the linear equality equations.
- lb and ub are respectively the lower and upper bounds on the design variables in the vector x.

4.3.1.2 Objective function

The objective function, named the total cost function, J_{tot}, in Chapter 3, was the weighted sum of the operation cost function J_{oc}, the pollutant gas emissions cost function $J_{emissions}$, and the converters' losses cost function J_{conv_losses}. Each of J_{oc}, $J_{emissions}$, and J_{conv_losses} corresponds to a distinct optimization goal. The preference between the three optimization goals was investigated in detail in the previous chapter through the combination of different weight selections. As the main purpose of this chapter is the representation of an online optimization stage

that updates the offline optimized power references due to the mismatches between predicted and actual data, weights of J_{oc}, $J_{emissions}$, and J_{conv_losses} are all set to one (ζ_{oc} = $\zeta_{emissions}$ = ζ_{conv_losses}=1). Hence, there are no preferences between the optimization goals during the online optimization process. Besides, as seen in Chapter 3, the accomplishment of the minimization of the operation cost goal automatically favors the minimization of the converter's losses and vice-versa as the two goals are reconcilable. Thus, and to further simplify the formulation of the online optimization problem, the minimization of converters losses' goal is not considered in the objective function in this chapter. Yet, if the online optimization yields improved results of the operation cost compared to the offline ones, this will automatically improve the results of the converter's losses. This reasoning will be validated in the simulation results section.

By this, the newly applied total cost function only includes the operation cost and the pollutant gas emissions cost functions. An offline and online total cost functions, denoted respectively $J_{tot_offline}(k^*)$ and $J_{tot_online}(k^*)$ and expressed in ($), are established following equations (IV.8) and (IV.9):

$$J_{tot_offline}\,(k^*) = J_{oc_offline}(k^*) + J_{emissions_offline}(k^*) \quad \text{(IV.8)}$$

$$J_{tot_online}\,(k^*) = J_{oc_online}(k^*) + J_{emissions_online}(k^*) \quad \text{(IV.9)}$$

Where, $J_{oc_offline}(k^*)$, $J_{oc_online}(k^*)$, $J_{emissions_offline}(k^*)$, and $J_{emissions_online}(k^*)$ are respectively the offline and online operation costs at the time k^* expressed in ($) and the offline and online pollutant gas emissions costs at the time k^*, expressed in ($).

As the main purpose of the online optimization stage is to improve the offline obtained results, the objective function, $f(x)$ to minimize, is established as the difference between the online and the offline cost functions as expressed in equation (IV.4). Then, $f(x)$ is expressed as follows:

$$f(x) = J_{tot_online}\,(k^*) - J_{tot_offline}\,(k^*) = \Delta J_{oc}(k^*) + \Delta J_{emissions}(k^*) \quad \text{(IV.10)}$$

Where, $\Delta J_{oc}(k^*)$ and $\Delta J_{emissions}\,(k^*)$ are respectively the resulting difference between the online and offline operation costs and the difference between the online and offline pollutant gas emissions costs at the time k^*, expressed in ($).

$\Delta J_{oc}(k^*)$ and $\Delta J_{emissions}(k^*)$ are expressed as follows:

$$\begin{cases} \Delta J_{oc}(k^*) = J_{oc_online}(k^*) - J_{oc_offline}(k^*) \\ \Delta J_{emissions}(k^*) = J_{emissions_online}(k^*) - J_{emissions_offline}(k^*) \end{cases} \quad \text{(IV.11)}$$

Same as Chapter 3, $J_{oc_online}(k^*)$ is expressed as the sum of the power grid cost function at the time k^*, $J_{grid_online}(k^*)$, the battery storage cost function at the time k^*, $J_{batt_online}(k^*)$, and the diesel generator cost function at the time k^*, $J_{DG_online}\,(k^*)$. The same for $J_{oc_offline}(k^*)$ which is expressed as the sum of $J_{grid_offline}(k^*)$, $J_{batt_offline}(k^*)$, and $J_{DG_offline}(k^*)$.

$J_{oc_online}(k^*)$ and $J_{oc_offline}(k^*)$ are represented in equations (IV.5) and (IV.6).

$$J_{oc_online}(k^*) = J_{grid_online}(k^*) + J_{batt_online}(k^*) + J_{DG_online}(k^*) \quad \text{(IV.12)}$$

$$J_{oc_offline}(k^*) = J_{grid_offline}(k^*) + J_{batt_offline}(k^*) + J_{DG_offline}(k^*) \quad \text{(IV.13)}$$

The offline and online power grid cost functions at the time k^* are expressed as follows:

$$J_{grid_offline}(k^*) = \left(\delta^{pur}_{grid_real}(k^*), max(0\ P_{grid_ref_offline}(k^*)) + \delta^{sold}_{grid}, min(0\ P_{grid_ref_offline}(k^*))\right), T_s \quad \text{(IV.14)}$$

$$J_{grid_online}(k^*) = \left(\delta^{pur}_{grid_real}(k^*), max\left(0\ P_{grid_ref_online}(k^*)\right) + \delta^{sold}_{grid}, min\left(0\ P_{grid_ref_online}(k^*)\right)\right), T_s \quad \text{(IV.15)}$$

Where $\delta^{pur}_{grid_real}(k^*)$ and $P_{grid_ref_offline}(k^*)$ are respectively the electricity real purchased price at the time k^* in (¢/KWh) and the grid power reference at the time k^* in (W) that is obtained when no online optimization stage is applied and the utility grid converter compensates for all power mismatches.

At any intrasample step time k^*, $P_{grid_ref_online}(k^*)$ is computed using equation (IV.3). However, $P_{grid_ref_offline}(k^*)$ can be retrieved by solving the following equation:

$$P_{grid_ref_offline}(k^*) = P_{load_real}(k^*) - P_{PV_{real}}(k^*) - P_{wind_{real}}(k^*) + P_{batt_{ref}}(k) - P_{DG_{ref}}(k) - \sum P_{conv_losses_offline}(k^*) \quad \text{(IV.16)}$$

$$\sum P_{conv_losses_offline}(k^*) = P_{losses_bidirec_conv}(k) + P_{losses_3\phi_DG_conv}(k) + P_{boost_losses}(k^*) + P_{losses_3\phi_grid_conv}(k^*) + P_{losses_3\phi_WT_rec}(k^*) \quad \text{(IV.17)}$$

with $k^* = 1 + 10.(k-1),\ 2 + 10.(k-1), \ldots, 10 + 10\ (k-1)$ for $k = 1, 2, \ldots,\ N$

Where,

- $P_{load_real}(k^*)$, is the real load consumption at the time k^*.
- $P_{PV_real}(k^*)$, is the real PV-generated power at the time k^*.
- $P_{wind_real}(k^*)$, is the real wind-generated power at the time k^*.
- $P_{batt_ref}(k)$, is the offline battery reference power at the time k.
- $P_{DG_ref}(k)$, is the offline (DG) reference power at the time k.
- $\sum P_{conv_losses_}\text{offline}(k^*)$, are the total losses in all operating converters if no online optimization stage is applied at the time k^*.
- $P_{losses_bidirec_conv}(k)$, are the losses in the battery converter at the time k.
- $P_{losses_3\phi_DG_conv}(k)$, are the losses in the (DG) converter at the time k.
- $P_{losses_3\phi_WT_rec}$, are the losses in the (WT) 3ϕ rectifier at the time k^*.
- $P_{losses_3\phi_grid_conv}(k^*)$, are the losses in the grid converter if no online optimization stage is applied at the time k^*.

- $P_{boost_losses}(k^*)$, are the losses in the PV converter at the time k^*.

As seen in Chapter 2, $P_{losses_3\phi_grid_conv}(k^*)$ is a function of $P_{grid_ref_offline}(k^*)$ then, $P_{grid_ref_offline}(k^*)$ is the only unknown variable of the equation. Besides, as equations (IV.16) and (IV.17) denote the power balance equation of the system without the online optimization stage, the battery and (DG) power references and corresponding converters' losses are all the same for all intrasample periods (T_{is}) comprising in a sampling period T_s. As stated before, after 10 intrasample steps, all read offline input data moves one period forward from the time k to $k+1$. To solve equation (IV.9), the syntax "*solve*" in MATLAB is applied to find $P_{grid_ref_offline}(k^*)$.

The expressions of the battery online and offline cost functions are the same as equation (III.13) in Chapter 3. The only difference is that they are computed for one intrasample period and not for the whole time horizon as in Chapter 3. They are expressed as follows:

$$J_{batt_online}(k^*) = \left(\frac{CC}{2.Cycles}.P_{batt_ref_online}(k^*) + \delta_{deg}.P(k^*)^2_{batt_ref_online}\right)T_{is} \quad \text{(IV.18)}$$

$$J_{batt_offline}(k^*) = \left(\frac{CC}{2,Cycles},P_{batt_ref}(k) + \delta_{deg},P(k)^2_{batt_ref}\right)T_{is} \quad \text{(IV.19)}$$

$P_{batt_ref_online}(k^*)$ is computed following the bellow equation:

$$P_{batt_ref_online}(k^*) = P_{batt_ref}(k) + \Delta P_{batt_ref}(k^*) \quad \text{(IV.20)}$$

With $k^* = 1 + 10.(k-1),\ 2 + 10.(k-1), \dots, 10 + 10\,(k-1)$ for $k = 1, 2, \dots,\ N$

$\Delta P_{batt_ref}(k^*)$ at the time k^*can be found through the online variable $\Delta SOC_{ref}(k^*)$ using the bellow expression:

$$\Delta P_{batt_ref}(k^*) = -\frac{Q(T_a),V_{batt}(k^*)}{T_{is}}\Delta SOC_{ref}(k^*) \quad \text{(IV.21)}$$

$\Delta SOC_{ref}(k^*)$ is the change in the battery's SOC over one intrasample period. It is expressed as follows:

$$\Delta SOC_{ref}(k^*) = SOC_{online}\,(k^*+1) - SOC_{online}\,(k^*) \quad \text{(IV.22)}$$

The calculation of $Q(T_a)$ and $V_{batt}(k^*)$ is detailed in Appendix E.

The (DG) online and offline cost functions at the time k^*, $J_{DG_online}(k^*)$ and $J_{DG_offline}(k^*)$, consist of the fuel consumption cost function at the time k^*, $J_{DG}^{fuel}(k^*)$, expressed as follows:

$$J_{DG}^{fuel}(k^*) = \lambda_{fuel},F(k^*),T_{is} \quad \text{(IV.23)}$$

Knowing $F(k^*)$ is a function of $P_{DG_ref}(k)$ for the offline optimization and a function of $P_{DG_ref_online}(k^*)$ for the online optimization process. To obtain $F(k^*)$, we refer to the plotted curve of Fig.3.5. $P_{DG_ref_online}(k^*)$ is calculated using equation (IV.3).

The start-up cost function and the maintenance cost functions of the (DG) are not included in the online optimization feedback as they account for a minor cost from the (DG) total operating cost as well as they were considered in the day ahead offline optimization.

Finally, as the pollutant gas emissions cost function is a linear equation (equation (III.19)), the resulting difference between the online and offline pollutant gas emissions costs at the time k^* can be directly expressed as:

$$\Delta J_{emissions}(k^*) = \beta_{emiss}, (P_{DG_ref_online}(k^*) - P_{DG_ref}(k)), T_{is} \quad \text{(IV.24)}$$

With $k^* = 1 + 10.(k-1),\ 2 + 10.(k-1), \dots, 10 + 10\,(k-1)$ for $k = 1, 2, \dots,\ N$

4.3.1.3 Lower and upper bounds (lb & ub)

The lower and upper bounds, respectively $lb(k^*)$ and $ub(k^*)$ of the online variables $[\Delta P_{grid_ref}(k^*)\ \Delta SOC_{ref}(k^*)\ \Delta P_{DG_ref}(k^*)]$, at any given time k^* are defined following the flow chart of Fig.4.2 and equations (IV.2) and (IV.5).

4.3.1.4 Constraints

In the online optimization stage, all equality and inequality constraints which are shown in Chapter 3 are defined as nonlinear constraints. Hence, the linear equality and inequality constraint matrices A_{eq} and A equal empty matrices ($A_{eq} = []$, $A = []$) and their corresponding vectors, respectively b_{eq} and b, equal empty vectors ($b_{eq} = []$, $b = []$). Therefore, $c(x) \leq 0$ and $ceq(x) = 0$ functions are utilized to define respectively all inequality and equality constraints. In this case, $c(x)$ and $ceq(x)$ consist each of an array of functions represented as follows:

$$c(x) = \begin{bmatrix} c_1(x); \\ c_2(x); \\ \dots; \\ c_{n_ic}(x); \end{bmatrix} \quad \text{and} \quad ceq(x) = \begin{bmatrix} ceq_1(x); \\ ceq_2(x); \\ \dots; \\ ceq_{n_ec}(x); \end{bmatrix} \quad \text{(IV.25)}$$

Where, $c_1(x)$, $c_2(x)$, $c_{n_c}(x)$, $ceq_1(x)$, $ceq_2(x)$, and $ceq_{n_c}(x)$ are respectively the inequality and equality constraints functions. n_ic and n_ec are respectively the total numbers of inequality and equality constraints.

In our case, two inequality functions are needed to express the two constraints on the (DG) that were presented in Chapter 3 by equations (III.27) and (III.28). The two constraints are expressed as follows:

$$c_1\big(x(k^*)\big) = P_{DG_min}.sign\left(P_{DG_ref_online}(k^*)\right) - P_{DG_ref_online}(k^*) \quad \text{(IV.26)}$$

$$c_2\big(x(k^*)\big) = -sign\left(P_{DG_ref_online}(k^*)\right), P_{grid_ref_online}\ (k^*) \quad \text{(IV.27)}$$

One equality function is required to express the power balance equation represented in Chapter 3 by equations (III.21) and (III.22). The equality constraint is expressed as follows:

$$ceq_1\big(x(k^*)\big) = P_{grid_ref_online}\ (k^*) + P_{batt_ref_online}\ (k^*) + P_{DG_ref_online}(k^*) - \sum P_{conv_losses_online}(k^*) - P_{load_real}\ (k^*) + P_{PV_real}\ (k^*) + P_{wind_real}\ (k^*) \quad \text{(IV.28)}$$

$$\sum P_{conv_losses_online}(k^*) = P_{losses_bidirec_conv}\ (k^*) + P_{boost_losses}(k^*) + P_{losses_3\phi_DG_conv}(k^*) + P_{losses_3\phi_WT_rec}(k^*) + P_{losses_3\phi_grid_conv}(k^*) \quad \text{(IV.29)}$$

An additional constraint should be added on $\Delta P_{batt_ref}(k^*)$ to restrict the changes in the battery-charged/discharged power at each intrasample time k^*. In normal operating conditions, $\Delta P_{batt_ref}(k^*)$ should range between a minimum and a maximum value, denoted respectively ΔP_{batt_min} and ΔP_{batt_max}. The normal operating conditions correspond to an admissible battery SOC at a given time k^*, $SOC_{online}\ (k^*)$, within the minimum and maximum thresholds, respectively SOC_{min} and SOC_{max}.

To verify if $SOC_{online}\ (k^*)$ lies within the admissible limits, we refer to the lower and upper bounds of $\Delta SOC_{ref}(k^*)$ variable, denoted respectively $lb_{\Delta SOC_{ref}}(k^*)$ and $ub_{\Delta SOC_{ref}}(k^*)$. At a given time k^*, $lb_{\Delta SOC_{ref}}(k^*)$ and $ub_{\Delta SOC_{ref}}(k^*)$ are expressed as follows:

$$\begin{cases} lb_{\Delta SOC_{ref}}(k^*) = SOC_{min} - SOC_{online}\ (k^*) \\ ub_{\Delta SOC_{ref}}(k^*) = SOC_{max} - SOC_{online}\ (k^*) \end{cases} \quad \text{(IV.30)}$$

Hence, If $lb_{\Delta SOC_{ref}}(k^*) < 0$ and $ub_{\Delta SOC_{ref}}(k^*) > 0$, then $SOC_{min} < SOC_{online}\ (k^*) < SOC_{max}$ and the ESS can contribute either by charging/discharging to the power mix of the DC microgrid. In this operating condition, named "*normal_ESS*", an additional inequality constraint function is added to limit $\Delta P_{batt_ref}(k^*)$ within ΔP_{batt_min} and ΔP_{batt_max}. The constraint is expressed as follows:

$$c_3\big(x(k^*)\big) = \left|\Delta P_{batt_ref}(k^*)\right| - \Delta P_{batt_max} \quad \text{(IV.31)}$$

We take note that ΔP_{batt_min} and ΔP_{batt_max} are respectively the minimum and maximum admissible changes in the battery power and have negative and positive constant values. In the rest, we consider equal magnitudes of ΔP_{batt_min} and ΔP_{batt_max}. Then, $\Delta P_{batt_max} = |\Delta P_{batt_min}|$.

On the other hand, If $lb_{\Delta SOC_{ref}}(k^*) \geq 0$ or $ub_{\Delta SOC_{ref}}(k^*) \leq 0$, then $SOC_{online}\ (k^*)$ has reached one of the allowable thresholds, SOC_{min} or SOC_{max}. In this operating condition, four subcases arise following the value of $P_{batt_ref_online}\ (k^*)$ which equals $P_{batt_ref}(k) + \Delta P_{batt_ref}(k^*)$ (equation (IV.20)). The four subcases are the following:

1. $lb_{\Delta SOC_{ref}}(k^*) \geq 0$ & $P_{batt_ref}(k) + \Delta P_{batt_ref}(k^*) > 0$: the battery has reached SOC_{min} and the proposed solution requires discharging power from the battery. To guarantee the safe operation of the ESS, this request is denied and the battery switches to a floating mode in which $P_{batt_ref}(k) + \Delta P_{batt_ref}(k^*) = 0$ to maintain $SOC_{online}\ (k^*)$ at SOC_{min}. In this operating condition, named "*low_limit_ESS*", $c_3\big(x(k^*)\big)$ is not included as a constraint and substituted instead with an equality constraint, $ceq_2\big(x(k^*)\big)$, expressed as follows:

   $$ceq_2\big(x(k^*)\big) = P_{batt_ref}(k) + \Delta P_{batt_ref}(k^*) \quad \text{(IV.32)}$$

2. $lb_{\Delta SOC_{ref}}(k^*) \geq 0$ & $P_{batt_ref}(k) + \Delta P_{batt_ref}(k^*) \leq 0$: the battery has reached SOC_{min} and the proposed solution requires charging power in the battery. In this condition, named "*low_limit_charge_ESS"*, there is no need to activate the floating mode and the system constraints are the same as in the "*normal_ESS*" condition.

3. $ub_{\Delta SOC_{ref}}(k^*) \leq 0$ & $P_{batt_ref}(k) + \Delta P_{batt_ref}(k^*) < 0$: the battery has reached SOC_{max} and the proposed solution requires charging power in the battery. To guarantee the safe operation of the ESS, this request is denied and the battery switches to a floating mode in which $P_{batt_ref}(k) + \Delta P_{batt_ref}(k^*) = 0$ to maintain $SOC_{online}\ (k^*)$ at SOC_{max}. This operating condition is named "*high_limit_ESS*" and has the same system constraints as the "*low_limit_ESS*" condition.

4. $ub_{\Delta SOC_{ref}}(k^*) \leq 0$ & $P_{batt_ref}(k) + \Delta P_{batt_ref}(k^*) \geq 0$: the battery has reached SOC_{max} and the proposed solution requires discharging power from the battery. In this condition, named "*high_limit_discharge_ESS"*, there is no need to activate the floating mode and the system constraints are the same as in the "*normal_ESS*" condition.

Finally, included in Chapter 3 by equation (III.26), the constraint of retrievement of the battery's SOC initial state ($k = 0$) at the end of the time horizon ($k = N$) is not retained in this chapter. By this, the battery's online state at the end of the time horizon, $SOC_{online}\ (k^* = N^*)$, can have any

random value between SOC_{min} and SOC_{max}. All system constraints based on the defined operating conditions of the ESS are summarized in Table 4.1.

Operating condition	Inequality constraints: $c(x(k^*))$	Equality constraints: $ceq(x(k^*))$
normal_ESS	$[c_1(x(k^*)); c_2(x(k^*)); c_3(x(k^*))]$	$ceq_1(x(k^*))$
low_limit_ESS	$[c_1(x(k^*)); c_2(x(k^*))]$	$[ceq_1(x(k^*)); ceq_2(x(k^*))]$
high_limit_ESS	$[c_1(x(k^*)); c_2(x(k^*))]$	$[ceq_1(x(k^*)); ceq_2(x(k^*))]$
low_limit_charge_ESS	$[c_1(x(k^*)); c_2(x(k^*)); c_3(x(k^*))]$	$ceq_1(x(k^*))$
high_limit_discharge_ESS	$[c_1(x(k^*)); c_2(x(k^*)); c_3(x(k^*))]$	$ceq_1(x(k^*))$

Table 4.1 Corresponding inequality and equality constraints of all operating conditions.

4.3.1.5 GS algorithm

This section advances a brief description of the main steps performed by the GS algorithm when it is run along with corresponding Matlab functions and parameters. For a detailed description of the GS algorithm, it can be referred to [158]. First, to run the GS algorithm through Matlab, a GS object containing several properties is created using the command "*GlobalSearch*". If the object is named gs, then the syntax: $gs = GlobalSearch$ creates gs, a GlobalSearch solver with its properties set to the defaults. The main properties of the GS are detailed as the main steps performed by the algorithm are cited.

Second, GS requires a local solver that will be started from multiple start points. In this case, the chosen solver is " *fmincon* " and it can be added as a local solver for the GS algorithm by creating an optimization problem structure using the command: "*CreateOptimProblem*". The command has the following syntax: problem = *CreateOptimProblem* ('solverName', 'ParameterName', ParameterValue,…). In our case, the syntax is the following:

problem = *CreateOptimProblem* ('fmincon', 'x0', x_0, 'objective', $f(x)$, 'Aineq', A, 'bineq', b, 'Aeq', A_{eq}, 'beq', b_{eq}, 'lb', lb, 'ub', ub, 'nonlcon', [$c(x), ceq(x)$]).

Where,

- 'x0', is the starting point from which *fmincon* is run. In this case, it is a starting vector with the same structure and dimension as the online variable Δx which is an array of 3 variables $[\Delta P_{grid_ref} \quad \Delta SOC_{ref} \quad \Delta P_{DG_ref}]$. The starting vector is denoted x_0 and is set as follows:

$$x_0 = lb + rand(size(lb)), (ub - lb) \tag{IV.33}$$

The command "$rand$" is used to generate a random vector with the same size as the lower bound vector. As *fmincon* solver is run N^* times from the start to the end of the time horizon, we may have the interest to run each time the solver from a different starting vector which favors the exploitation of all possible solutions and the finding of a global minimum.

- 'objective', is the objective function to minimize, it is $f(x)$ in this case (equation (IV.10)).
- 'Aineq', 'bineq', 'Aeq', and 'beq', are respectively the linear inequality matrix and corresponding vector, and the equality matrix and corresponding vector. They are respectively equal to A, b, A_{eq}, and b_{eq}.
- 'lb' and 'ub', are respectively the lower and upper bounds and are equal to lb and ub (equations (IV.2) and (IV.5)).
- 'nonlcon', are the nonlinear inequality and equality constraints and are equal in this case to the two arrays $[c(x), ceq(x)]$.

Finally, several parameters and functions of the local solver *fmincon* must be set appropriately to the formulated problem to correctly run the solver. These parameters have default values set by Matlab and can be modified in the optimization options. Among several parameters, we cite the fundamental ones that were selected in this case study and yielded optimal results in terms of solution feasibility, accuracy, and convergence time.

The first parameter is the Algorithm, in which the optimization algorithm is chosen. In our case, we select the default algorithm *"interior-point"* recommended by Matlab as it handles large, sparse problems, as well as small dense problems. Besides, the maximum number of allowed function evaluations is modified from 3,000 (default value) to 100,000 through the parameter MaxFunctionEvaluations. The maximum number of allowed iterations is set to its default value equal to 1,000 using the parameter MaxIterations. The rest of the parameters are kept at their default values and can be reviewed in detail in the Matlab Help Center. The applied parameters, values, and descriptions are summarized in Table 4.2.

Parameter	Value	Description
Algorithm	Interior-point	Selection of optimization algorithm
MaxFunctionEvaluations	1,000,000	Maximum number of function evaluations allowed
MaxIterations	1,000	Maximum number of allowed iterations

Table 4.2 Parameters for setting the *fmincon* solver.

Once the local solver is selected, the GS algorithm can run to find the optimal solution to the proposed problem. The function "*run*" is utilized to initiate the GS which performs several steps

at each intrasample period. Before citing the main steps, we define the fundamental functions and parameters that are used by the GS algorithm when running.

- *Score*: a function, denoted sc, consisting of the sum of the objective function value, denoted f, at a point and a multiple of the sum of the constraint violations, denoted M_{cv}. So, a feasible point has a score equal to its objective function value. The multiple for constraint violations is initially $M_{cv} = 1000$. GS updates the multiple during the run.
- NumTrialPoints: a parameter that indicates the number of potential start points, specified as a positive integer.
- NumStageOnePoints: a parameter that indicates the number of Stage 1 points, specified as a positive integer.
- localSolverThreshold: a parameter that is initially equal to the smaller of the two objective function values at the solution points. The solution points are the *fmincon* solutions starting from x_0 and the Stage 1 start point, x_{s1}. When running the algorithm, the localSolverThreshold value varies depending on several conditions that are detailed in the main steps below.
- Counters: there are two sets of counters associated with the algorithm. Each counter is the number of consecutive trial points that:
    - lie within a basin of attraction. This counter is denoted c_b and there is one counter for each basin. For instance, the counter of the basin corresponding to the solution x_{0e}, is denoted $c_{b_x_{0e}}$.
    - have a score function greater than localSolverThreshold. This counter is denoted c_{th}.

  All counters are initially set to zero.

- GlobalOptimSolution: an object that contains information on a local minimum, including location, objective function value, and start point or points that lead to the minimum. GS generates a vector of GlobalOptimSolution objects. The vector is ordered by objective function value, from lowest (best) to highest (worst). GS combines solutions that coincide with previously found solutions within tolerances.

- $X_{tolerance}$: a parameter that indicates the tolerance on distance for considering solutions equal, specified as a nonnegative scalar.

- $F_{tolerance}$: a parameter that indicates the tolerance on function values for considering solutions equal, specified as a nonnegative scalar. Solvers consider two solutions identical if they are within $X_{tolerance}$ relative distance from each other and have objective function values within $F_{tolerance}$ relative difference from each other. If both conditions are not met, solvers report the solutions as distinct.

- MaxWaitCycle: a parameter, specified as a positive integer. When c_b and c_{th} reach this parameter value, the basin radius of the corresponding solution point and the localSolverThreshold are modified following the steps mentioned in the branch “react to large counter values” in the main steps performed by GS below.

- BasinRadiusFactor: a basin radius decrease factor, specified as a scalar from 0 to 1. A basin radius decreases after MaxWaitCycle consecutive start points are within the basin.
- PenaltyThresholdFactor: a parameter of increase in the penalty threshold, specified as a positive scalar.

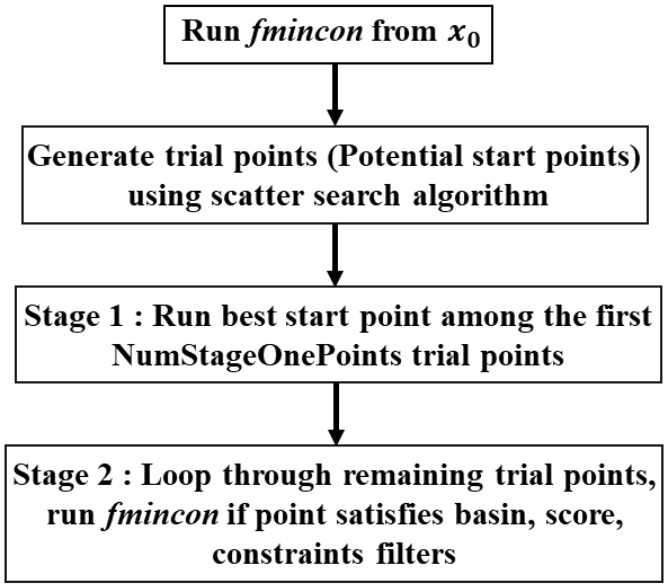


Fig.4.5 Flow chart of the main steps performed by the GS when running.

The main steps performed by the GS when running are represented in Fig.4.2 and detailed as follows:

1. Run *fmincon* from x_0: GS runs *fmincon* from the starting point x_0. If the run converges, GS records the starting point, x_0, and end point, x_{0e}, for an initial estimate of the radius of a basin of attraction. Besides, it records the final objective function value, f_{0e}, for use in the *score* function, $sc_{0e} = f_{0e} + M_{cv_0e}$.
2. Generate trial Points: GS uses the scatter search algorithm, which can be reviewed in detail in [159], to generate a set of NumTrialPoints. These trial points are generated within the defined lower and upper bounds ($\boldsymbol{lb}$ & $\boldsymbol{ub}$) and are not symmetric about the origin. All these trials are potential start points.
3. Obtain Stage 1 Start Point, Run: GS evaluates the *score* function of a set of NumStageOnePoints trial points. Normally, NumStageOnePoints is a fraction of NumTrialPoints. In default settings, NumStageOnePoints = 0.2 × NumTrialPoints. GS then takes the point with the best *score*, x_{s1}, and runs *fmincon* from that point and get the end point, x_{s1e}. It removes the set of NumStageOnePoints trial points from its list of points to examine.
4. Initialize Basins, Counters, Threshold: GS heuristic assumption is that basins of attraction are spherical. The initial estimate of basins of attraction for the solution point of x_0,

x_{0e}, and the solution point from Stage 1 x_{s1}, x_{s1e}, are spheres centered at the solution points. The radius of each sphere is the distance from the initial point to the solution point. These estimated basins can overlap. Fig.4.3 shows an illustrative example of a two-dimensional variable plotted in the space as a function of the objective function. The illustrative example includes 3 spherical basins of attraction for the solution points, x_{0e}, x_{s1e}, and a third solution point denoted x_{pe}.

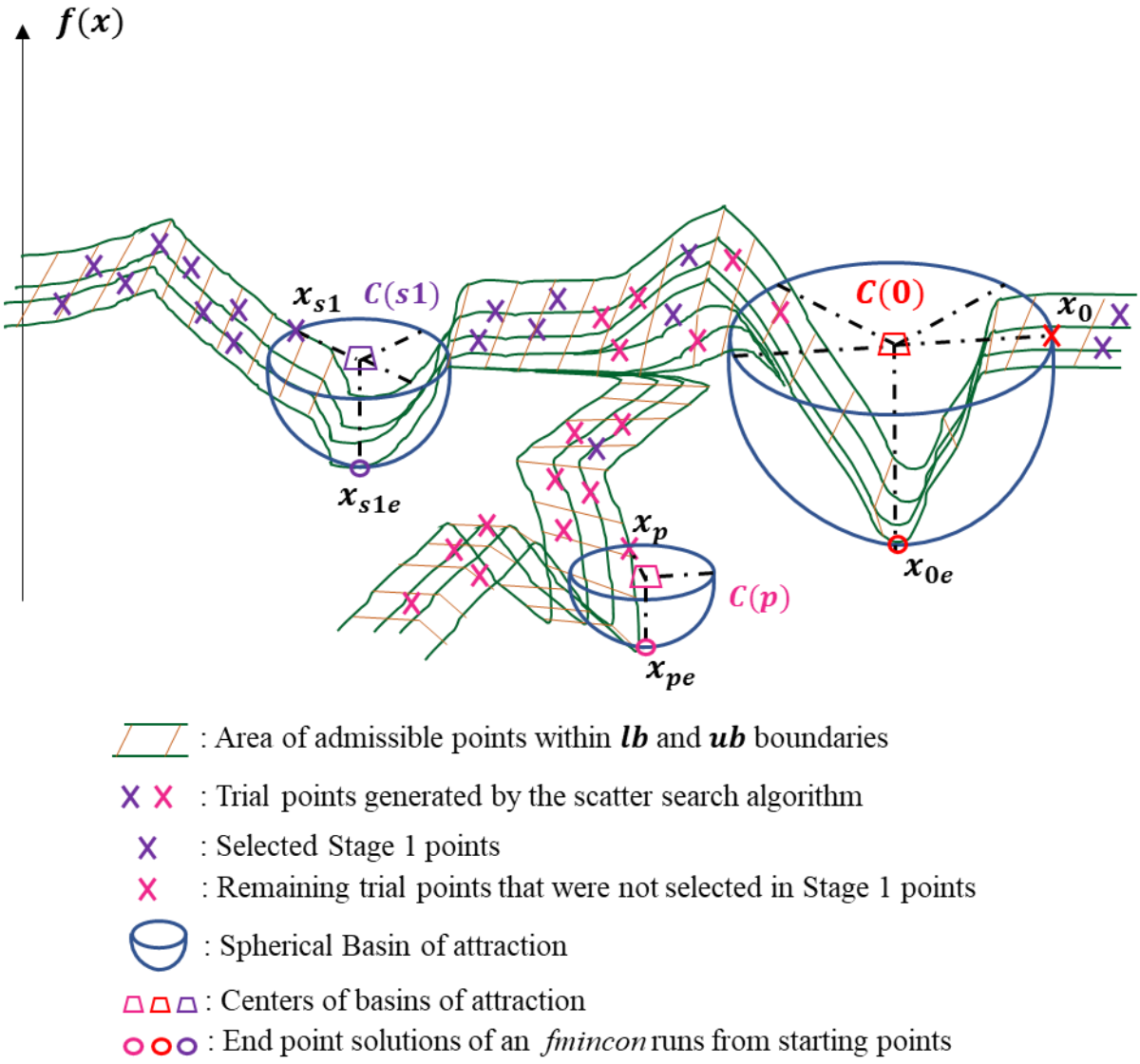


Fig.4.6 An illustrative example of a two-dimensional variable curve plotted in the space as a function of the objective function, showing the basins of attraction and GS-generated trial points.

5. Begin Main Loop: GS repeatedly examines a remaining trial point from the list, continually monitors the time, and stops the search if elapsed time exceeds MaxTime seconds. In this

case, MaxTime seconds is set to infinity then, the algorithm only stops after running out of trial points. The examination of a point consists of the following steps:

- Examine Stage 2 Trial Point to see if *fmincon* runs: call the trial point x_p and run *fmincon* from x_p if the following conditions hold:

  1) x_p is not in any existing basin. The criterion for every basin i is:

     $|x_p - C(i)| >$ DistanceThresholdFactor $\times radius(i)$.

     Where $C(i)$, DistanceThresholdFactor, and $radius$ are respectively the center of a basin (i.e. x_{0e} for the basin of x_0 point, x_{s1e} for the basin of x_{s1} point, etc.), a GS optimization option with a default value of 0.75 and an estimated radius value that is updated in the Update Basin Radius and Threshold and React to Large Counter Values.

  2) $sc_p <$ localSolverThreshold.

  A trial point x_p that verifies the above-mentioned criteria is shown in Fig.4.6.

- When *fmincon* runs :

  1) Reset counters: Set all c_b and c_{th} counters to zero.
  2) Update solution set: If *fmincon* runs starting from x_p, it can converge. In that case, GS updates the vector of GlobalOptimSolution objects. Call the solution point x_{pe} and the objective function value f_p . There are two cases:
     - For every other solution point x_{qe} with an objective function value f_q,

       $|x_{qe} - x_{pe}| > X_{tolerance} \times \max(1, |x_{pe}|)$

       or

       $|f_q - f_p| > F_{tolerance} \times \max(1, |f_p|)$

       In this case, GS creates a new element in the vector of the GlobalOptimSolution objects.
     - For some other solution point x_{qe} with an objective function value f_q,

       $|x_{qe} - x_{pe}| \leq X_{tolerance} \times \max(1, |x_{pe}|)$

       and

       $|f_q - f_p| \leq F_{tolerance} \times \max(1, |f_p|)$

       In this case, GS regards x_{pe} as equivalent to x_{qe} . GS algorithm modifies the GlobalOptimSolution of x_{qe} by adding x_p to the cell array of the already existing points.
  3) Update $c_{b_x_{pe}}$ and c_{th} : if the current *fmincon* run converges, set the localSolverThreshold to the score value at the start point x_p, localSolverThreshold

$= sc_p$, and set the basin radius for x_{pe} equal to the maximum of the existing radius (if any) and the distance between x_p and x_{pe}.

- When *fmincon* does not run:
  1) Update counters: Increment c_b for every basin containing x_p and reset the counter of every other basin to zero. Increment c_{th} if $sc_p \geq$ localSolverThreshold and reset it otherwise.
  2) React to large counter values: For each basin with c_b equal to MaxWaitCycle, multiply the basin radius by 1 − BasinRadiusFactor. Reset c_b to zero.

     If c_{th} equals MaxWaitCycle, increase the localSolverthreshold:

     Set a new localSolverThreshold equal to:

     localSolverThreshold + PenaltyThresholdFactor× (1 + |localSolverThreshold|)

     And, reset c_{th} to zero.

6. Create GlobalOptimSolution: After running out of trial points, GS creates a vector of GlobalOptimSolution objects and orders the vector by objective function value, from lowest (best) to highest (worst). This concludes the algorithm.

Finally, the values of all applied parameters are summarized in Table 4.3.

Parameter	Value	Parameter	Value
NumTrialPoints	1,000	PenaltyThresholdFactor	0.2
BasinRadiusFactor	0.2	$F_{tolerance}$	10^{-6}
MaxWaitCycle	20	$X_{tolerance}$	10^{-6}
NumStageOnePoints	200	MaxTime	infinity

Table 4.3 Applied parameters of the GS algorithm.

4.4 Simulation tests

To prove the viability and effectiveness of the proposed online optimization stage, several simulations with different scenarios are conducted on the two test days that were presented in Chapter 3. Based on the offline predicted input vectors : $\delta^{pur}_{grid_pred}(k)$ and $P_{diff_pred}(k)$ with $k = 1, 2, \dots, N$, new vectors corresponding to the actual data, $\delta^{pur}_{grid_actual}(k^*)$ and $P_{diff_actual}(k^*)$ with $k^* = 1, 2, \dots, N^*$, are created to mimic the mismatches between predicted and actual data inputs.

- $\delta^{pur}_{grid_pred}(k)$ and $\delta^{pur}_{grid_actual}(k^*)$ are respectively the electricity predicted and actual purchased price in $(¢/KWh)$.
- $P_{diff_pred}(k)$ and $P_{diff_actual}(k^*)$ are respectively the predicted and the actual power difference between the load demand and RESs generated power. $P_{diff_pred}(k)$ and $P_{diff_actual}(k^*)$ are expressed as follows:

$$P_{diff_pred}(k) = P_{load_pred}(k) - P_{RESs_bus_pred}(k) \quad \text{(IV.34)}$$

$$P_{diff_actual}(k^*) = P_{load_actual}(k^*) - P_{RESs_bus_actual}(k^*) \quad \text{(IV.35)}$$

Where, $P_{load_pred}(k)$, $P_{load_actual}(k^*)$, $P_{RESs_bus_pred}(k)$, and $P_{RESs_bus_actual}(k^*)$ are respectively the predicted/actual load demand and the predicted/actual RESs generated power taking into consideration the losses in RESs' converters.

All optimization parameters are the same as in Chapter 3 and can be found in Table 3.2. The minimum and maximum admissible changes in the battery power ΔP_{batt_min} and ΔP_{batt_max} are key factors that influence tremendously the results of the online optimization stage. Directly linked to the nominal capacity of the battery, high values of ΔP_{batt_min} and ΔP_{batt_max} leads to extensive usage of the ESS and then, a suboptimal solution meanwhile, extra low values lead to results that approximate the offline optimization ones. Therefore, after several trials and errors, the dedication of a one-sixth ratio out of the nominal storage capacity for the online optimization stage over the whole 24 hours yielded the best results. Knowing that 70% of the total storage capacity is usable, this corresponds to an energy of $87.5\ KWh$, one-sixth of this energy equals $14.6\ KWh$ for the whole time horizon. Then, for one hour the admissible charged/discharged energy approximately equals $600\ Wh$. As a result, ΔP_{batt_min} and ΔP_{batt_max} are set as follows: $\Delta P_{batt_max} = |\Delta P_{batt_min}| = 600\ W$.

Three different tests are performed to validate the proposed online optimization stage:

Simulation test 1: this simulation test is performed to prove the effectiveness of the online optimization stage in finding an improved solution, compared to the offline strategy, in response to the fast dynamic variation in $\delta^{pur}_{grid_actual}$ and P_{diff_actual} inputs. Thus, in this test the mean values of the actual input vectors, $\delta^{pur}_{grid_actual}$ and P_{diff_actual}, are kept the same as the predicted ones : $\delta^{pur}_{grid_pred}$ and P_{diff_pred} and additional fast disturbances are added to the actual inputs. To generate random signals with zero mean value and faster dynamics than the predicted data, white Gaussian noise (WGN) signals are added to the offline predicted signals. The introduced (WGN) signals are vectors consisting of N^* random values.

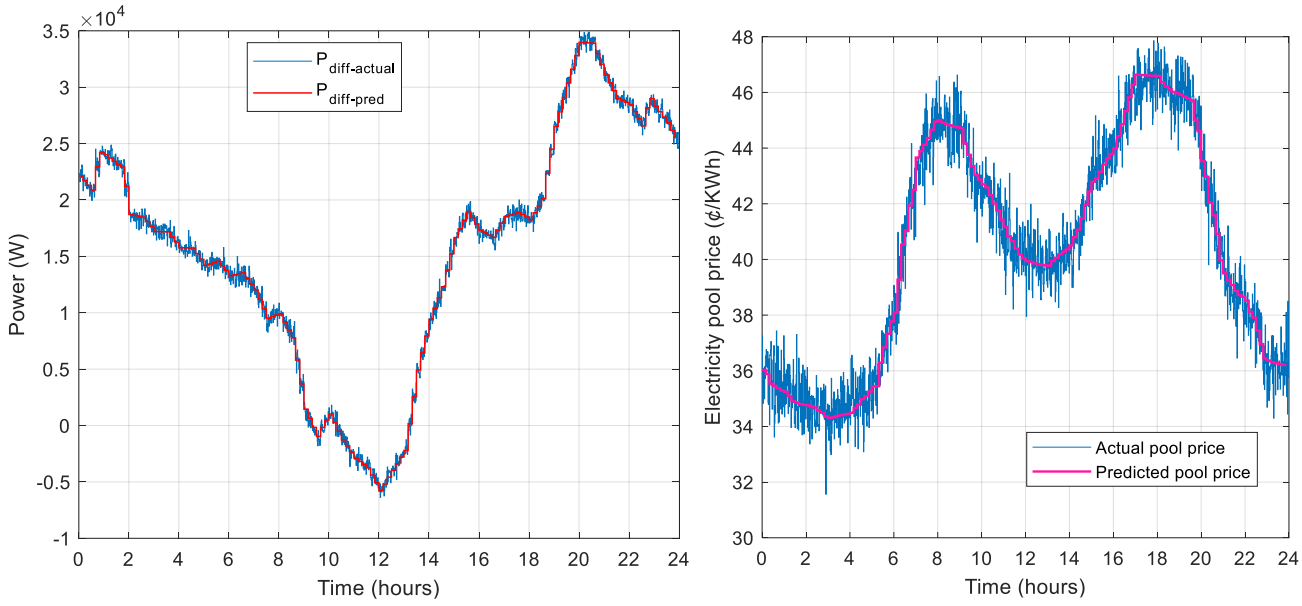


Fig.4.7 Predicted and actual data inputs P_{diff} and δ_{grid}^{pur} on the winter day (18/02/2021).

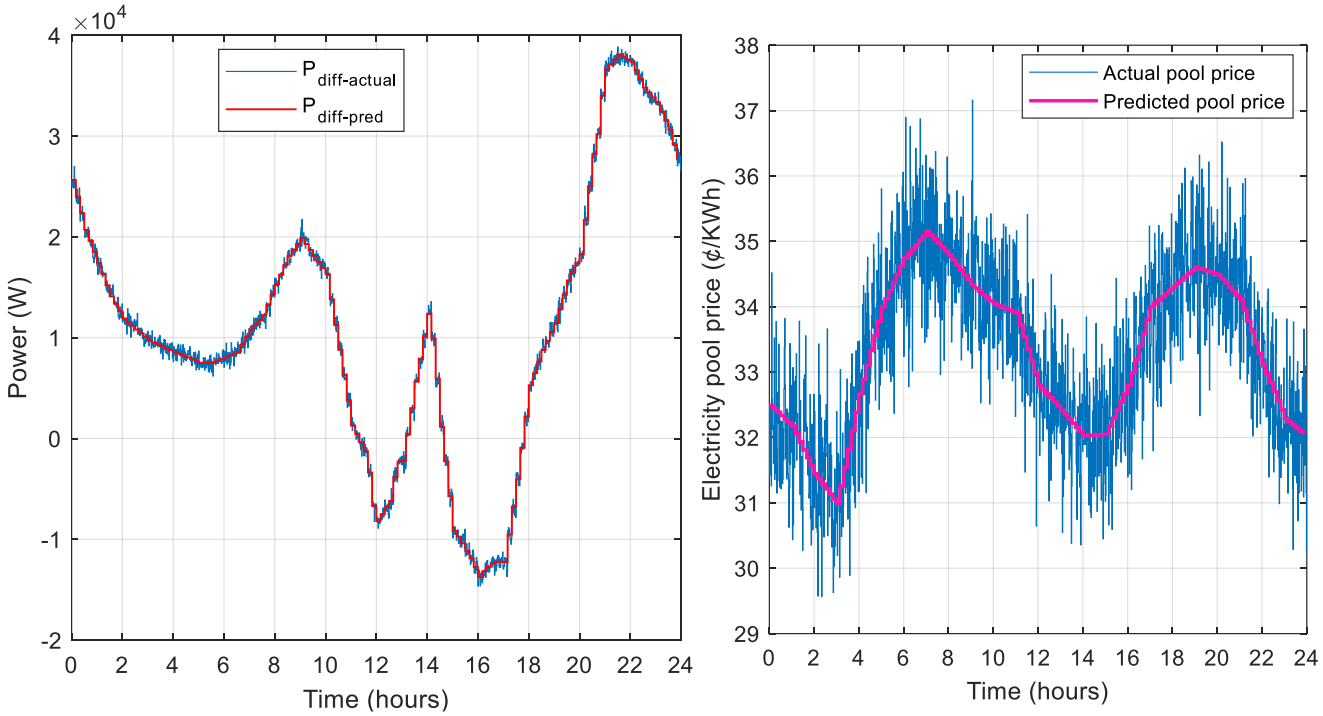


Fig.4.8 Predicted and actual data inputs P_{diff} and δ_{grid}^{pur} on the summer day (16/07/2021).

For the two tested days, the power of the (WGN) added to P_{diff_pred} is approximately 58 dB and the one added to $\delta_{grid_pred}^{pur}$ is approximately 0.6 dB. The obtained predicted and actual inputs for

the winter and summer days are respectively shown in Figures 4.4 and 4.5. As seen in Fig.4.7 and 4.8, the added (WGN) signals appear in the actual inputs' curves (curves plotted in blue).

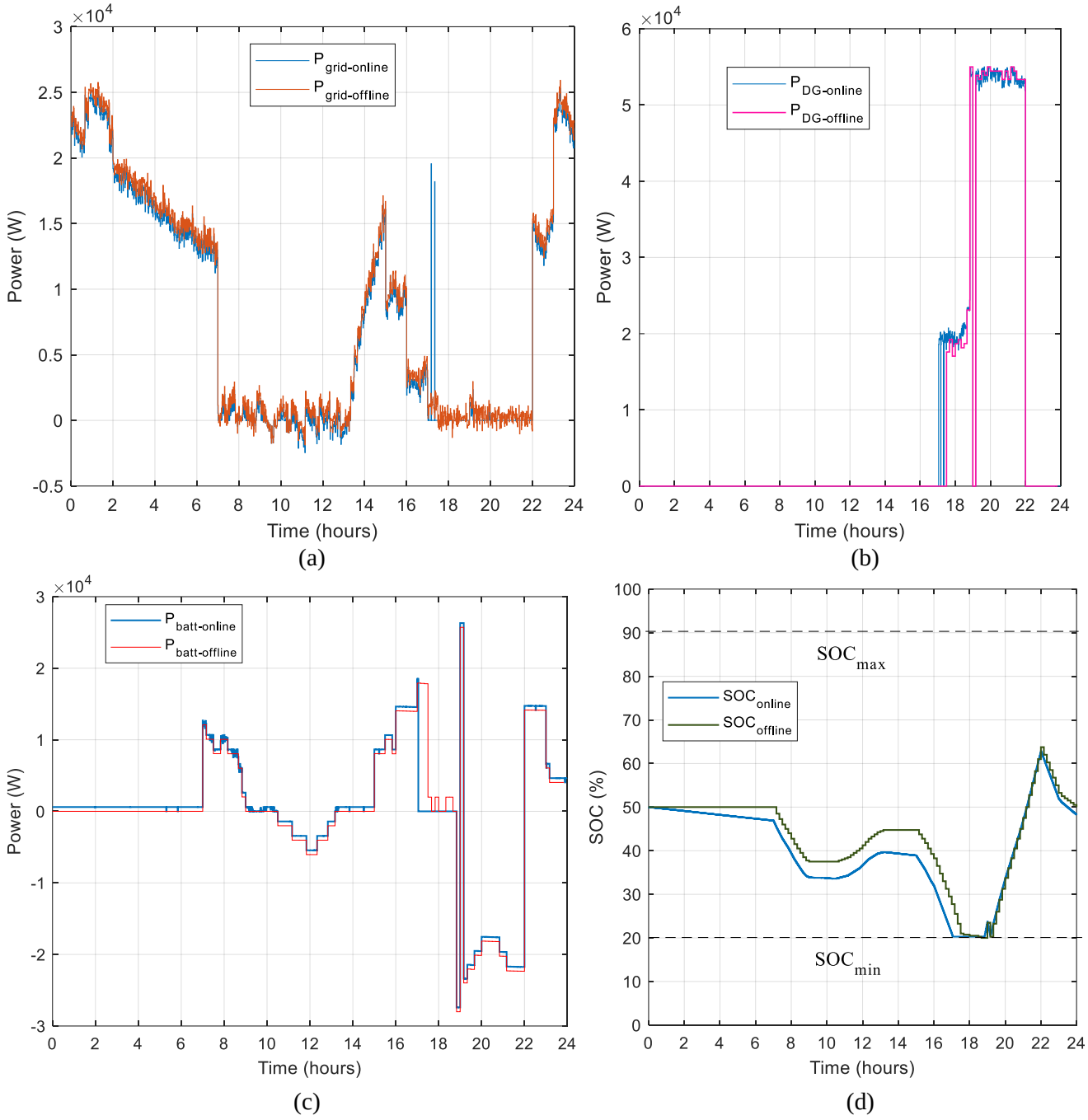


Fig.4.9 Winter Day (18/02/2021) results of (a) the grid power, (b) (DG) power, (c) battery power, and (d) the battery's SOC with and without online optimization stage.

Finally, the predicted and actual total energy differences on the winter and summer days are the same (for the winter day : $E_{diff_pred} = E_{diff_actual} = 370\ KWh$ and for the summer day: $E_{diff_pred} = E_{diff_actual} = 263\ KWh$).

The obtained results on the winter and summer days are shown respectively in Fig.4.6 (a), (b), (c), and (d), and Fig.4.7 (a), (b), (c), and (d).

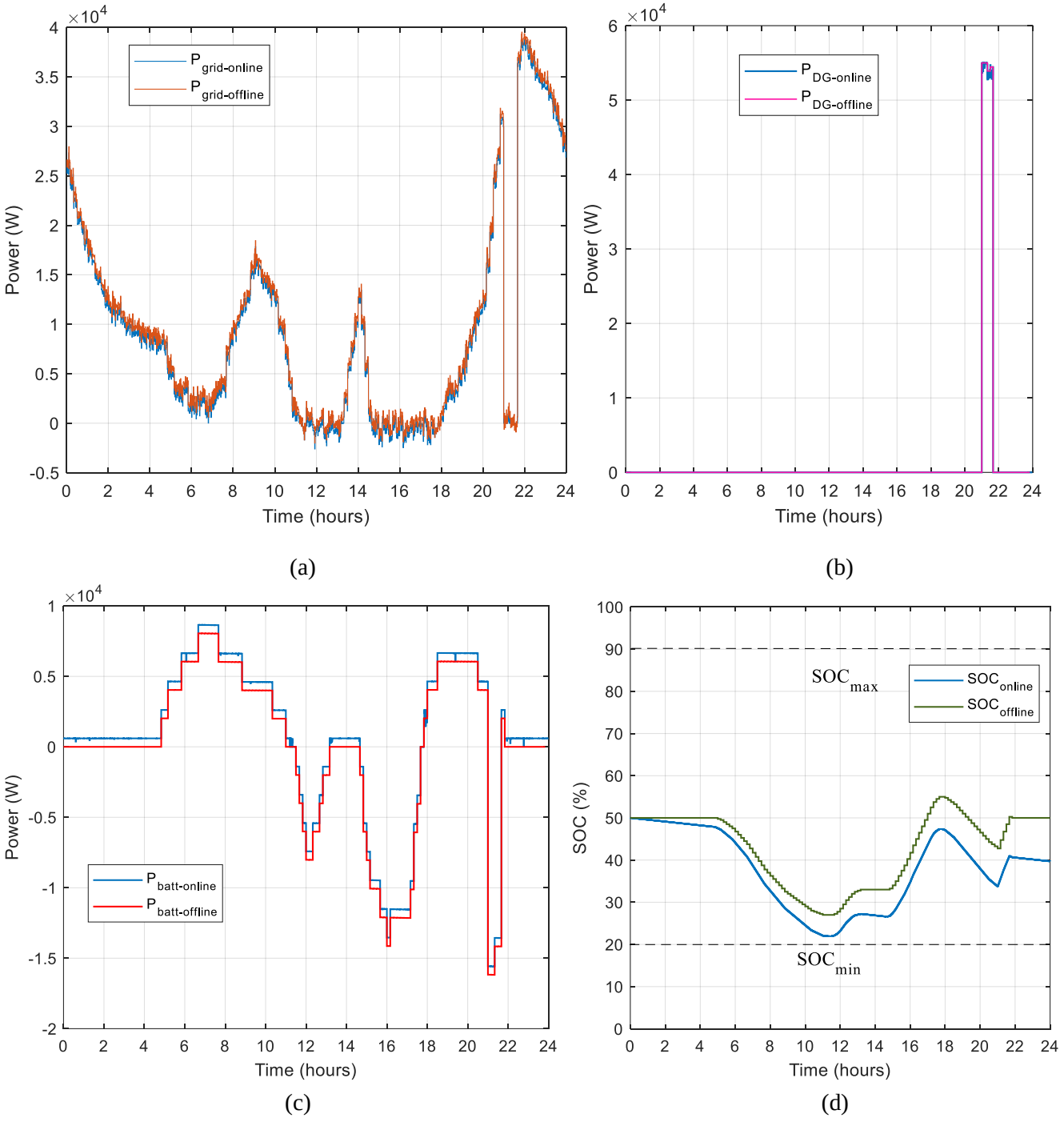


Fig.4.10 Summer Day (16/07/2021) results of (a) the grid power, (b) (DG) power, (c) battery power, and (d) the battery's SOC with and without online optimization stage.

As a general strategy and as seen from the obtained curves, the online optimization stage uses the allowable variation in the battery power, ΔP_{batt}, to rely more on the ESS and less on the utility grid and the (DG) over the time horizon. This can be justified by the fact that the average price of a Kilowatt-hour purchased from the grid or generated by the (DG) is always higher than the one provided by the battery. Meanwhile, as ΔP_{batt} is limited to $\pm$ 600 W, P_{grid_online}, P_{DG_online}, and P_{batt_online} curves obtained with online optimization on the two tested days (curves in the blue line of Fig.4.9 (a), (b), (c) and Fig.4.10 (a), (b), (c)) always maintain a close path to the offline optimization. The increasing reliance on the battery can be seen from the online and offline SOC curves in Fig. 4.9 (d) and 4.10 (d). SOC_{online} curves on the winter and summer days are below their corresponding $SOC_{offline}$ curves. Finally, the battery's SOCs with online optimization at the end of the winter and summer days are no longer equal to the initial state $SOC_{init} = 50$ ($SOC_{end} = 48.25\%$ at the end of the winter and $SOC_{end} = 39.5\%$ at the end of the summer day).

Table 4.4 and Table 4.5 summarize the results of the winter and summer days respectively. We note that the results with no online optimization stage are found under the heading offline optimization as in this case, the EMS only relies on the achieved day ahead offline optimization. By comparing the results, the online optimization stage brings a profit in the total operating cost of 0.53 \$ on the winter day and a profit of 3.68 \$ on the summer day. The higher profit on the summer day is justified by the availability of the ESS energy which can be further exploited in summer than in winter. As seen in Fig.4.9 (d), the minimum admissible SOC value, SOC_{min}, is reached for the winter day which restricts the solution of the online optimization problem. On the other hand, the storage is further utilized in the summer with no restriction on the lower SOC bound, Fig. 4.10 (d). The (DG) produced energy is approximately the same in the online and offline optimization as the price of Killowatt-hour is the same as the predicted one and the reduction of toxic gas emissions goal is always included in the objective function. Finally, though not included as a goal in the objective function in this Chapter, the losses in dispatchable converters are slightly reduced (losses reduction of 0.18 KWh (*i.e.,* 1%) on the winter day and 0.19 (i.e., 1.6%) on the summer day) when applying the online optimization. Thanks to the reduction of the operating cost achieved by the online optimization, the converter's losses are automatically decreased as the two optimization goals are reconcilable.

Simulation test 2: this simulation test is carried out to prove the viability and effectiveness of the proposed online optimization stage in finding an improved solution compared to the offline optimized results in response to a shift of the overall predicted data input signals. Based on the results of **simulation test 1**, the winter day represents a worst-case scenario for the online optimization stage to yield improved results compared to the summer day. This is due to the extensive usage of the ESS in the winter which reaches the minimum admissible SOC limit. Therefore, and in order not to weigh down the content with duplicated results, the winter day is exclusively applied as a case study and its results suffice to prove the viability of the online optimization stage.

	Winter day (18/02/2021)	
	Online optimization	Offline optimization
Initial and final SOC values	$SOC_{init} = 50$ - $SOC_{end} = 48.25$	$SOC_{init} = 50$ - $SOC_{end} = 50$
Total energy difference: $E_{diff} = E_{load} - E_{RESs_bus}$	$370.17\ KWh$	$370.17\ KWh$
Utility grid	$E_{pur_online} = 199.2\ KWh$ $E_{sold_online} = 1.74\ KWh$	$E_{pur_offline} = 201.7\ KWh$ $E_{sold_offline} = 1.57\ KWh$
	$J_{grid_online} = 74.02$ \$	$J_{grid_offline} = 74.4$ \$
Battery	$E_{dis_batt_online} = 71.93\ KWh$ $E_{ch_batt_online} = 69.56\ KWh$	$E_{dis_batt_offline} = 72.55\ KWh$ $E_{ch_batt_offline} = 72.96\ KWh$
	$J_{batt_online} = 12.16$ \$	$J_{batt_offline} = 12.62$ \$
(DG)	$E_{DG_online} = 187.34\ KWh$ Total emitted toxic gas: $44.8\ Kg$	$E_{DG_offline} = 187.64\ KWh$ Total emitted toxic gas: $44.9\ Kg$
	$J_{DG_online} = 63.99$ \$	$J_{DG_offline} = 63.68$ \$
Losses in dispatchable converters	$E_{loss_conv_online} = 17.00\ KWh$	$E_{loss_conv_offline} = 17.18\ KWh$
Total operating cost function	$J_{oc_online} = 150.17$ \$	$J_{oc_offline} = 150.7$ \$

Table 4.4 Summary of the obtained results with and without the online optimization stage on the winter day (18/02/2021).

	Summer day (16/07/2021)	
	Online optimization	Offline optimization
Initial and final SOC values	$SOC_{init} = 50$ - $SOC_{end} = 39.7$	$SOC_{init} = 50$ - $SOC_{end} = 50$
Total energy difference: $E_{diff} = E_{load} - E_{RESs_bus}$	$263.54\ KWh$	$263.54\ KWh$
Utility grid	$E_{pur_online} = 228.72\ KWh$ $E_{sold_online} = 3.43\ KWh$	$E_{pur_offline} = 240.98\ KWh$ $E_{sold_offline} = 1.79\ KWh$
	$J_{grid_online} = 75.33$ \$	$J_{grid_offline} = 79.52$ \$
Battery	$E_{dis_batt_online} = 58.4\ KWh$ $E_{ch_batt_online} = 44.55\ KWh$	$E_{dis_batt_offline} = 47.61\ KWh$ $E_{ch_batt_offline} = 47.74\ KWh$
	$J_{batt_online} = 7.97$ \$	$J_{batt_offline} = 7.44$ \$
(DG)	$E_{DG_online} = 36.11\ KWh$ Total emitted toxic gas: $8.64\ Kg$	$E_{DG_offline} = 36.39\ KWh$ Total emitted toxic gas: $8.7\ Kg$
	$J_{DG_online} = 11.43$ \$	$J_{DG_offline} = 11.45$ \$
Losses in dispatchable converters	$E_{loss_conv_online} = 11.72\ KWh$	$E_{loss_conv_offline} = 11.91\ KWh$
Total operating cost function	$J_{oc_online} = 94.73$ \$	$J_{oc_offline} = 98.41$ \$

Table 4.5 Summary of the obtained results with and without the online optimization stage on the summer day (16/07/2021).

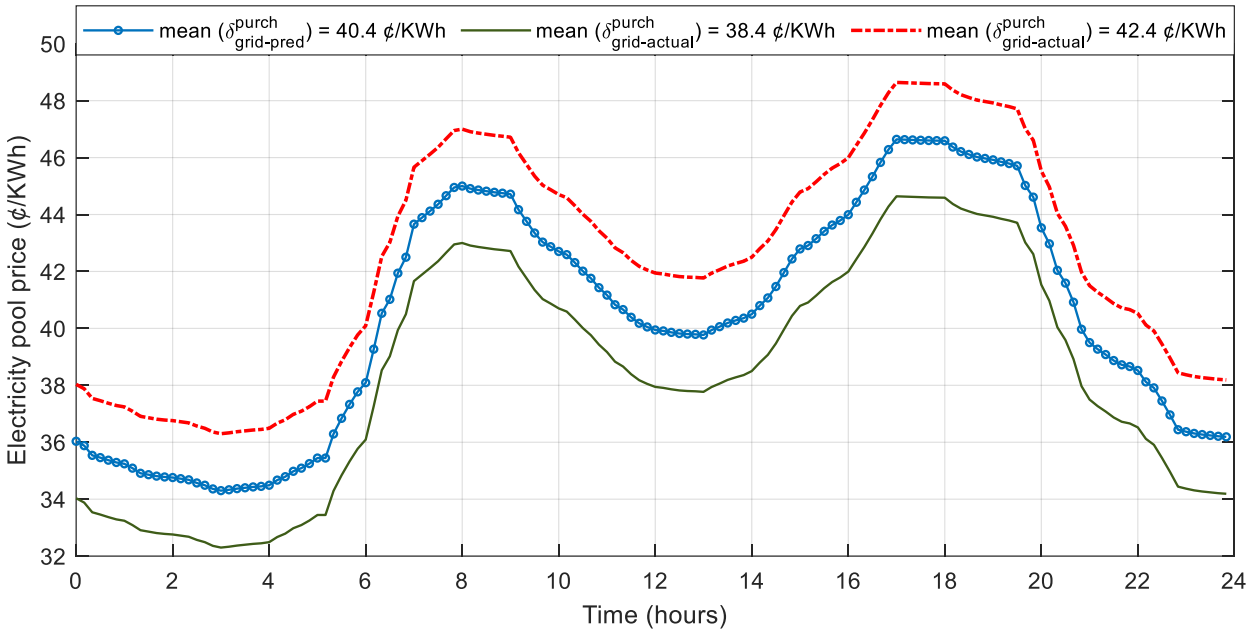


Fig.4.11 Predicted electricity pool price and applied actual scenarios of simulation test 2.

The predicted data input signals $\delta^{pur}_{grid_pred}$ and P_{diff_pred} of the winter day are modified in conformity with Fig.4.11 and Fig.4.12. Fig.4.11, shows the curves of the predicted pool price $\delta^{pur}_{grid_pred}$ (blue marked line) which has a mean value of 40.4 $¢/KWh$ and two tested actual pool price curves, $\delta^{pur}_{grid_actual}$. The first one in the dash-dot red line corresponds to a mean price higher than the predicted one with a mean value of 42.4 $¢/KWh$ and the second curve in the solid green line corresponds to a $\delta^{pur}_{grid_actual}$ lower than the predicted one with a mean value of 38.4 $¢/KWh$. For P_{diff_pred}, the overall predicted curve is shifted up and down to simulate all possible scenarios. As seen in Fig.4.12, the plotted curves correspond to different mismatches in the total energy difference over the whole time horizon. The curves of P_{diff_actual} in solid marked black and solid magenta lines correspond to a higher total energy difference than the predicted one (the dash-dot blue line curve). P_{diff_actual} in solid marked black line corresponds to $E_{diff_actual} = 390\ KWh$ (i.e. $20\ KWh$ greater than $E_{diff_pred} = 370\ KWh$) and the one in the solid magenta line corresponds to $E_{diff_actual} = 410\ KWh$ (i.e. $40\ KWh$ greater than E_{diff_pred}). Similarly, the curves of P_{diff_actual} in dashed red and solid green lines correspond to a lower total energy difference than the predicted one. P_{diff_actual} in solid green line corresponds to $E_{diff_actual} = 350\ KWh$ (i.e. $20\ KWh$ lower than $E_{diff_pred} = 370\ KWh$) and the one in the dashed line corresponds to $E_{diff_actual} = 330\ KWh$ (i.e. $40\ KWh$ lower than E_{diff_pred}).
Hence, the solid magenta and dashed red lines' curves represent, respectively, the biggest positive and negative margins of error between the predicted and actual power difference.

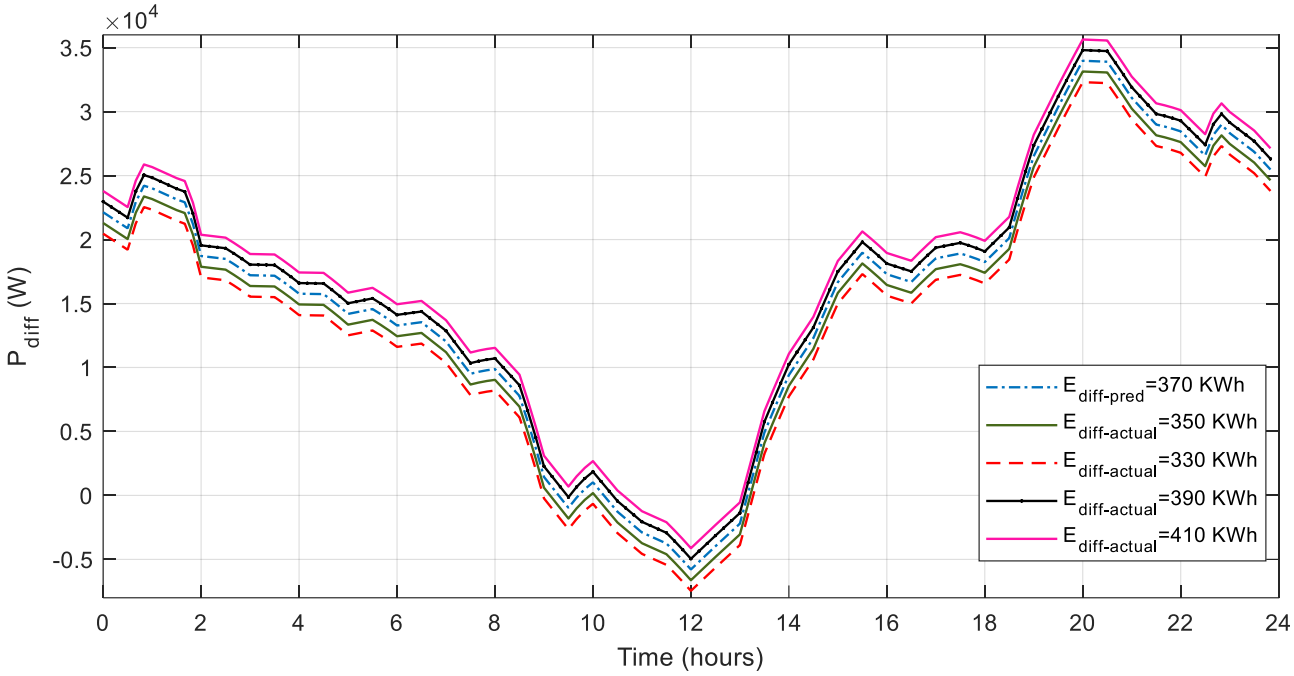


Fig.4.12 Predicted total energy difference and applied actual scenarios of simulation test 2.

Finally, we take note that the added WGN signals in **simulation test 1** are always kept in **simulation test 2** but weren't plotted in Fig.4.11, and 4.12 to intelligibly show all curve shapes together.

$\delta_{grid}^{pur}(¢/KWh)$ / $E_{diff}(KWh)$	$\overline{\delta_{grid_actual}^{pur}} = 38.4$	$\overline{\delta_{grid_pred}^{pur}} = 40.4$	$\overline{\delta_{grid_actual}^{pur}} = 42.4$
$E_{diff_actual} = 330$	**1**	**2**	**3**
$E_{diff_actual} = 350$	**4**	**5**	**6**
$E_{diff_pred} = 370$	**7**	**8**	**9**
$E_{diff_actual} = 390$	**10**	**11**	**12**
$E_{diff_actual} = 410$	**13**	**14**	**15**

Table 4.6 All possible scenarios of simulation test 2

All possible scenarios' combinations of **simulation test 2** are regrouped in Table 4.6. The scenarios are numbered from 1 to 15. The obtained results of all scenarios are detailed in Table 4.7. The "Δ" symbol corresponds to the difference between the online and offline variables ($\Delta X = X_{online} - X_{offline}$). Consequently, negative values of ΔX denote that the online optimization outperforms the offline optimization for the corresponding variable "X" and vice

Scenario	$\Delta M_{gas}(Kg)$	$\Delta E_{loss_conv}(Wh)$	ΔJ_{grid} (\$)	ΔJ_{batt} (\$)	ΔJ_{DG}(\$)	ΔJ_{OC}(\$)
1	-3.06	-616	2.66	-0.45	-3.36	-1.15
2	-1.82	-606	0.33	-0.45	-1.01	-1.13
3	-1.63	-605	-0.07	-0.45	-0.65	-1.17
4	-2.39	-346	2.99	-0.44	-3.13	-0.58
5	-0.94	-333	0.28	-0.45	-0.35	-0.52
6	-0.74	-333	-0.19	-0.44	0.06	-0.57
7	-1.77	-199	2.79	-0.45	-2.92	-0.58
8	-0.07	-180	-0.39	-0.46	0.31	-0.54
9	0.16	-179	-0.91	-0.46	0.77	-0.6
10	-1.24	-185	1.9	-0.45	-2.73	-1.28
11	0.7	-169	-1.82	-0.45	0.95	-1.32
12	1.57	-160	-3.55	-0.47	2.69	-1.33
13	-0.93	-192	1.41	-0.48	-2.6	-1.67
14	1.24	-176	-2.85	-0.46	1.51	-1.8
15	2.18	-170	-4.9	-0.46	3.37	-1.99

Table 4.7 Results of the ten applied scenarios of simulation test 2.

versa. M_{gas} denotes the total mass of emitted toxic gas in Kg.

Based on the figures provided in Table 4.8, the online optimization stage finds an improved solution over offline optimization in all applied scenarios. This can be seen through the negative values of ΔJ_{OC} in all scenarios. As the operating cost of the DC microgrid is always lower when adding the online optimization stage, the same result is obtained for the losses in dispatchable converters which decrease by adding the online optimization stage as ΔE_{loss_conv} is negative in all tested scenarios. To further analyze the impact of the online optimization stage, Fig.4.8 shows the absolute value of ΔJ_{OC} as a function of E_{diff} for the different δ_{grid}^{purch} mean values. As seen in Fig.4.13, the gain in the total operation cost increases as the margin of error between the predicted and actual data inputs increases and vice versa. The lowest gain, $\Delta J_{OC} = -0.54$ \$, is obtained in **scenario 8** corresponding to equal actual and predicted data inputs. The highest gain, $\Delta J_{OC} = -1.99$ \$, is obtained in **scenario 15** corresponding to actual data inputs $\overline{\delta_{grid_actual}^{pur}} = 42.4\ ¢/KWh$ and $E_{diff_actual} = 410\ KWh$ that are the furthest from the predictions. Therefore, the further the actual data inputs deviate from the predictions, the more the online optimization yields improved results compared to the offline approach. Contrarily, when the actual data are closer to the forecasted ones the online optimization stage delivers results that approximate the offline optimization which always provides the optimal solution.

Fig.4.14 shows the difference in the total emitted toxic gas (kg) over the obtained total emitted toxic gas without the online optimization stage (i.e., 44.9 Kg) in percentage as a function of E_{diff} for different δ_{grid}^{purch} mean values.

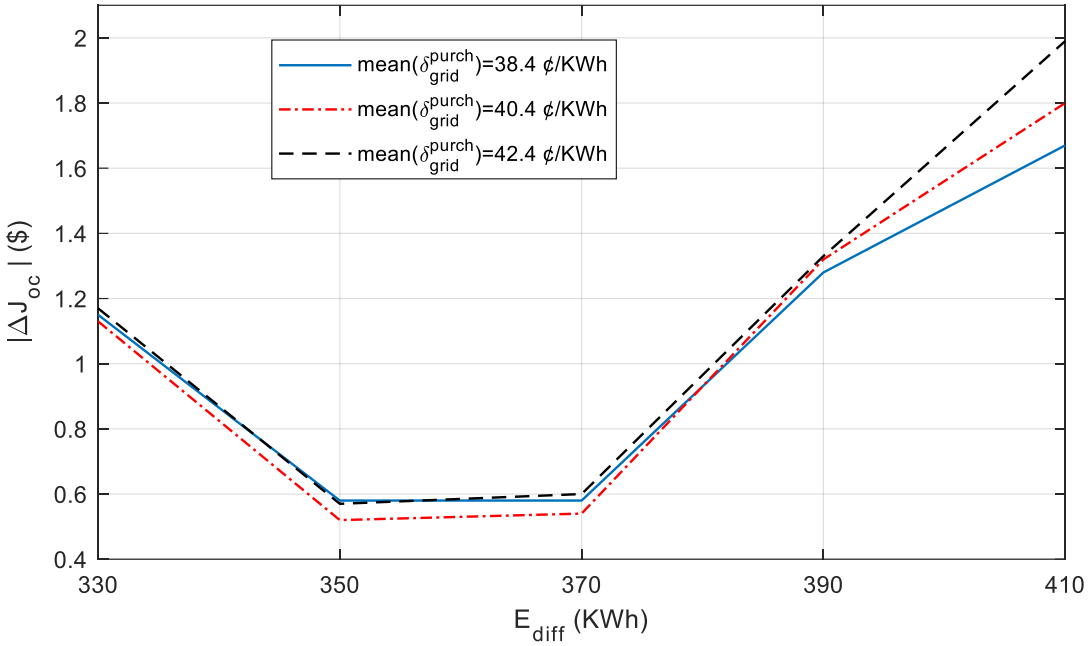


Fig.4.13 Absolute value of ΔJ_{OC} as a function of E_{diff} for different δ_{grid}^{purch} mean values.

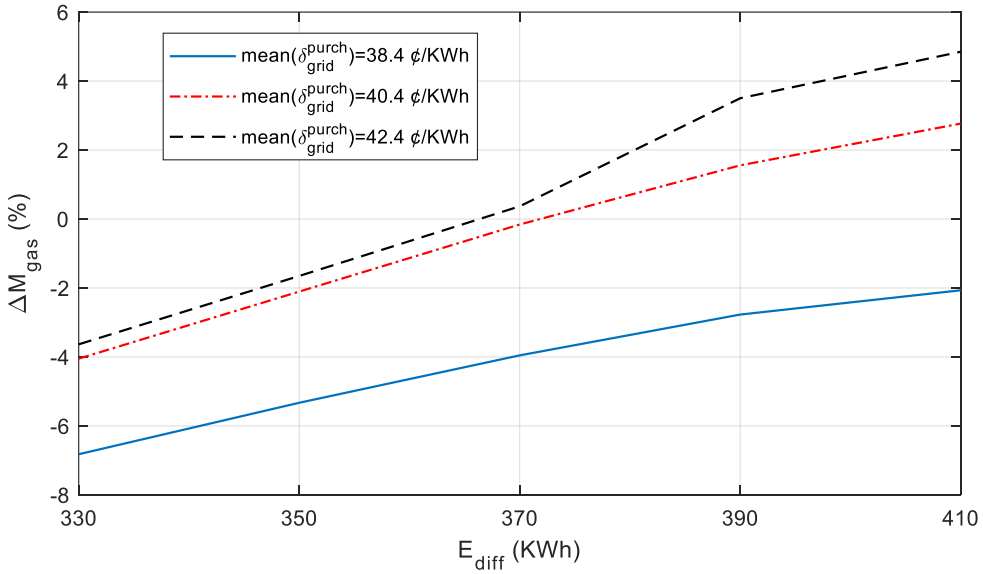


Fig.4.14 ΔM_{gas} (%) *as* a function of E_{diff} for different δ_{grid}^{purch} mean values.

Referring to Fig.4.14, the online optimization stage relies less on the (DG) compared to the offline approach when the energy difference is lower than the predicted one (i.e., $E_{diff} = 330 - 350\ KWh$) as the actual load demand is lower than the predicted one. This can be deduced from the negative values of ΔM_{gas} (%). Similarly, the reliance on the (DG) in the total energy mix of the DC microgrid decreases as the actual electricity pool price decreases in comparison with the predicted one (solid blue line curve). In such a case, to compensate for subtracted (DG) energy

from the total energy mix and to reestablish the power balance equation, the online EMS purchases additional energy from the utility grid.

This result can be verified in Fig.4.15 (a) which represents the difference in purchased energy from the utility grid, ΔE_{pur}, over the total offline purchased energy, $E_{pur_offline}$, in (%), as a function of E_{diff} for different δ_{grid}^{purch} mean values.

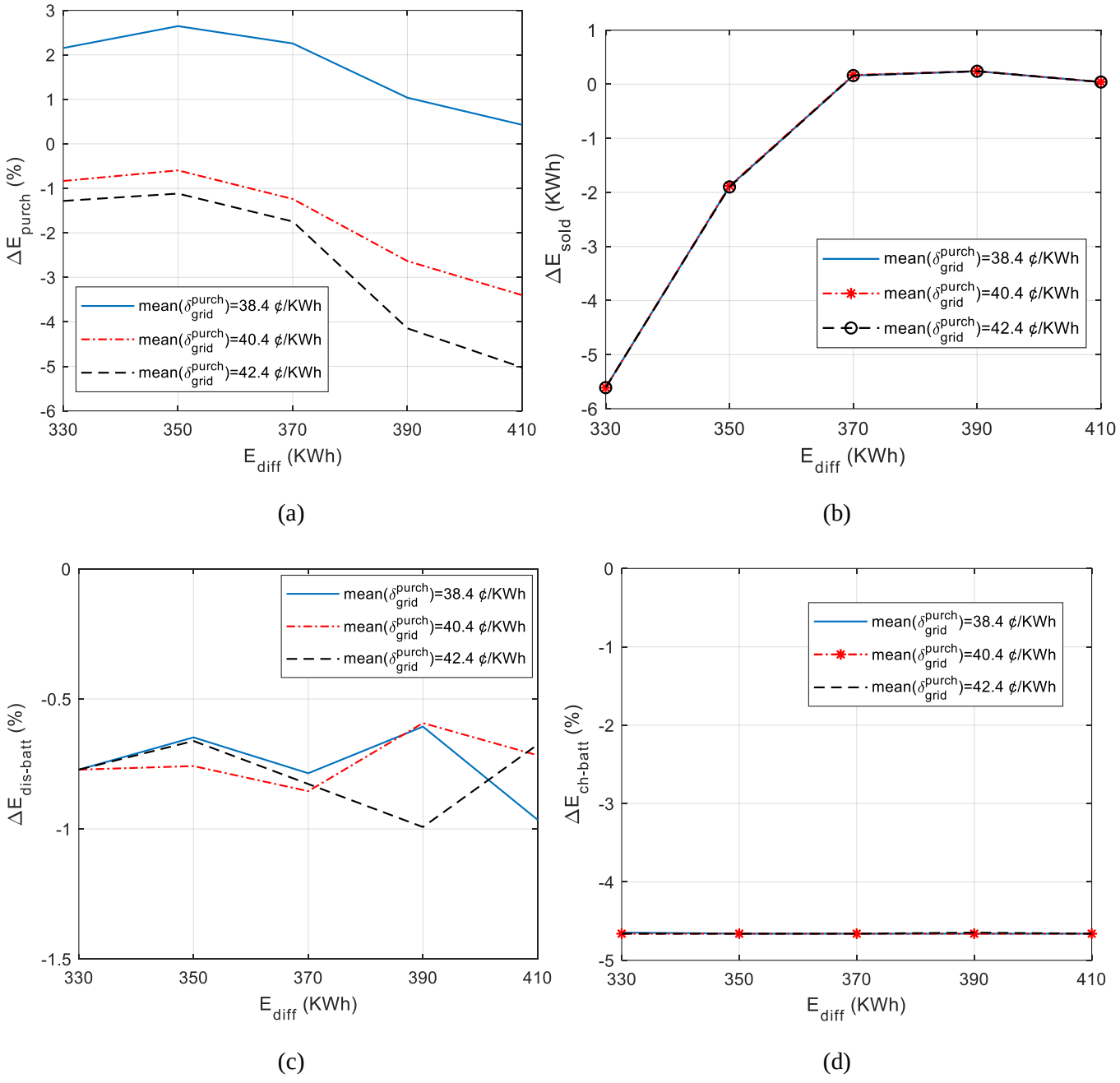


Fig.4.15 (a) ΔE_{pur} (%), (b) ΔE_{sold} (KWh), (c) ΔE_{dis_batt} (%), and (d) ΔE_{ch_batt} (%) as a function of E_{diff} for different δ_{grid}^{purch} mean values.

The plotted curves show that additional energy is purchased from the utility grid by the online EMS when the electricity pool price is lower than the predictions. This can be seen by the positive values of ΔE_{pur} (%) (solid blue line curve). Contrarily, when the electricity pool price and the energy difference are higher than the predictions (i.e. **scenarios 12** and **15**) or when the electricity pool price is equal to the predictions and the energy difference is higher than the predictions (i.e. **scenarios 11** and **14**), (dash-dot red line and dash black line curves of Fig.4.15 (a)), the online EMS purchases lower energy from the grid compared to the offline optimization and relies more on the (DG) in the total energy mix.

Additional energy from the (DG) is produced compared to the offline optimization and this can be seen by the positive values of ΔM_{gas} (%) (dash-dot red line and dash black line curves of Fig.4.14). In such a case, though the offline optimization produces less toxic gas emissions, the online EMS always maintains limited amounts of additional toxic gas production that don't surpass 5% of the offline total emitted amount. Toxic gas emissions are always limited in the online EMS as the corresponding objective of emissions reduction is included in the objective function to minimize by equation (IV.24).

Fig.4.15 (b) shows the difference in the energy sold to the utility grid, ΔE_{sold}, in (KWh). The three curves plotted corresponding to the different δ_{grid}^{purch} mean values are merged which means energy sold to the grid is independent of the electricity purchase price which turns out to be logical. However, E_{diff} values highly impact the energy sold to the grid and so ΔE_{sold}. When the energy difference is lower than the predicted one (i.e., $E_{diff} = 330 - 350\ KWh$), the online EMS sells less energy to the utility grid than the offline approach. This can be seen by negative values of ΔE_{sold}. Meanwhile, for $E_{diff_actual} = E_{diff_pred} = 370\ KWh$, the online EMS sells the same amount to the utility as the offline approach (ΔE_{sold} approximates zero). For higher values than the predicted one (i.e. $E_{diff} = 390 - 410\ KWh$), both E_{sold_online} and $E_{sold_offline}$ tend to zero which results in a ΔE_{sold} equal to zero.

Finally, Fig.4.15 (c) and (b) show respectively the difference in discharged/charged energy from/into the battery, ΔE_{dis_batt} and ΔE_{ch_batt}, over the total offline discharged/charged energy, $E_{dis_batt_offline} = 72.55\ KWh$ and $E_{ch_batt_offline} = 72.96\ KWh$, in (%), as functions of E_{diff} for different δ_{grid}^{purch} mean values. From Fig.4.15 (c), the amount of energy discharged from the battery when applying the online EMS is almost the same as in the offline case. A slightly higher amount of discharged energy in the offline case is noted and does not surpass 1% of the total discharged energy. Fig.4.15 (d) shows that almost 4.7% less energy is charged into the battery when applying the online EMS compared to the offline approach. The three curves are merged as the online EMS always uses the full amount of admissible energy to the extent possible (As set in the constraints, $\pm 600\ Wh$ are admissible each charging/discharging hour. On this day, the battery was charged for a total of 5 hours and 40 minutes. During these 5 hours and 40 minutes, the online EMS can charge $5.67 \times -600 = -3.4\ KWh$ less energy into the battery compared to the offline approach. Dividing the $-3.4\ KWh$ over $E_{ch_batt_offline} = 72.96\ KWh$, this yields the -4.66%

obtained in Fig.4.15 (d)). Finally, the mismatch between the total charged and discharged energy into/from the battery when applying the online EMS can be justified by the relaxation of the constraint on the last SOC value, $SOC(k = N)$, which can have different values than the battery's initial state $SOC(k = 0)$. In all scenarios, $SOC(k = N) \approx 48.2\ \%$ which is less than $SOC(k = 0) = 50\ \%$. This release from the last SOC constraint allowed the online EMS to make an additional profit in the operating cost.

4.5 Conclusion

In this chapter, the online optimization of the DC microgrid is presented. An online optimization stage is added to update the offline optimized power references of dispatchable sources due to the uncertainties in the RES-generated power, load demand, and electricity pool price. Unlike most applications that rely on one operating converter to compensate for uncertainties, a new approach is proposed in which the power references of all dispatchable sources are updated to optimally respond to the occurring mismatches.

The proposed online optimization stage is not advanced as an alternative to offline optimization. Instead, it is applied each intrasample period, $T_{is} = 1$ minute, to accomplish corrective action to the offline optimized power references which have a sampling period of $T_s = 10$ minutes. Hence, online EMS, which has a faster dynamic than offline optimization performs a local time-invariant optimization at each intrasample period and only outputs the new optimal power references for the next step. To solve the online optimization problem, (GS) algorithm was selected due to its high convergence speed and potential to find a global minimum. As the (GS) algorithm requires the selection of a local solver which is started from multiple start points to sample multiple basins of attraction and search for a global minimum, $fmincon$ solver is chosen as it fits best our optimization problem. The optimization problem is formulated conveniently to the $fmincon$ format with the same optimization objectives and constraints as in Chapter 3.

To prove the viability and effectiveness of the proposed online optimization stage, two simulation tests are conducted in which two operating modes, with and without the online optimization stage, are compared. The simulation tests yielded three main outcomes:

1. The online EMS showed an improved solution compared to the offline approach in response to fast dynamics and disturbances in the actual data inputs. This can be justified by the intra-sampling period of the online optimization stage which is ten times faster than the offline optimization and so, has a better response to fast disturbances in the input signals. Hence, online EMS increases the control time resolution of the overall system.

2. The size of the ESS plays an instrumental role in the online optimization stage which always uses all the allowable charged/discharged energy into/from the battery to rely

more on the ESS and less on the utility grid and the (DG) over the time horizon. This can be justified by the fact that the average price of a Kilowatt-hour purchased from the grid or generated by the (DG) is always higher than the one provided by the battery. A higher profit is obtained on the summer day (3.68 $) compared to the winter day (0.53$) as further ESS energy is available and can be exploited in summer than in winter.

3. The online EMS showed improved results over the offline approach of total operating cost in 15 different scenarios of simulation test 2. These scenarios simulate different positive and negative margins of error between predicted and actual data inputs. As a result, the further the actual input profiles are close to the predicted ones, the less gain is achieved by the online optimization stage. In this case, the online EMS approximates the offline optimization results which provides the optimal solution. Contrarily, the furthest the actual data inputs are from the predictions, the higher gain in the total operating cost is achieved by the online EMS compared to the offline approach.

Chapter 5 : Conclusion and Perspectives

Following the transition from a centralized monopolized energy generation approach to a distributed one at the end of the 20th century and the advent of the microgrid concept, especially DC microgrids during the last decade, new research works are witnessing an increased interest in the control and power management of DC microgrids. To control a DC microgrid, researchers adopted the traditional hierarchical control strategy inherited from AC grids. Consisting of three distinct control levels, the primary and secondary control levels in a DC microgrid differ from the AC ones in terms of control objectives. A much simpler control on the primary control level in a DC microgrid is required in which the prime concerns are the stabilization of the common DC bus voltage and the proper power sharing among operating DERs. The secondary control level is usually adopted to improve the primary control level results and apply source-dependent functions such as the MPPT. As the primary and secondary control levels were extensively investigated in the literature, researchers are lately diverting their attention to the tertiary control level. At this control level, with much slower dynamics compared to the primary and secondary levels, advanced energy management functionalities can be achieved over long time horizons.

On the other hand, a surge in awareness is noted concerning global climate change and the resulting critical risks. As carbon dioxide emissions and other greenhouse gases are the principal cause of the earth's temperature rise and climate change, most nations are setting net-zero emissions targets and pledges to slash their emissions for the next decade. To reach their decarbonization target, countries are placing roadmaps based on the further proliferation of RESs, the rationalizing of energy usage, and the improvement of the overall electrical system efficiency. Technically, these energy policies and targets are being integrated into the EMS of microgrids under the so-called "smart" control systems on the tertiary control level by transforming the defined objectives into an optimization problem.

From here and based on the above-mentioned actualities in DC microgrids and worldwide energy management policies, this thesis proposes an energy management strategy of a DC microgrid over a 24-hour time horizon to achieve multi-objective optimization. The DC microgrid consists of several DERs including RESs such as the PV array and WT, a (DG) as a traditional pollutant source, an ESS consisting of a lithium-ion battery, and a residential DC-type load. The DC microgrid can operate in grid-connected as well as in islanded mode. Three main objectives of the EMS are defined: the minimization of the total operating cost of the DC microgrid, the reduction of the toxic gas emissions produced by the (DG), and the minimization of converters' losses of dispatchable sources. This thesis presents three main contributions on different levels. Firstly, at the modeling level, precise modeling of the DC microgrid is proposed, and new averaging mathematical techniques are advanced. These techniques ensure the best trade-off between model accuracy, complexity, and simulation speed. The second contribution is the achievement of a

multi-objective optimization by finding a Pareto solution through convenient weights' selection. Finally, the last contribution is the integration of an online optimization stage that updates the offline optimized power references due to existent mismatches between predicted and actual data inputs. Next, each of the three contributions is detailed separately following each chapter of the thesis.

First from the modeling perspective, as seen from the targeted objectives and the time horizon, the thesis work is located at the tertiary level of hierarchical control. At this control level, the targeted variables of the system are much slower than the primary and secondary control levels. This makes the inclusion of all system variables in one model over a 24-hour time horizon a complicated matter on a standard computer with limited CPU performance and memory. To overcome this hurdle and by taking advantage of the wide span in time constants of variables, researchers usually adopt simplified mathematical models to formulate the optimization problem. These simplified models represent the operating sources in steady-state and do not depend on fast electrical variables such as the current and voltage. Instead, the applied mathematical equations only include slow variables such as temperature, wind speed, solar irradiance, etc. to compute the power of the corresponding energy source. By omitting the electrical variables from the model, the primary and secondary control levels are automatically excluded and considered as already established. Though yielding decent results, this modeling approach incurs power computing errors that won't appear unless the EMS control is tested experimentally on a real DC microgrid. In such cases, one of the operating converters takes charge of compensating for the resulting power computing errors which may lead to a suboptimal solution if the power mismatches are large. As a result, this approach favors the model's simplicity over its accuracy.

Chapter 2 presents a new approach to modeling the DC microgrid in which a trade-off between model precision, complexity, and simulation speed was created. Though all simulations are conducted on a standard core-i7 @ 2 GHz computer with 8 GB installed RAM, the advanced averaging techniques made possible the 24-hour modeling while maintaining an accurate calculation of energy sources' power. First, each energy source along with its proper converter was modeled, the detailed model includes the mathematical modeling of the energy source itself, the converter, the control including the primary and secondary level hierarchical control, and the common DC bus. Though the detailed model is the most accurate and serves as a benchmark for precision, it does not work for long-time simulations as in this case. Mainly, this is due to the high complexity of the model and reduced calculation step size. Hence, the main target of advancing averaging techniques is increasing the calculation step size which automatically reduces the model complexity and simulation time while maintaining a decent accuracy.
At the DC units modeling level (i.e., the PV array and the lithium-ion battery), the detailed models that include the current and voltage electrical variables to compute the output power were maintained as they don't limit the calculation step size. For AC units (i.e., the WT, the utility grid, and the (DG)), the problem does not show up on the unit modeling level but in the sinusoidal

waveforms of the electrical variables. As known, the electrical variables of AC systems are periodic and require a small calculation step size to yield proper power calculation. As a solution, the phasor domain was advanced to express the electrical sinusoidal components in the complex number domain. By this, all AC electrical variables are transformed from the time domain into the complex number domain and explicit in the form of magnitude and phase shift. This transformation toward the phasor domain increases the calculation step size 356 times and the simulation speed 880 times compared to the detailed model while maintaining accurate computing of source power. At the converter modeling level, average modeling of all operating AC and DC converters was proposed to increase the calculation step size of models. The switching devices of all converters operate at high switching frequencies of the order of tens of KHz. The switching phenomenon automatically limits the calculation step size to one-hundredth of the switching frequency and slows down the simulation speed. As our control objective does not target this phenomenon by itself, it can be removed. This is what the average modeling makes by omitting the switching devices and replacing them with controllable voltage and current sources. This assumption increases the calculation step size 100 times compared to the most detailed model and maintains a decent mathematical model of the converter that includes the duty cycle ratio. As the passive component of converters, electrical variables, and duty cycle ratio are always included in the average model, the conduction and the switching losses which are the major sources of losses in all operating converters were accurately modeled. The precise power efficiency curves of all converters were deduced and can then be included when formulating the optimization problem to achieve the minimization of converters' losses goal.
On the converters' control level, the primary and secondary control levels were maintained for all operating converters. A detailed study was conducted on RESs that always operate in MPPT mode as MPPT techniques highly impact the calculation of outputted power. In this context, a new MPPT table search technique was proposed for the PV array as traditional ones require small calculation step sizes. As a result, the proposed modeling strategy provided the best tradeoff between model precision, complexity, and simulation speed. Only variables and phenomena that limit the calculation step size and do not impact the precise calculation of power sources were neglected.

The second contribution of this thesis is the achievement of multi-objective optimization. To reach the three predefined objectives of the EMS, an optimization problem is formulated in Chapter 3. The optimization problem outputs the optimal power references of dispatchable sources for the next 24 hours. As the PV array and the WT are always operating in MPPT mode to continuously extract the maximum available clean energy, the optimal EMS has three remaining degrees of freedom. These degrees of freedom are the power references of the battery, the (DG), and the utility grid. Hence, by setting the power references of these three units for the next 24 hours, the EMS optimally controls the power flow in the DC microgrid. The models of the PV and (WT) power sources that were derived in Chapter 2 serve as inputs for the optimization problem. Besides, as presented in Chapter 2, the detailed battery model which includes the exponential zone of the battery's voltage and accurately computes the battery's state of charge (SOC) is adopted in Chapter

3. The complexity of the formulated optimization problem lies at the variables' level of which the power references of the (DG) and utility grid are time-invariant, whereas the battery's SOC is time variant. Being a fundamental parameter that affects the battery's power over the entire control range, the battery's SOC discrete equation was included in the optimization problem to correctly guess the SOC and set the battery power reference over the whole time horizon.

Among several methods, the unique weighted objective function method is applied. Distinct weights that vary from zero to one were assigned to the three predefined optimization goals. The objective function, expressed in \$, consists of the weighted sum of the total operation cost, the toxic gas emissions cost, and the converters' losses cost functions expressed all in \$. To compute all these cost functions, several mathematical equations that relate the optimization variables (i.e. the optimal power references of dispatchable sources) to the operation and maintenance costs of operating units, the total mass of emitted toxic gas, the fuel price, and the converters' losses penalty factor were included. By this, a total energy bill, in \$, is obtained at the end of each day consisting of the total cost of purchased/sold energy from/to the grid, the (O&M) cost of all operating units, and the penalty cost related to the toxic gas emissions and the losses in operating converters. On the one hand, expressing all cost functions in dollars and including them in one objective function offers a mathematical solution to enable the preference criterion between the three optimization goals. On the other hand, it provides a unified energy bill at the end of each day that can be intelligible on the consumer side.

Besides, to emulate a real DC microgrid scenario, upper and lower bounds for decision variables were added as well as several constraints. For instance, constraints on the minimum and maximum admissible SOC values, the final SOC value that should retrieve the battery's initial state, etc. were introduced to guarantee a safe operation of the ESS and all operating units. Applying all these equations resulted in a time-variant optimization problem with nonlinear and non-smooth constraints and objective function. To solve the formulated optimization problem, two algorithms were represented and applied. A first deterministic algorithm called dynamic programming (DP) and a second metaheuristic algorithm called the genetic algorithm (GA) were applied to further prove that the found solution is a global minimum. Both algorithms converged and yielded close results with a preference for the (DP) which solved the problem in an extremely lower convergence time and higher time resolution compared to the (GA). The convergence time ratios for the winter and summer days are respectively: $GA_{CT}/DP_{CT} = 15.44$ and 24.54. For the time resolution, (DP) is run with a sampling period of $T_s = 1/6$ hour meanwhile, the sampling period of (GA) is limited to $T_s = 1$ hour since the number of optimization variables increases exponentially as the sampling period decreases.
Next, the preference criterion between the three defined goals was assessed by varying the corresponding weight of each objective in the unified objective function. As a result, a Pareto of all possible optimal solutions with corresponding weight variation intervals was deduced for the tested winter day. Besides, although the three optimization goals are expressed distinctly in the

main objective function, the achievement of any of them fosters or restricts the attainment of the remaining ones. Thus, the results showed that the accomplishment of the minimization of the total operation cost goal automatically favors the minimization of the converter's losses and vice-versa as the two goals are reconcilable. However, the minimization of the toxic gas emissions goal contradicts the minimization of total operating cost and converters' losses goals. Here lies the importance of the defined Pareto of solutions following the user preference for goal achievement. Consequently, the Pareto solution analysis is instrumental and must precede the offline optimization process.

Chapter 4 highlights a third contribution of this thesis, the inclusion of an online optimization stage that updates the offline optimized power references. The uncertainties in the RES-generated power, load demand, and electricity pool price are the main causes of mismatches between predictions and actual data inputs. To compensate for these mismatches, one of the operating converters, mostly the utility grid converter, takes charge of stabilizing the common DC bus voltage and reestablishing the power balance in the DC microgrid. Though this preponderant approach ensures a stable operation of the microgrid regardless of the occurring mismatches, it may engender a suboptimal solution far from the offline proposed one. For this, a new online control strategy is advanced in which an online optimization stage is added to update the power references of all dispatchable sources. By this, all dispatchable sources share the corrective actions needed to compensate for the uncertainties and not only one of the operating converters. The new power share of each dispatchable source is defined according to the formulated online optimization problem.

Setting the same three optimization goals of offline optimization, the online optimization stage is not advanced as an alternative to the offline one and does not rebuild the optimal path over the whole-time horizon. Instead, the online EMS, which is ten times faster than the offline output power references, carries out a local optimization for each one-minute intrasample period. At each intrasample period, it assures the corrective action by outputting the updated optimal power references for one next-time step. The online optimization problem was formulated appropriately for the selected local solver of the main algorithm which is Global Search (GS). The chosen local solver is $fmincon$. To simplify the mathematical expressions of the problem, all weights in the objective function are set to one so that there are no preferences between the three goals at this stage. Besides, as the minimization of the total operation cost and the converter's losses are reconcilable objectives, the latter objective wasn't included in the objective function. Knowing that, if the above-stated hypothesis is correct, any reduction in the total operating cost should automatically result in a reduction of converters' losses. Furthermore, the constraint on the last battery's SOC is released.

The effectiveness and viability of the proposed online optimization stage were proved in two different simulation tests. The first simulation test assesses the response of the system in the presence and absence of the online EMS toward fast dynamics and disturbances in the actual data inputs. To simulate the fast disturbances in the actual data inputs, white Gaussian noises (WGN)s are added to the predicted input signals. The obtained results show that the online EMS yields

better results than the offline approach in this simulation test as it has a higher time resolution. Hence, the first benefit of online EMS is its robustness in responding to fast disturbances in the input signals compared to the offline approach. The second simulation test simulates several scenarios in which positive and negative margins of error between predicted and actual data inputs are created. The online EMS showed improved results of the total operating cost in all applied scenarios compared to the offline approach. Besides, lower converters' loss values were noted in all scenarios which validated the hypothesis of reconcilable objectives. For toxic gas emissions, depending on each case scenario the online EMS produces less or further toxic gas. In case of additional emitted toxic gas, the amount remained limited (i.e., a maximum 5% additional amount of emitted toxic gas in the worst-case scenario) as the corresponding optimization goal is included in the objective function to minimize.

Finally, it is worth mentioning that the size of the ESS plays a significant role in online EMS-obtained results. Referring to all simulation tests, the well-defined amount of extra storage energy allocated to the online EMS was entirely used in all simulations and scenarios to ensure a profit in the total operating cost at the end of the 24 hours. This extensive reliance on the ESS can be justified by the low average price of a kilowatt-hour discharged from the battery compared to the one purchased from the utility grid or produced by the (DG). As a result, the further the battery is exploited during the day the less the profit from the online EMS is at the end of the time horizon. This can be seen by the higher profit obtained on the summer day (3.68 $) compared to the winter day (0.53$) as further ESS energy is available and can be exploited in summer than in winter.

The future work may include four different perspectives that can be followed and developed:

- The first is the experimental validation of all the simulation results. A real implementation of the proposed offline and online EMS on a real DC microgrid with the same configuration is essential so that the project does not remain theoretical. This can be achieved through a Hardware In the Loop (HIL) simulation such as OPAL-RT systems which enables the assessment for several days.
- The second aspect is the integration of an additional type of ESS such as the supercapacitors that respond to rapid and high peaks of power demand while the battery takes charge of supplying the permanent energy demand. The attribution of the fast power discharge/charge to the supercapacitor and the slow power discharge/charge to the lithium-ion battery must be reflected in the formulation of the new optimization problem.
- Third, the load was not considered a dispatchable unit when formulating the optimization problem in this thesis. However, the load can provide an additional degree of freedom if added to optimally manage the energy of the DC microgrid. This can be achieved by the load-shedding and the deferrable/ undeferrable load strategy. The load shedding offers an additional economical solution when the consumption surpasses the RES production, and the battery is entirely discharged.

- Finally, in the last chapter to model the mismatches between the predicted and actual data inputs, we have added white Gaussian noises to the predicted input signals and shifted them up and down to create non-zero average variations. Yet, the prediction model can be improved by integrating Artificial Intelligence (AI) which offers a better solution to fit reality. AI makes it possible to better integrate changes in production and consumption through data fusion, big data, etc.

Appendix A

A.1 PV module data

SunPower SPR -415E-WHT-D is selected as a module out of several PV module manufacturers around the world proposed through the MATLAB/Simulink library:

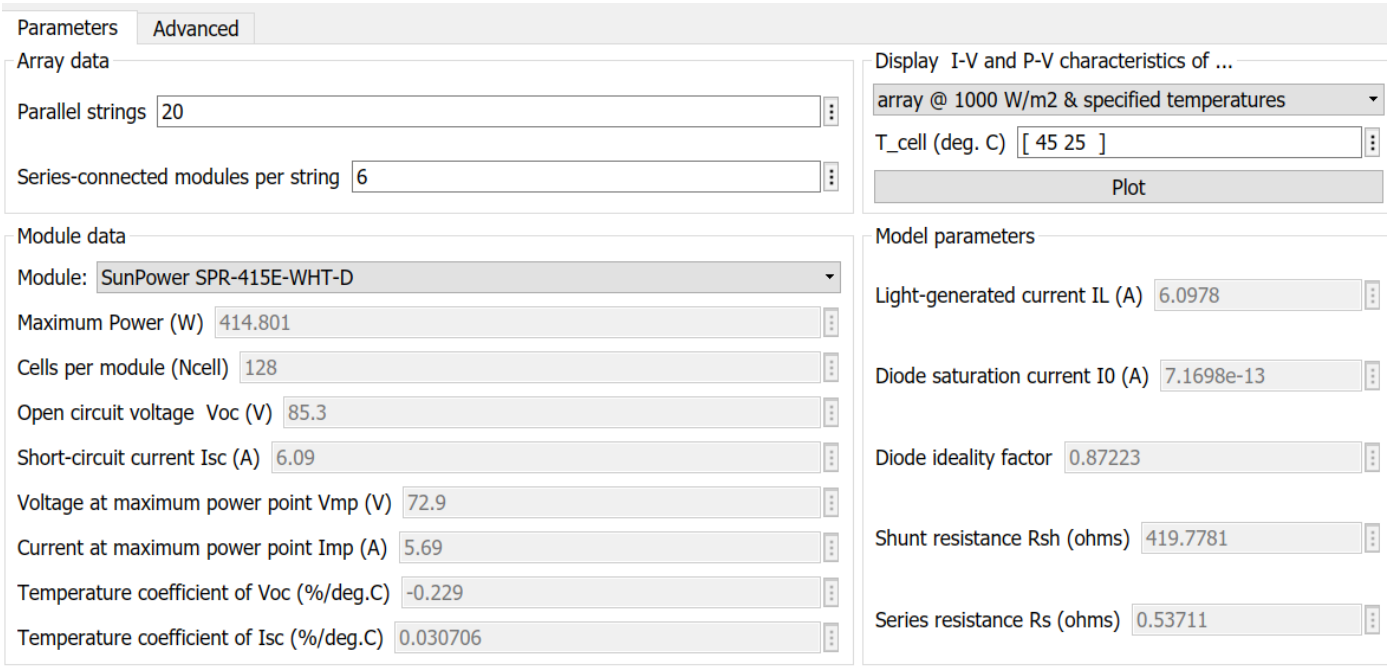


Fig.a.1 SunPower SPR -415E-WHT-D module data.

- The PV maximum outputted power can be computed by multiplying the module maximum power by the number of parallels and series strings:

  $P_{PV_max} = 414.801 \times 20 \times 6 = 49\,776\,W \approx 50\,KW.$

- The reference irradiance and cell temperature under standard test conditions (STC)s are respectively equal to: $S_{ref} = 1000\ W/m^2$ and $T_{ref_K} = 25°C = 298.15\,K$
- The reference light-generated current: $I_{L_ref} = 6.0978\,A$ as seen in Fig.a.1.
- The temperature coefficient of short-circuit current (I_{SC}) in ($A/°C$) is equal to the temperature coefficient of I_{SC} ($\%/°C$) multiplied by the short-circuit current (I_{SC}):
  $\alpha_{i_{sc}} = \frac{0.030706}{100} \times 6.09 = 1.87 \times 10^{-3}\ A/°C.$
- The diode current of the PV array (I_d) is expressed as a function of the diode voltage (V_d), the diode saturation current (I_0), and the diode temperature voltage (V_T):

  $$I_d = I_0 \left[exp\left(\frac{V_d}{V_T}\right) - 1 \right] \quad \text{(A.1)}$$

  Referring to fig.2.4 (chapter 2), V_d can be expressed as: $V_d = V_{PV} + R_s . I_{PV}$

I_0 and V_T are expressed as functions of the input variable T_K (the cell temperature in Kelvin)

- $I_0 = f(T_K) = I_{0_ref} \times \left(\frac{T_K}{T_{ref_K}}\right)^3 \times exp\left[\left(\frac{E_{g_ref}}{K_1 \times T_{ref_K}}\right) - \left(\frac{E_g}{K_1 \times T_K}\right)\right]$ (A.2)

where:

I_{0_ref} is the diode reference saturation current $= 7.169810^{-13} A$
E_{g_ref} is the reference material bandgap energy $= 1.12\ eV$ (for silicon)
K_1 is the Boltzmann constant = $8.618 \times 10^{-5}\ eV/K$.
E_g is the material bandgap energy, and is computed as follows:

- $E_g = E_{g_ref} \times \left[1 + dE_g dT \times (T_K - T_{ref_K})\right]$ (A.3)

$dE_g dT$ is a coefficient for silicon [160] $= -0.0002677$

- $V_T = f(T_K) = V_{T_ref} \times N_{ser} \times \frac{T_K}{T_{ref_K}}$ (A.4)

where:
N_{ser} is the number of the series-connected modules per string$= 6$.
V_{T_ref} is computed as follows: $V_{T_ref} = \frac{K \times T_{ref_K}}{q} \times nI \times Ncell$ (A.5)

where:

K is the Boltzmann constant = $1.3806 \times 10^{-23}\ J/K$.
q is the electron charge =$1.6022 \times 10^{-19}\ C$.
nI is the diode ideality factor (a number close to 1) $= 0.87223$ for this module.
$Ncell$ is the number of cells connected in series in a module $= 128$.

A.2 Incremental conductance MPPT technique

This method uses two current and voltage sensors to measure the PV array voltage and current. As a concept, the maximum-power point corresponds to a $\frac{dP_{PV}}{dV_{PV}} = 0$ (having $P_{PV} = I_{PV} \times V_{PV}$):

$$dP_{PV} = \frac{\partial P_{PV}}{\partial I_{PV}} dI_{PV} + \frac{\partial P_{PV}}{\partial V_{PV}} dV_{PV} = V_{PV}.dI_{PV} + I_{PV}.dV_{PV} \rightarrow \frac{dP_{PV}}{dV_{PV}} = V_{PV}.\frac{dI_{PV}}{dV_{PV}} + I_{PV} = 0$$

Which yields the following expression: $\frac{dI_{PV}}{dV_{PV}} + \frac{I_{PV}}{V_{PV}} = 0$ (A.6)

At each MPPT control sliding window time, the expression of (A.6) is computed, and the resulting error is minimized to continuously track the maximum available power. In the Simscape library of Simulink, the incremental conductance method can be implemented as a single block in which the PWM switching frequency (f_{sw_PV}), the sliding time window of the MPPT control (T_{MPPT}), and the initial duty cycle (D_{init}) are the parameters to be defined. The block has as inputs the PV array

current and voltage and the firing pulses (u) as output [121]. Inside the block, two Fourier analysis blocks are applied to I_{PV} and V_{PV} to get the fundamental components of ripples measured with a sliding time window T_{MPPT}. The Fourier blocks output dI_{PV} and dV_{PV}. Besides, the mean values of I_{PV} and V_{PV} are computed and utilized to form the (A.6) expression which can be written as:

$$\frac{dI_{PV}}{dV_{PV}} + \frac{I_{PV_mean}}{V_{PV_mean}} \tag{A.7}$$

Where, I_{PV_mean}, and V_{PV_mean} are respectively the mean values of the PV array current and voltage over the sliding time window (T_{MPPT}). A PI regulator minimizes the resulting error from (A.7) expression with a default proportional gain of 5. The regulator outputs the duty cycle correction ΔD to be added to the initial duty cycle D_{init}. Finally, $(\Delta D + D_{init})$ is connected to the PWM generator to generate the firing pulses that control the IGBT with the specified switching frequency. For this study, the parameters' values are: $D_{init} = 0.5$, $f_{sw_PV} = 20\ KHz$, and $T_{mppt} = 0.2\ ms$.

Appendix B

B.1 DC/DC boost components' selection and parameters calculation for conduction losses

B.1.1 Diode selection

To select the DC/DC boost diode, the maximum continuous DC forward current and the maximum peak reverse voltage should be evaluated:

- The maximum peak reverse voltage that the diode withstands in this application is equal to the DC bus voltage: $V_{RM} = V_{BUS} = 800\ V$.
- The maximum continuous DC forward current is equal to the maximum inductor current since the conduction equivalent resistor is placed in series with the inductor L: $I_{D_f_max} \approx I_{L_max}$. By referring to Fig.a.1, the PV maximum rated power is $P_{PV_max} \approx 50\ KW$ corresponding to a maximum PV current: I_{PV_max} = current at the maximum power point of a module × number of parallel strings $= 5.69 \times 20 = 114\ A$.

The Infineon semiconductor manufacturer is chosen for the diode and IGBT real sizing. The "DD400S45KL3_B5 "diode is selected with the below maximum rated values:

- $V_{RRM} = 4500\ V$, V_{RRM} : the repetitive peak reverse voltage
- $I_F = 400\ A$, I_F : the continuous DC forward current

As seen the maximum rated values outstrip the above-computed ones (V_{RM} and $I_{D_f_max}$) which guarantees a safe operation with an additional range for the safety factor.

V_{f0} and R_{D_f} values can be extracted from the $I_f = f(V_f)$ characteristic found in the manufacturer's datasheet and represented in Fig. b. (a). A tangent line to the curve of $T_{vj} = 25°C$, at the maximum DC forward current rated value ($I_F = 400\ A$), is drawn (red dashed line). The point of intersection of the tangent with the x-axis corresponds to the diode forward voltage source (V), and the inverse of the tangent's slope corresponds to the diode forward resistance (Ω). By referring to Fig.b.1 (a), $V_{f0} = 1.65\ V$ and $R_{D_f} = 2.1\ m\Omega$ are retrieved.

B.1.2 IGBT selection

The same approach of the diode selection is applied to size the IGBT and find the conduction loss parameters (V_{IGBT_CE0} and R_{IGBT_on}). The maximum continuous DC collector current and the maximum collector-emitter voltage should be evaluated:

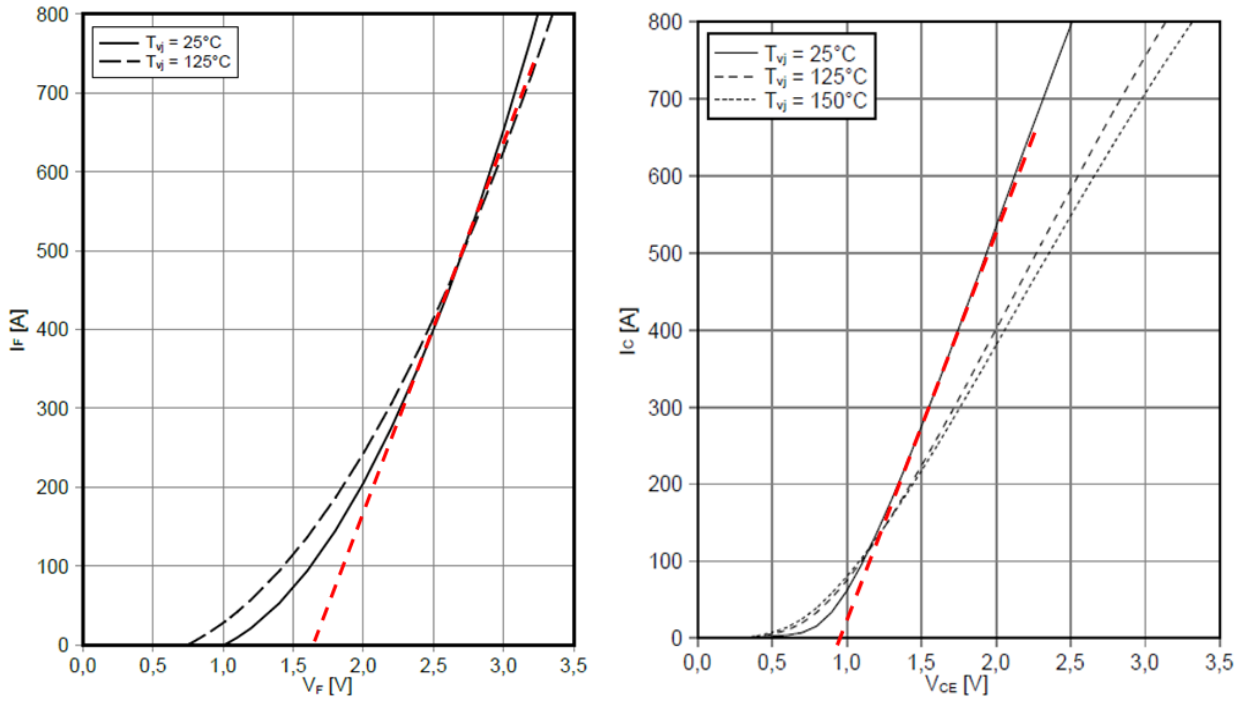
- The maximum collector-emitter voltage is retrieved when the IGBT is blocked:

$$V_{CE} = V_{BUS} = 800\ V$$

- The maximum continuous DC collector current is retrieved when the IGBT is ON and is equal to the maximum inductor current I_{L_max}: $I_{IGBT_on_max} \approx I_{L_max} = 114\ A$.

The "FZ400R12KE4 "IGBT is selected, from Infineon manufacturer, with the below maximum rated values:

- $V_{CES} = 1200\ V$, V_{CES} : the collector-emitter voltage
- $I_{c\ nom} = 400\ A$, $I_{c\ nom}$: the continuous DC collector current



(a) (b)

Fig.b.1 (a) $I_f = f(V_f)$, and (b) $I_c = f(V_{CE})$ characteristics from the Infineon datasheets.

Same to the diode selection criteria, the safe operation of the IGBT is guaranteed with an additional range for the safety factor.

V_{IGBT_CE0} and R_{IGBT_on} values are extracted from the $I_c = f(V_{CE})$ characteristic found in the manufacturer's datasheet and represented in Fig.b.1 (b). By drawing the tangent to the black curve and applying the same method of diode selection, the following values are obtained:

$V_{IGBT_CE0} = 0.9\ V$ and $R_{IGBT_on} = 2.1\ m\Omega$.

B.2 DC/DC boost parameters calculation for switching losses

B.2.1 IGBT parameters

Referring to the manufacturer's datasheet, the turn-on and turn-off delay time (s) are provided

for a collector-current $I_C = 400\ A$, and collector-emitter voltage $V_{CE} = 600\ V$:

$$t_{on_IGBT} = 0.24\ \mu s$$

$$t_{off_IGBT} = 0.61\ \mu s$$

B.2.2 Calculation of t_{f_D} and I_{RM_D}

The manufacturer doesn't provide t_{f_D}, then it should be computed using the diode parameters provided in the datasheet:

- The peak reverse recovery current: $I_{RM_ds} = 500\ A$
- The recovered charge: $Q_r = 390\ \mu C$
- The reverse recovery energy: $E_{rec} = 590\ mJ$

These parameters are provided under the below test conditions:

- $I_F = 400\ A$
- $dI_F/dt = 1650\ A/\mu s$
- $V_R = 2800\ V$

To compute t_{f_D}, the softness factor "s" is computed based on the below formula[128] :

$$s = \frac{t_{f_D}}{t_{s_D}} = \frac{Q_r}{0.5 I_{RM_ds}^2 / \frac{dI_F}{dt}} - 1 = 4.148 \qquad \text{(B.1)}$$

t_{s_D} : the time required by the diode current to fall from zero and reach its peak reverse recovery value (fig. b.2(b)).

Referring to fig.b.2(b), the reverse recovery time t_{rr_D} can be computed as follows:

$$t_{rr_D} = t_{s_D} + t_{f_D} = \frac{2.Q_r}{I_{RM_ds}} = 1.56\ \mu s \qquad \text{(B.2)}$$

Thus, $t_{f_D} = t_{rr_D}\left(\frac{s}{s+1}\right) = 0.8057 t_{rr_D} = 1.26\ \mu s.$

E_{rec} can be expressed as follows:

$$E_{rec} = k_E V_R Q_r \left(\frac{s}{s+1}\right) \qquad \text{(B.3)}$$

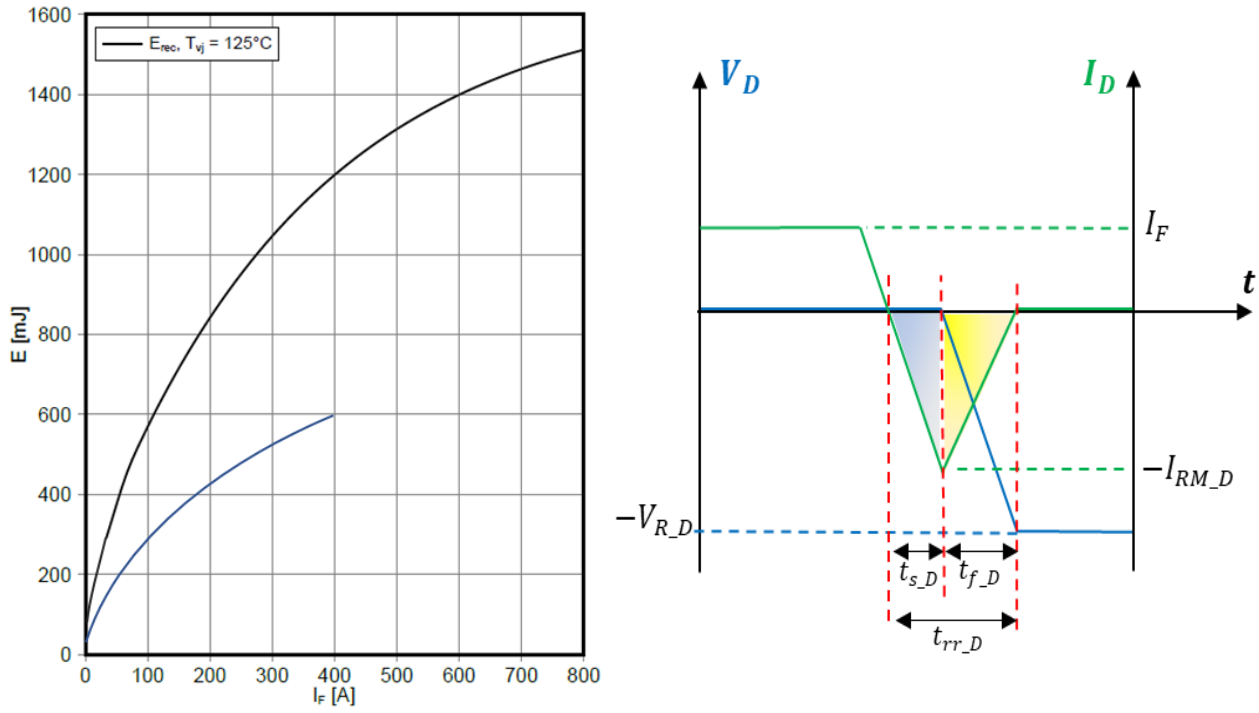
k_E : a constant depending on both the characteristics of the diode and the commutation circuit. Using equation (B.3), we find $k_E = 0.6706$.

To determine I_{RM_D} which is directly affected by the value of the forward current I_F, we refer to the datasheet curve showing the reverse recovery energy E_{rec} as a function of I_F as seen in Fig.b.2(a). The manufacturer provides the reverse recovery energy as a function of the forward

voltage at a 125°C condition (black curve). As the detailed curve of E_{rec} is not provided at 25°C, and only one value is provided for $I_F = 400\ A$ at T=25°C, the ratio of E_{rec} between the two temperature conditions is computed for $I_F = 400\ A$:

$$\left(\frac{E_{rec_125°}}{E_{rec_25°}}\right)_{I_F=400\ A} = \frac{1200}{590} \approx 2$$

To draw E_{rec} waveform (indigo curve) at T=25°C, the same ratio is considered for all I_F values. When the diode conducts, the forward current I_F is almost equal to the inductor current $I_L (I_F \approx I_L)$. Finally, MATLAB basic fitting tool is used to obtain $E_{rec} = f(I_F)$ equation. A fourth-degree polynomial fit gives a best-fitting result with a coefficient of determination $R^2 = 0.9997$.



(a) (b)

Fig.b.2 (a) diode switching losses $E_{rec} = F(I_F)$, (b) approximation of the reverse recovery current and reverse voltage.

The obtained equation is:

$$E_{rec} = (-4.31 \times 10^{-8})\ I_F^4 + (4.51 \times 10^{-5})\ I_F^3 - 0.018\ I_F^2 + 4.15\ I_F + 0.65 \qquad \text{(B.4)}$$

Hence, E_{rec} is calculated using equation (B.4), and by using equations (B.1), (B.2), and (B.3), I_{RM_D} is expressed as a function of E_{rec} :

$$I_{RM_D} = f(E_{rec}) = \sqrt{\frac{2E_{rec}(dI_F/dt)}{s\ k_E\ V_R}} \qquad \text{(B.5)}$$

Appendix C

C.1 PMSM parameters

A PMSM made by the German manufacturer VEM is chosen. The PMSM has the following data:



- Rated output power: $P_n = 55\ KW$
- Nominal speed: $N_n = 3000\ rpm$
- Nominal torque : $T_n = 175\ Nm$
- Rated frequency: $f_n = 100\ Hz$
- Number of pole pairs: $p = 2$
- Stator nominal phase-to-phase voltage: $U_n = 358\ V$
- Stator nominal phase-to-neutral voltage: $V_n = 206.7\ V$
- Stator base voltage: $V_{s_base} = V_n\sqrt{2} = 292.3\ V$
- Nominal current: $I_n = 95\ A$
- Nominal efficiency for motor operation: $\eta_{n,m} = 93.2\ \%$
- Nominal efficiency for generator operation: $\eta_{n,G} = 92.85\ \%$
- Power factor: $PF = 1$
- Motor inertia: $J = 0.264\ Kgm^2$
- Stator d-axis inductance: $L_d = 0.3445\ mH$
- Stator q-axis inductance: $L_q = 0.3445\ mH$
- Stator self-inductance per phase: $L_s = 0.153\ mH$
- The equivalent resistance of each stator winding: $R_s = 4.325\ m\Omega$
- Permanent magnet flux linkage: $\psi_m = 0.46392\ V.s$
- Viscous damping: $F = 0{,}0386\ Nm, s$

C.2 3ϕ rectifier IGBTs and diodes selection, and parameters calculation for conduction and switching losses

To select the IGBTs and the diodes of the 3ϕ rectifier, the maximum continuous collector current and the maximum collector-emitter voltage of the IGBT should be evaluated. As each diode is placed in parallel to one IGBT:

- the maximum continuous forward current in the diode is equal to the maximum continuous collector current of the IGBT.
- the maximum peak reverse voltage of the diode is equal to the maximum collector-emitter voltage of the IGBT.
- The maximum collector-emitter voltage is retrieved when the IGBT is blocked:

$$V_{CE} = V_{BUS} = 800\ V$$

- The maximum continuous DC collector current is retrieved when the IGBT is ON and is equal to the maximum sinusoidal phase current $\hat{\imath}_l$ of the PMSM (PMSM parameters): $\hat{\imath}_l = \sqrt{2} I_n = 134.35\ A$.

The "FS300R12OE4 "IGBT module is selected, from Infineon manufacturer. The module consists of 6 IGBTs connected to an anti-parallel diode each. The rated values of each IGBT and diode are extracted from the manufacturer's datasheet. The IGBT-rated values are:

- $V_{CES} = 1200\ V$, V_{CES} : the collector-emitter voltage
- $I_{c\,nom} = 300\ A$, $I_{c\,nom}$: the continuous DC collector current
- $\mathrm{V_{ref}} = 600V$, V_{ref} : the voltage reference of the given switching losses
- $\mathrm{i_{ref}} = 300A$, i_{ref} : the current reference of the given switching losses
- $\mathrm{E_{on_IGBT}} = 19\ mJ$, $\mathrm{E_{on_IGBT}}$: turn-on energy loss per pulse
- $\mathrm{E_{off_IGBT}} = 24.5\ mJ$, E_{off_IGBT}: turn-off energy loss per pulse

The diode-rated values are:

- $V_{RRM} = 1200\ V$, V_{RRM} : the repetitive peak reverse voltage
- $I_F = 300\ A$, I_F : the continuous DC forward current
- $\mathrm{V_{ref}} = 600V$, V_{ref} : the voltage reference of the given switching losses
- $\mathrm{i_{ref}} = 300A$, i_{ref} : the current reference of the given switching losses
- $E_{off_diode} = 12.5\ mJ$, E_{off_diode} : the reverse recovery energy

To find $V_{CE,0}$, r_{CE}, $V_{F,0}$, r_F, applied to compute the conduction losses in the IGBT and diode, we refer to the characteristics provided by the manufacturer's datasheet. Fig.c.1 (a) and (b) show respectively the characteristics of $I_c = f(V_{CE})$ and $I_f = f(V_f)$. By drawing the tangents (dashed red line) to the black curves $I_c = f(V_{CE})$ and $I_f = f(V_f)$ at an operating temperature of $T_{vj} = 25\ °C$ and applying the same method of the DC/DC boost cited in Appendix B, the following values are obtained:

- $V_{CE,0} = 0.88\ V$ and $r_{CE} = 2.9\ m\Omega$.
- $V_{F,0} = 1.0941\ V$ and $r_F = 1.9\ m\Omega$.

C.3 Optimal torque MPPT technique

Referring to [42], the tip speed ratio, λ, can be expressed as the ratio of the linear speed of the blade tips, v_{wind}, to the rotational speed of the wind turbine w_r by:

$$\lambda = \frac{\omega_r R}{v_{wind}} \tag{C.1}$$

where R is the blade length (m) and the turbine-swept area is $A = \pi R^2$. Thus, equation (II.21) can be rewritten as follows:

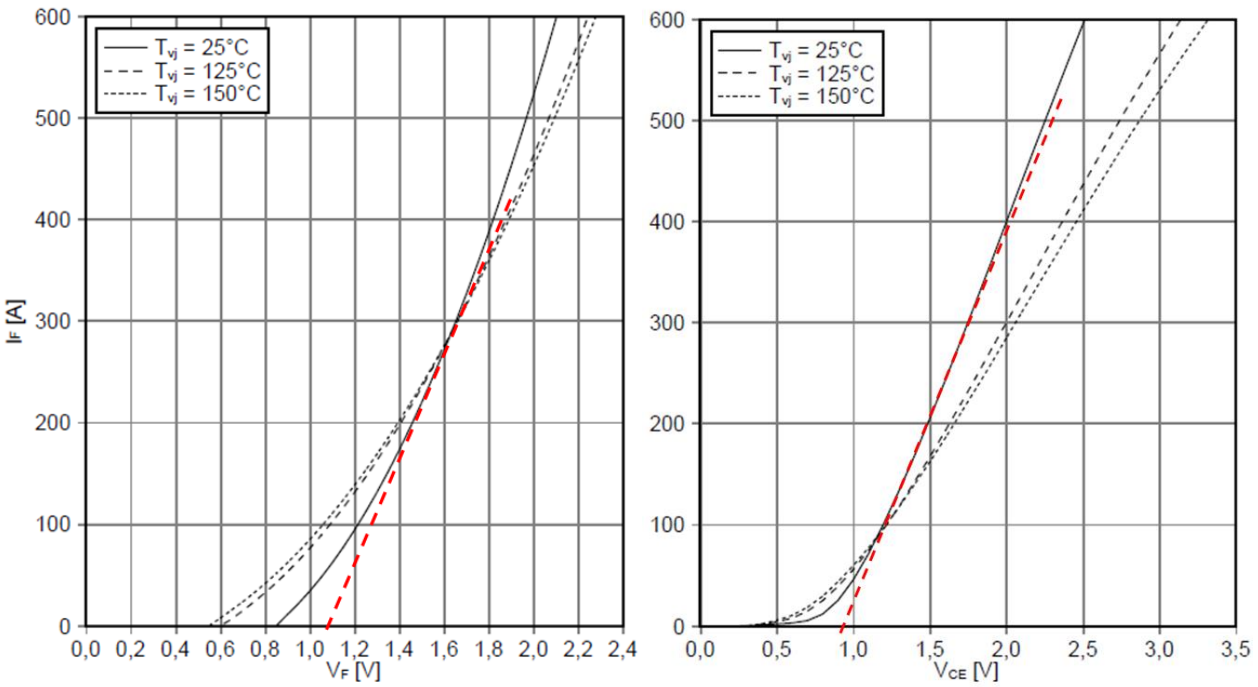


Fig.c.1 (a) $I_f = f(V_f)$, and (b) $I_c = f(V_{CE})$ characteristics from the Infineon datasheets.

$$P_{wind_m} = c_p(\lambda, \beta)\frac{\rho\pi R^5}{2\lambda^3}\omega_r^3 \tag{C.2}$$

To extract the maximum available power from the wind turbine, the rotor of the PMSM should always run at $c_p = c_{p_max}$ corresponding to the value of $\lambda = \lambda_{nom}$. Hence, the following expression is obtained:

$$P_{wind_m_opt} = \frac{1}{2}\rho\pi R^5 \frac{c_{p_max}}{\lambda_{nom}^3}\omega_r^3 = k_{opt}\omega_r^3 \tag{C.3}$$

where $k_{opt} = \frac{1}{2}\rho\pi R^5 \frac{c_{p_max}}{\lambda_{nom}^3}$ is constant.

The block diagram of the optimal torque MPPT method is shown in Fig. c.2. As seen, $P_{wind_m_opt}$ is calculated using equation (C.3) (denoted P_{mec_ref} in Fig. c.2). Then the mechanical losses, P_{m_PMSM}, and the ohmic losses, P_{J_PMSM}, of the PMSM are computed and subtracted from P_{mec_ref} to generate the electrical reference P_{elec_ref}. Then, P_{elec_ref} is compared to the actual electrical power, computed in the (dq) frame, and the resulting error is minimized by a P.I. controller. The regulator outputs the d-axis current reference (i_{d_ref}), while i_{q_ref} is always set to zero to obtain zero reactive power in the electrical circuit. The regulator parameters are $K_{i_pr} = 1$ and $T_{i_pr} = 100$. Finally, Fig. c.3 shows the MPPT characteristic in which the turbine output power (in $p.u.$ of the nominal mechanical power) is plotted as a function of the wind speed (in $p.u.$ of the rated wind speed). Six different zones of operation can be identified:

Zone 1: $0 \leq v_{wind} < V_{ci_pu}$. The wind speed is less than the cut-in speed $V_{ci_pu} = 0.44\ p.u. \leftrightarrow V_{ci} = 5.28\ m/s$. In this zone, $P_{wind_m_pu} = 0$.

Zone 2: $V_{ci_pu} \leq v_{wind} < b$. This zone precedes the MPPT zone, it starts at $v_{wind} = V_{ci_pu}$ and ends at $v_{wind} = b = 0.45\ p.u\ (5.4\ m/s)$. $P_{wind_m_pu}$ is linear in this zone and reaches $0.08\ p.u.$ at its end.

Zone 3: $b \leq v_{wind} < c$. It is the MPPT zone in which the optimal torque MPPT technique is applied. It starts at $v_{wind} = b = 0.45\ p.u$ and ends at $v_{wind} = c = 1\ p.u\ (12\ m/s)$ where $P_{wind_m_pu} = 0.9\ p.u. \leftrightarrow P_{wind_m} = 0.9 \times 55 = 49.5\ KW$.

Zone 4: $c \leq v_{wind} < d$. This zone follows the MPPT zone, it starts at $v_{wind} = c$ and ends at $v_{wind} = d = 1.01\ p.u.\ (12.12\ m/s)$. $P_{wind_m_pu}$ is linear in this zone and reaches at its end $1\ p.u.$ $\leftrightarrow P_{wind_m} = 55\ KW$.

Zone 5: $d \leq v_{wind} < V_{co_pu}$. In this zone, the wind power is constant and equal to its maximum $P_{wind_m_pu} = 1 \leftrightarrow P_{wind_m} = 55\ KW$. It ends when the wind speed reaches the cut-out speed V_{co_pu}.

Zone 6: $v_{wind} \geq V_{co_pu}$. This zone is attained when the wind speed reaches the cut-out speed $V_{co_pu} = 2\ p.u. \leftrightarrow V_{co} = 24\ m/s$ .The wind power is null ($P_{wind_m_pu} = 0$) to prevent the destruction of the turbine.

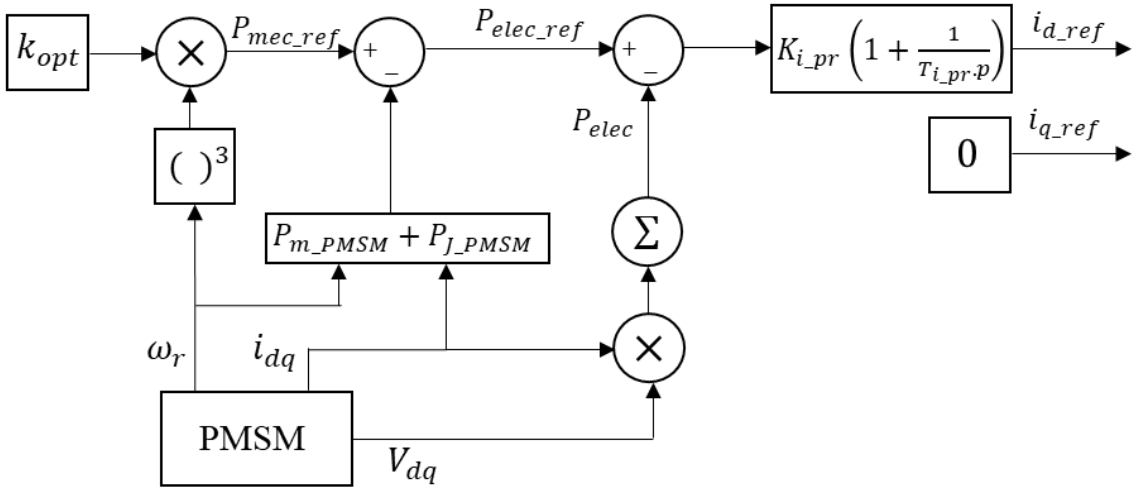
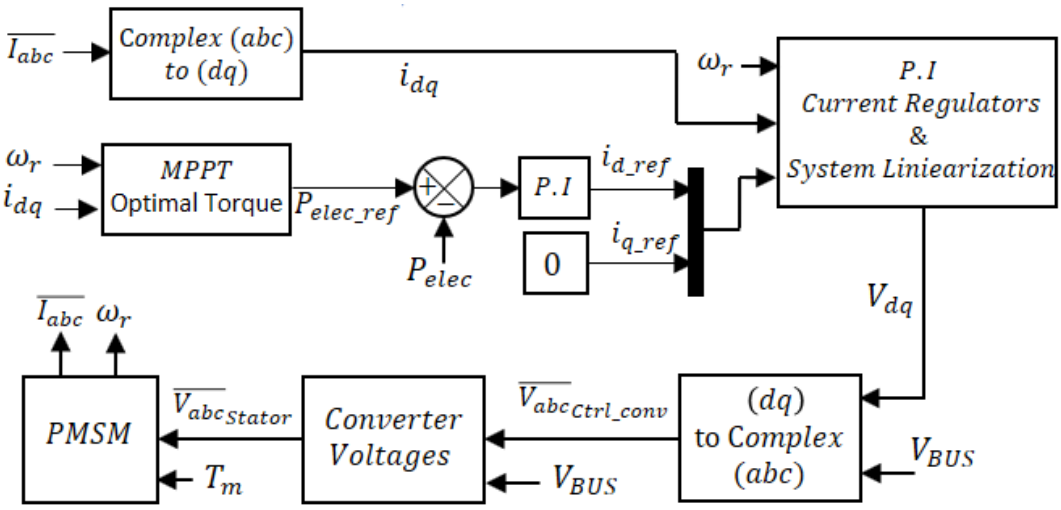


Fig.c.2 The block diagram of optimal torque control MPPT method.



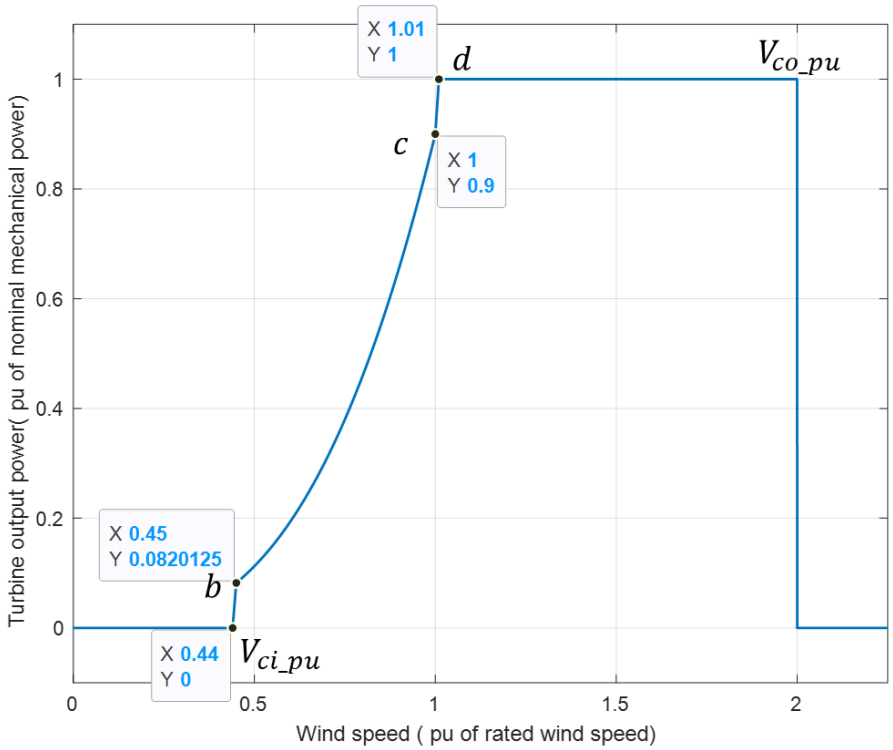


Fig.c.3 MPPT characteristic curve as a function of the wind speed ($p.u.$ of rated wind speed).

Appendix D

D.1 Battery thermal expressions and parameters

$E_0(T)$, $K(T)$, $Q(T_a)$, and $R(T)$ can be expressed as functions of the cell temperature as the following:

- $E_0(T) = E_0|_{T_{ref}} + \frac{\partial E}{\partial T}(T - T_{ref})$ (D.1)
- $K(T) = K|_{T_{ref}} + exp\left(\alpha\left(\frac{1}{T} - \frac{1}{T_{ref}}\right)\right)$ (D.2)
- $Q(T_a) = Q|_{T_{ref}} + \frac{\Delta Q}{\Delta T}(T_a - T_{ref})$ (D.3)
- $R(T) = R|_{T_{ref}} + exp\left(\beta\left(\frac{1}{T} - \frac{1}{T_{ref}}\right)\right)$ (D.4)

Where,

- T_{ref} is the nominal ambient temperature, in K.
- $E_0|_{T_{ref}}$ is the constant voltage at T_{ref}, in V.
- $\frac{\partial E}{\partial T}$ is the reversible voltage temperature coefficient, in V/K.
- $K|_{T_{ref}}$ is the polarization constant at T_{ref}, in V/Ah.
- α is the Arrhenius rate constant for polarization resistance.
- $Q|_{T_{ref}}$ is the maximum battery capacity constant at T_{ref}, in Ah.
- $\frac{\Delta Q}{\Delta T}$ is the maximum capacity temperature coefficient, in Ah/K.
- $R|_{T_{ref}}$ is the internal resistance constant at T_{ref}, in Ω.
- β is the Arrhenius rate constant for internal resistance.

The cell temperature T, at any given time, t, is expressed as:

$$T(t) = L^{-1}\left(\frac{P_{loss}R_{th} + T_a}{1 + (t_{c_th})p}\right) \quad \text{(D.5)}$$

Where,

R_{th} is the thermal resistance, cell to ambient ($°C/W$).

t_{c_th} is the thermal time constant, cell to ambient (s).

P_{loss} is the overall heat generated (W) during the charge/discharge process and is expressed as follows:

$$P_{loss} = (E_0(T) - V_{batt}(T))I_{batt} + \frac{\partial E}{\partial T} I_{batt} T \quad \text{(D.6)}$$

To determine the battery parameters, one can refer to the manufacturer's datasheet or apply the automatic discharge parameter determination in MATLAB. This option is found in the battery block of the Simscape library in which MATLAB/Simulink determines all the battery parameters from the discharge characteristics based on the battery's rated capacity and nominal voltage. This option is selected for this study and the below battery parameters are extracted:

Parameter	*Value*	*Parameter*	*Value*
A	$7.47\ V$	$Q\|_{T_{ref}}$	$517\ A.h$
B	$0.122\ A.h^{-1}$	$K\|_{T_{ref}}$	$0.0045\ V/Ah$
T_{ref}	$298.15\ K$	$E_0\|_{T_{ref}}$	$283.95\ V$
$R\|_{T_{ref}}$	$5\ m\Omega$	β	1
α	1.000043	$\frac{\partial E}{\partial T}$	$1 \times 10^{-6}\ V/K$
$\frac{\Delta Q}{\Delta T}$	$0.8\ Ah/K$	R_{th}	$0.0012\ °C/W$
t_{c_th}	$1800\ s$	τ_{batt}	$10\ s$

Table.D.1 Lithium-ion battery parameters extracted from MATLAB/Simulink.

D.2 Bidirectional DC/DC converter parameters

By analyzing the detailed electrical circuit of the bidirectional DC/DC converter (Fig.2.36), it can be seen that:

- the maximum continuous forward current in the $D_{sw1}$and D_{sw2} is equal to the maximum continuous collector current of $sw1$ and $sw2$.
- the maximum peak reverse voltage of D_{sw1} and D_{sw2} is equal to the maximum collector-emitter voltage of the $sw1$ and $sw2$.

- The maximum collector-emitter voltage is retrieved when $sw1$(boost mode) or $sw2$ (buck mode) is blocked:

$$V_{CE} = V_{RM} = V_{BUS} = 800\ V$$

- The maximum continuous DC collector current is retrieved when $sw1$(boost mode) or $sw2$ (buck mode) is ON and is equal to the maximum allowable discharge/charge current from/in the battery. Having a nominal battery capacity of $500\ Ah$, a maximum allowable charge/ discharge current of 0.434C is fixed, then $I_{batt_max} = \pm 217\ A$.

$$I_{IGBT_on_max} = I_{D_F_max} = 217\ A$$

As they withstand the same reverse voltage and forward current, $sw1$ and $sw2$ are identical.

$sw1$ and $sw2$ switches are chosen from the Infineon semiconductor manufacturer. The "FF600R12ME7_B11 "module is selected. It consists of two identical IGBTs in parallel with two identical diodes. The maximum rated values of the IGBT and parallel diode are the following:

- $V_{CES} = 1200\ V$, V_{CES} : the collector-emitter voltage
- $I_{c\,nom} = 600\ A$, $I_{c\,nom}$: the continuous DC collector current
- $V_{RRM} = 1200\ V$, V_{RRM} : the repetitive peak reverse voltage
- $I_F = 600\ A$, I_F : the continuous DC forward current

The turn-on and turn-off delay time (s) are provided for a collector-current $I_C = 600\ A$, and collector-emitter voltage $V_{CE} = 600\ V$:

- $t_{on_IGBT} = 0.25\ \mu s$
- $t_{off_IGBT} = 0.420\ \mu s$

Based on $I_f = f(V_f)$, and $I_c = f(V_{CE})$ characteristics from the Infineon datasheets, V_{f0_sw1} , V_{CE0_sw1}, $R_{D_f_sw1}$, and R_{on_sw1} are identified following the same approach as Appendices B and C. The following values are obtained:

- $V_{f0_sw1} = 1.225\ V$
- $V_{CE0_sw1} = 0.8864\ V$
- $R_{D_f_sw1} = 0.958\ m\Omega$
- $R_{on_sw1} = 1.022\ m\Omega$

The provided diode parameters are:

- The peak reverse recovery current: $I_{RM_ds} = 400\ A$
- The recovered charge: $Q_r = 38\ \mu C$
- The reverse recovery energy: $E_{rec} = 19\ mJ$

These parameters are provided under the below test conditions:

- $I_F = 600\ A$
- $dI_F/dt = 7800\ A/\mu s$
- $V_R = 600\ V$

Using the given parameters and the same equations of Appendix B.2.2, $t_{f_D} = 0.139\ \mu s$.

To define I_{RM_D}, E_{rec} is expressed as a function of I_F by adopting the same method as in Appendix B.2.2. The expression of $E_{rec} = f(I_F)$ is the following:

$$E_{rec} = (-3.9 \times 10^{-12})\, I_F^4 + (1.4 \times 10^{-8})\, I_F^3 - (2.78 \times 10^{-5})\, I_F^2 + 0.038\, I_F + 3.978 \qquad \text{(D.7)}$$

Once E_{rec} is defined using equation (D.7), I_{RM_D} can be found using equation (B.5):

$$I_{RM_D} = f(E_{rec}) = \sqrt{\frac{2E_{rec}(dI_F/dt)}{s\, k_E\, V_R}}$$

With $k_E = 1$ and $s = 2.705$.

Appendix E

E.1 Battery-discretized dynamic model

The battery dynamic model is represented in the continuous state in Chapter 2 (equations II.52, II.53, and II.54). To apply the optimization solvers such as the (DP) and (GA) in Chapter 3, a discretized version of the battery dynamic model is required as the battery SOC evolves as a function of the P_{batt} and the time. Hence, the discretized version of the lithium-ion battery in which the SOC at time $k+1$ can be expressed as a function of the SOC at time k , the battery charged/discharged power at time k, and the battery voltage at time k is:

$$SOC(k+1) = SOC(k) - \frac{P_{dis}(k).T_s}{Q(T_a).V_{batt}(k)} - \frac{P_{ch}(k).T_s}{Q(T_a).V_{batt}(k)} \quad \text{(E.1)}$$

Where, $P_{ch}(k)$, $P_{dis}(k)$, T_s, $V_{batt}(k)$, and $\mathrm{Q}(T_\mathrm{a})$ are respectively the battery-charged power at time k in (W), the battery-discharged power at time k in (W), the sampling period (hours), the battery voltage at time k in Volts, and the battery maximum capacity at ambient temperature (Ah). The applied algorithm is shown in Algorithm E.1. As seen in discharge mode, $P_{dis}(k)$ equals $P_{batt}(k) > 0$ and $P_{ch}(k)$ is set to zero, then $SOC(k+1) < SOC(k)$. However, in charge mode, $P_{ch}(k)$ equals $P_{batt}(k) < 0$ and $P_{dis}(k)$ is set to zero, then $SOC(k+1) > SOC(k)$. Applying the discrete equation format (E.1), SOC is considered the state of the system and $P_{batt}(k)$ is the decision variable.

Algorithm E.1 : Battery-discretized dynamic model

$$[\mathbf{SOC(k+1)}, \mathbf{V_{batt}(k+1)}, \mathbf{it(k+1)}] = \mathbf{f_{batt}(SOC(k), P_{batt}(k), V_{batt}(k), it(k), T_a(k)})$$

1- Computing T(k) out of $\mathrm{T_a(k)}$ *% computing cell temperature out of the ambient temperature*
2- $i_{batt}(k) = \frac{P_{batt}(k)}{V_{batt}(k)}$; *% battery current in A*
3- Computing $i^*_{batt}(k)$ from $i_{batt}(k)$ *% low frequency current dynamics in A*
4- $it(k+1) = it(k) + i_{batt}(k).T_s$; *% extracted capacity in Ah*
5- $if\ (i_{batt}(k) > 0)$ *% testing charge/discharge mode*
6- $P_{ch}(k) = 0$; *% setting discharge mode*
7- $P_{dis}(k) = P_{batt}(k)$;
8- Computing $V_{batt}(k+1)$ following equation (II.52):
$V_{batt}(k+1) = f_{dis}(it(k+1), i^*_{batt}(k), i_{batt}(k), \mathrm{T(k)}, \mathrm{T_a(k)}) - R_{batt}\ (\mathrm{T(k)}).i_{batt}(k)$;
9- else
10- $P_{dis}(k) = 0$; *% setting charge mode*
11- $P_{ch}(k) = P_{batt}(k)$;
12- Computing $V_{batt}(k+1)$ following equation (II.53):
$V_{batt}(k+1) = f_{ch}(it(k+1), i^*_{batt}(k), i_{batt}(k), \mathrm{T(k)}, \mathrm{T_a(k)}) - R_{batt}\ (\mathrm{T(k)}).i_{batt}(k)$;
13- end
14- Computing $SOC(k+1)$ using equation (E.1)
15- **end**

E.2 Dynamic programming principle

The basic model to treat through (DP) should have two main aspects[154]:

- The dynamic of the system is described in the form of a discretized dynamic equation (such as equation E.1).
- The cost function is additive as a function of time.

The discretized equation (E.1) can be represented in canonical form as the following:

$$x(k+1) = f_k(x(k), u(k)), \qquad k = 0,1, \dots, N-1 \tag{E.2}$$

Wehre, $x(k)$, k, $u(k)$, N, and f_k are respectively the state of the system, the decision variable, the discrete-time index, the number of total steps for the whole time horizon, and the function describing the dynamic of the system.

The cost function is additive in the sense that the cost calculated at time k, and denoted $\gamma_k(x(k), u(k))$ accumulates over time. The total cost, denoted $\mathfrak{R}$, is given by:

$$\mathfrak{R} = \gamma_N\big(x(N)\big) + \sum_{k=0}^{N-1} \gamma_k(x(k), u(k)) \tag{E.3}$$

Where $\gamma_N\big(x(N)\big)$, is the terminal cost applied at the end of the process.

A control strategy $\pi = \{\mu_0, \mu_1, \dots, \mu_{N-1}\}$ is defined by linking each step k of the applied control to the state of the system:

$$u(k) = \mu_k\big(x(k)\big) \tag{E.4}$$

Given an initial state $x(0)$ and an admissible control strategy $\pi = \{\mu_0, \mu_1, \dots, \mu_{N-1}\}$, then for a given cost function γ_k, from $k = 0$ to N, the total cost of the strategy is defined by the following equation:

$$\mathfrak{R}_\pi(x(0)) = \gamma_N\big(x(N)\big) + \sum_{k=0}^{N-1} \gamma_k(x(k), u(k)) \tag{E.5}$$

The optimal control strategy, π^*, is the one that minimizes this cost:

$$\mathfrak{R}_{\pi^*}\big(x(0)\big) = \min_{\pi} \mathfrak{R}_\pi\big((x(0))\big) \tag{E.6}$$

We can consider this cost as a function which, for each initial state $x(0)$, links the optimal cost value $\mathfrak{R}_{\pi^*}\big(x(0)\big)$. This function is called the optimal cost function.

(DP) is based on the principle of the maximum or the principle of Bellman. The principle can be stated as follows:

Let $\pi^* = \{\mu_0^*, \mu_1^*, \dots, \mu_{N-1}^*\}$ be an optimal control strategy for the considered problem. Suppose that when π^* is used, the state $x(i)$ is reached at time i. By considering the subproblem for which, from state $x(i)$ at time i, the cost from i till N to minimize is expressed as follows:

$$\Re = \gamma_N\big(x(N)\big) + \sum_{k=i}^{N-1} \gamma_k(x(k), u(k))$$

(E.7)

Then, the truncated control strategy $\pi^* = \{\mu_i^*, \mu_{i+1}^*, \dots, \mu_{N-1}^*\}$ is optimal for this subproblem. From this principle, we can formulate that for each initial state $x(0)$, the optimal cost $\Re^*\big(x(0)\big)$ of the considered problem is equal to the value of $\Re_0\big(x(0)\big)$ given by the following recurrent algorithm:

$$\Re_N = \gamma_N\big(x(N)\big) \tag{E.8}$$

$$\Re_k\big(x(k)\big) = \min_{u_k}\Big(\gamma_k\big(x(k), u(k)\big) + \Re_{k+1}\Big(f_k\big(x(k), u(k)\big)\Big)\Big) \quad \text{for } k = N-1, \dots, 0 \tag{E.9}$$

Appendix F

F.1 Parameters of the " ga " function

The problem constraints represented in equations (III.21) to (III.28) are included in the "ga" function parameters $A, b, A_{eq}, b_{eq}, lb, ub,$ and $nonlcon$ as follows:

- There are no linear inequalities in the problem, then A and b that correspond to the linear inequalities' parameters equal empty vectors, $A = [\,]$ and $B = [\,]$.
- One linear equality is included and corresponds to the last SOC value which should be equal to the initial state, $SOC(N) = 50\%$. To include this constraint, A_{eq} and b_{eq} that form the linear equalities in "ga" are utilized. Given that the (GA) evaluates the matrix product $A_{eq}.x = b_{eq}$. If N_{lin_equ} is the number of linear equalities then, A_{eq} is a $(N_{lin_equ} \times 72)$ matrix and b_{eq} is a $(N_{lin_equ} \times 1)$ vector. In our case, we have one linear equality then, A_{eq} is a (1×72) vector and b_{eq} is a (1×1) vector. $A_{eq}(1, 72) = 1$ and $b_{eq} = 50$.
- To set the lower and upper bounds on decision variables the lb and ub vectors are utilized. lb and ub form two (1×72) vectors including respectively the lower and upper bounds of P_{grid_ref}, P_{DG_ref}, and SOC. They are expressed as follows:

$$lb = \begin{bmatrix} P_{grid_min} \\ 0 \\ SOC_{min} \\ P_{grid_min} \\ 0 \\ SOC_{min} \\ \dots \\ \dots \\ \dots \\ P_{grid_min} \\ 0 \\ SOC_{min} \end{bmatrix} \qquad ub = \begin{bmatrix} P_{grid_max} \\ P_{DG_max} \\ SOC_{max} \\ P_{grid_max} \\ P_{DG_max} \\ SOC_{max} \\ \dots \\ \dots \\ \dots \\ P_{grid_max} \\ P_{DG_max} \\ SOC_{max} \end{bmatrix} \tag{F.1}$$

  By this, a feasible solution is always found in the range of $lb \leq x \leq ub$.
- The remaining constraints are included as nonlinear constraints through the "$Nonlcon$" function. $Nonlcon$ accepts x and returns vectors C and C_{eq}, representing the nonlinear inequalities and equalities respectively. ga minimizes the function such that $C(x) \leq 0$ and $C_{eq}(x) = 0$. Each time the $Nonlcon$ function is called, P_{grid_ref}, P_{DG_ref}, and SOC reference vectors are extracted from the individual vector x, and the P_{batt_ref} vector is retrieved from the SOC vector following the equation (E.1). By dividing the individual vector x into the subvectors P_{grid_ref}, P_{DG_ref}, and P_{batt_ref}, C and C_{eq} can

now be expressed more comprehensibly as functions of these three vectors. Besides, the converters' loss vectors can now be computed based on P_{grid_ref}, P_{DG_ref}, and P_{batt_ref} vectors. The losses in grid, (DG), and battery converters vectors are respectively denoted $P_{losses_3\phi_grid_conv}$, $P_{losses_3\phi_DG_rec}$, and $P_{losses_bidirec_conv}$. Thus, C_{eq} and C expressions are respectively the following:

$$C_{eq} = P_{load} - P_{RESs_bus} - P_{grid_ref} - P_{DG_ref} - P_{batt_ref} + P_{losses_3\phi_grid_conv} + P_{losses_3\phi_DG_rec} + P_{losses_bidirec_conv} \quad \text{(F.2)}$$

$$C = \begin{bmatrix} P_{DG_min}.sign(P_{DG_ref}) - P_{DG_ref}\,; \\ -sign(P_{DG_ref}).P_{grid_ref}; \\ \left|P_{batt_ref}\right| - P_{batt_max}; \end{bmatrix} \quad \text{(F.3)}$$

Where, P_{DG_min} and P_{batt_max} are respectively the (DG) minimum admissible operating power (W) and the maximum allowable power to be discharged from the battery (W). All variables are vectors of dimension (24×1), then C_{eq} is a (24×1) vector and C is a (24×3) matrix.

References

[1] U. S. (DOE, *The potential benefits of distributed generation and rate-related issues that may impede their expansion, A study pursuant to section 1817 of the energy policy act of 2005*. 2007.

[2] "Electric Power Annual 2004." U.S. Department of Energy, Energy Information Administration,2004. Available:http://www.eia.doe.gov/cneaf/electricity/epa/epa_sum.html.

[3] "Electric power transmission and distribution losses (% of output) | Data." Available:https://data.worldbank.org/indicator/EG.ELC.LOSS.ZS?end=2014&start=1990&view=chart.

[4] "EIA - State Electricity Profiles." Available: https://www.eia.gov/electricity/state/unitedstates/.

[5] "Access to electricity, rural (% of rural population) | Data." Available:https://data.worldbank.org/indicator/EG.ELC.ACCS.RU.ZS?end=2020&start=1990&type=shaded&view=chart.

[6] "Development Projects : DRC Electricity Access & Services Expansion (EASE) - P156208," World Bank. Available: https://projects.worldbank.org/en/projects-operations/project-detail/P156208.

[7] "Centralized Electricity Grid and the Rural Economy of Nigeria - IOPscience." Available: https://iopscience.iop.org/article/10.1088/1755-1315/730/1/012015/meta.

[8] "U.S. Energy Information Administration - EIA - Independent Statistics and Analysis." Available: https://www.eia.gov/todayinenergy/detail.php?id=48136.

[9] "Severe power cuts in Texas highlight energy security risks related to extreme weather events – Analysis - IEA." Available: https://www.iea.org/commentaries/severe-power-cuts-in-texas-highlight-energy-security-risks-related-to-extreme-weather-events.

[10] President's Council of Economic Advisers, U.S. Department of Energy Office of and Electricity Delivery and Energy Reliability., "Economic benefits of increasing electric grid resilience to weather outages.," Executive Office of the President, 2013. Available: https://www.energy.gov/sites/default/files/2013/08/f2/Grid%20Resiliency%20Report_FINAL.pdf.

[11] "IEA (2021), Climate Resilience," International Energy Agency (IEA), Paris, Apr. 2021. Available: https://www.iea.org/reports/climate-resilience.

[12] H. Ritchie, M. Roser, and P. Rosado, "Nuclear Energy," *Our World in Data*, Nov. 2020, Available: https://ourworldindata.org/nuclear-energy.

[13] "Years of fossil fuel reserves left," Our World in Data. Available: https://ourworldindata.org/grapher/years-of-fossil-fuel-reserves-left.

[14] D. Abbott, "Is Nuclear Power Globally Scalable? [Point of View]," *Proceedings of the IEEE*, vol. 99, no. 10, pp. 1611–1617, Oct. 2011, doi: 10.1109/JPROC.2011.2161806.

[15] H. Ritchie, M. Roser, and P. Rosado, "Energy," *Our World in Data*, Nov. 2020. Available: https://ourworldindata.org/fossil-fuels.

[16] "Europe prepares for energy crisis as Russia slashes supplies of natural gas," France 24. Available: https://www.france24.com/en/europe/20220907-europe-prepares-for-energy-crisis-as-russia-reins-in-natural-gas-supply.

[17] "Six million homes could face winter power cuts due to energy shortages - report," Sky News. Available: https://news.sky.com/story/six-million-homes-could-face-winter-power-cuts-due-to-energy-shortages-report-12624000.

[18] J. Martin, "Distributed vs. Centralized Electricity Generation: Are We Witnessing a Change of Paradigm. An Introduction to Distributed Generation." HEC, Paris, May 2009.

[19] Wuebbles, D.J., D.W. Fahey, K.A. Hibbard, B. DeAngelo, S. Doherty, K. Hayhoe, R. Horton, J.P. Kossin, P.C. Taylor, A.M. Waple, and C.P. Weaver, "Executive Summary - Climate Science Special Report," U.S. Global Change Research Program, Washington, DC, USA, 4, 2017. Available: https://science2017.globalchange.gov/chapter/executive-summary/#fig-3.

[20] H. Ritchie, M. Roser, and P. Rosado, "CO_2 and Greenhouse Gas Emissions," *Our World in Data*, May 2020, Available: https://ourworldindata.org/co2-and-other-greenhouse-gas-emissions.

[21] "Distributed energy resources for net zero: An asset or a hassle to the electricity grid? – Analysis," IEA.
Available: https://www.iea.org/commentaries/distributed-energy-resources-for-net-zero-an-asset-or-a-hassle-to-the-electricity-grid.

[22] "Fit for 55: how the EU plans to boost renewable energy."
Available: https://www.consilium.europa.eu/en/infographics/fit-for-55-how-the-eu-plans-to-boost-renewable-energy/.

[23] "La France et la transition énergétique, vers la neutralité carbone grâce à un mix énergétique équilibré," ENGIE, Paris, France, 2002.
Available:https://www.engie.com/sites/default/files/assets/documents/2022-03/Dossier%20-%20La%20France%20et%20la%20transition%20énergétique.pdf.

[24] A. Hirsch, Y. Parag, and J. Guerrero, "Microgrids: A review of technologies, key drivers, and outstanding issues," *Renewable and Sustainable Energy Reviews*, vol. 90, pp. 402–411, Jul. 2018, doi: 10.1016/j.rser.2018.03.040.

[25] M. Green, "Community power," *Nat Energy*, vol. 1, no. 3, Art. no. 3, Feb. 2016, doi: 10.1038/nenergy.2016.14.

[26] E. Wood, "Concentric to Build 35-MW Microgrid in California with Innovative Wholesale Power Agreement," Concentric Microgrid Gonzales.
Available: https://microgridknowledge.com/concentric-microgrid-gonzales/.

[27] S. Parhizi, H. Lotfi, A. Khodaei, and S. Bahramirad, "State of the Art in Research on Microgrids: A Review," *IEEE Access*, vol. 3, pp. 1–1, Jan. 2015,
doi: 10.1109/ACCESS.2015.2443119.

[28] F. Katiraei, R. Iravani, N. Hatziargyriou, and A. Dimeas, “Microgrids Management,” *Power and Energy Magazine, IEEE*, vol. 6, pp. 54–65, Jun. 2008, doi: 10.1109/MPE.2008.918702.

[29] W. Bai, “DC Microgrid optimized energy management and real-time control of power systems for grid-connected and off-grid operating modes,” phdthesis, Université de Technologie de Compiègne, 2021. Available: https://theses.hal.science/tel-03313913.

[30] “DC, Come Home: DC Microgrids and the Birth of the ‘Enernet’ | Request PDF.” Available:https://www.researchgate.net/publication/260494120_DC_Come_Home_DC_Microgrids_and_the_Birth_of_the_Enernet.

[31] T. Dragicevic, J. C. Vasquez, J. M. Guerrero, and D. Skrlec, “Advanced LVDC Electrical Power Architectures and Microgrids: A step toward a new generation of power distribution networks,” *IEEE Electrification Magazine*, vol. 2, no. 1, pp. 54–65, Mar. 2014, doi: 10.1109/MELE.2013.2297033.

[32] T. Dragičević, “Hierarchical control of a direct current microgrid with energy storage systems in a distributed topology,” info:eu-repo/semantics/doctoralThesis, University of Zagreb. Faculty of Electrical Engineering and Computing. Department of Energy and Power Systems, 2013. Available: https://urn.nsk.hr/urn:nbn:hr:168:629440.

[33] Y.-X. Wang, F.-F. Qin, and Y.-B. Kim, “Bidirectional DC-DC converter design and implementation for lithium-ion battery application,” in *2014 IEEE PES Asia-Pacific Power and Energy Engineering Conference (APPEEC)*, Dec. 2014, pp. 1–5. doi: 10.1109/APPEEC.2014.7066140.

[34] D. J. Hammerstrom, “AC Versus DC Distribution SystemsDid We Get it Right?,” in *2007 IEEE Power Engineering Society General Meeting*, Jun. 2007, pp. 1–5. doi: 10.1109/PES.2007.386130.

[35] D. Fregosi *et al.*, “A comparative study of DC and AC microgrids in commercial buildings across different climates and operating profiles,” in *2015 IEEE First International Conference on DC Microgrids (ICDCM)*, Jun. 2015, pp. 159–164. doi: 10.1109/ICDCM.2015.7152031.

[36] R. S. Balog and P. T. Krein, “Bus Selection in Multibus DC Microgrids,” *IEEE Transactions on Power Electronics*, vol. 26, no. 3, pp. 860–867, Mar. 2011, doi: 10.1109/TPEL.2010.2094208.

[37] R. M. Cuzner and G. Venkataramanan, “The Status of DC Micro-Grid Protection,” in *2008 IEEE Industry Applications Society Annual Meeting*, Oct. 2008, pp. 1–8. doi: 10.1109/08IAS.2008.382.

[38] “ETSI EN 300 132-3-1.” ETSI, 2011. [Online]. Available: http://www.etsi.org/deliver/etsi_en/300100_300199/3001320301/02.01.01_40/en_3001320 301v020101o.pdf.

[39] “IEEE Standard for DC Microgrids for Rural and Remote Electricity Access Applications,” *IEEE Std 2030.10-2021*, pp. 1–47, Dec. 2021, doi: 10.1109/IEEESTD.2021.9646866.

[40] “Autonomous local control in distributed DC power systems - ProQuest.” Available: https://www.proquest.com/openview/af72bcde297f0a3109c52c12b1ec0d3a/1?pq-origsite=gscholar&cbl=18750&diss=y.

[41] S. K. Sahoo, A. K. Sinha, and N. K. Kishore, “Control Techniques in AC, DC, and Hybrid AC–DC Microgrid: A Review,” *IEEE Journal of Emerging and Selected Topics in Power Electronics*, vol. 6, no. 2, pp. 738–759, Jun. 2018, doi: 10.1109/JESTPE.2017.2786588.

[42] M. A. Abdullah, A. H. M. Yatim, C. W. Tan, and R. Saidur, “A review of maximum power point tracking algorithms for wind energy systems,” *Renewable and Sustainable Energy Reviews*, vol. 16, no. 5, pp. 3220–3227, Jun. 2012, doi: 10.1016/j.rser.2012.02.016.

[43] V. Salas, E. Olías, A. Barrado, and A. Lazaro, “Review of the maximum power point tracking algorithms for stand-alone photovoltaic systems,” *Solar Energy Materials and Solar Cells*, vol. 90, pp. 1555–1578, Jul. 2006, doi: 10.1016/j.solmat.2005.10.023.

[44] M. Danko, J. Adamec, M. Taraba, and P. Drgona, “Overview of batteries State of Charge estimation methods,” *Transportation Research Procedia*, vol. 40, pp. 186–192, Jan. 2019, doi: 10.1016/j.trpro.2019.07.029.

[45] J. M. Guerrero, J. C. Vasquez, J. Matas, L. G. de Vicuna, and M. Castilla, “Hierarchical Control of Droop-Controlled AC and DC Microgrids—A General Approach Toward Standardization,” *IEEE Transactions on Industrial Electronics*, vol. 58, no. 1, pp. 158–172, Jan. 2011, doi: 10.1109/TIE.2010.2066534.

[46] S. Augustine, M. K. Mishra, and N. Lakshminarasamma, “Adaptive Droop Control Strategy for Load Sharing and Circulating Current Minimization in Low-Voltage Standalone DC Microgrid,” *IEEE Transactions on Sustainable Energy*, vol. 6, no. 1, pp. 132–141, Jan. 2015, doi: 10.1109/TSTE.2014.2360628.

[47] L. Zhang, T. Wu, Y. Xing, K. Sun, and Josep. M. Gurrero, “Power control of DC microgrid using DC bus signaling,” in *2011 Twenty-Sixth Annual IEEE Applied Power Electronics Conference and Exposition (APEC)*, Mar. 2011, pp. 1926–1932. doi: 10.1109/APEC.2011.5744859.

[48] T. Dragičević, J. M. Guerrero, and J. C. Vasquez, “A Distributed Control Strategy for Coordination of an Autonomous LVDC Microgrid Based on Power-Line Signaling,” *IEEE Transactions on Industrial Electronics*, vol. 61, no. 7, pp. 3313–3326, Jul. 2014, doi: 10.1109/TIE.2013.2282597.

[49] M. F. Zia, E. Elbouchikhi, and M. Benbouzid, “Microgrids energy management systems: A critical review on methods, solutions, and prospects,” *Applied Energy*, vol. 222, pp. 1033–1055, Jun. 2018, doi: 10.1016/j.apenergy.2018.04.103.

[50] A. Bidram and A. Davoudi, “Hierarchical Structure of Microgrids Control System,” *IEEE Transactions on Smart Grid*, vol. 3, no. 4, pp. 1963–1976, Dec. 2012, doi: 10.1109/TSG.2012.2197425.

[51] M. F. Zia, M. Benbouzid, E. Elbouchikhi, S. M. Muyeen, K. Techato, and J. Guerrero, “Microgrid Transactive Energy: Review, Architectures, Distributed Ledger Technologies, and Market Analysis,” *IEEE Access*, vol. 8, pp. 19410–19432, Jan. 2020, doi: 10.1109/ACCESS.2020.2968402.

[52] Q. Shafiee, J. M. Guerrero, and J. C. Vasquez, "Distributed Secondary Control for Islanded Microgrids—A Novel Approach," *IEEE Transactions on Power Electronics*, vol. 29, no. 2, pp. 1018–1031, Feb. 2014, doi: 10.1109/TPEL.2013.2259506.

[53] W. Su and J. Wang, "Energy Management Systems in Microgrid Operations," *The Electricity Journal*, vol. 25, no. 8, pp. 45–60, Oct. 2012, doi: 10.1016/j.tej.2012.09.010.

[54] Z. Zhao, J. Hu, and H. Chen, "Bus Voltage Control Strategy for Low Voltage DC Microgrid Based on AC Power Grid and Battery," in *2017 IEEE International Conference on Energy Internet (ICEI)*, Apr. 2017, pp. 349–354. doi: 10.1109/ICEI.2017.68.

[55] Xiao. Zhaoxia, S. Xudong, Z. Xian, and Y. Qingxin, "Control of DC Microgrid for Electrical Vehicles(EV s) Wireless Charging," in *2018 China International Conference on Electricity Distribution (CICED)*, Sep. 2018, pp. 2082–2087. doi: 10.1109/CICED.2018.8592469.

[56] C. Wang, J. Duan, B. Fan, Q. Yang, and W. Liu, "Decentralized High-Performance Control of DC Microgrids," *IEEE Transactions on Smart Grid*, vol. 10, no. 3, pp. 3355–3363, May 2019, doi: 10.1109/TSG.2018.2825199.

[57] S. Anand, B. G. Fernandes, and J. Guerrero, "Distributed Control to Ensure Proportional Load Sharing and Improve Voltage Regulation in Low-Voltage DC Microgrids," *IEEE Transactions on Power Electronics*, vol. 28, no. 4, pp. 1900–1913, Apr. 2013, doi: 10.1109/TPEL.2012.2215055.

[58] V. Nasirian, S. Moayedi, A. Davoudi, and F. L. Lewis, "Distributed Cooperative Control of DC Microgrids," *IEEE Transactions on Power Electronics*, vol. 30, no. 4, pp. 2288–2303, Apr. 2015, doi: 10.1109/TPEL.2014.2324579.

[59] E. Sindi, L. Y. Wang, M. Polis, G. Yin, and L. Ding, "Distributed Optimal Power and Voltage Management in DC Microgrids: Applications to Dual-Source Trolleybus Systems," *IEEE Transactions on Transportation Electrification*, vol. 4, no. 3, pp. 778–788, Sep. 2018, doi: 10.1109/TTE.2018.2844367.

[60] L. Meng, T. Dragicevic, J. M. Guerrero, and J. C. Vasquez, "Dynamic consensus algorithm based distributed global efficiency optimization of a droop controlled DC microgrid," in *2014 IEEE International Energy Conference (ENERGYCON)*, May 2014, pp. 1276–1283. doi: 10.1109/ENERGYCON.2014.6850587.

[61] Y. Yang, W. Pei, and Z. Qi, "Optimal sizing of renewable energy and CHP hybrid energy microgrid system," in *IEEE PES Innovative Smart Grid Technologies*, May 2012, pp. 1–5. doi: 10.1109/ISGT-Asia.2012.6303122.

[62] M. Xu, T. Gu, J. Qin, and W. Zheng, "GA Based Multi-objective Operation Optimization of Power Microgrid," in *2019 International Conference on Intelligent Transportation, Big Data & Smart City (ICITBS)*, Jan. 2019, pp. 103–107. doi: 10.1109/ICITBS.2019.00032.

[63] P. Wang, W. Wang, and D. Xu, "Optimal Sizing of Distributed Generations in DC Microgrids With Comprehensive Consideration of System Operation Modes and Operation Targets," *IEEE Access*, vol. 6, pp. 31129–31140, 2018, doi: 10.1109/ACCESS.2018.2842119.

[64] H. Tao, F. W. Ahmed, H. Abdalqadir kh ahmed, M. Latifi, H. Nakamura, and Y. Li, "Hybrid whale optimization and pattern search algorithm for day-ahead operation of a microgrid in the presence of electric vehicles and renewable energies," *Journal of Cleaner Production*, vol. 308, p. 127215, Jul. 2021, doi: 10.1016/j.jclepro.2021.127215.

[65] M. Iqbal, M. F. Zia, K. Beddiar, and M. Benbouzid, "Optimal Scheduling of Grid Transactive Home Demand Responsive Appliances Using Polar Bear Optimization Algorithm," *IEEE Access*, vol. 8, pp. 222285–222296, Dec. 2020, doi: 10.1109/ACCESS.2020.3043639.

[66] C. Gamarra and J. M. Guerrero, "Computational optimization techniques applied to microgrids planning: A review," *Renewable and Sustainable Energy Reviews*, vol. 48, pp. 413–424, Aug. 2015, doi: 10.1016/j.rser.2015.04.025.

[67] S. Moayedi and A. Davoudi, "Unifying Distributed Dynamic Optimization and Control of Islanded DC Microgrids," *IEEE Transactions on Power Electronics*, vol. 32, no. 3, pp. 2329–2346, Mar. 2017, doi: 10.1109/TPEL.2016.2565517.

[68] D. Zhang, L. Y. Wang, J. Jiang, and W. Zhang, "Optimal Power Management in DC Microgrids With Applications to Dual-Source Trolleybus Systems," *IEEE Transactions on Intelligent Transportation Systems*, vol. 19, no. 4, pp. 1188–1197, Apr. 2018, doi: 10.1109/TITS.2017.2717699.

[69] G. Binetti, A. Davoudi, F. L. Lewis, D. Naso, and B. Turchiano, "Distributed Consensus-Based Economic Dispatch With Transmission Losses," *IEEE Transactions on Power Systems*, vol. 29, no. 4, pp. 1711–1720, Jul. 2014, doi: 10.1109/TPWRS.2014.2299436.

[70] L. Meng, T. Dragicevic, J. M. Guerrero, and J. C. Vásquez, "Optimization with system damping restoration for droop controlled DC-DC converters," in *2013 IEEE Energy Conversion Congress and Exposition*, Sep. 2013, pp. 65–72. doi: 10.1109/ECCE.2013.6646682.

[71] C. Li, F. de Bosio, S. K. Chaudhary, M. Graells, J. C. Vasquez, and J. M. Guerrero, "Operation cost minimization of droop-controlled DC microgrids based on real-time pricing and optimal power flow," in *IECON 2015 - 41st Annual Conference of the IEEE Industrial Electronics Society*, Nov. 2015, pp. 003905–003909. doi: 10.1109/IECON.2015.7392709.

[72] I. U. Nutkani, W. Peng, P. C. Loh, and F. Blaabjerg, "Cost-based droop scheme for DC microgrid," in *2014 IEEE Energy Conversion Congress and Exposition (ECCE)*, Sep. 2014, pp. 765–769. doi: 10.1109/ECCE.2014.6953473.

[73] M. Moradi, M. Eskandari, and S. Hosseinian, "Operational Strategy Optimization in an Optimal Sized Smart Microgrid," *IEEE Transactions on Smart Grid*, vol. 6, pp. 1087–1095, May 2015, doi: 10.1109/TSG.2014.2349795.

[74] S. Benelghali, R. Outbib, and M. Benbouzid, "Selecting and optimal sizing of hybridized energy storage systems for tidal energy integration into power grid," vol. 7, pp. 113–122, Jan. 2019, doi: 10.1007/s40565-018-0442-0.

[75] G. K. Suman, J. M. Guerrero, and O. P. Roy, “Optimisation of solar/wind/bio-generator/diesel/battery based microgrids for rural areas: A PSO-GWO approach,” *Sustainable Cities and Society*, vol. 67, p. 102723, Apr. 2021, doi: 10.1016/j.scs.2021.102723.

[76] M. B. Shadmand and R. S. Balog, “Multi-Objective Optimization and Design of Photovoltaic-Wind Hybrid System for Community Smart DC Microgrid,” *IEEE Transactions on Smart Grid*, vol. 5, no. 5, pp. 2635–2643, Sep. 2014, doi: 10.1109/TSG.2014.2315043.

[77] C. Phurailatpam, B. S. Rajpurohit, and L. Wang, “Optimization of DC microgrid for rural applications in India,” in *2016 IEEE Region 10 Conference (TENCON)*, Nov. 2016, pp. 3610–3613. doi: 10.1109/TENCON.2016.7848731.

[78] R. Dufo-López and J. L. Bernal-Agustín, “Multi-objective design of PV–wind–diesel–hydrogen–battery systems,” *Renewable Energy*, vol. 33, no. 12, pp. 2559–2572, Dec. 2008, doi: 10.1016/j.renene.2008.02.027.

[79] O. Erdinc and M. Uzunoglu, “Optimum design of hybrid renewable energy systems: Overview of different approaches,” *Renewable and Sustainable Energy Reviews*, vol. 16, no. 3, pp. 1412–1425, Apr. 2012, doi: 10.1016/j.rser.2011.11.011.

[80] C. Chen, S. Duan, T. Cai, B. Liu, and G. Hu, “Smart energy management system for optimal microgrid economic operation,” *Renewable Power Generation, IET*, vol. 5, pp. 258–267, Jun. 2011, doi: 10.1049/iet-rpg.2010.0052.

[81] A. H. Fathima and K. Palanisamy, “Optimization in microgrids with hybrid energy systems – A review,” *Renewable and Sustainable Energy Reviews*, vol. 45, pp. 431–446, May 2015, doi: 10.1016/j.rser.2015.01.059.

[82] B. Ramachandran, S. K. Srivastava, C. S. Edrington, and D. A. Cartes, “An Intelligent Auction Scheme for Smart Grid Market Using a Hybrid Immune Algorithm,” *IEEE Transactions on Industrial Electronics*, vol. 58, no. 10, pp. 4603–4612, Oct. 2011, doi: 10.1109/TIE.2010.2102319.

[83] A. Elgammal and M. El-Naggar, “Energy management in smart grids for the integration of hybrid Wind-PV-FC-Battery renewable energy resources Using Multi-Objective Particle Swarm Optimization (MOPSO),” *The Journal of Engineering*, vol. 2018, Sep. 2018, doi: 10.1049/joe.2018.5036.

[84] F. Mohamed and H. Koivo, “Multiobjective optimization using modified game theory for online management of microgrid,” *European Transactions on Electrical Power*, vol. 21, pp. 839–854, Jan. 2011, doi: 10.1002/etep.480.

[85] S. Tan, J. Xu, and S. K. Panda, “Optimization of distribution network incorporating microgrid using vaccine-AIS,” in *IECON 2012 - 38th Annual Conference on IEEE Industrial Electronics Society*, Oct. 2012, pp. 1381–1386. doi: 10.1109/IECON.2012.6388539.

[86] F. A. Mohamed and H. N. Koivo, “System modelling and online optimal management of MicroGrid using Mesh Adaptive Direct Search,” *International Journal of Electrical Power & Energy Systems*, vol. 32, no. 5, pp. 398–407, Jun. 2010, doi: 10.1016/j.ijepes.2009.11.003.

[87] M. A. Mosa and A. A. Ali, “Energy management system of low voltage dc microgrid using mixed-integer nonlinear programing and a global optimization technique,” *Electric Power Systems Research*, vol. 192, p. 106971, Mar. 2021, doi: 10.1016/j.epsr.2020.106971.

[88] R. Rigo-Mariani, “Méthodes de conception intégrée ‘dimensionnement-gestion’ par optimisation d’un micro-réseau avec stockage,” phd, 2014. Available: http://ethesis.inp-toulouse.fr/archive/00002989/.

[89] R. Bellman, “Some Applications of the Theory of Dynamic Programming---A Review,” *Operations Research*, vol. 2, no. 3, pp. 275–288, 1954.

[90] F. Ramahatana and M. David, “Economic optimization of micro-grid operations by dynamic programming with real energy forecast,” *J. Phys.: Conf. Ser.*, vol. 1343, no. 1, p. 012067, Nov. 2019, doi: 10.1088/1742-6596/1343/1/012067.

[91] “Mixed-Integer Linear Programming in MATLAB - Video.” Available:https://www.mathworks.com/videos/mixed-integer-linear-programming-in-matlab-91541.html.

[92] A. C. Luna, N. L. Diaz, M. Graells, J. C. Vasquez, and J. M. Guerrero, “Mixed-Integer-Linear-Programming-Based Energy Management System for Hybrid PV-Wind-Battery Microgrids: Modeling, Design, and Experimental Verification,” *IEEE Transactions on Power Electronics*, vol. 32, no. 4, pp. 2769–2783, Apr. 2017, doi: 10.1109/TPEL.2016.2581021.

[93] J. Hu, Y. Shan, J. Guerrero, A. Ioinovici, K. W. Chan, and J. Rodriguez, “Model predictive control of microgrids – An overview,” *Renewable and Sustainable Energy Reviews*, vol. 136, pp. 1–12, Oct. 2020, doi: 10.1016/j.rser.2020.110422.

[94] W. Gu, Z. Wang, Z. Wu, Z. Luo, Y. Tang, and J. Wang, “An Online Optimal Dispatch Schedule for CCHP Microgrids Based on Model Predictive Control,” *IEEE Transactions on Smart Grid*, vol. 8, no. 5, pp. 2332–2342, Sep. 2017, doi: 10.1109/TSG.2016.2523504.

[95] J. Ospina *et al.*, “Sampling-Based Model Predictive Control of PV-Integrated Energy Storage System Considering Power Generation Forecast and Real-Time Price,” *IEEE Power and Energy Technology Systems Journal*, vol. 6, no. 4, pp. 195–207, Dec. 2019, doi: 10.1109/JPETS.2019.2935703.

[96] R. Palma-Behnke *et al.*, “A Microgrid Energy Management System Based on the Rolling Horizon Strategy,” *IEEE Transactions on Smart Grid*, vol. 4, no. 2, pp. 996–1006, Jun. 2013, doi: 10.1109/TSG.2012.2231440.

[97] W. Su, S. S. Yu, H. Li, H. H.-C. Iu, and T. Fernando, “An MPC-Based Dual-Solver Optimization Method for DC Microgrids With Simultaneous Consideration of Operation Cost and Power Loss,” *IEEE Transactions on Power Systems*, vol. 36, no. 2, pp. 936–947, Mar. 2021, doi: 10.1109/TPWRS.2020.3011038.

[98] M. Taha, H. Abdeltawab, and Y. Mohamed, “An Online Energy Management System for a Grid-Connected Hybrid Energy Source,” *IEEE Journal of Emerging and Selected Topics in Power Electronics*, vol. PP, pp. 1–1, Apr. 2018, doi: 10.1109/JESTPE.2018.2828803.

[99] K. Gao, T. Wang, C. Han, J. Xie, Y. Ma, and R. Peng, “A Review of Optimization of Microgrid Operation,” *Energies*, vol. 14, no. 10, Art. no. 10, Jan. 2021, doi: 10.3390/en14102842.

[100] F. Garcia-Torres and C. Bordons, “Optimal Economical Schedule of Hydrogen-Based Microgrids With Hybrid Storage Using Model Predictive Control,” *IEEE Transactions on Industrial Electronics*, vol. 62, pp. 1–1, Aug. 2015, doi: 10.1109/TIE.2015.2412524.

[101] M. Laera, S. Roggia, M. Dicorato, G. Forte, and M. Trovato, “A procedure for day-ahead optimal operation planning of a MicroGrid,” presented at the 2013 4th IEEE/PES Innovative Smart Grid Technologies Europe, ISGT Europe 2013, Oct. 2013, pp. 1–5. doi: 10.1109/ISGTEurope.2013.6695416.

[102] E. Hleihel, M. Fadel, and H. Y. Kanaan, “Control and Power Management of a 24-Hour DC Microgrid Improved Model,” in *2021 22nd IEEE International Conference on Industrial Technology (ICIT)*, Mar. 2021, pp. 585–592. doi: 10.1109/ICIT46573.2021.9453661.

[103] T. Dragičević, X. Lu, J. C. Vasquez, and J. M. Guerrero, “DC Microgrids—Part II: A Review of Power Architectures, Applications, and Standardization Issues,” *IEEE Transactions on Power Electronics*, vol. 31, no. 5, pp. 3528–3549, May 2016, doi: 10.1109/TPEL.2015.2464277.

[104] W. Hankache, “Gestion optimisée de l’énergie électrique d’un groupe électrogène hybride à pile à combustible,” phdthesis, Institut National Polytechnique de Toulouse - INPT, 2008. Available: https://tel.archives-ouvertes.fr/tel-00567577.

[105] C. Zhou, K. Qian, M. Allan, and W. Zhou, “Modeling of the Cost of EV Battery Wear Due to V2G Application in Power Systems,” *IEEE Transactions on Energy Conversion*, vol. 26, no. 4, pp. 1041–1050, Dec. 2011, doi: 10.1109/TEC.2011.2159977.

[106] “IEEE Recommended Practice for 1 kV to 35 kV Medium-Voltage DC Power Systems on Ships,” *IEEE Std 1709-2010*, pp. 1–54, Nov. 2010, doi: 10.1109/IEEESTD.2010.5623440.

[107] G. T. Heydt, “Future renewable electrical energy delivery and management systems: Energy reliability assessment of FREEDM systems,” in *IEEE PES General Meeting*, Jul. 2010, pp. 1–4. doi: 10.1109/PES.2010.5589348.

[108] “Energy China, Commission of Suzhou Medium and Low Voltage DC Distribution and Utilization System.”
Available: http://www.jspdi. ceec.net.cn/art/2021/10/11/art_8540_2511475.html.

[109] Z. Ma, Y. Li, Y. Sun, and K. Sun, “Low voltage direct current supply and utilization system: Definition, key technologies and development,” *CSEE Journal of Power and Energy Systems*, pp. 1–20, 2022, doi: 10.17775/CSEEJPES.2022.02130.

[110] “IEC 60038 - IEC standard voltages,” iTeh Standards.
Available:https://standards.iteh.ai/catalog/standards/iec/ff6a9c53-5a77-4fe8-a1f9-3dcd90e73e30/iec-60038.

[111] “IEC 61140:2016 - Protection against electric shock - Common aspects for installation and equipment,” iTeh Standards. Available:https://standards.iteh.ai/catalog/standards/iec/4a8d46c1-eafd-48ff-8727-18c1faef3aec/iec-61140-2016.

[112] “HD 60364-4-41:2017 - Low-voltage electrical installations - Part 4-41: Protection for safety - Protection against electric shock,” iTeh Standards. Available:https://standards.iteh.ai/catalog/standards/clc/ba30ce0f-1ce1-49e3-8ba2-18cfe4714b8c/hd-60364-4-41-2017.

[113] W. Li, X. Mou, Y. Zhou, and C. Marnay, “On voltage standards for DC home microgrids energized by distributed sources,” in *Proceedings of The 7th International Power Electronics and Motion Control Conference*, Jun. 2012, pp. 2282–2286. doi: 10.1109/IPEMC.2012.6259203.

[114] R. F. Miranda *et al.*, “Distributed generation in low-voltage DC systems by wind energy in the Baja California Peninsula, Mexico,” *Energy*, vol. 242, no. C, 2022, Available: https://ideas.repec.org//a/eee/energy/v242y2022ics0360544221027791.html.

[115] “IEEE Recommended Practice for the Design of DC Power Systems for Stationary Applications,” *IEEE Std 946-2020 (Revision of IEEE Std 946-2004)*, pp. 1–74, Sep. 2020, doi: 10.1109/IEEESTD.2020.9206101.

[116] “Implement PV array modules - Simulink.” Available: https://www.mathworks.com/help/sps/powersys/ref/pvarray.html.

[117] On Semiconductor, “IGBT Technologies and Applications Overview: How and When to Use an IGBT.” Semiconductor Components Industries, Sep. 2018.

[118] A. Elnaggar, “Standard Calculation of Fault Current Contribution of Doubly Fed Induction Generator-Based Wind Turbine,” 2016, pp. 277–301. doi: 10.5772/63450.

[119] “What is the Nyquist theorem?,” WhatIs.com. Available: https://www.techtarget.com/whatis/definition/Nyquist-Theorem.

[120] “250-kW Grid-Connected PV Array - MATLAB & Simulink.” Available:https://www.mathworks.com/help/sps/ug/250-kw-grid-connected-pv-array.html;jsessionid=123920d5e2b4ecad79ff44a2b48b.

[121] “Detailed Model of a 100-kW Grid-Connected PV Array - MATLAB & Simulink.” Available: https://www.mathworks.com/help/sps/ug/detailed-model-of-a-100-kw-grid-connected-pv-array.html.

[122] M. Faifer, L. Piegari, M. Rossi, and S. Toscani, “An Average Model of DC-DC Step-Up Converter Considering Switching Losses and Parasitic Elements,” *Energies*, vol. 14, p. 7780, Nov. 2021, doi: 10.3390/en14227780.

[123] D. Maksimovic, A. M. Stankovic, V. J. Thottuvelil, and G. C. Verghese, “Modeling and simulation of power electronic converters,” *Proceedings of the IEEE*, vol. 89, no. 6, pp. 898–912, Jun. 2001, doi: 10.1109/5.931486.

[124] “Power Electronics for Renewable Energy Systems, Transportation and Industrial Applications | Wiley,” Wiley.com.

Available:https://www.wiley.com/en-us/Power+Electronics+for+Renewable+Energy+Systems%2C+Transportation+and+Industrial+Applications-p-9781118634035.

[125] R. Erickson and D. Maksimovic, *Fundamentals of Power Electronics Second Edition*, Second Edition. University of Colarado Boulder, Colorado: Kluwer Academic Publishers, 2004.Available:http://www.pdfdrive.com/fundamentals-of-power-electronics-e5904858.html.

[126] A. Ayachit and M. K. Kazimierczuk, "Averaged Small-Signal Model of PWM DC-DC Converters in CCM Including Switching Power Loss," *IEEE Transactions on Circuits and Systems II: Express Briefs*, vol. 66, no. 2, pp. 262–266, Feb. 2019, doi: 10.1109/TCSII.2018.2848623.

[127] T. Halder, *Study of rectifier diode loss model of the Flyback converter*. 2012, p. 6. doi: 10.1109/PEDES.2012.6484492.

[128] J. Schonberger and G. Feix, *Modelling turn-off losses in power diodes*. 2008, p. 6. doi: 10.1109/COMPEL.2008.4634701.

[129] "AN-301 - Qspeed Reverse Recovery Charge, Current and Time | Power Integrations, Inc." Available:https://www.power.com/design-support/application-notes/an-301-qspeed-reverse-recovery-charge-current-and-time.

[130] M. M. Awan, *A Technical Review of MPPT Algorithms for Solar Photovoltaic System: SWOT Analysis of MPPT Algorithms*, vol. 12. 2022. doi: 10.33317/ssurj.433.

[131] R. B. Bollipo, S. Mikkili, and P. K. Bonthagorla, "Critical Review on PV MPPT Techniques: Classical, Intelligent and Optimisation," *IET Renewable Power Generation*, vol. 14, no. 9, pp. 1433–1452, 2020, doi: 10.1049/iet-rpg.2019.1163.

[132] S. Sumathi, L. Ashok Kumar, and P. Surekha, *Solar PV and Wind Energy Conversion Systems*. in Green Energy and Technology. Cham: Springer International Publishing, 2015. doi: 10.1007/978-3-319-14941-7.

[133] "Grid Integration of Wind Energy Conversion Systems by Siegfried Heier - 1998-11-13," Biblio.co.uk. Available:https://biblio.co.uk/book/grid-integration-wind-energy-conversion-systems/d/456495862.

[134] M. A. A. E. Hamied and N. H. El. Amary, "Permanent Magnet Synchronous Generator Stability Analysis and Control," *Procedia Computer Science*, vol. 95, pp. 507–515, Jan. 2016, doi: 10.1016/j.procs.2016.09.328.

[135] M. Cheah-Mane, J. Liang, and N. Jenkins, "Permanent magnet synchronous generator for wind turbines: Modelling, control and Inertial Frequency Response," in *2014 49th International Universities Power Engineering Conference (UPEC)*, Sep. 2014, pp. 1–6. doi: 10.1109/UPEC.2014.6934799.

[136] "Introducing the Phasor Simulation Method - MATLAB & Simulink." Available: https://www.mathworks.com/help/sps/powersys/ug/introducing-the-phasor-simulation-method.html.

[137] Z. Chen, L. Yuan, Z. Zhao, and X. Sun, “Power losses in two- and three-level three phase photovoltaic inverters equipped with IGBTs,” in *2012 15th International Conference on Electrical Machines and Systems (ICEMS)*, Oct. 2012, pp. 1–6.

[138] K. Zhou and D. Wang, “Relationship between space-vector modulation and three-phase carrier-based PWM: a comprehensive analysis [three-phase inverters],” *Industrial Electronics, IEEE Transactions on*, vol. 49, pp. 186–196, Mar. 2002, doi: 10.1109/41.982262.

[139] M. H. Bierhoff and F. W. Fuchs, “Semiconductor losses in voltage source and current source IGBT converters based on analytical derivation,” in *2004 IEEE 35th Annual Power Electronics Specialists Conference (IEEE Cat. No.04CH37551)*, Jun. 2004, pp. 2836-2842 Vol.4. doi: 10.1109/PESC.2004.1355283.

[140] U. Mulleriyawage and W. Shen, “A Review of Battery Energy Storage Systems for Residential DC Microgrids and Their Economical Comparisons,” *DEStech Transactions on Environment, Energy and Earth Sciences*, Feb. 2019, doi: 10.12783/dteees/iceee2018/27856.

[141] K. Li and K. J. Tseng, “Energy efficiency of lithium-ion battery used as energy storage devices in micro-grid,” in *IECON 2015 - 41st Annual Conference of the IEEE Industrial Electronics Society*, Nov. 2015, pp. 005235–005240. doi: 10.1109/IECON.2015.7392923.

[142] A. Assunção, P. S. Moura, and A. T. de Almeida, “Technical and economic assessment of the secondary use of repurposed electric vehicle batteries in the residential sector to support solar energy,” *Applied Energy*, vol. 181, pp. 120–131, Nov. 2016, doi: 10.1016/j.apenergy.2016.08.056.

[143] O. Tremblay and L.-A. Dessaint, “Experimental validation of a battery dynamic model,” *World Electr Veh J*, vol. 3, pp. 1–10, Jun. 2009, doi: 10.3390/wevj3020289.

[144] L. H. Saw, K. Somasundaram, Y. Ye, and A. A. O. Tay, “Electro-thermal analysis of Lithium Iron Phosphate battery for electric vehicles,” *Journal of Power Sources*, vol. 249, pp. 231–238, Mar. 2014, doi: 10.1016/j.jpowsour.2013.10.052.

[145] C. Zhu, X. Li, L. Song, and L. Xiang, “Development of a theoretically based thermal model for lithium ion battery pack,” *Journal of Power Sources*, vol. 223, pp. 155–164, Feb. 2013, doi: 10.1016/j.jpowsour.2012.09.035.

[146] J. Wang, B. Wang, L. Zhang, J. Wang, N. I. Shchurov, and B. V. Malozyomov, “Review of bidirectional DC–DC converter topologies for hybrid energy storage system of new energy vehicles,” *Green Energy and Intelligent Transportation*, vol. 1, no. 2, p. 100010, Sep. 2022, doi: 10.1016/j.geits.2022.100010.

[147] Windfinder.com, “Windfinder.com - Wind & weather forecast Toulouse-Blagnac Airport,” Windfinder.com. Available: https://www.windfinder.com/forecast/toulouse_blagnac.

[148] “éCO2mix - Les données de marché.” Available: https://www.rte-france.com/eco2mix/les-donnees-de-marche.

[149] “Coefficients de profils dynamiques en J+1.”

Available:https://data.enedis.fr/explore/dataset/coefficients-de-profils-dynamiques-anticipes-en-j1/.

[150] "Free Solar Radiation Historical Data for Researchers." Available: https://solcast.com/data-for-researchers.

[151] B. Fox *et al.*, *Wind Power Integration: Connection and System Operational Aspects*. 2007. doi: 10.1049/PBPO050E.

[152] A. A. Moghaddam, A. Seifi, T. Niknam, and M. R. Alizadeh Pahlavani, "Multi-objective operation management of a renewable MG (micro-grid) with back-up micro-turbine/fuel cell/battery hybrid power source," *Energy*, vol. 36, no. 11, pp. 6490–6507, Nov. 2011, doi: 10.1016/j.energy.2011.09.017.

[153] A. Hoke, A. Brissette, S. Chandler, A. Pratt, and D. Maksimović, "Look-ahead economic dispatch of microgrids with energy storage, using linear programming," in *2013 1st IEEE Conference on Technologies for Sustainability (SusTech)*, Aug. 2013, pp. 154–161. doi: 10.1109/SusTech.2013.6617313.

[154] R. Bellman, "The theory of dynamic programming," *Bulletin of the American Mathematical Society*, vol. 60, no. 6, pp. 503–515, Nov. 1954.

[155] R. Torkan, A. Ilinca, and M. Ghorbanzadeh, "A genetic algorithm optimization approach for smart energy management of microgrids," *Renewable Energy*, vol. 197, pp. 852–863, Sep. 2022, doi: 10.1016/j.renene.2022.07.055.

[156] T. Dragičević, X. Lu, J. C. Vasquez, and J. M. Guerrero, "DC Microgrids—Part I: A Review of Control Strategies and Stabilization Techniques," *IEEE Transactions on Power Electronics*, vol. 31, no. 7, pp. 4876–4891, Jul. 2016, doi: 10.1109/TPEL.2015.2478859.

[157] A. C. Luna, L. Meng, N. L. Diaz, M. Graells, J. C. Vasquez, and J. M. Guerrero, "Online Energy Management Systems for Microgrids: Experimental Validation and Assessment Framework," *IEEE Transactions on Power Electronics*, vol. 33, no. 3, pp. 2201–2215, Mar. 2018, doi: 10.1109/TPEL.2017.2700083.

[158] Z. Ugray, L. Lasdon, J. Plummer, F. Glover, J. Kelly, and R. Marti, "Scatter Search and Local NLP Solvers: A Multistart Framework for Global Optimization," *INFORMS Journal on Computing*, vol. 19, pp. 328–340, Aug. 2007, doi: 10.2139/ssrn.886559.

[159] F. Glover, "A template for scatter search and path relinking," in *Artificial Evolution*, J.-K. Hao, E. Lutton, E. Ronald, M. Schoenauer, and D. Snyers, Eds., in Lecture Notes in Computer Science. Berlin, Heidelberg: Springer, 1998, pp. 1–51. doi: 10.1007/BFb0026589.

[160] J. A. Duffie, W. A. Beckman, and N. Blair, *Solar Engineering of Thermal Processes, Photovoltaics and Wind*. John Wiley & Sons, 2020.

[161] E. Hleihel, M. Fadel, and H. Kanaan, "Simulation of an Islanded DC Microgrid Using Instantaneous and Average Modeling Approaches," 2020, pp. 193–207. doi: 10.1007/978-3-030-37161-6_15.

[162] E. Hleihel, M. Fadel, and H. Kanaan, "Multi-objective Optimization of a DC Microgrid with a Back-up Diesel Generator," in *2022 3rd International Conference on Smart Grid and*

Renewable Energy (SGRE), Doha, Qatar: IEEE, Mar. 2022, pp. 1–7. doi: 10.1109/SGRE53517.2022.9774128.

[163] E. Hleihel, M. Fadel, and H. Kanaan, “Control and Power Sharing of an Islanded DC Microgrid Integrating a Back-up Diesel Generator,” Jun. 2020, pp. 1–8. doi: 10.1109/REDEC49234.2020.9163831.